

CRANFIELD UNIVERSITY

MARCO BOSCOLO

**A FINITE ELEMENT ANALYSIS OF
BONDED CRACK RETARDERS FOR
INTEGRAL AIRCRAFT
STRUCTURES**

SCHOOL OF ENGINEERING
Department of Aerospace Engineering

PhD THESIS
Academic Year 2008-09

Supervisor: Dr. Xiang Zhang
April 2009

CRANFIELD UNIVERSITY

SCHOOL OF ENGINEERING
Department of Aerospace Engineering

PhD THESIS

Academic Year 2008-09

MARCO BOSCOLO

A finite element analysis of bonded crack retarders for
integral aircraft structures

Supervisor: Dr. Xiang Zhang

April 2009

This thesis is submitted in partial fulfillment of the requirements for the degree
of Doctor of Philosophy

©Cranfield University 2009. All rights reserved. No part of this publication
may be reproduced without the written permission of the copyright owner.

Abstract

Trends in aircraft design and manufacture are towards the reduction of manufacturing cost and structural weight while maintaining high level of safety. These reductions can be achieved by using integral structures. However, integral structures lack redundant structural members, hence fail safety is not guaranteed. Bonded selective reinforcements (straps) can obviate this problem and improve the damage tolerance capability of integral structures, although increase the design difficulties.

The objective of this research is to develop an effective analysis method to predict the fatigue crack growth (FCG) life of integral structures reinforced by bonded crack retarders, determine the effectiveness of the reinforcements, and assess the important strap design parameters.

The main mechanisms that influence the crack propagation have been identified, modelled, and discussed. When a crack propagates in the panel skin, bonded straps delay the fracture growth by exerting bridging forces at the crack tip. Nevertheless damage also affects the strap due to the stiffness mismatch and high stress concentration, and the strap/substrate interface is affected by a progressive delamination that advances together with the substrate crack and limits the strap bridging action. Tensile thermal residual stresses (TRS) in the cracked substrate, caused by the adhesive cure process, act to open the crack and hence increase the growth rate. Last but not least, secondary bending caused by the non-symmetric configurations induces a stress gradient along the crack front. This reduces the effectiveness of the bridging action and causes a curved crack front.

An enhanced 2D FE modelling technique that takes into account of these mechanisms and their interactions has been developed and implemented in a computer

program that interfaces the commercial code NASTRAN. This program is used to calculate the stress intensity factors and the FCG life of bonded strap reinforced integral structures.

This modelling technique has been validated for a wide range of test samples in terms of TRS and their redistribution with crack propagation, disbond areas, and FCG lives. The FCG life of a large scale integral skin-stringer panel reinforced by various bonded straps has also been predicted and compared with the experiments. Numerical predictions have shown good agreement with the experimental measurements.

Parametric studies have been conducted to understand the effectiveness of different strap configurations on crack growth retardation; these include different strap materials, strap dimensions and locations on the substrate.

A design tool has been developed aimed at achieving optimal crack retarder design in terms of prescribed fatigue life target and minimum structural weight.

In conclusion, a novel modelling tool has been developed, the effectiveness of bonded straps in retarding fatigue crack growth has been demonstrated and, following the parametric analysis, the most important parameters in the design of bonded straps have been identified.

Acknowledgements

First and foremost I offer my sincere gratitude to my supervisor, Dr Xiang Zhang, who has led me through this pleasantly challenging journey that was my PhD course, who has always been available at the moment of need and who has offered me precious technical advice and guidance without which this research work and thesis would have never been accomplished.

I also would like to thank Dr Giuliano Allegri for his valuable contribution in getting me started on this research project as well as his advice on mechanics of continuum, delamination analysis, FE modelling and many other subjects.

A vote of thanks to each of the members of the research consortium with whom I enjoyed working for the past three years: Prof Philip E. Irving, who has led the project and helped me interface with what he likes to call the “real world”, that is the experimental world; Dr Douglas Figueroa-Gordon and Dr David Liljedahl for providing me experimental data for validation purposes; Prof Ivana K. Partridge who made me improve my presentation skills with her tough but constructive criticisms; the industrial sponsors, Markus Heinemann, Gerry Shepherd, Frank Shoup, Ben Tovey, and Jiazhen Zhang, for providing financial support and to keep me focused on the objectives and deadlines of a research project which offered many scientific distractions.

Beyond the university life, I am very glad to have met some people who I am honoured to call friends: Geppo and Laura, with whom I had countless good times and helped me out in my everyday life in a foreign country; Harry or Harrifer, my big fat Greek pal and gym buddy with whom I always have a good laugh or an intellectual discussion spiced up by his colourful language; Guido, with whom I spent most of my Saturdays playing snooker, winning dinners, playing Xbox/Wii and eating junk food; Mattia who made me face some of the

most difficult integrals and existential problems I have ever seen; Matteo and Ryoko with whom I had endless Romeo&Juliet-like conversations (please, don't get me wrong, it is because we used to chat through his office window); Andrea and Fra, the last arrived at Cranfield but always present when we were having a good time. I must say that them all were also fellow students with whom, I have had loads of fun and many of coffee, cigarette, lunch and I'm-really-tired-I-don't-wanna-work-anymore breaks.

A special thank goes to my family, who, although far in miles, is always close to my heart. My mum, who is always busy and leaves me on the phone wondering whether the line dropped; my dad, who waits for me to say "ehh!?!?" so that he can blow a "pernacchia" to me; and my sister, who always wants to play on line or ask me some chemistry questions. What a lovely crazy family I have. I love you to bits.

Last but not least, the biggest thanks go to my girlfriend and life partner, Jenny Presta, with whom I shared each and every single day of my life here at Cranfield and who had to put up with me during many of my ups and downs encountered in my PhD. I would like to thank you for your encouragement and support but more than anything for loving me.

Thanks to you all for making of my time at Cranfield such a wonderful and unforgettable experience.

Contents

Abstract	i
Acknowledgements	iii
Contents	v
List of figures	xiii
List of tables	xxi
List of abbreviations, nomenclature and symbols	xxiii
1 Introduction	1
1.1 Overview	1
1.1.1 Trends in aircraft design: new design techniques	1
1.1.2 Integral structures: a possible solution	4
1.1.3 Fatigue design philosophies: safe life, fail safe and damage tolerance	6
1.1.4 Selective reinforcements to ensure fail safety for integral structures	8
1.2 The project scope	10

1.3	Objectives	10
1.4	Structure of the thesis	11
2	Theoretical Framework	17
2.1	Linear elastic fracture mechanics	17
2.1.1	Stress intensity factor	18
2.1.2	The energy approach: strain energy release rate	21
2.1.3	How to calculate the SIF of a structure	22
2.2	SIF computation through FE method	23
2.2.1	Virtual crack closure technique	26
2.3	Fatigue crack growth	30
2.3.1	Importance of stress intensity factor range and R-ratio	30
2.3.2	Paris Equation	32
2.3.3	NASGRO equation	33
2.3.4	Tabular look-up and Harther T-method	34
2.3.5	Numerical integration to obtain the FCG life	36
2.3.6	Consideration on FCG life prediction	39
3	Literature Review	41
3.1	Bonded patch repair for metallic aircraft structures	42
3.1.1	Purpose and use	42
3.1.2	Important aspects in the design of the patch	44
3.1.3	Analytical methods to study bonded repairs	47
3.1.4	Numerical methods to study adhesively patched structures	55
3.1.5	Room for improvement for numerical modelling techniques	64

3.2	Delamination and progressive adhesive failure modelling	65
3.2.1	Static loading	66
3.2.2	Fatigue loading	68
3.3	Bonded crack retarders	71
4	Modelling methodology	75
4.1	Mechanisms	75
4.2	Two layer plus spring modelling technique	78
4.2.1	Employed finite elements	78
4.2.2	Stress intensity factor with secondary bending effect	81
4.2.3	Disbond failure modelling	84
4.2.4	Thermal residual stress (TRS) calculation	88
4.3	Fatigue crack growth prediction	91
4.3.1	Geometric non-linearity effect	91
4.3.2	Equivalent stress intensity factor: weight function	93
4.3.3	Integration and FCG life prediction	95
4.3.4	Life Increment Crack Retarders Analysis (LICRA) computer code	97
4.4	3D modelling technique	98
5	Validation: test coupon level	101
5.1	Un-reinforced plates	102
5.1.1	Mesh convergence	102
5.1.2	β solution accuracy	103
5.1.3	FCG validation	105

5.2	Reinforced plates	109
5.2.1	Specimen geometries and materials	109
5.2.2	SIF distribution through the plate thickness	110
5.2.3	Progressive disbond failure	112
5.2.4	Thermal residual stresses and redistribution	116
5.2.5	Influence of geometric nonlinearity and thermo mechanical load coupling	119
5.2.6	FCG life predictions	124
5.3	Modelling technique critique: strong and weak points	130
6	Parametric Studies	133
6.1	Room temperature cure: no TRS	134
6.1.1	Strap material	134
6.1.2	Strap dimension	139
6.1.3	Stiffness ratio	141
6.1.4	Sensitivity analysis	142
6.2	Elevated temperature cure	147
6.2.1	TRS effect	147
6.2.2	Effect of TRS at high and low applied load	148
6.2.3	Effect of strap dimension on TRS	150
6.2.4	Strap material	152
6.2.5	Strap dimension	153
6.3	Design graph	154
6.4	Design guidelines	156

7	Large-scale integral skin-stringer panels	159
7.1	From samples to large scale structures	159
7.2	Un-reinforced panel	161
7.2.1	Geometry, material and applied load	161
7.2.2	FE model simplifications: meshing, stress and secondary bending analysis	163
7.2.3	β solution and FCG life validation	167
7.3	Reinforced panel	171
7.3.1	Strap geometries and materials	171
7.3.2	Stiffening effect	173
7.3.3	Stress analysis of the straps	175
7.3.4	Thermal residual stress analysis	178
7.3.5	FCG life validation: GLARE wide	180
7.3.6	Strap configuration comparison	183
8	Conclusions and future studies	189
8.1	Predictive model development	189
8.2	Design parameter studies	190
8.3	Contributions to knowledge	191
8.4	Recommended future studies	192
	References	195
A	List of publications	211
B	Validation of predicted FCG rates and lives	215

C Large panel: technical drawings	219
D LICRA package user's instructions	223
D.1 How to build the FE model	223
D.1.1 Geometry and orientation	223
D.1.2 Meshing and boundary conditions	224
D.1.3 Load Application	224
D.1.4 Strap modelling and adhesive modelling	225
D.1.5 Preparing the model for analysis	227
D.1.6 Creating files for analysis	228
D.2 Multi point constrain application program: MPC.m	238
D.3 SIF computation program: analysis_v2.m	240
D.3.1 How to run the program	240
D.3.2 Output files	248
D.4 Averaged SIF range computation program: beta_Max_min.m . . .	250
D.4.1 How to run the program	250
D.4.2 Output files	252
D.5 FCG life computation program: FCG_tabular.m	253
D.5.1 Input files	253
D.5.2 How to run the program	254
D.5.3 Output files	256
D.6 Through-thickness SERR and SIF distribution: plot_2D_result.m .	258
D.6.1 How to run the program	258

D.6.2	Output files	259
E	User's instructions to the 3D-VCCT program code	261
E.1	How to build the FE model	261
E.2	SIF computation program	262
E.2.1	How to run the code	262
E.2.2	Output files	267

List of Figures

1.1	Direct operating cost of an aircraft	2
1.2	Build-up and integral structures: different design concept	4
1.3	Use of stringer panels in an aircraft	5
1.4	Damage tolerance: FCG and residual strength curves	8
1.5	Sketch of a integral wing panel with selective reinforcements	9
1.6	Weigh-cost analysis carried out by Alcoa on hybrid structures	9
2.1	The three modes to load a crack in a solid.	18
2.2	Stress condition at the crack tip.	19
2.3	Stress field at the crack tip.	19
2.4	Effect of specimen thickness on fracture toughness	21
2.5	Virtual crack closure technique; two-step analysis; two-dimensional four-noded plate/shell element.	27
2.6	Modified virtual crack closure technique; one-step analysis; two-dimensional four-node plate/shell elements.	28
2.7	Modified virtual crack closure technique for delamination study.	29
2.8	Modified virtual crack closure technique for 3D 8-noded brick elements.	29
2.9	Example of fatigue crack growth life graph.	30

2.10	Relation between stress intensity factor range and crack growth rate. The three crack growth regimes are shown.	31
2.11	Effect of the R -ratio	32
2.12	Harter T-method	36
2.13	Use of the material law for the FCG life computation	37
2.14	Fatigue crack growth life: integration process.	39
3.1	Cross-section view of examples of single-sided and double-sided path repairs.	46
3.2	Sketch of two adhesively bonded plates with a centre crack in one.	48
3.3	Example of a strip-like patch repair	51
3.4	Effect of patch position and thickness on the stress intensity factor.	57
3.5	Decohesion element constitutive relations	66
3.6	Cohesive zone response and parameters needed to characterise it.	67
3.7	Example of delamination growth rate law.	69
4.1	Diagram of employed finite elements for modelling the substrate plate, reinforcement strap and adhesive.	78
4.2	Area A_a for calculating the stiffness of the spring elements used to model the adhesive element in the centre of the picture.	79
4.3	Diagram of plate modelling approximations: from real plate to plate finite element.	80
4.4	Schematic of the modified virtual crack closure technique (MVCCT) for the lead crack in substrate.	82
4.5	Schematic of MVCCT for computing the strain energy release rate for candidate spring elements along the disbond front.	86
4.6	Example of introduction of adhesive defect to model adhesive failure initiation.	87

4.7	Cross section of two bonded plates subjected to a temperature load ΔT	88
4.8	Side view sketch of a reinforced plate showing the difference in applying the superposition rule and non-linear analysis when secondary bending and non-linearity are involved in the problem. . .	92
4.9	LICRA flow chart	99
4.10	Flow diagram of 3D-VCCT computer code to computed distribution of SIF through the thickness by 3D FE models.	100
5.1	M(T) sample geometry	102
5.2	Mesh convergence test for a un-reinforced M(T) plate.	103
5.3	Validation of β solutions against analytical solutions.	104
5.4	Dimension and geometry of the specimens without straps. (Sketches not to scale)	106
5.5	Material law of fatigue crack growth rate for aluminium alloy 7085-T7651.	107
5.6	Validation of FCG rate and life against test results for un-reinforced SENT and M(T) samples.	108
5.7	Geometry and dimension of two test specimens. Strap dimensions are variable.	110
5.8	SERR through-thickness distribution: SENT sample with titanium strap $w20d5t2l200$	113
5.9	SIF through-thickness distribution: SENT sample with titanium strap $w20d5t2l200$	114
5.10	Comparison of 2D and 3D model calculated SERR and SIF values in two different thickness positions.	115
5.11	Final disbond shapes: modelling vs. experimental measurements.	116

5.12	Definition of lines along which the TRS were calculated for the SENT specimens.	117
5.13	Distributions of initial residual stresses in the longitudinal direction in the SENT bonded with various straps: computation vs. measurement	120
5.14	Redistribution of TRS with crack propagation: computation vs. measurement for SENT sample with titanium strap $w20d20t2l200$. 121	
5.15	Influence of geometric nonlinearity on the dimensionless SIF (β) due to different magnitude of secondary bending and disbond. . .	122
5.16	Interaction of mechanical and thermal loads at low and high applied load. SENT sample with titanium strap $w20d20t2l200$	123
5.17	Validation of FCG rate and life against test results: SENT, Ti6Al4V strap $w20d5t2l200$, HT cure.	124
5.18	Validation of FCG rate and life against test results: SENT, CFRP strap $w20d5t2l200$, HT cure.	125
5.19	Validation of FCG rate and life against test results: M(T), GFRP strap $w20d2.5t4.4l180$, HT cure.	126
5.20	Validation of FCG rate and life against test results: M(T), Al strap $w20d2.5t5l180$, HT cure.	127
5.21	Validation of FCG rate and life against test results: M(T), GLARE strap $w10d8t5.4l180$, RT cure.	127
5.22	Summary of the prediction errors.	128
6.1	M(T) sample with CFRP straps; comparison of different lay-ups: unidirectional (UD) $[0]_4$, cross-ply (CP) $[90/0]_s$, angle $[30/60]_s$, bias $[-45/45]_s$	135
6.2	Comparison of different strap materials. M(T) sample.	136
6.3	Crack length of complete disbond for three different strap configurations under different load values.	136

6.4	Comparison of grade 5 titanium and grade 2 titanium straps. . . .	138
6.5	Comparison von Mises stress in titanium straps for a crack length $a = 124$ mm	139
6.6	Influence of different strap positions and dimensions. SENT sample.	140
6.7	σ_{yy} stress in the substrate as a function of the strap stiffness: stiffening effect.	142
6.8	Stress carried by the strap as a function of the stiffening ratio. Applied stress 70 MPa.	143
6.9	Shear stress in the adhesive as a function of the stiffness ratio. Applied stress 70 MPa	143
6.10	Effect of strap elastic modulus on the FCG live. Strap dimension $w20d2.5t5l180$. No TRS. Applied stress $\sigma_{max} = 60$ MPa.	144
6.11	Effect of strap elastic modulus on the FCG live for different applied stresses.	145
6.12	Effect of adhesive toughness (G_{IIc}) on FCG life. Strap dimension $w20d2.5t5l180$	145
6.13	Effect of the critical strain energy release rate of the adhesive on the FCG life	146
6.14	FCG lives due to ideal adhesive at low and high applied load. . .	147
6.15	Effect of TRS for a GFRP strap of dimension $w20d5t2l200$ loaded at $\sigma_{max} = 18.57$ MPa	148
6.16	Comparison of SIF ranges and R ratios at low and high applied load.	149
6.17	Effect of the TRS on FCG rates at low and high applied load, with and without TRS.	149
6.18	Comparison of TRS and residual SIF for straps of different thick- nesses $t = 2, 4, 6$ mm.	150

6.19 Comparison of TRS and residual SIF for straps of different widths $w = 20, 60, 100 \text{ mm}$	151
6.20 Comparison of TRS and residual SIF for straps of different lengths $l = 200, 160, 90 \text{ mm}$	151
6.21 Comparison of TRS and residual SIF by keeping the strap cross section area constant.	152
6.22 Comparison of FCG rate and life for different strap materials with the same dimension $w20t2d5l200$	152
6.23 Effect of strap width in the presence of TRS.	153
6.24 Comparison of FCG rate and life for constant cross section area GLARE straps.	154
6.25 Example of using the design graph to find strap geometry (CFRP cross ply)	155
7.1 Cross section sketch of the integral panel.	161
7.2 Sketch of the un-reinforced large-scale integral skin-stringer panel	161
7.3 Applied variable amplitude load spectrum.	162
7.4 Summary of the possible fatigue load cycles and their contribution to the FCG.	163
7.5 Un-reinforced panel: 3D FE model.	163
7.6 3D FE model to 2D FE model simplification.	164
7.7 Un-reinforced panel: 2D FE model.	165
7.8 Stresses contour and and deformed shape by 2D and 3D FE models.	166
7.9 Out-of-plane displacement (w): comparison of 3D and 2D FE models.	167
7.10 Stresses contour and and deformed shape of the cracked panel: comparison of 2D and 3D FE models.	168

7.11	Model of crack growing into the stringer till stringer failure.	169
7.12	β solutions of the un-reinforced stringer panel.	169
7.13	Validation of FCG rate and life against test results: un-reinforced integral stringer panel	170
7.14	Difference between modelling of crack propagating in the stringer and real situation.	170
7.15	Cross section sketch of the reinforced integral panels.	173
7.16	Reinforced panels: 2D FE mesh.	174
7.17	Comparison of von Mises stresses in the substrate at the maximum applied load for the different strap configurations.	176
7.18	Stiffening effect: σ_{yy} stress in the substrate.	177
7.19	Aluminium strap configurations: von Mises stresses in the straps .	177
7.20	GLARE strap configurations: von Mises stress in the straps in the absence of TRS effect.	178
7.21	TRS comparison between wide and narrow GLARE strap config- uration: σ_{yy} at the top of the substrate.	179
7.22	Comparison of TRS between the two GLARE strap configurations.	179
7.23	Residual SIF for the wide and narrow GLARE strap configurations.	180
7.24	GLARE wide strap configuration: β solutions.	181
7.25	GLARE wide strap configuration: FCG rate and life validation against experiments.	182
7.26	GLARE wide strap configuration: von Mises stress contours on the bottom ply (nearest to substrate and most stressed) as a function of the substrate crack length.	184
7.27	β solutions for the different strap configurations without modelling disbond failure.	185

7.28 β solutions for the different strap configurations with disbond analysis.	185
7.29 FCG rate and life comparisons for the four strap configurations: GLARE and aluminium, wide and narrow	186
7.30 Von Mises stress contours for a substrate crack $a = 165$ mm for aluminium strap configurations.	188
B.1 Validation of FCG rate and life against test results: SENT, Ti grade2 strap $w20d5t2l200$, HT cure.	215
B.2 Validation of FCG rate and life against test results: SENT, GFRP strap $w20d5t2l200$, RT cure.	216
B.3 Validation of FCG rate and life against test results: SENT, GFRP strap $w20d5t2l200$, HT cure.	216
B.4 Validation of FCG rate and life against test results: SENT, GLARE strap $w20d5t1.8l200$, HT cure.	216
B.5 Validation of FCG rate and life against test results: SENT, GLARE strap $w20d5t5.4l200$, HT cure.	217
B.6 Validation of FCG rate and life against test results: SENT, GLARE strap $w30d5t3.6l200$, HT cure.	217
B.7 Validation of FCG rate and life against test results: SENT, GLARE strap $w60d5t1.8l200$, HT cure.	217
B.8 Validation of FCG rate and life against test results: SENT, GLARE strap $w100d5t1.8l200$, HT cure.	218
C.1 Technical drawing of the un-reinforced large-scale integral skin-stringer panel.	220
C.2 Technical drawing of the top plate of the end fitting.	221
C.3 Technical drawing of the bottom plate of the end fitting.	222

List of Tables

1.1	Use of integral skin-stringer panels in aircraft	5
1.2	Pros and cons of built-up and integral skin-stringer panels	6
2.1	Pros and cons of various FE methods to compute SIF	25
3.1	Practical applications of bonded patches to military aircraft	44
3.2	Typical mechanical properties of unidirectional (UD) CFRP and BFRP and generic aluminium alloy.	45
4.1	Mechanisms involved in bonded strap reinforced structures.	77
5.1	Sample dimensions	103
5.2	Mechanical properties of aluminum alloys used in this study.	105
5.3	Mechanical properties of substrate, strap and adhesive materials.	111
5.4	Predicted FCG lives and error ranges in comparison with test results.	129
6.1	Mechanical properties of the strap materials and adhesive employed in the constant weight analysis.	134
6.2	Mechanical properties of titanium alloy straps.	138

List of abbreviations, nomenclature and symbols

Abbreviations

2D	Two dimensional
3D	Three dimensional
AA	Aluminium alloy
BCR	Bonded crack retarders
BEM	Boundary element method
BFRP	Boron fibre reinforced plastic
CFRP	Carbon fibre reinforced plastic
CP	Cross ply
CT	Compact tension
CTE	Coefficient of thermal expansion
DOC	Direct operating cost
FCG	Fatigue crack growth
FEM	Finite element method
GFRP	Glass fibre reinforced plastic
GUI	Graphical user interface
HT	Elevated (or high) temperature
LEFM	Linear elastic fracture mechanics
LICRA	Life increment crack retarders analysis
MPC	Multi point constraint
MSD	Multiple site damage
M(T)	Middle crack tension
MVCCT	Modified virtual crack closure technique
RMS	Root mean square

RT	Room temperature
SERR	Strain energy release rate
SENT	Single edge notch tension
SIF	Stress intensity factor
TRS	Thermal residual stress
UD	Unidirectional
VCCT	Virtual crack closure technique

Nomenclature

A	Area
a	Crack length
b	Specimen width, stringer pitch
C, n, m, p, q	Material crack growth rate constants
D	Adhesive disbond growth rate constant
d	Distance
E	Elastic modulus
e	Specific life increment
F	Force
G	Strain energy release rate
J	J-integral
K	Stress intensity factor
l	Strap length
M	Moment
N	Number of cycles
R	R ratio
t	Strap thickness
T	Temperature
u, v, w	Displacements
U	Elastic energy
W	Weight function
w	Strap width
x, y, z	Axes, coordinates

Symbols

α	Coefficients of thermal expansions
----------	------------------------------------

β	Dimensionless stress intensity factor
ε	Strain
θ	Angle
μ	Stiffness ratio
ν	Poisson's ratio
Π	Potential energy
ρ	Density
σ	Stress
τ	Shear
ϕ	Rotation

Super and Subscripts

0	Membrane
<i>I, II, III</i>	Opening, sliding, tearing modes
<i>a</i>	Adhesive
<i>app</i>	Applied
<i>bot</i>	Bottom
<i>C</i>	Cure
<i>c</i>	Toughness
<i>cri</i>	Critical
<i>eff</i>	Effective
<i>F</i>	Tensile or mechanical
<i>i</i>	<i>ith</i> index
<i>lin</i>	Linear
<i>M</i>	Bending or mechanical
<i>max</i>	Maximum
<i>min</i>	Minimum
<i>op</i>	operational or opening
<i>par</i>	Parabolic
<i>R</i>	Room
<i>RMS</i>	Root mean square
<i>r</i>	Reinforcement
<i>s</i>	Substrate
<i>T</i>	Thermal
<i>th</i>	Threshold
<i>top</i>	Top
<i>w</i>	weighted

x, y, z	Directions
ys	Yield strength
∞	Remote

Chapter 1

Introduction

1.1 Overview

1.1.1 Trends in aircraft design: new design techniques

Trends in civil aircraft industry are towards the creation of high durability aircraft with minimum weight and high efficiency to create products in a highly competitive market. Aircraft designers are pushed towards new design techniques which would allow reduction in weight and production cost without affecting the safety of the structures [1].

Direct operating cost (DOC) of an aircraft is shown in figure 1.1 [2]. It can be seen that the ownership cost covers 40 – 50% of DOC. The remaining 50 – 60% are expenses which burden the airlines. Recurring production cost covers almost a third of the DOC. For this reason reducing manufacturing cost is one of the primary objectives sought by aircraft manufacturing companies. The weight of the structures also plays an important role. A lighter aircraft would reduce the aircraft DOC under many points of view such as fuel consumption and material acquisition, and allow a higher payload percentage. Therefore, new design techniques should focus on the following primary objectives [1]:

1. Development:
 - Low weight structures
 - Low non-recurring cost

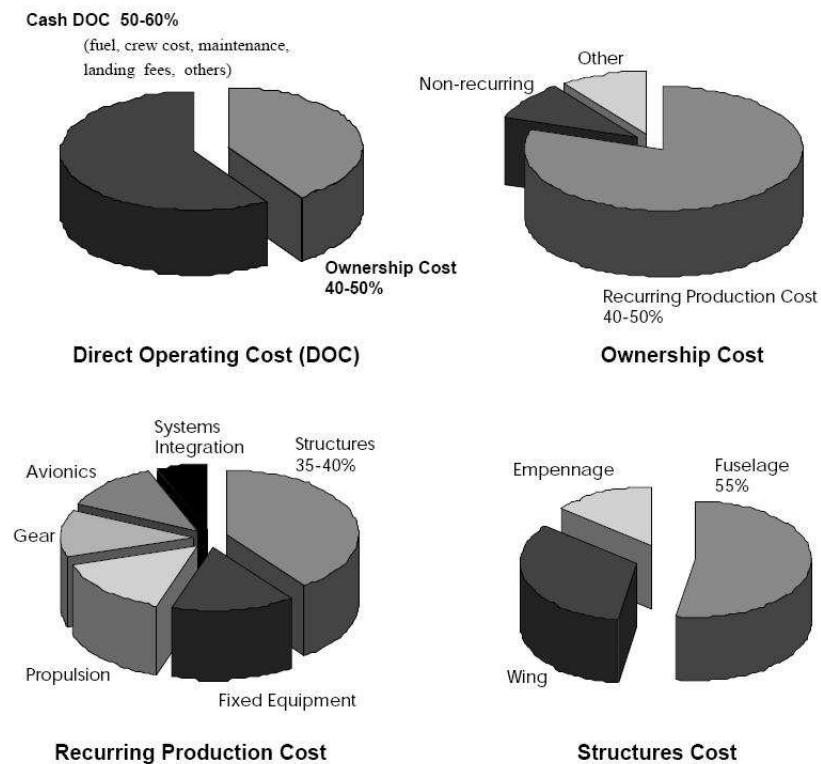


Figure 1.1: Direct operating cost of an aircraft [2]

- High performance aircraft
2. Manufacturing:
 - Low recurring costs
 - Reduced impact on environment
 3. Operation:
 - Increased safety and reliability
 - Reduced inspections and improved reparability
 - Low operating costs

These primary objectives can be achieved essentially by working on the following two aspects: reducing manufacturing cost and structural weight.

Conventional metallic built-up structures have been used for more than 60 years and the design and manufacturing process have been optimised. In order to obtain a further reduction of weight and cost new material and/or design techniques need to be developed.

For those reasons composite materials are often used in new generation aircraft. Composite materials offer high specific strength and a directional stiffness that can be tailored in the direction where needed. Those factors picture composites as the future aircraft materials. Composites are though relatively new materials, thus the usage is still limited. In fact, it requires years of study and practical experience before a material can be fully exploited and all the possible failure mechanisms understood. Although there are probably thousands of research projects on aerospace composites, our understanding of them is still a fraction of the one gained for metals. Failure mechanisms of composites materials are far more complicated than those of metallic structures. Durability of composites under environmental factors is still under study, not to mention the modelling capability. Composite materials are still modelled with the classical lamination theory where an equivalent stiffness is computed for a multi-layer structure. Displacements, which in fact have a zigzag distribution through the thickness, are modelled as a straight line. Although research has been conducted on improving the modelling capability for composite materials, those methods are still not implemented in commercial finite element codes [3–7]. All these uncertain factors penalise the use of composites for the design of new generation aircraft. Composite structures are a great tool that cannot be completely exploited yet.

On the other hand, metallic structures are well known and can be exploited to the limits. The problem of reducing cost and weight can be solved by seeking new unconventional manufacturing and/or design techniques such as metallic integral structure (obtained from a monolithic piece of material) or advanced hybrid structures (structures made of both metal and composite materials such as GLARE) [1, 2].

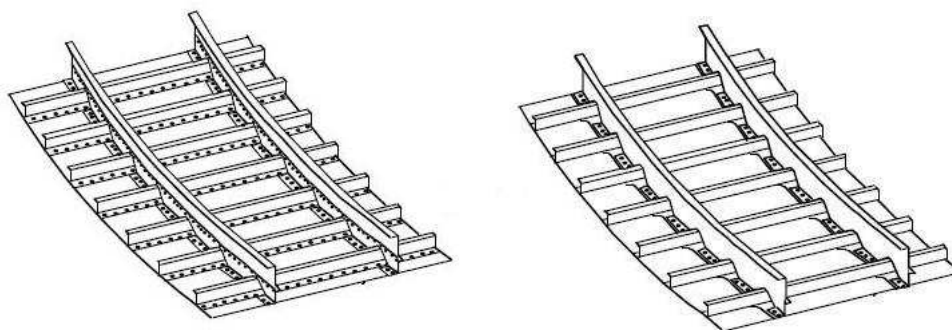
Both composites and metals are currently been explored and as Pacchione from Airbus [8] wrote:

“The progress of metal technologies is not concluded and, with the strong pressure of the composite challenge, the rate of development is even increased showing further remarkable possibilities”

1.1.2 Integral structures: a possible solution

Integral structures are fabricated via manufacturing processes such as welding, casting, forging, large scale extrusion and high speed machining from aluminium plate without the need of fasteners. This permits modular pre fabrication of large sections of aircraft prior to final assembly [1,2,8,9]. A study conducted by NASA in collaboration with the Boeing on the feasibility of integrally stiffened metallic fuselage panels [2] shows that part count drops from 78 parts for a rivetted baseline panel to 7 parts for a integral airframe structures. Moreover, a 61% recurring cost saving can be obtained compared to conventional built-up manufacturing. Different manufacturing process were also compared. The most efficient manufacture technique is extrusion; this consists in extruding skin and channel stiffeners in one piece extrusion (near-net-shaped), shaping by three-axis machine and then joining by rivetting or welding. In fact, the extruded panels need to be connected one another. One of the most efficient way to connect them would be welding [1,8]. In this way the number of rivets is considerably reduced, further reducing manufacturing cost and stress concentration sites.

In figure 1.2 a conventional built-up structure is compared to a integral one.



(a) Built-up structure

(b) Integral structure

Figure 1.2: Build-up and integral structures: different design concept [2].

Weight reduction and cost savings are especially true for skin/stringer panels, which constitute the majority components of aircraft wing and fuselage shells (figure 1.3). Integral or “unitised” panels benefit from a delay in fatigue crack initiation, because local stress concentrations are considerably mitigated compared to the traditional built-up structures, e.g. fasteners are not needed. Unfortunately, the use of integral stringer panels does not have only advantages;

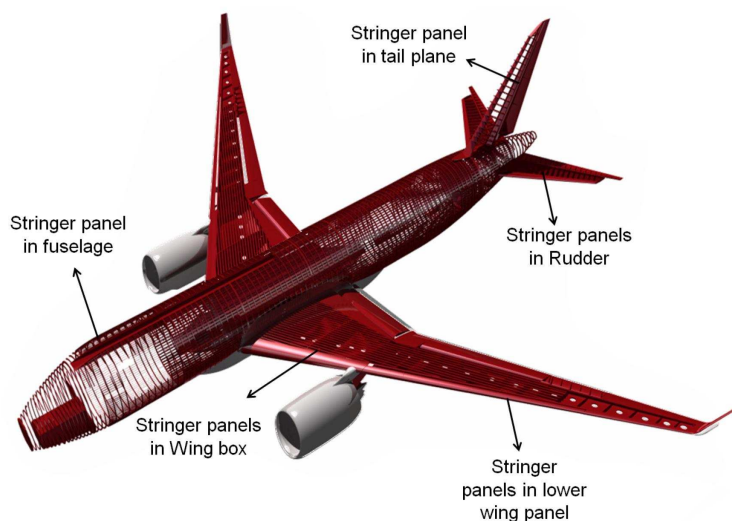


Figure 1.3: Use of stringer panels in an aircraft [10]

they lack fail safety and damage tolerance [11–14]. Although these structures have been used in many Russian aircraft (table 1.1), multi load path is not ensured. The delay in crack propagation, which is shown by convectional built-up structures when the crack passes the stringers, is not present [11–14]. Pros and cons of conventional built-up skin-stringer panels and integral skin-stinger panels are listed in table 1.2.

The lack of damage tolerance of integral structures is a problem that needs to be solved to completely exploit the advantages of these structures without incurring in additional safety factor impose by the regulators.

A solution to these problems can be found in hybrid structures and selective reinforcements. Before analysing possible solutions to increase the damage tolerance capability of these structures, a brief description of the damage tolerance design approach is presented in the next section together with the other design philosophies.

Table 1.1: Use of integral skin-stringer panels in aircraft [13]

Aerospatale British Aerospace	Lockheed	Dornier	Vickers	Antonov	Il'ushin	Tupelov	
Concorde	C-188	Do 228	VC 10	AN-22	AN-70	IL-62	TU-144
	C-141			AN-24	AN-72	IL-76	
	C-5			AN-26	AN-74	IL-86	
				AN-30	AN-124		
				AN-32	AN-225		

Table 1.2: Pros and cons of built-up and integral skin-stringer panels

	Pros	Cons
Built-up skin-stringer panel	<ul style="list-style-type: none"> - Redundant structural member to promote fail safety - In-built crack retarders, e.g stringers 	<ul style="list-style-type: none"> - Stress concentration spots - Problems with multiple site damage (MSD) - High manufacturing cost - Heavy - Inspection difficulties
Integral skin-stringer panel	<ul style="list-style-type: none"> - Simple to manufacture and assembly - Reduced manufacturing cost - Reduced weight - MSD can be avoided - Longer crack initiation time 	<ul style="list-style-type: none"> - Absence of multi load paths - Reduced damage tolerance capability

1.1.3 Fatigue design philosophies: safe life, fail safe and damage tolerance

In the design of a civil aircraft, safety is the most important issue. Aircraft manufacture industries do their best to assure it and regulators verify that all the safety criteria are met.

In the 1950s the design approach was **safe life**. It entails that a structure is considered to be in pristine condition after manufacturing. This design approach requires a fatigue analysis of the structure and the application of a safety factor to determine the number of flights a component will work without failing. At the end of the safe life, the component will be replaced by a new one even if it may be still in good condition. Three main drawbacks affect this design approach. First, the fact that the component might have an initial damage cannot be completely excluded. Second, secondary load path is not necessarily present, thus failure of the component may be catastrophic, i.e. the component may not be fail-safe. Thirdly, this approach increase the direct operating cost since a component must be substituted at the end of the calculated safe life, even if it may still be in good condition.

Due to those drawbacks a second design approach emerged. It is called **fail-safe**.

In this design approach possible failure of a component is taken into account and a second load path must be designed to allow a component to fail without catastrophic consequences. For instance, a built-up stringer panel is fail safe because, if a crack generates in the skin, the stringer can still stand the load. Still, these approach does not solve all the problems of the safe life approach. A cracked component will be replaced when broken, even though it might stand the loads for other 1000 flights and initial flaws are competently neglected.

Nowadays, the fail-safe design approach is used along with the **damage tolerance** one. In this approach the structure is considered to have some initial damage, e.g. manufacture defects. In order to be damage tolerant, the damaged structure must not only be able to stand the load, but it must be able to do it until the next scheduled inspection without affecting the safety. It means that the initial crack must grow slow enough, so that the structure still has enough residual strength to reach the next scheduled inspection.

The previous sentence included all three key concepts of damage tolerance: slow and stable crack growth, adequate residual strength, and inspections. In order to correctly design a damage tolerant structure, each of the three aspects must be considered. The crack growth behaviour and residual strength must be known and an inspection programme planned.

The crack growth behaviour can be described by an a versus N graph, where a is the crack length and N is the number of load cycles (figure 1.4(a)). The number of cycle can be related to the number of flights. A curve like that is often called fatigue crack growth (FCG) life.

The residual strength is the load which would cause catastrophic failure for given crack length (or number of cycle or number of flights since they can be related by the FCG life). An example is shown in figure 1.4(b). By using that graph the critical crack length (a_{cri}) at which the structure is not able to withstand the operational limit load (σ_{op}) can be found and the component can be replaced or repaired in time. By knowing both graphs in figure 1.4 an appropriate inspection programme can be scheduled.

Nowadays, airworthiness regulators require both theoretical and experimental demonstration that the aircraft can stand design limit load in worst case scenarios without catastrophic failure till the damage can be detected during inspections [15, 16].

Going back to the integral structures, it is now clear why they might not be fail safe nor damage tolerant. When a crack initiates in a integral structure, it

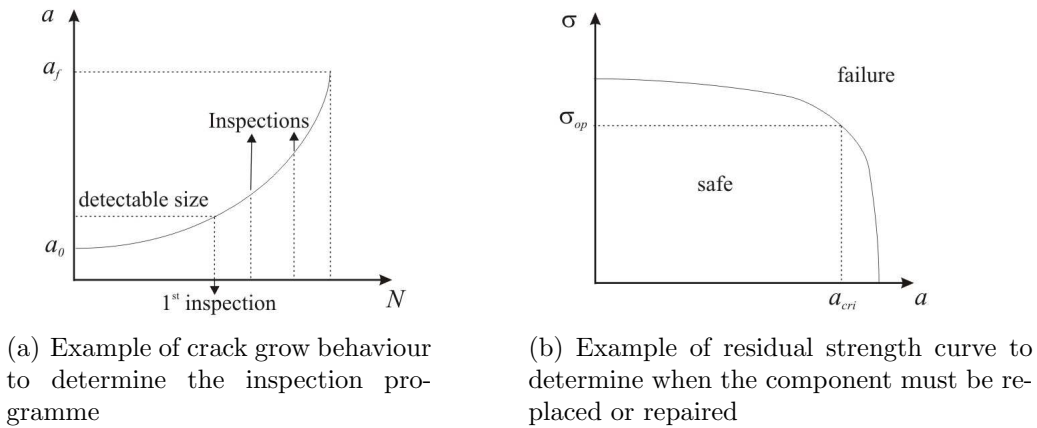


Figure 1.4: Damage tolerance: FCG and residual strength curves

might propagate fast. Moreover, secondary load path are not present since a crack in the skin of a integral stiffened panel propagates also in the stiffeners. A solution to these problems must be found before integral stiffened structures can efficiently be used and all their benefits exploited.

1.1.4 Selective reinforcements to ensure fail safety for integral structures

The solution to the lack of damage tolerance of integral stiffened panels can be found in bonded selective reinforcements [11, 12, 17–21]. These reinforcements are bonded straps of material placed in critical points of the structure to re-establish the loss of structural strength, provide an alternative load path, and slow down the crack propagations. An example of the use of bonded selective reinforcements can be seen in figure 1.5. The use of adhesive instead of rivets or bolts to join substrate and reinforcements allows to fully exploit the benefit of integral structures (table 1.2) without incurring in the drawbacks of build-up structures.

These selective reinforcement straps could be made of fibre polymer composites, fibre-metal laminates, or metallic alloys. They will be part of the original aircraft structure and subjected to operative loads and environments throughout the entire service life. The damage tolerance capability is added to the integral panels “ab initio”. In this way lighter and cheaper structures can be built without affecting safety. The use of straps made of composite materials on metallic structure gives birth to the so-called hybrid structures which merge the advan-

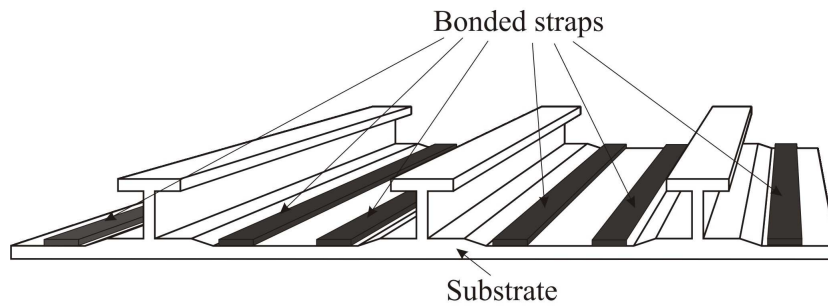


Figure 1.5: Sketch of a integral wing panel with selective reinforcements

tages of both materials.

Alcoa conducted a study on the weight and cost savings that can be achieved by using these structures (figure 1.6). It shows that a reduction of 20 – 30% in structural weight can be obtained [21]. That reduction entails a reduction on the direct operating cost. Moreover, a further reduction on structural cost can be reached.

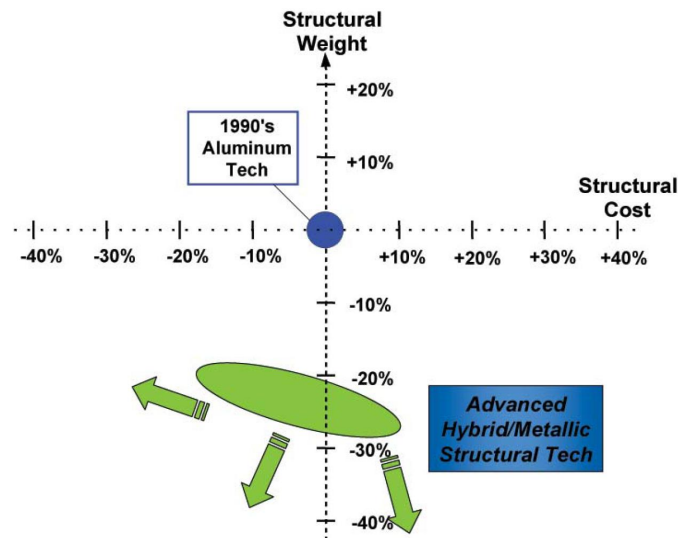


Figure 1.6: Weigh-cost analysis carried out by Alcoa on hybrid structures [21].

This technology could really allow the creations of a lighter, cheaper and safer new generation of aircraft. Although the concept sounds great, further studies are required to quantitatively evaluate its benefits, understand the governing parameters in the design, and produce design guidelines. Those unknown factors have motivated and initiated the research project reported in this thesis.

1.2 The project scope

This project was founded by the Airbus, Alcoa Inc. and EPSRC/IMRC and run by a consortium consisting of Cranfield University, Open University, Airbus, Alcoa and Cytec. Two PhD students, four post-doctoral researchers and five academics and industrial partners have been working on this project for three years (2006-2009).

This project is divided into three distinct but related parts:

- Manufacture and tests of fail-safe integral aircraft structures using adhesively bonded crack retarders and determine mechanical properties (mainly performed by Cranfield University, School of Applied Sciences, 5 researchers)
- Fail-safe design of integral panels and numerical simulation (author's working package, Cranfield University, School of Engineering, 3 researchers for one year, 2 for the remaining 2 years)
- Determination of residual stresses in bonded structures and prediction of residual stress changes during fatigue crack propagation (Open University, 3 researchers)

The author's study is mainly focussed on part two of the overall research project, although strong interactions between the three research groups were required. Cranfield University team of eight researchers met once per month and the consortium met every three months. At each consortium meeting each research team reports the progress on their studies.

1.3 Objectives

The design study focuses on fully establishing the benefits of bonded crack retarders via numerical simulation of a selection of bonded straps (different material and size) and large scale skin-stringer panels; the latter cannot easily be physically tested. The ultimate aim is to find strap material, size and location to maximise the fatigue crack growth (FCG) life and minimise the structural weight.

The objectives of this thesis can be summarised in three points:

- To develop effective analysis methods to predict fatigue crack growth (FCG) life of strap reinforced integral structures. Firstly, for sample plates; subsequently for large-scale integral stiffened panels;
- To conduct parametric studies of different crack retarders (materials, adhesives, dimension and positions) to find the key variables which influence the effectiveness of the strap;
- To provide the aircraft manufacture companies with a fully operational and validated numerical tool to design efficient selective reinforcements for realistic large-scale skin-stringer in terms of FCG life and weight.

In order to reach those objectives, firstly, modelling techniques and analysis methods to study panels with bonded straps are developed. Fatigue crack growth is then calculated. Results are validated by experimental tests of simple plates. Then, parametric studies of crack retarders and their effectiveness on FCG life are conducted on sample geometries. Finally, the modelling technique is used to produce fatigue crack growth life predictions of 5-stringer integral panels reinforced by bonded straps.

1.4 Structure of the thesis

The structure of the thesis is herein described to help the reader create a clear picture of the problem and the way the research was conducted. A description of the following chapters is given below.

2. Theoretical framework:

Fundamentals of linear elastic fracture mechanics (LEFM) are introduced. The concept of the stress intensity factor (SIF) and strain energy release rate (SERR) is described. The main methods to calculate them for a generic structure are listed and references are given, not only for the numerical analysis, but experimental and analytical, too. A brief literature review on the different methods to compute the SIF through the finite element method (FEM) is given along with the pros and cons of each method.

Attention is paid on the virtual crack closure technique, because it is the one employed.

While in the introduction chapter the damage tolerance design approach was described and the importance of the fatigue crack growth (FCG) life highlighted, in this chapter some of the methods to compute FCG life are described. A brief discussion on the problems which can be encountered in FCG life prediction closes the chapter.

3. Literature review:

The purpose of this chapter is to draw a picture of the state of the art for this technology. In fact, the bonded selective reinforcement is a new idea and not much can be found in the literature. For this reason the literature review is conducted mainly on the bonded patch repair problem which, although is conceptually different, shows essentially the same mechanisms. Some analytical and FE modelling methods have been developed to study this problem and are herein described. More emphasis is placed on the FE modelling techniques which helped the author to develop his own.

4. Methodology:

In this chapter the author's enhanced 2D FE modelling technique to calculate the SIF of bonded strap reinforced integral structure and, consequently the FCG life, is described. The chapter opens with the mechanisms which influence, positively and negatively, the FCG propagation of this kind of structures. The way the structure is modelled and how each mechanism is simulated is described. The problems which are encountered in computing the FCG life of the structure are highlighted. This methodology is implemented in a computer program, LICRA (Life Improvement Crack Retarder Analysis), which interfaces with the commercial FE package NASTRAN. The flow chart of the code is described. Finally a 3D FE approach to the problem is given for comparison with the enhanced 2D modelling technique.

5. Validation: test coupon level:

Before applying this methodology for design analysis and parametric studies it is necessary to prove that it works. Firstly, the SIF was calculated for un-reinforced plates and secondly, for plates with bonded straps. Each single modelled effect is validated against experimental tests which were conducted by the other team members working on the project. The final validation test is to compare the predicted lives against the experimental ones. This is done for a number of specimens reinforced by straps made of different materials and dimensions. At this point the modelling technique can be considered validated.

6. Parametric Studies:

In this chapter, now fully confident of the potentiality of the modelling technique and knowing also its weak spots, parametric studies are conducted to understand the effect of different parameters on the final FCG life. Effect of strap material, strap dimension, and adhesive properties are studied. A design graph is developed. This graph relates the FCG life and strap weight of different strap dimensions. By using this graph, designers can find the lightest strap dimension to achieve a given life target.

Finally, based on the modelling results and experience gained during the research project and guided by the industrial sponsors, guidelines to the design of an integral structure with bonded selective reinforcements are suggested.

7. Large-scale integral skin-stringer panels:

The validated modelling technique is applied to predict the FCG lives of four large-scale integral-stringer panels reinforced by bonded straps. In this chapter geometry and model of the panels are presented. A 2D FE analysis of the un-reinforced stringer panel was compared with a 3D FE one in terms of stresses and displacements to find an as-simple-as-possible 2D model to reduce the computational time. Finally, the SIF of the reinforced stringer panels were computed and the FCG lives calculated. One of

the obtained FCG lives is compared to the experiment result for validation purposes. The chapter closes with a comparison of the four different strap configurations to determine the most effective one.

8. Conclusions and future studies:

In this last chapter the conclusions are drawn. Moreover, during the execution of the project some possible further studies opened. Unfortunately, some of them could not have been pursued. In this final part, the work that is either necessary to enlarge the knowledge of the problem or that could be done to improve the modelling technique is listed in the hope that it might be taken for future projects.

Appendix A. List of publications:

A list of the author's publications is given.

Appendix B. Validation of predicted FCG rates and lives:

The FCG rate and life graphs obtained for validation purposes are reported.

Appendix C. Large panel: technical drawings:

Technical drawings of the large-scale integral skin-stringer panel are shown.

Appendix D. LICRA user's instructions:

This appendix is meant to be a user-manual for LICRA computer code which has been developed by the author. The code interfaces NASTRAN package and is used to apply the multi point constraints (MPC), calculate the SIF and the FCG life of selective reinforced integral structures. Firstly, how to build the model is explained. Secondly, the use of the code to apply

the MPC is described. The input files and values needed to calculate the SIF of the structure are listed and explained. The simple graphical user interface (GUI) of the code is described. Output files are analysed and explained. Finally, the use of the computer code to integrate the SIF and compute the FCG life of the structure is described.

This appendix is served to help the knowledge transfer process that should be included in any research process. Through this user-manual a researcher can learn how to use the code and, if necessary, improve it.

Appendix E. User's instructions to the 3D-VCCT program code:

Instructions for the use of the 3D-VCCT computer program developed by the author to compute the through thickness SIF distribution by using 3D FE models are reported.

Chapter 2

Theoretical Framework

This chapter covers the basics of linear elastic fracture mechanics (LEFM) in order to introduce the equations and parameters which are employed in the thesis. This does not mean to be a summary of a fracture mechanics textbook, but a quick guide to the the equations and methodologies which build the basis for more advanced applications.

The stress intensity factor (SIF, K), strain energy release rate (SEER, G), and the failure criterion are introduced in section (2.1). The methods to compute them by using the finite element method (FEM) are discussed in section (2.2). Finally, some of the most important fatigue crack propagation laws along with the integration process to calculate the fatigue crack growth (FCG) life are explained in section (2.3).

More notions of fracture mechanics can be gained by reading Broek [22], Anderson [23], and Gdoutos [24].

2.1 Linear elastic fracture mechanics

Fracture mechanics is the study of cracked structure. The objective is to estimate the stresses and the remaining life of a cracked structural component. In order to do that the stress intensity factor K is introduced along with a failure criterion.

2.1.1 Stress intensity factor

A cracked plate can be loaded in three different modes: mode I or opening mode, mode II or sliding mode, and mode III or tearing mode (see figure 2.1). The superimposition of those three modes can describe any general load condition. Considering a through-the-thickness crack of arbitrary size a , in a body

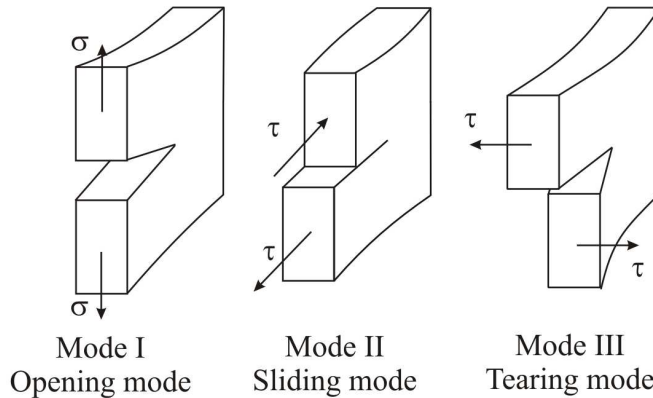


Figure 2.1: The three modes to load a crack in a solid.

of arbitrary size and shape, loaded by an arbitrary mode I loading, in the coordinate system of figure (2.2), the in-plane crack tip stresses can be expressed as:

$$\sigma_{ij} = \frac{K_I}{\sqrt{2\pi r}} f_{ij}(\theta) \quad (2.1)$$

where σ_{ij} are the stresses acting on a material element at a distance r and angle θ from the crack tip and f_{ij} are known function of θ . K_I is the stress intensity factor (SIF) for mode I load. A similar solution can be obtained for the other modes with different f functions and with SIF called K_{II} and K_{III} . For any geometry and load configuration the SIF can be expressed as:

$$K_I = \beta \sigma_\infty \sqrt{\pi a} \quad (2.2)$$

where β is the dimensionless SIF. The β -factor is a purely geometric parameter which relates the SIF for a geometrically defined plate to the SIF of an infinite plate. It could be considered as a geometric correction to the SIF of the centre-cracked infinite plate. If the β factor is know for a given geometry then the SIF can be computed by using equation (2.2). Once the SIF is known, the stress field

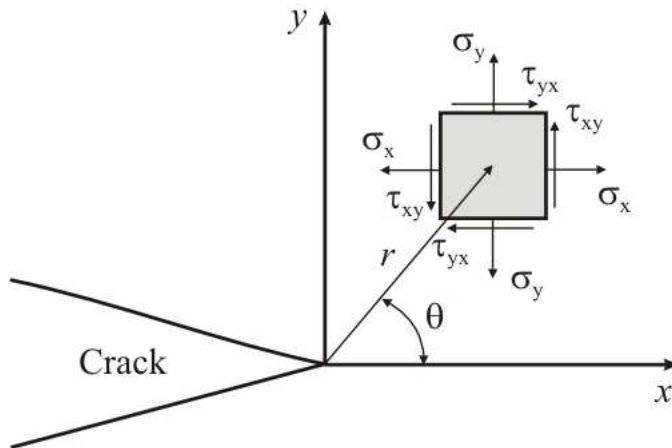


Figure 2.2: Stress condition at the crack tip.

around the crack tip is known:

$$\begin{aligned}
 \sigma_x &= \frac{K_I}{\sqrt{2\pi r}} \cos \frac{\theta}{2} \left(1 - \sin \frac{\theta}{3} \sin \frac{3\theta}{2} \right) \\
 \sigma_y &= \frac{K_I}{\sqrt{2\pi r}} \cos \frac{\theta}{2} \left(1 + \sin \frac{\theta}{3} \sin \frac{3\theta}{2} \right) \\
 \tau_{xy} &= \frac{K_I}{\sqrt{2\pi r}} \sin \frac{\theta}{2} \cos \frac{\theta}{2} \cos \frac{3\theta}{2}
 \end{aligned} \tag{2.3}$$

where ν is the Poisson's ratio.

The σ_{yy} trend can be seen in figure (2.3). In a linear elastic model the stress goes to infinity due to the singularity introduced by the crack. The SIF is consequently and indication of how “fast” it goes to infinity. Displacements can be obtained

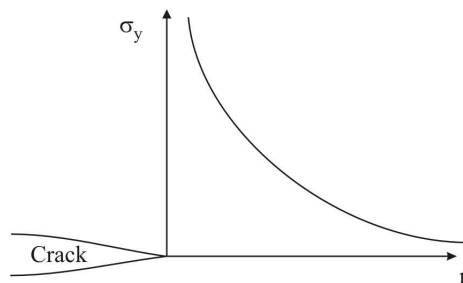


Figure 2.3: Stress field at the crack tip.

from equation (2.3) and the use of the constitutive relations:

$$\begin{aligned} u &= \frac{K_I}{4\mu} \sqrt{\frac{r}{2\pi}} \left((2\kappa - 1) \cos \frac{\theta}{2} - \cos \frac{3\theta}{2} \right) \\ v &= \frac{K_I}{4\mu} \sqrt{\frac{r}{2\pi}} \left((2\kappa + 1) \sin \frac{\theta}{2} - \sin \frac{3\theta}{2} \right) \end{aligned} \quad (2.4)$$

Where $\mu = \frac{E}{2(1+\nu)}$ is the shear modulus and κ :

$$\kappa = \begin{cases} 3 - 4\nu : & \text{plane strain} \Leftrightarrow \varepsilon_{zz} = 0 \\ \frac{3-\nu}{1+\nu} : & \text{plane stress} \Leftrightarrow \sigma_{zz} = 0 \end{cases} \quad (2.5)$$

The SIF is the most important parameter in the LEFM. Knowing the SIF of a structure, the stress field and the displacements at the crack tip can be computed by equations (2.3) and (2.4). Moreover the SIF is a similitude parameter, i.e. two different cracked structures with different loads and crack lengths but made of the same material and with the same SIF should behave the same way. This means that if the crack grows in one structure it will also grow in the other. This similitude property lays the basis of a failure criteria based on the SIF. In fact, for a given material in plane strain condition, failure occurs always at the same value of SIF. This value is called fracture toughness and denoted by K_{Ic} . Thus the fracture criterion is:

$$K_I \geq K_{Ic} \quad (2.6)$$

Fracture toughness is a material property only for thick plates (figure 2.4). To understand that, it is necessary to point out the difference between plane stress and plane strain conditions. If a generic plate is loaded by a tensile load, it is known that the transverse stresses (σ_{zz} , τ_{xz} , τ_{yz}) must be zero at the top and bottom free surfaces to solve the equilibrium equations. If the studied plate is an isotropic thin plate, it is understandable that also the stresses in the middle of the plate must be close to zero; this situation is called plane stress condition. Differently, if a thick plate is studied, it is assumed that the transverse strains (ε_{zz} , ε_{xz} , ε_{yz}) are equal to zero. In the real world neither plane stress nor plane strain state can be fully achieved but the stress condition is always 3-dimensional. Following a completely empirical approach it was found that the toughness of a material is constant only for plates whose thickness t is greater than:

$$t \geq 2.5 \left(\frac{K_{Ic}}{\sigma_{ys}} \right)^2 \quad (2.7)$$

where σ_{ys} is the yield strength of the material. The fracture toughness K_{Ic} can be found only in plane strain condition. In the case of plane stress condition the critical SIF K_{Icri} must be found by an empirical fitting law of the graph in figure (2.4).

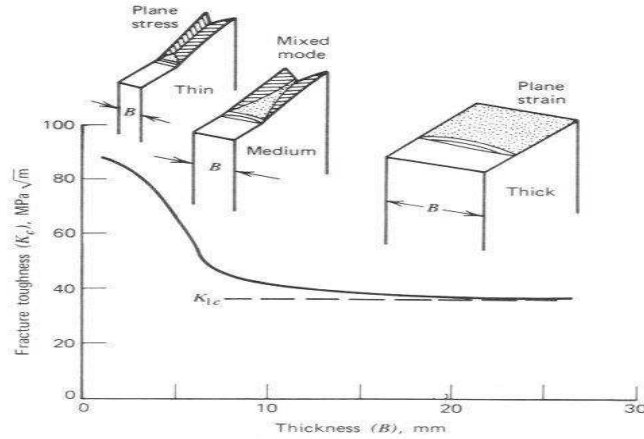


Figure 2.4: Effect of specimen thickness on fracture toughness [25].

2.1.2 The energy approach: strain energy release rate

The Griffith energy criterion for fracture states: crack growth can occur if the energy required to form an additional crack of size da can be released by the system [26]. Although Griffith was the first to propose the energy criterion for fracture, Irwin [27] reformulated it in an easier-to-apply way by introducing the strain energy release rate (SERR or G).

Let us consider a cracked plate, the crack growth condition can be written as:

$$\frac{d\Pi}{dA} + \frac{dW}{dA} = 0 \quad (2.8)$$

where Π is the potential energy, W the energy required to create new surfaces, and A is the crack area. The energy release rate is defined as:

$$G = -\frac{d\Pi}{dA} \quad (2.9)$$

The potential energy can be expressed as:

$$\Pi = U - F \quad (2.10)$$

where U is the elastic energy and F the work done by the external force. It can be demonstrated that G is always equal to the derivative of the elastic energy [28]:

$$G = -\frac{d\Pi}{dA} = \frac{1}{t} \left(\frac{dU}{da} \right)_P = -\frac{1}{t} \left(\frac{dU}{da} \right)_v \quad (2.11)$$

where t is the thickness and the subscripts P, v indicate constant load and fixed grips respectively. Thus, by computing the variation of elastic energy, the strain energy release rate is computed.

The second term of equation 2.8 is the material resistance:

$$R = \frac{dW}{dA} \quad (2.12)$$

For brittle materials, R is a constant and called critical SERR (G_c), thus a failure criterium can be written:

$$G \geq G_c \quad (2.13)$$

For elasto-plastic materials usually R is function of the crack length and called *R-curve* or *resistance curve* [29].

It was shown that the SERR quantify the change in potential energy and the SIF characterise the stresses, strains, and displacements near the crack tip. A relationship between the two parameters can be obtained by using the crack closure integral [27, 30] and states:

$$\begin{aligned} K_I &= \sqrt{G_I E} & : & \quad \text{plane stress} \Leftrightarrow \sigma_{zz} = 0 \\ K_I &= \sqrt{\frac{G_I E}{1 - \nu^2}} & : & \quad \text{plane strain} \Leftrightarrow \varepsilon_{zz} = 0 \end{aligned} \quad (2.14)$$

If the strain energy release rate (G) of a structure is known, by using equation (2.14) the SIF (K) can be calculated and consequently the β (equation 2.2).

2.1.3 How to calculate the SIF of a structure

For a general structure, usually it is β -solution that is calculated and presented as a fracture mechanics parameter.

Once the β -solution of a structure is known, the SIF can be calculated for any applied load and crack length. Many β -solutions are already available in compendiums of stress intensity factor [31, 32]. If a β -solution is not available in the

compendiums, then it can be evaluated in one the following ways:

- **Experimental methods:** photoelasticity, compliance measurement, fatigue crack growth data extrapolation;
- **Analytical methods:** Westergaard stress functions [33], superposition, Green's functions [34], weight functions [35], dislocation method [36];
- **Numerical methods:** finite element method (FEM), boundary element method (BEM)

Reviews on the methods to calculate stress intensity factors are available [37,38]. In the next section only the numerical methods using the FEM are reviewed.

2.2 SIF computation through FE method

Since 1970s the finite element method (FEM) has become firmly established as a standard procedure to evaluate the SIF for complex geometries. In fact, standard solutions which can be found in reference books [31,32] are not enough to describe the complex configurations present in many structural components.

When the computational power was limited and fine meshes could not be used, so-called special elements that could represent the crack tip singularity were developed. These elements have special shape functions. The first attempt was presented by Tracey [39] employing a polynomial displacement field within a triangular element. Other attempts followed, e.g. [40–42]. Isoparametric elements able to model the stress singularity were formulated by Barsoum [43] and Henshell and Shaw [44]. The most convenient way of introducing a $\frac{1}{\sqrt{r}}$ singularity into a quadratic isoparametric element is by manipulating the mid-side node positions. The best results were obtained with singular hybrid finite elements based on mixed formulations (Heyliger [45]). Since the computation power has been increasing, a good accuracy can be obtained using conventional isoparametric elements and sufficiently fine regular mesh near the crack tip.

After the crack tip stress singularity is accurately dealt with, the FE analysis results can be interpreted to obtain the SIF of the structure. The most employed methods are:

- **Displacement extrapolations:** knowing the crack tip region displacements u and v from the FE analysis for different coordinates θ and r , the SIF can be extrapolated by using equation (2.4);
- **Stress extrapolation:** knowing the stress field from the FE analysis, the SIF can be calculated by using equation (2.3);
- **Finite crack extension method:** it is based on the definition of strain energy release rate (equation 2.11); the elastic energy U is computed at a crack length of a and $a + \delta a$ [46]; the strain energy can be calculated by using Clapeyron's theorem, i.e. the strain energy stored for an elastic body is equal to one-half the work that would be done by the applied forces; for the FE method it means multiplying the applied force for half of the displacements of the nodes at which the forces are applied;
- **Virtual crack extension method:** a variant of the previous method which require only one complete FE analysis and an additional calculation of the stiffness matrix of the elements in the crack tip zone [47–50];
- **J-integral method:** this method was firstly introduced by Rice [51]; it involves computing a line integral (J-integral), which is independent of the chosen integration path and can be connected to the SIF;
- **Virtual crack closure technique:** the energy to keep the crack closed is computed and related to the SERR [30, 52, 53]. This method is extensively used in the thesis and described in details in section 2.2.1;

Displacement and stress extrapolation methods are also called direct methods and are more mesh size dependent and less accurate than the other energy based methods [47]. Energy methods are more accurate because of the very nature of the FEM. The FEM is used to find a, numerically speaking, weak solution of the elastic energy. Consequently the energy obtained is very accurate, hence errors are lower than methods which require computation of stresses and strains. In the literature, comparison between some of the methods are available, e.g. [46, 47, 54]. A full comparison between the methods is, though, not available. For this reason, pros and cons of the methods are gathered in table (2.1).

Table 2.1: Pros and cons of various FE methods to compute SIF

Method	Pros	Cons
Displacements extrapolation	<ul style="list-style-type: none"> - One FE analysis - Easy to apply 	<ul style="list-style-type: none"> - Strongly mesh dependent
Stress extrapolation	<ul style="list-style-type: none"> - One FE analysis - Easy to apply 	<ul style="list-style-type: none"> - Strongly mesh dependent - Very fine mesh is required to obtain accurate results
Finite crack extension	<ul style="list-style-type: none"> - Less mesh dependent - Easy to apply - Accurate 	<ul style="list-style-type: none"> - Two FE analysis are required for each crack length - Only the total G can be computed, not the contributions of each single loading mode G_I, G_{II}, and G_{III}
Virtual crack extension	<ul style="list-style-type: none"> - Can be applied without computing stress and displacements but just knowing the stiffness matrix i.e., stresses and displacements do not need computing - Less mesh dependent - Accurate - Crack propagation directions can be evaluated with no further computational effort 	<ul style="list-style-type: none"> - Access to the stiffness matrix of the model is required - Only the total G can be computed, not the contributions of each single loading mode G_I, G_{II}, and G_{III}
J-integral	<ul style="list-style-type: none"> - One FE analysis required - Less mesh dependent - Accurate 	<ul style="list-style-type: none"> - Require some complicated post-processing work to numerically evaluate the integral - Only the total G can be computed, not the contributions of each single loading mode G_I, G_{II}, and G_{III}
Virtual crack closure	<ul style="list-style-type: none"> - Can be applied by running just one FE analysis although two analysis should be required - Less mesh dependent - Contributions of each single loading mode G_I, G_{II}, and G_{III} can be computed - Accurate - Easy to apply 	<ul style="list-style-type: none"> - Two-step analysis is more accurate but also time demanding

2.2.1 Virtual crack closure technique

The virtual crack closure technique (VCCT) is based on Irwin's crack closure integral [28] and the following statement:

The energy released when a crack is extended from “a” to “a + Δa” is identical to the energy required to close the crack of “Δa” .

This method was firstly introduced by Rybicki and Kanninen [30] for simple four-noded quadrilateral elements. Subsequently this procedure was extended to high order and singular FEs by Raju [52, 53].

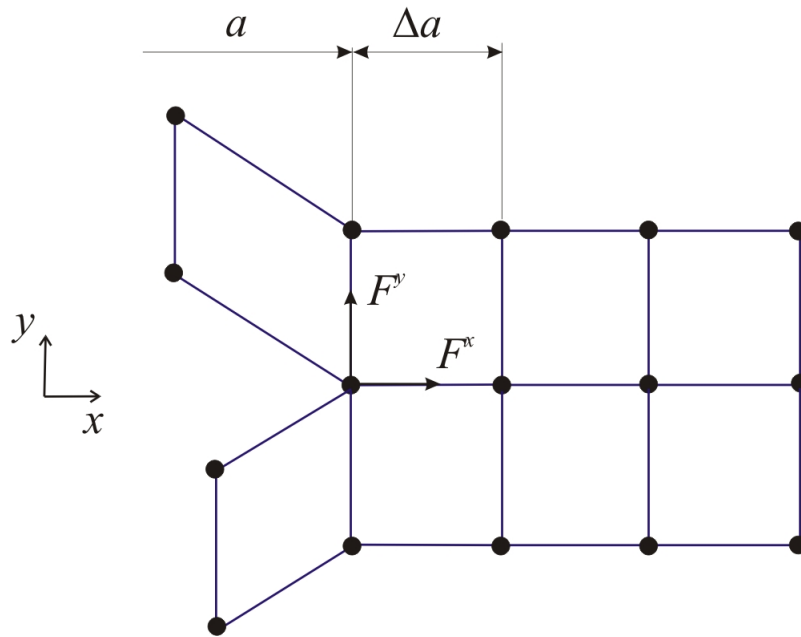
Let us consider the case of 4-noded plate elements (see figure 2.5). Two analysis steps are required to compute the strain energy release rate for a crack length a . At the first step the crack increment Δa is closed and the constraint forces F^y and F^x can be calculated (figure 2.5(a)). At the second step the crack tip node is released and the crack is open of a length Δa . The opening displacements at the back-node Δv and Δu can be calculated (figure 2.5(b)). The energy necessary to keep the crack closed of Δa can so be computed by multiplying forces and displacements, i.e. the strain energy release rate of a crack of length a can be written as:

$$G_I = -\frac{1}{2\Delta at} F^y \Delta v \quad , \quad G_{II} = -\frac{1}{2\Delta at} F^x \Delta u \quad (2.15)$$

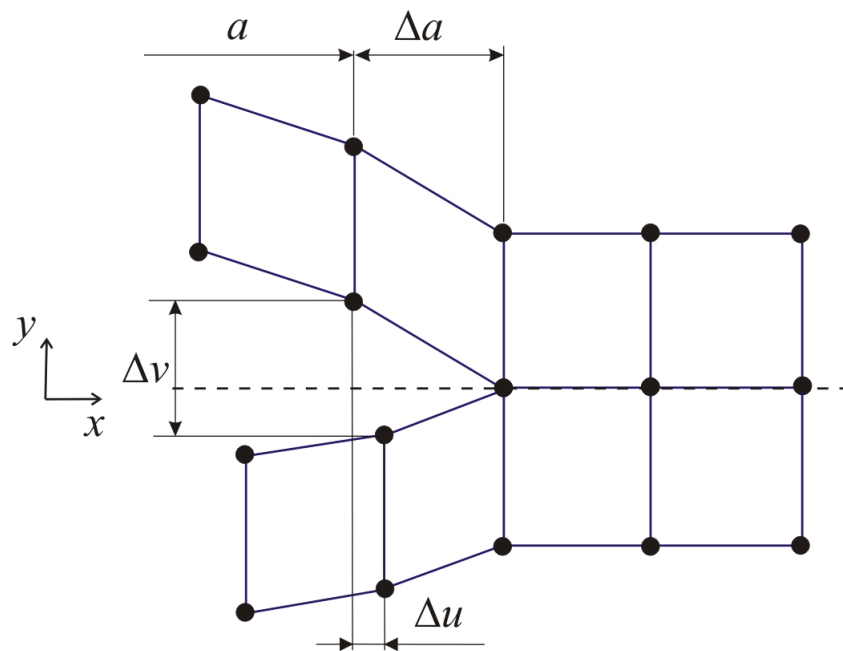
where t is the thickness of the plate and Δat is the cross section area that is kept closed.

The main drawback of this technique is that two FE analyses are required to obtain a single value of strain energy release rate. In order to solve that issue and be able to compute the SERR through a single analysis, the modified virtual crack closure technique (MVCCT) was developed. Nowadays the MVCCT is often simply called VCCT.

The MVCCT is based on the same assumptions of the VCCT, but additionally, assumes that a Δa increment does not significantly affect the forces at the crack tip. Based on this assumption, instead of calculating the forces at the first step, the crack is directly open of Δa and the forces are calculated directly at the second step (that, in this case is the only step)(see figure 2.6). Therefore,



(a) Step 1: the crack is closed and the forces can be calculated.



(b) Step 2: the crack has been extended and the displacements can be calculated.

Figure 2.5: Virtual crack closure technique; two-step analysis; two-dimensional four-noded plate/shell element.

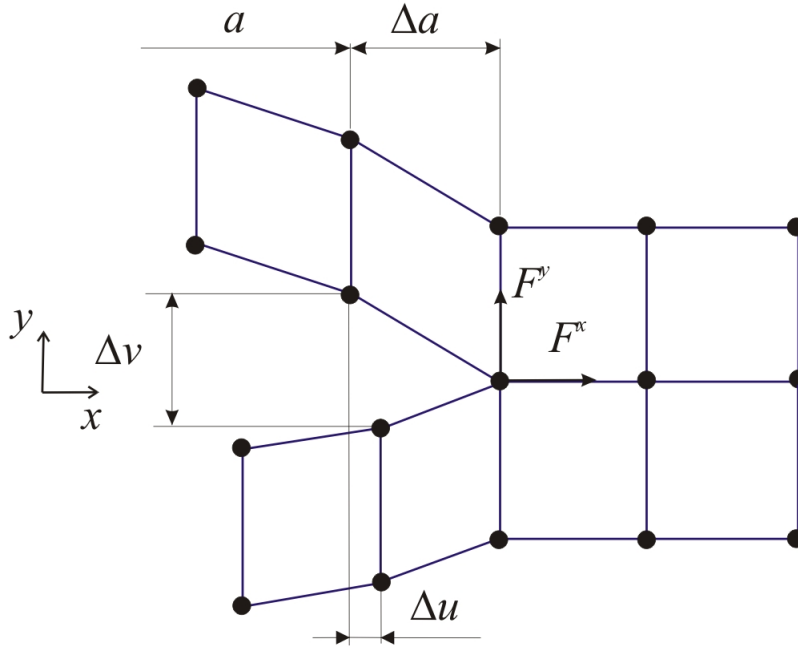


Figure 2.6: Modified virtual crack closure technique; one-step analysis; two-dimensional four-node plate/shell elements.

equation (2.15) still holds to compute the SERR.

The VCCT can be used in the study of delamination in delaminated composites (see figure 2.7). In this case the equations to compute the SERR for the different fracture modes are:

$$G_I = -\frac{F^z (w_t - w_b)}{2\Delta A} \quad , \quad G_{II} = -\frac{F^x (u_t - u_b)}{2\Delta A} \quad , \quad G_{III} = -\frac{F^y (v_t - v_b)}{2\Delta A} \quad (2.16)$$

where ΔA is the created delamination crack surface.

When applied to 3D 8-noded brick elements (figure 2.8) the SERR is written as:

$$G_I = -\frac{F^y 2v}{2\Delta A} \quad , \quad G_{II} = -\frac{F^x 2u}{2\Delta A} \quad , \quad G_{III} = -\frac{F^z 2w}{2\Delta A} \quad (2.17)$$

where instead the substitution $\Delta v = 2v$ has already made for symmetrical considerations.

The key concept is that the energy necessary to keep the crack closed per unit of thickness is equal to the SERR. This method is easy to apply since displacements and crack tip constraint forces are output by any commercial FE code. It is accurate and not strongly mesh dependent since it is an energy method. Moreover, it is not computational demanding since only one FEA is required and the contributions of each loading mode can be calculated.

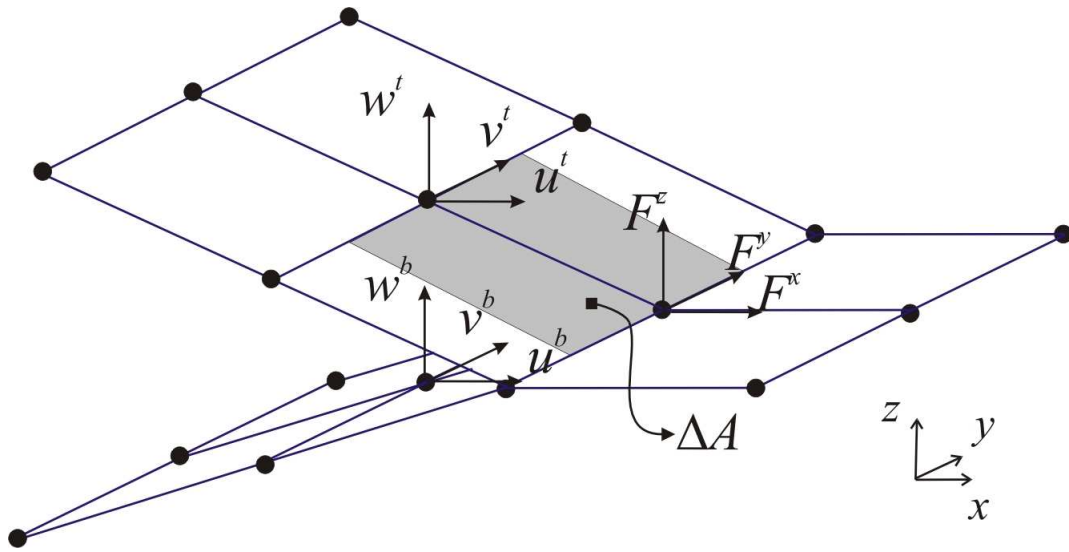


Figure 2.7: Modified virtual crack closure technique for delamination study.

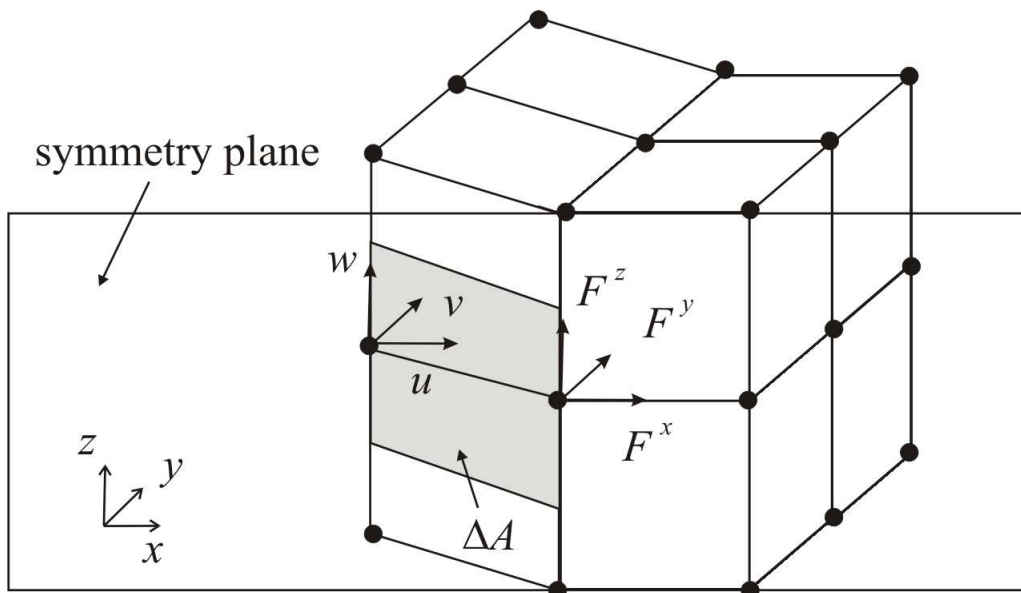


Figure 2.8: Modified virtual crack closure technique for 3D 8-noded brick elements.

A review on the virtual crack closure technique can be found in [55].

2.3 Fatigue crack growth

2.3.1 Importance of stress intensity factor range and R-ratio

Computing the life of a crack under fatigue load is an important part of damage tolerance design approach. The objective is to find the fatigue crack growth (FCG) life of the structure, i.e. a vs. N curve, starting from the initial crack length a_0 . The final number of cycles (N_f) and the final crack length (a_f) can be read on that graph. An example is shown in figure (2.9). The way to obtain the

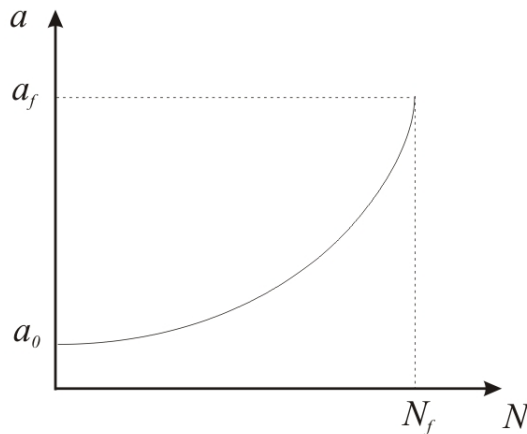


Figure 2.9: Example of fatigue crack growth life graph.

FCG life of a cracked structure is based on similitude, that is that if two different cracks in the same material have the same SIF range, they should have the same crack growth rate. That implicates that the rate of fatigue crack propagation da/dN should be a function of the SIF range $\Delta K = K_{max} - K_{min}$.

$$\frac{da}{dN} = f(\Delta K) = f\{\beta(\sigma_{max} - \sigma_{min})\sqrt{\pi a}\} \quad (2.18)$$

where σ_{max} and σ_{min} are the maximum and minimum applied stresses per cycle. Equation 2.18, i.e. da/dN vs. ΔK is a property of the material, also called material law.

The material law is found experimentally by running different tests on specimen

geometries whose β -solution is known. For a generic material, a typical material law curve can be found in figure 2.10. Three regions can be highlighted:

- **Region I:** Slow crack growth rate regime, also called near threshold regime where a small change in SIF range causes a large difference in crack growth rate and for a ΔK lower than the threshold one there is no crack growth at all;
- **Region II:** Stable crack growth period; this region is represented by a straight line in logarithmic scale. This is also call the Paris' regime because Paris developed an equation to describe the behaviour of a crack under fatigue in this region.
- **Region III:** high ΔK , unstable growth and final failure.

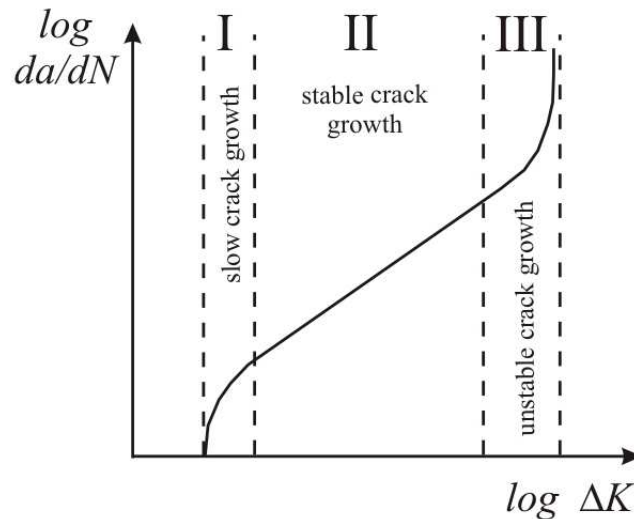


Figure 2.10: Relation between stress intensity factor range and crack growth rate. The three crack growth regimes are shown.

A fatigue load cycle is defined by two stress parameters, which can be any two of the following: maximum stress (σ_{max}), minimum stress (σ_{min}), mean stress (σ_m), or amplitude (σ_a). Also for fatigue crack growth propagation the SIF range alone is not enough to define the cyclic stress but another parameter is necessary. By convention this parameter is the R ratio:

$$R = \frac{K_{min}}{K_{max}} = \frac{\sigma_{min}\beta\sqrt{\pi a}}{\sigma_{max}\beta\sqrt{\pi a}} = \frac{\sigma_{min}}{\sigma_{max}} \quad (2.19)$$

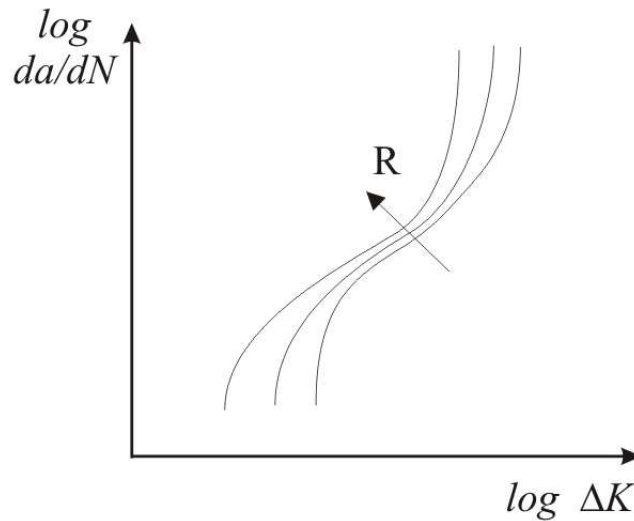


Figure 2.11: Effect of the R -ratio

The effect of the R ratio on the material law can be seen in figure (2.11). Under the same ΔK the crack propagates faster under a higher R -ratio. It should be noted that the effect of the R -ratio is greater in the region I and III of the material law. The effect on the second region is smaller.

In fact, there are many more factor that influence the material law than just the ΔK and R -ratio, e.g. loading history, specimen thickness, temperature etc., thus large scatter in test data is expected and an excellent accuracy in the prediction can not be always achieved.

Many empirical equations have been developed to describe the fatigue crack propagation rate, e.g Paris equation [56], Forman equation [57], Harter T-method [58], Walker [59], and NASGRO equation [60]. Some of these laws are discussed in the following sections.

2.3.2 Paris Equation

Paris was the first to notice that da/dN vs. ΔK curve was a property of the materials by running many tests under different applied loads and for different specimen geometries [56]. Paris decided to fit the experiential curves with a straight line in log-log scale and proposed the so-called Paris equation [56].

$$\frac{da}{dN} = C (\Delta K)^n \quad (2.20)$$

where C and n are material constants which are obtained by fitting the experimental data curve. Paris equation is the oldest and simplest of the laws. It just describes the second region of figure (2.10) where the effect of the R -ratio is limited, also called Paris region.

Further laws have been developed to model the slow crack growth and unstable crack growth regimes as well as the effect of the R -ratio.

2.3.3 NASGRO equation

A law which takes into account of more effects on the fatigue crack propagation is NASGRO equation [60]:

$$\frac{da}{dN} = C \left[\left(\frac{1-f}{1-R} \right) \Delta K \right]^n \frac{\left(1 - \frac{\Delta K_{th}}{\Delta K} \right)^p}{\left(1 - \frac{K_{max}}{K_{crit}} \right)^q} \quad (2.21)$$

where C , n , p , q are material constants empirically derived and:

$$f = \frac{K_{op}}{K_{max}} \begin{cases} \max(R, A_0 + A_1R + A_2R^2 + A_3R^3) & R \geq 0 \\ A_0 + A_1R & -2 \leq R < 0 \\ A_0 - 2A_1 & R < -2 \end{cases} \quad (2.22)$$

the coefficients are:

$$\begin{aligned} A_0 &= (0.825 - 0.34\alpha + 0.05\alpha^2) \left[\cos \left(\frac{\pi S_{max}}{2 \sigma_0} \right) \right]^{\frac{1}{\alpha}} \\ A_1 &= (0.415 - 0.071\alpha) \frac{S_{max}}{\sigma_0} \\ A_2 &= 1 - A_0 - A_1 - A_3 \\ A_3 &= 2A_0 + A_1 - 1 \end{aligned} \quad (2.23)$$

α is the plane stress/strain constraint factor and S_{max}/σ_0 the ratio of the maximum applied stress to the flow stress.

$$\Delta K_{th} = \Delta K_0 \frac{\left(\frac{a}{a+a_0} \right)^{\frac{1}{2}}}{\left(\frac{1-f}{(1-A_0)(1-R)} \right)^{(1+C_{th}R)}} \quad (2.24)$$

ΔK_{th} is the threshold stress intensity range, ΔK_0 the threshold stress intensity factor range for $R = 0$, a the crack length, $a_0 = 0.0381mm$ the intrinsic crack length and C_{th} the threshold coefficient.

NASGRO equation accounts for the thickness effect (see figure 2.4) by using K_{crit} as the fracture toughness:

$$\frac{K_{crit}}{K_{Ic}} = 1 + B_k e^{-A_k \frac{t}{t_0}} \quad (2.25)$$

where K_{Ic} is the plane strain fracture toughness, A_k and B_k material fit parameters, t the thickness and, t_0 the reference thickness for plane strain condition. Coefficients A_k and B_k are obtained by fitting the experimental curve shown in figure (2.4). The plane strain condition is:

$$t_0 = 2.5 \left(\frac{K_{Ic}}{\sigma_{ys}} \right) \quad (2.26)$$

Material constants in NASGRO equation are available from the freeware computer program AFGROW [61].

2.3.4 Tabular look-up and Harther T-method

Another way to describe a material law as the one shown in figure (2.10) is point by point. It means that, instead of using an equation that in the case of Paris equation is a simple straight line and in the case of NASGRO equation is an S-shaped curve, the best-fitted line of the experimental tests is expressed point by point. This way of inputting the material law is called in AFGROW [61] “tabular look-up”.

As shown in figure (2.11) in order to describe the effect of the R -ratio it is necessary to have more than one curve. Using the point-by-point description of the material law it is possible to describe as many curves as needed (provided you have enough test data for every R -ratio you want to analyse); it might be necessary to interpolate between two different R -ratio curves to find the curve one needs for the right R -ratio. The interpolation can be carried out by using the Harter T-method [58].

The Harter T-method makes use of the Walker equation [59]:

$$\frac{da}{dN} = C (\Delta K (1 - R)^{m-1})^n \quad (2.27)$$

where C , n are the Paris law constants, and m another material constant to take into account of the shift to the curve due to variable R -ratios. Basically, the Walker equation is an enhanced Paris equation that takes into account of the R -ratio effect as well.

In the Harter T-method the Walker equation is used on point-by-point basis at any given value of crack growth rate da/dN . Let us suppose that two material curves for two different R -ratios, R_1 and R_2 , are known and we want to find the one for R_3 (see figure 2.12). At any given $(da/dN)_i$ the following equations can be written:

$$\begin{aligned} \left(\frac{da}{dN}\right)_i &= \Delta K_{1i}(1 - R_1)^{m_i-1} \\ \left(\frac{da}{dN}\right)_i &= \Delta K_{2i}(1 - R_2)^{m_i-1} \end{aligned} \quad (2.28)$$

thus:

$$\Delta K_{1i}(1 - R_1)^{m_i-1} = \Delta K_{2i}(1 - R_2)^{m_i-1} \quad (2.29)$$

solving for m_i yields:

$$m_i = 1 + \left(\frac{\log\left(\frac{\Delta K_{1i}}{\Delta K_{2i}}\right)}{\log\left(\frac{1-R_1}{1-R_2}\right)} \right) \quad \text{for } R_1 \text{ and } R_2 \geq 0 \quad (2.30)$$

consequently we can write for R_3 :

$$\left(\frac{da}{dN}\right)_i = \Delta K_{3i}(1 - R_3)^{m_i-1} \quad (2.31)$$

and equalising one equation from (2.28) and (2.31) the i^{th} stress intensity factor range for the crack growth rate $(da/dN)_i$ and ratio R_3 states:

$$\Delta K_{3i} = \Delta K_{1i} \frac{(1 - R_1)^{m_i-1}}{(1 - R_3)^{m_i-1}} \quad (2.32)$$

this can be repeated for $i = 1 \dots n$ to find the new material curve for R_3 point-by-point as described. The graphic representation of this method can be seen in figure (2.12)

This method offers a true description of the material law as it was obtained by the experimental tests for different R -ratios. At least two curves for two different

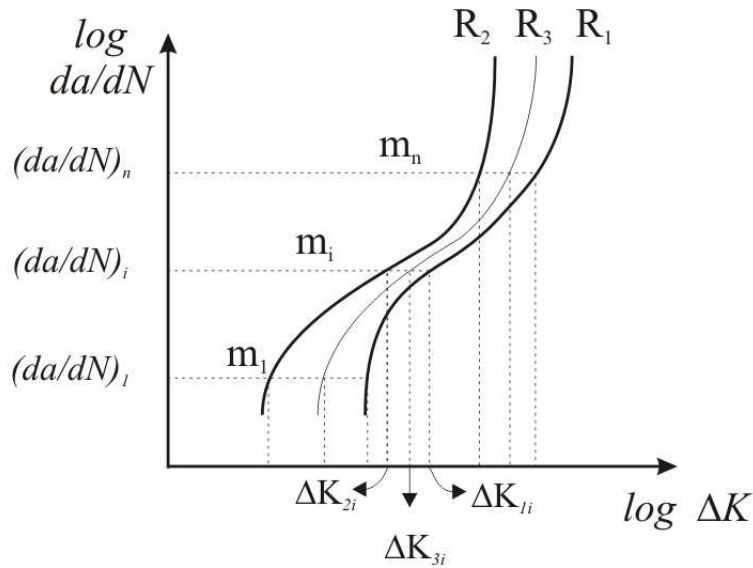


Figure 2.12: Harter T-method

R -ratios are needed for the interpolation; however the more, the better.

2.3.5 Numerical integration to obtain the FCG life

Different methods to describe the material law have been shown but still, how to compute the FCG life of a generic structure has not been explained.

First of all, it is necessary to know the β -solution of the structure to study. That can be achieved by using one of the methods shown in section (2.2). Secondly, the FCG law for the material (any of the ones shown in the previous sections). Finally the applied load $\Delta\sigma$ and R -ratio should be known. In order to obtain the FCG life, it is necessary to integrate the material law along with the β -solution. The explanation of a first order algorithm of integration follows.

- **Integration step 0:** The initial crack length is a_0 and the initial number of cycles is $N_0 = 0$; the integration step is a variation of number of cycles ΔN ; the β -solution is known for any crack length so for $a = a_0$, one can find $\beta = \beta_0$ hence in this way the SIF range can be computed for this step:

$$\Delta K_0 = K_{max0} - K_{min0} = \beta_0 \Delta \sigma \sqrt{\pi a_0} \quad (2.33)$$

after knowing ΔK_0 and the R -ratio that is the applied stress ratio (equation 2.19) the crack growth rate $(da/dN)_0$ can be obtained by using the chosen

material law (see figure 2.13):

$$\Delta K_0 \text{ and } R = \frac{\sigma_{min}}{\sigma_{max}} \Rightarrow \left(\frac{da}{dN} \right)_0 \quad (2.34)$$

considering that ΔN is small enough so that ΔK can be considered constant in the interval, although the crack length is changing within the number of cycle increment, the crack length increment yields:

$$\frac{\Delta a_0}{\Delta N} = \left(\frac{da}{dN} \right)_0 \Rightarrow \Delta a_0 = \left(\frac{da}{dN} \right)_0 \Delta N \quad (2.35)$$

thus:

$$a_1 = a_0 + \Delta a_0 \quad \text{and} \quad N_1 = N_0 + \Delta N \quad (2.36)$$

at the end of the initial step we obtain how much the crack has grown in ΔN increment of number of cycles.

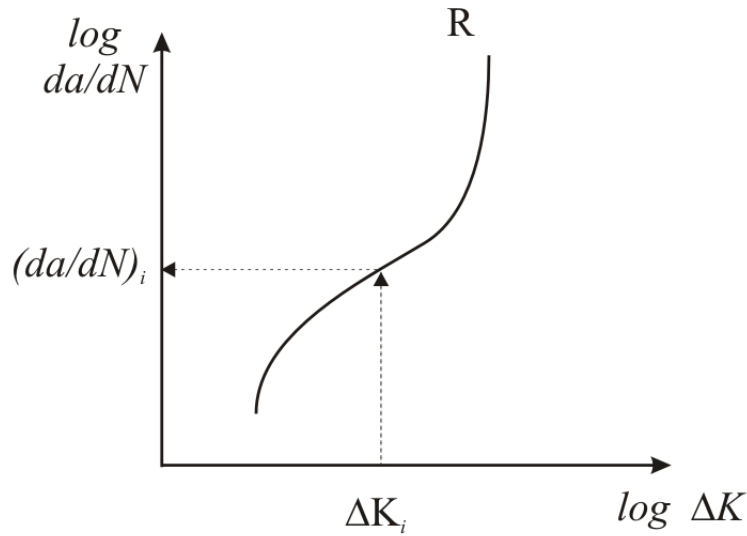


Figure 2.13: Use of the material law for the FCG life computation

- **Integration step 1:** the previous procedure is repeated by starting from a crack length a_1 :

$$\Delta K_1 = \beta_1 \Delta \sigma \sqrt{\pi a_1} \quad (2.37)$$

$$\Delta K_1 \text{ and } R = \frac{\sigma_{min}}{\sigma_{max}} \Rightarrow \left(\frac{da}{dN} \right)_1 \quad (2.38)$$

$$\frac{\Delta a_1}{\Delta N} = \left(\frac{da}{dN} \right)_1 \Rightarrow \Delta a_1 = \left(\frac{da}{dN} \right)_1 \Delta N \quad (2.39)$$

thus:

$$a_2 = a_1 + \Delta a_1 \quad \text{and} \quad N_2 = N_1 + \Delta N \quad (2.40)$$

the new crack length has been found for 2 increments of number of cycles.

- **Integration step i :** let us generalise the algorithm for the i^{th} step:

$$\Delta K_i = \beta_i \Delta \sigma \sqrt{\pi a_i} \quad (2.41)$$

$$\Delta K_i \quad \text{and} \quad R = \frac{\sigma_{min}}{\sigma_{max}} \Rightarrow \left(\frac{da}{dN} \right)_i \quad (2.42)$$

$$\frac{\Delta a_i}{\Delta N} = \left(\frac{da}{dN} \right)_i \Rightarrow \Delta a_i = \left(\frac{da}{dN} \right)_i \Delta N \quad (2.43)$$

thus:

$$a_{i+1} = a_i + \Delta a_i \quad \text{and} \quad N_{i+1} = N_i + \Delta N \quad (2.44)$$

- **Failure and FCG life:** the integration process stops when a failure criterion is met. Usually there are two failure criteria: fracture criterion and net section yield.

The fracture criterion is met when the maximum SIF is greater then or equal to the material fracture toughness:

$$K_{max} = \beta \sigma_{max} \sqrt{\pi a} \geq K_{Ic} \quad (2.45)$$

the net section yield criteria is met when:

$$\sigma_{net} \geq \sigma_{yl} \quad (2.46)$$

where σ_{yl} is the material yield strength and σ_{net} is the stress in the net cross section, i.e. the cross section considering that the crack has reduced it:

$$\sigma_{net} = \frac{\sigma_{max} W}{W - a} \quad (2.47)$$

where W is either half of the width of the specimen for middle cracks or the width for edge cracks. Combining equations (2.46) with (2.47) a critical crack (a_{crit}) length at which the net section stress equals the yielding one

can be found:

$$a_{crit} = W \left(1 - \frac{\sigma_{max}}{\sigma_{yl}} \right) \quad (2.48)$$

Thus, the integration stops at the n^{th} step when either

$$K_{maxn} = \beta_n \sigma_{max} \sqrt{\pi a_n} \geq K_{Ic} \quad (2.49)$$

or

$$a_n \geq a_{crit} \quad (2.50)$$

At this point the FCG life is obtained in terms of a_i , N_i , and $(da/dN)_i$ for $i = 0, 1, \dots, n$ and the final life (N_f) and crack length (a_f) are found. The result can be seen in figure (2.14).

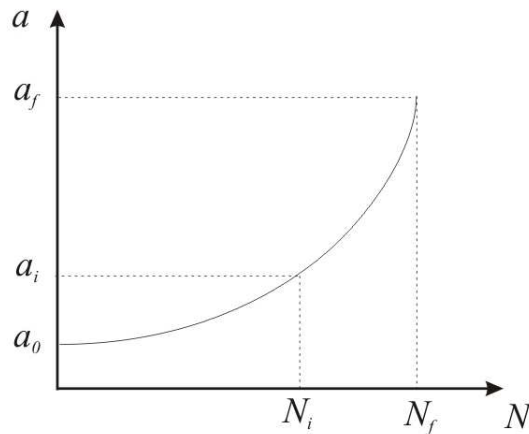


Figure 2.14: Fatigue crack growth life: integration process.

2.3.6 Consideration on FCG life prediction

At this point the FCG life of a structure can be calculated but how accurate will the life prediction be? Unfortunately, the answer of this question is: not very. Although a fatigue crack growth life prediction is usually more accurate than fatigue crack initiation life prediction, many factors influence the crack propagation causing notable scatter. On this subject Broek said [62]:

“Crack growth properties of most materials show considerable scatter.[...] Therefore, discrepancies between predicted and experimental crack growth is not a

shortcoming of the predictive method per se, but it is due to anomalies in material behaviour. In analogy, the theory of elasticity would be poor predictor of strain if Young's modulus of a material showed as much variation as crack growth properties."

Broek [62] showed that an error of 5% in the stress analysis would cause an error of 45% in the crack growth prediction. For the considerations herein made, in the design analysis, a safety factor should be used on the predicted FCG life.

Chapter 3

Literature Review

In this chapter an analysis of the state-of-the-art of the topic is carried out. Unfortunately, not many papers are available on modelling bonded selective reinforcement. For this reason the literature review is mainly focused on the bonded patch repair technology. The study of a cracked plate repaired by a patch is similar to that of a strap reinforced plate. The mechanisms involved in the two problems are similar. In both cases an additional plate is bonded to the structure to improve the residual strength and reduce the fatigue crack propagation rate. The main differences are that:

1. the patch is applied on the structure after it has cracked whereas the straps are part of the structure at manufacture and are subjected to operative loads and environments throughout the entire service life;
2. patches are usually applied above the crack and wide enough to cover a large area of the substrate, so that the crack spends its whole FCG life underneath the patch; on the other hand, straps are placed in strategic positions to retard the crack propagation when the structure actually cracks and they keep working also after the crack has passed them.

These two differences do not affect the way the two problem can be modelled. In both cases the patch and the straps are used to slow down the crack propagation rate by exerting closure forces on the substrate.

Due to the similarities of the mechanisms to model, in section (3.1) the bonded patch repair technology is reviewed. Some history of the use of bonded patch

repair is also reported in section (3.1.1). Important aspects in the design of the patch can be found in section (3.1.2). Both analytical and numerical modelling techniques have been developed to study the bonded patch repair problem. A review of these modelling methods is reported in sections (3.1.3) and (3.1.4). Capabilities of these modelling technique are analysed and some gaps in the knowledge identified (section 3.1.5). Some of these gaps have been covered in the literature for other kinds of problems. These are discussed in section (3.2). The last section (3.3) summarises what is know from the literature about bonded selective reinforcement for integral structures.

3.1 Bonded patch repair for metallic aircraft structures

3.1.1 Purpose and use

Metallic aircraft components might be subjected to fatigue cracking during service. Replacing the cracked component can be very expensive and time consuming so repair techniques have been developed. Traditional method included the use of either bolted or riveted patches. These methods are inefficient for many reasons [63]. Firstly, additional fastener holes are introduced into the structure causing other high stress concentration spots from where cracks can develop. Secondly, since the repair may be done in situ, internal damage could be caused by drilling the holes. These factors pushed towards the creation of other repair technologies.

Work conducted by Baker for the Australian defence organisation has resulted in the development of a repair scheme based on the use of bonded composite patches [63–68].

The bonding provides a very efficient load transfer from cracked components into the patch without introducing any stress concentration into the structure [63]. Practical applications have demonstrated that this repair method is fast to apply, relatively cheap, and more than anything effective in slowing or arresting crack propagation [63–68]. However, some drawbacks are introduced. The bonding process requires preparation of the surfaces and, pressure and temperature for curing the adhesive [63]. Due to the difference of the coefficients of thermal

expansion (CTE) between the patch and substrate materials associated with the elevated curing temperature of the adhesive, thermal residual stresses (TRS) are generated in the structure [66].

Composite patches can be used for a wide range of reasons. A list of applications which are reported in [64,67] is:

- Reduce stress intensity factors in regions:
 - { with fatigue cracks;
 - { with stress-corrosion cracks;
 - { badly designed;
 - { badly manufactured;
 - { with battle damage.

- Stiffen under-designed regions to:
 - { increase static strength;
 - { increase fatigue strength;
 - { increase buckling strength;
 - { reduce flutter;
 - { reduce deflection.

- Restore residual strength or stiffness:
 - { after corrosion removal;
 - { after expiration of nominal fatigue life;
 - { after reshaping to reduce stress concentration;
 - { after flaw/crack removal;
 - { in regions with widespread cracking.

In the past 30 years the Australian defence organisation has been successfully applying bonded patches for one of the aforementioned reasons on many aircraft. The first applications were on the Hercules wing plank to repair stress corrosion cracks which had initiated from rivet holes [64] and re-establish the buckling stability. Subsequently many more repair applications followed on a range of aircraft. The repairs effectuated till 1984 are reported in table 3.1 from [63].

Table 3.1: Practical application of bonded patches to military aircraft [63].

Cracking	Material	Component	Aircraft	Comments
Stress corrosion	7075T6	Wing plank	Hercules	Over 300 repairs since 1975
Fatigue	Mg alloy	Landing wheel	Macchi	Life doubled at least
Fatigue	AU4SG	Fin skin	Mirage	In service since 1978
Fatigue	AU4SG	Lower wing skin	Mirage	Over 150 repairs since 1979
Fatigue	2024T3	Upper wing skin	Nomad (fatigue test)	Over 105900 simulated flying hours
Fatigue	2024T3	Door frame	Nomad (fatigue test)	Over 106619 simulated flying hours
Stress corrosion	7075T6	Console truss	F111	Service since 1980
Lighting burn	2024T3	Fuselage skin	Orion	Service since 1980

Many other applications followed those ones on aircraft such as C130, F111-C, Boeing 747 and even on the Sea King helicopter showing none or minor bond durability problems [67].

3.1.2 Important aspects in the design of the patch

In order to design an appropriate bonded repair, many factors ought to be considered. Choice of patch material, geometry, and adhesive influences the effectiveness of the patch. Based on the practical experience gathered by the Australian researchers [63–68] the important aspects to consider in the design of a patch repair are described below.

Patch Material. The most used materials for patch repair applications are carbon fibre reinforced polymer (CFRP) and boron fibre reinforced polymer (BFRP) [63,66,67]. The reason comes from their high longitudinal Young’s modulus (table 3.2). That allows the use of thin patches to restore the stiffness of the structure [66]. The main drawback of these materials is the low coefficient of thermal expansion (CTE) in the longitudinal direction compared with the aluminium substrate (table 3.2). This difference generates

thermal residual stresses (TRS) after elevated temperature curing. Due to higher elastic modulus, lower mismatching of CTE with the aluminium, low electrical conductivity¹ and no danger of galvanic corrosion BFRP is preferred to CFRP [63].

Table 3.2: Typical mechanical properties of unidirectional (UD) CFRP and BFRP and generic aluminium alloy [66]. 1 is the fibre orientation or longitudinal direction and 2 is the transverse direction.

Material Dimension	E_1 GPa	E_2 GPa	G_{12} GPa	α_1 $\mu \text{ } ^\circ\text{C}^{-1}$	α_2 $\mu \text{ } ^\circ\text{C}^{-1}$
CFRP UD	130	12	5	0.4	28
BFRP UD	210	20	7	4.5	23
Aluminium	72	72	27	23	23

Geometry. The geometry of the repair influences the stress redistribution in the cracked substrate and consequently the efficiency of the repair. Before analysing the geometry effect, it is important to distinguish between a double-sided repair and single-sided repair. A double-side repair is obtained when the cracked substrate is patched on both sides, i.e. top and bottom (figure 3.1(a)). A single-sided repair is made by using only one patch on one side of the cracked substrate (figure 3.1(b)). Double-sided patch repairs are preferred for they are more effective in retarding the crack propagation [69]. Unfortunately, single-sided asymmetric repairs must be applied most of the times instead. This is because, in many cases, just one side of the structure can be patched due to other design needs, i.e. aerodynamic performance for the wings. Due to the asymmetric geometry, so-called secondary bending is generated, that reduces the effectiveness of the repair causing a higher stress intensity factor on the un-patched side of the plate and a curved crack front. For what concern the shape of the patch, some optimisation studies on the cross section of the patch to reduce the adhesive stresses have been carried out by Heller and Kaye in [70]. They found out the a tapered patch reduces the stresses in the adhesive. A further reduction of stress can be achieved by using a cross-ply laminate for the first two layers; hence reducing the stiffness mismatch between patch and substrate. It is, though, worth noticing that a reduced stiffness of the patch does not only reduce the

¹Necessary to conduct non-destructive inspection methods (NDI), such as eddy current techniques.

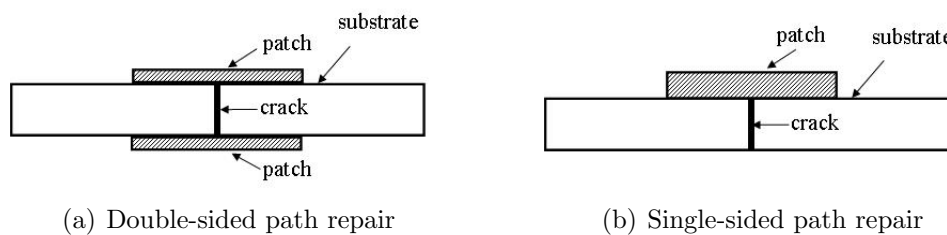


Figure 3.1: Cross-section view of examples of single-sided and double-sided patch repairs.

stresses in the adhesive, but also, the bridging effect that is applied by the patch to the substrate. Thus, minimising the stresses in the adhesive is not the most appropriate objective for a patch shape optimisation study, since it can be achieved by using a patch as weak as possible but that would not improve the life of the structure. A more appropriate optimisation objective would be to maximise the FCG life increment produced by the patch by using the adhesive stresses as a constraint.

Adhesive. The adhesive choice influences the joint durability as well as the patch repair efficiency if the adhesive failure can be limited. A good adhesive for crack patching should have the following properties [66]:

- Fatigue resistance under shear and peel stressing;
- Minimum curing temperature, close to ambient;
- Durable bond after simple surface treatment.

Different adhesives have been studied by Baker [65]. Also several epoxy adhesives that can be cured at room temperature have been employed for less stringent repairs.

Thermal residual stresses. Another important aspect that ought to be considered in the design of a patch repair is the thermal residual stresses. These stresses are caused by the curing process of the adhesive at elevated temperature and the mismatch of CTE between the patch and substrate. These generated tensile stresses reduce the effect of the patch because they promote the crack opening. Some studies were conducted in [66] to reduce them and some simple tricks were found:

- Curing the adhesive at the lowest possible temperature;

- Minimising the heated area so that, the heated area will be constrained by the unheated one [71];
- Pre-curing the adhesive at a low temperature in order to have a bonding, although weaker, at lower temperature; then, post-curing at higher temperature to make the bonding stronger;
- Prestressing the repair region in compression in order to neutralise the tensile stress;
- Employing the minimum thickness reinforcement in order to reduce the bending effect (for single-sided repair).

Baker wrote in [66] that the effectiveness of a patch repair can be evaluated by estimating the following values:

- the SIF in the repaired component;
- the shear strain or its range in the adhesive layer;
- the tensile strain or its range in the reinforcing patch.

The SIF provides an indication of the rate of the crack propagation (equation 2.20), while the other two parameters provide an indicator of the durability of the repair. The FCG life of the repair component should also be added as an important factor.

Since it is both time consuming and expensive to conduct physical tests on a wide range patch configuration, analysis tools and simulation models are required.

3.1.3 Analytical methods to study bonded repairs

Ratwani [72] was the first to develop an analytical model to study an adhesively bonded structure where one of the two plates was cracked . The structure consisted of two isotropic plates bonded together with a crack in one of them (figure 3.2). The structure was loaded in tension. The stress intensity factor of the structure was obtained by computing the forces applied by the sound plate to the cracked one and subsequently, using the Green's function of concentrate body forces to obtain the SIF. That SIF was summed to the one caused by the external load. The forces were computed under the assumptions that:

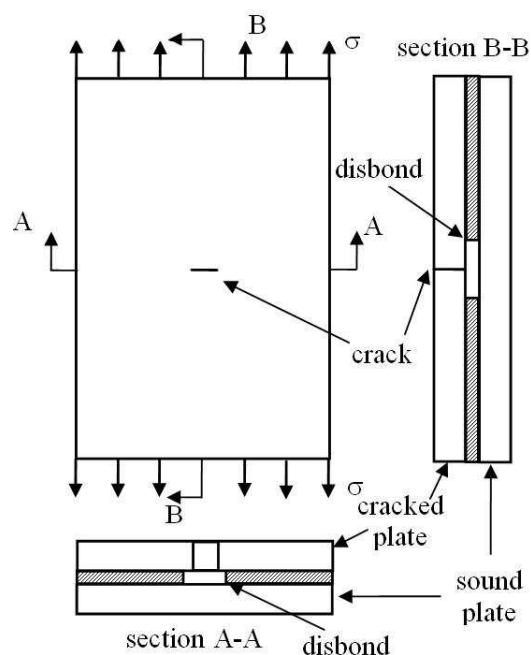


Figure 3.2: Sketch of two adhesively bonded plates with a centre crack in one studied by Ratwani in [72].

- each single layer is in plane-stress condition;
- the adhesive can be considered as an elastic shear spring since its thickness is small compared to the thickness of the plate;
- the plates are infinitely wide.

The effect of adhesive failure or disbond was included although the disbond shape was assumed by observation of experimental test and was not predicted. A correction for taking into account of the secondary bending was also developed. This correction was based on the fact that, due to the crack in one ply, more load was shifted to the sound ply. As it was noticed by Wang et al. [73] (20 years later) no shift in the neutral plane was considered. It means that this bending correction works only when the two plates are made of the same material and same thickness so that the only cause of bending would be the load shift due to the crack.

The validation was carried out on a structure made of two aluminium plates of identical thickness and geometry. The results obtained by this analytical method were in good agreement with finite element (FE) results and experiments when the corrections for disbond and secondary bending were used.

Ratwani [72] concluded that:

- secondary bending increases the SIF in the cracked plate;
- adhesive disbond reduces the stress transfer into the sound plate and consequently increase the SIF of the cracked plate;
- an increase in adhesive thickness or lower shear modulus reduces the load transfer into the sound layer causing an increase in the SIF;
- an increase in the thickness of the cracked plate or elastic modulus causes an increase in the SIF.

This analytical method proved to be a good qualitative tool to understand the effect of mechanical properties of bonded structures, but some weak points can be found. Firstly, this method is for infinite plates. Although that assumption may work to study short crack lengths, it still requires that the substrate and patch have the same width. In fact, stresses and displacements would change when the crack passed the patch. Secondly, the secondary bending correction holds only when patch and substrate have the same thickness and are made of the same material since the neutral axis shift was not taken into account. Thirdly, this method was developed for isotropic material and not for orthotropic composite materials. Lastly, thermal residual stresses were not considered, i.e either the adhesive was cured at room temperature or patch and substrate ought to have the same coefficient of thermal expansion.

Some years later, Rose [74–76] proposed another analytical method to study patched plates. This solution comes from a one-dimensional model of the patched plates. The assumptions of this model are as follows:

- the stress variation across the thickness is neglected and it is assumed to be constant; plates are in a plane strain condition;
- the adhesive layer is considered to be a shear spring;
- the shear traction that the adhesive layer yields to the substrate can be replaced by equivalent body forces.

Initially the effect of secondary bending was not taken into account consequently only double-sided symmetrical repair could be studied. The method consists of essentially three steps:

1. calculating the stress in the substrate in the patched region by using a inclusion analogy (σ_0);
2. calculating an upper limit of the SIF in the substrate produced by σ_0 ;
3. compute the TRS and the residual SIF caused by the TRS.

Mechanical and residual SIFs can be summed (superposition) to compute the total SIF.

The analytical method is based on an inclusion analogy [74]. It computes the mechanical properties of an equivalent inclusion constituted by patch and substrate. An assembly of patch and substrate can be seen as an inclusion only if the patch is longer than the load-transfer length². It consists of firstly calculating the stress in the equivalent inclusion and, secondly dividing that stress between the one which is carried by the patch and the one which stays in the substrate, i.e. σ_0 . The solution for an elliptical patch is reported in [74]. For a strip patch as the one in figure (3.3) the solution is [73]:

$$\sigma_0 = \frac{1}{1+S} \sigma^\infty \quad (3.1)$$

where σ^∞ is the applied stress and S is a stiffness ratio defined as:

$$S = \frac{E'_r t_r}{E'_s t_s} \quad (3.2)$$

where E' are the Young's modulus in plane strain condition ($E' = E/(1-\nu^2)$), ν the Poisson's ratio, t the thickness, and the suffixes r and s are for, respectively, reinforcement patch and substrate plate.

Now that the equivalent stress in the substrate (σ_0) has been computed, the upper limit of the strain energy release rate SERR (G_∞) and consequently the

²The load-transfer length is the length for which the load is transferred from the substrate to the patch starting from the overlap. After that distance from the overlap the stress in the patch and substrate will be constant

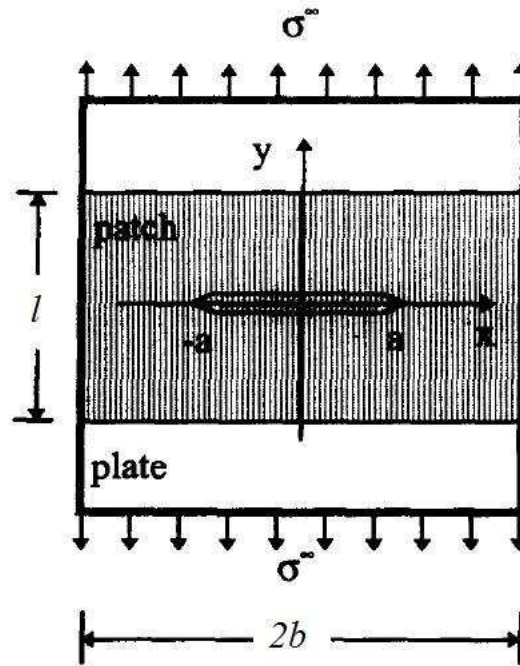


Figure 3.3: Example of a strip-like patch repair [73].

limit value of the SIF (K_∞) is³ [73–76]:

$$K_\infty = \frac{\sigma_0}{\sqrt{\kappa}} \tag{3.3}$$

where κ is given by:

$$\kappa = \frac{L_{tr}S}{(1+S)(1-\nu_s^2)} \tag{3.4}$$

and $1/L_{tr}$ is the load-transfer length:

$$L_{tr} = \sqrt{\frac{G_a}{t_a} \left(\frac{1}{E'_s t_s} + \frac{1}{E'_r t_r} \right)} \tag{3.5}$$

where G is the shear modulus and the suffix a stands for adhesive.

This solution provides an upper limit of the stress intensity factor when there is no secondary bending, i.e. double-sided symmetric patch repair.

In the case of single-sided asymmetric patch repair a correction for secondary bending ought to be introduced. Wang and Rose developed an analytical correction (ω) [73, 77]. This correction factor should multiply the strain energy release

³Since this section concerns the substrate only which is loaded in mode I (see section 2.1.1), for clarity, subscript “I” is omitted for SERR (G) and SIF (K)

rate of a double-sided patch repair (G_∞) in order to obtain the strain energy release rate of the single-side patch repair ($G_{\infty tot}$):

$$G_{\infty tot} = G_\infty \omega \quad (3.6)$$

Obviously, due to the bending, the SERR and the SIF are variable through the thickness. Wang et al. [73, 77] claimed that the energy method to compute the strain energy release rate cannot provide a solution for the membrane and bending component of the SIF. They demonstrated [73] that from the total SERR (G_{tot}), i.e. the sum of bending and membrane, only the through-thickness root mean square (RMS) value of the SIF (K_{RMS}) can be computed:

$$G_{tot} = \frac{K_{RMS}^2}{E_s} \quad (3.7)$$

where, K_{RMS} is defined as:

$$K_{RMS} = \sqrt{\frac{1}{t_s} \int_0^{t_s} K^2(z) dz} \quad (3.8)$$

At this point they needed to find a way to calculate the maximum SIF through the thickness (K_{bot}) since, in their opinion, it is the most important one. It was assumed that the SIF is linear through the thickness [73]:

$$K(z) = K_F + \frac{2z}{t} K_M \quad (3.9)$$

where one component of SIF is due to traction (K_F) and the other to bending (K_M). Substituting equation (3.9) into (3.8) the following equation was obtained [73]:

$$K_{RMS} = \sqrt{K_F^2 + \frac{1}{3} K_M^2} \quad (3.10)$$

due to the linearity assumption of the SIF through the thickness the membrane component of the SIF (K_F) and the bending component (K_M) can be linked to the maximum and minimum value of SIF through the thickness (K_{bot} and K_{top}):

$$K_F = \frac{K_{top} + K_{bot}}{2} \quad ; \quad K_M = \frac{K_{top} - K_{bot}}{2} \quad (3.11)$$

substituting equation (3.11) into (3.10):

$$K_{RMS} = \sqrt{\frac{1}{3} (K_{bot}^2 + K_{bot}K_{top} + K_{top}^2)} \quad (3.12)$$

Wang et al. [73] obtained a second equation to relate the RMS value of the SIF to the maximum and minimum SIF. This equation is based on the assumption that the traction (F) and bending (M) SIF can be expressed as:

$$K_F = \sigma_F \sqrt{\pi a} \quad ; \quad K_M = \sigma_M \sqrt{\pi a} \quad (3.13)$$

consequently the ratio (R_s) between maximum and minimum can be written as:

$$R_s = \frac{K_{top}}{K_{bot}} = \frac{\sigma_F - \sigma_M}{\sigma_F + \sigma_M} = \chi \quad (3.14)$$

where χ is a geometric factor that can be found in equation (46) of [73].

Now an algebraic system can be made with equations (3.12) and (3.14) to find the maximum and minimum value of the SIF through the thickness:

$$K_{bot} = \sqrt{\frac{3}{1 + R_s + R_s^2}} K_{RMS} \quad ; \quad K_{top} = \sqrt{\frac{3}{1 + R_s + R_s^2}} R_s K_{RMS} \quad (3.15)$$

At this point also the maximum and minimum limiting value of the SIF can be calculated. The maximum value through the thickness (i.e the unpatched or bottom side of the substrate) is the highest one and in Wang et al.'s opinion also the most important one since it limits the residual strength of the structure and determines the FCG life.

The analytical procedure for the case of single-sided patch repair can be summarised as:

1. computing the limiting value of the SIF (K_∞) by equation (3.3) as the repair were a double-sided one;
2. computing the limiting value of the SERR rate (G_∞) by equation (2.14);
3. applying the bending correction by using equation (3.6) in order to obtain the limiting value of the total SERR ($G_{\infty tot}$);
4. using equation (3.7) to compute the limiting value of the RMS of the SIF ($K_{\infty RMS}$);

5. computing the limiting values of the maximum and minimum SIF through the thickness ($K_{\infty_{bot}}$ and $K_{\infty_{top}}$) by equation (3.15).

In order to take into account of the thermal residual stresses the superposition principle is applied. Again the patch and substrate are considered as an inclusion and a thermal load is applied [78]. In that way the thermal stresses in the substrate can be computed and from the stress also the limiting thermal stress intensity factor can be calculated. The sum of the mechanical and thermal limiting values of the SIF is the one which characterise the effectiveness of the patch repair [76].

This analytical method presents some strong points. It provides simple equations to study the patch repair which are quick and easy to use. Moreover, the influence of the property of the patch on the effectiveness of the repair can easily be assessed. Unfortunately, though, this analytical method can provide solutions only for simple patch geometries due to the need to find a solution to the inclusion model. Furthermore, only the limiting values of the SIF at the top, bottom and RMS can be computed. This values can help finding the lowest residual strength of the patch repair but not the fatigue life.

To solve this problem Wang and Rose published in [79] a new analytical model to actually compute the SIF at the top, bottom and RMS value as a function of the crack length. The results in terms of SIF have been compared with a finite element model showing good agreement. They claimed that the most important value of the SIF through the thickness for each crack length is the maximum one. However, it was never used to compute the FCG life of the repair and compare it with experiments. Another problem is that they assumed that a limiting value of the SIF always exist for patch repair. That is true for infinitely wide substrates or for finite width substrate reinforced by a patch as wide as the substrate but, if the patch is narrower than the substrate, when the crack passes the patch or approach the edge of the substrate the value of the SIF ought to increase.

By using this analytical model the shear stress in the adhesive can be computed but nothing is done to take into account of the progressive disbond of the adhesive with the growing crack. In fact, progressive adhesive failure reduces the bridging effect resulting in higher SIF in the substrate.

Another problem to this analytical method is the way the secondary bending was modelled. Wang, Rose et al. claimed that from the energy method only

the RMS of the stress intensity factor can be computed, but actually Sun et al. [80–83] proved them wrong by applying the energy method (G) to compute the SIF distribution through the thickness. Whereas it is true that from the total strain energy release rate only the RMS of the SIF can be calculated (see equation 3.7), it will be shown by the author that from the SERR the distribution of SIF through the thickness can be computed. This subject will be addressed in details when the developed modelling technique is presented (chapter 4).

The last problem of this analytical methodology is that the interaction between the mechanical load and the thermal load are completely neglected. To correctly study the problem, a geometric nonlinear analysis is required. If nonlinearity are involved in the problem the superposition principle stands no longer. Also this aspect will be dealt with in the methodology chapter (chapter 4) and the error generated by neglecting this interaction will be shown in the validation chapter (chapter 5).

Analytical procedures are very useful to show the dependency of the SIF to the material properties and patch geometry and provides a rapid approach to the problem. Unfortunately, they provide accurate solutions only for simple geometries. Due to the complexity of the problem, very strict assumptions must be made and important factors neglected to allow the existence of a closed-form solution. In order to study complex structures, free the model of some assumptions and obtain a more accurate solution, numerical models ought to be used. In the next section some of the finite element modelling techniques which have been reported in the literature are presented.

3.1.4 Numerical methods to study adhesively patched structures

The first finite element (FE) models for patch repairs were made in the late 1970s. Ratwani [72] produced a FE model to validate his analytical methodology. A set of plate elements to model substrate and reinforcement and prismatic-shear element to model the adhesive were used. Disbond was not predicted by the FE, but modelled by adapting the shape of the adhesive mesh to the shape of the disbond found in experiments. The disbond shape imposed was elliptical with a major axis as long as the crack length and a minor to major axis ratio of 0.1.

The mesh of the model is coarse, but it must be said that it was done 30 years ago with the computing power of the time. Due to the coarse mesh a stress singularity element (see section 2.2) was used at the crack tip.

The result obtained by this model have been compared to the analytical one and show good agreement. Obviously, the imposed disbond shape in the analytical and numerical model was the same and the two bonded plates (see figure 3.2) were made of the same material reducing the secondary bending. The FCG life of this plates was not computed and no comparison was made with experiments.

Jones and Callinan [84–86] used the finite element method to study the bonded patch repair problem in the same year of Ratwani [72] (1979). They developed a special linear finite element with an equivalent stiffness to model the assembly of substrate, adhesive, and patch. Details on building and assembling the equivalent stiffness are given in [85]. A special crack-tip element developed by them in [84] is used to compute the SIF. The use of those elements permit calculation of the stresses in substrate, adhesive and patch as well as the SIF on the crack tip. Although in the abstract of [85] it is said that “debonding of the adhesive is permitted”, no details on how that was achieved are given in [85].

The modelling technique described by Jones and Callinan [84–86] is still a simple one where secondary bending and TRS are not included, but still, from it some good discussions on the patch repair problem were made. They showed that the presence of the patch considerably reduces the stress in the substrate. By increasing the thickness of the patch the load in the substrate is reduced, although the shear stress in the adhesive are increased. The position of the patch was also studied. It was shown that the most effective position of the patch is just after the crack tip (figure 3.4). This result is of particular interest and it will be confirmed in this thesis as well (see section 6.1.2).

The results obtained by this modelling technique was validate just in terms of SIF for one crack length and FCG lives were not computed.

Almost 10 years later (1987), Chandra [87] used special crack tip elements and J -integral to calculate the SIF of a patched plate. The assembly of substrate, adhesive, and patch was again modelled by a single equivalent 2D element. The only difference from Jones and Callinan’s model [84–86] was that in Chandra’s case the laminate element was already implemented in the finite element code

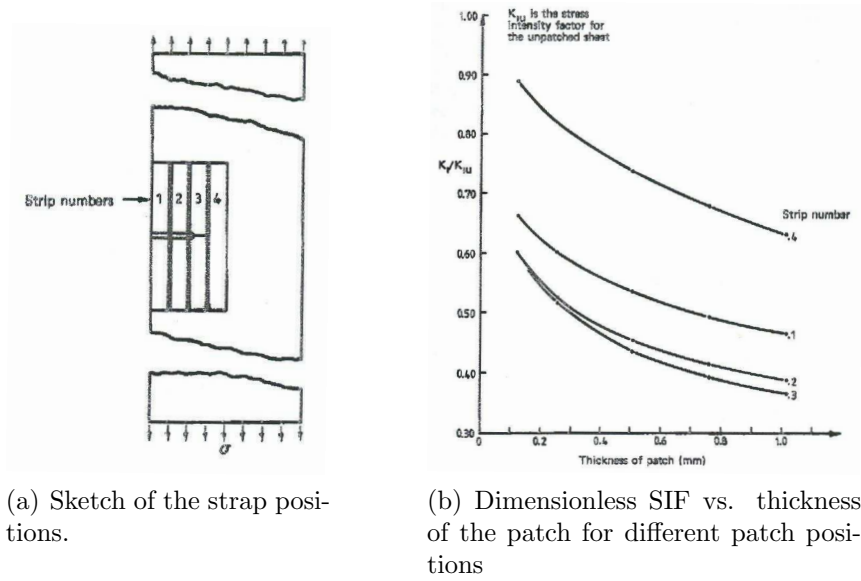


Figure 3.4: Effect of the patch position and thickness on the SIF [85]. Note: original paper was in poor quality of figures.

(called ASKA) and the stiffness of the element was internally computed. Secondary bending, adhesive progressive disbond, and TRS were not considered. The SIFs obtained by this modelling technique were validated against other analytical and numerical results in the literature. Again, FCG life was not computed.

The first “leap forward” in the study of patch repairs was in the second half of the 1990s when the secondary bending effect was the subject of study of many researchers.

Young and Sun [80] studied “the strain energy release rate for a cracked plate subject to out-of-plane bending moment”. They applied the MVCCT (see section 2.2.1) to finite plate elements subjected to bending⁴ and found that for a 4-node element the SERR (G_{IM}) can be written as:

$$G_{IM} = \frac{1}{t_s \Delta a} M_s \Delta \phi_s \tag{3.16}$$

where t_s is the thickness of the substrate, M_s the bending moment at the crack tip node, $\Delta \phi_s$ the difference of rotation in the opened nodes.

⁴It should be noted that bending falls still in mode I loading. The only difference with tension load is that the SIF is variable through the thickness.

The stress intensity factor (K_{I_M}) can then be computed as:

$$K_{I_M} = \sqrt{3G_{I_M}E} \quad (3.17)$$

Arendt and Sun subsequently (1994) developed the first modelling technique where the secondary bending effect was not neglected [81]. 2D plate elements were used to model substrate and patch. Attempt to model the adhesive layer with 3D brick elements were made, but due to the small thickness of the adhesive, numerical problems were encountered. Consequently, instead of brick elements, two shear springs were used to model the shear mechanical properties of the adhesive.

Constraint equations were also used to force the continuity of displacements through the thickness. The modified virtual crack closure technique was used to calculate two components of SERR, one due to bending (G_{I_M} , equation 3.16) and one due to tension (G_{I_F} , equation 2.15). The total SERR $G_{I_{tot}} = G_{I_F} + G_{I_M}$ was computed and, by equation 2.14, the SIF obtained. This SIF was not related to any particular position through the thickness. In fact, it was said that the variation of stress intensity factor through the thickness was negligible. In reality, Wang et al. showed while developing their analytical technique some years later [73, 77] that that SIF was the RMS value of the SIF distribution through the thickness.

Disbond progression was not modelled but was imposed following Ratwani's model [72], i.e. by forcing an elliptical shape. Thermal residual stress were not considered.

The results obtained by this modelling technique were impressive, since for the first time secondary bending was considered. It is worth noticing that the analytical correction for bending effect was developed three years later in 1997 [73, 77]. This modelling technique was used to compare the FE results against the analytical models of Ratwani [72] and Rose [74, 75]. Arendt and Sun showed that, for the configuration studied, both Ratwani's and Rose's models underpredicted the SIF although Ratwani's was more accurate. They showed that SERR decreases as the stiffness of the repair decreases and disbond affects the SIF more in the presence of secondary bending.

Although some light was shed on the secondary bending, this modelling technique still presents some problems. Firstly, only one value of SIF was computed through the thickness for each crack length, but it was not said how represen-

tative of the SIF distribution through the thickness that value was. Secondly, disbond shape was not predicted but imposed. Thirdly, thermal residual stresses were not considered.

Two years later (1996), two of the most used modelling techniques for patch repairs were published. One was developed by Sun et al. [82] and the other by Naboulsi and Mall [88].

Sun et al. [82] improved the modelling technique which had been developed two years before in [81]. Again two layer of plate elements were used to model substrate and patch, but this time, three springs elements were used to model the adhesive: two for shear and one for peel. In fact, the peel properties of the adhesive are also important to model secondary bending. The continuity of displacements through the substrate-adhesive-patch assembly thickness is assured by constraint equations. For the first time, an equation to compute the SIF through the thickness is given. As before two components of SERR, one for the bending (G_{I_M} action, equation 3.17) and one for tension (G_{I_F} , equation 2.15) were computed, but this time, instead of summing them to compute the total one, two components of SIF were also computed, one due to bending (K_{I_M} , equation 3.17) and one due to tension (K_{I_F} , equation 2.14). At this point they assumed that the distribution of SIF is linear and consequently the maximum stress intensity factor ($K_{I_{bot}}$) is on the unpatched side:

$$K_{I_{bot}} = K_{I_F} + K_{I_M} \quad (3.18)$$

The results obtained by the 2D models were compared with the one obtained by a 3D model. The errors were around 10 – 20%. The SERR distribution on an imposed elliptical disbond front in the adhesive was also computed.

Although this modelling technique improved the study of secondary bending effect, the problem of computing the life of a patched plate was not solved, yet. Firstly secondary bending is a geometrically non-linear effect and consequently a non-linear analysis should be required. Secondly, the maximum SIF through the thickness was computed and compared against 3D models but the FCG life was not calculated. The question “is it the maximum SIF that should be used to compute the FCG life?” was unsolved since no comparison with experimental results was presented. Thirdly, by using this modelling technique they were able to compute the SERR along an imposed disbond front, no prediction of the

disbond were made and no study of disbond under fatigue load was carried out. Lastly, TRS effect was not considered.

The other modelling technique which was developed in the same year (1996) is by Naboulsi and Mall [88]. It is called “three layer technique”. This modelling technique is very similar to the one developed by Sun et al. [82]. Constraint equations to force the through thickness continuity of the displacements were used; the same equations to compute the SERR and SIF in the substrate crack were employed. The only difference is that the adhesive layer is modelled by 2D plate elements instead of springs. Also in this case disbond shape was not modelled but was imposed. An elliptical shape was given to it and the SERR around the disbond front calculated. The drawbacks aforementioned are still unsolved.

One year later (1997) Callinan et al. [69] produced a 3D model to study the same configuration studied by Sun et al. [82]. Their results were in good agreement with Sun et al.’s. From the modelling point of view no improvement were brought by the 3D modelling technique to the 2D developed by Sun et al. [82]. In summary the modelling techniques developed by Sun et al. [82] and Naboulsi and Mall [88] are still the most used 2D modelling techniques for bonded patch repairs.

It was not until 1999 when comparisons between models and experiments in terms of FCG life were made. Klug, Maley and Sun [83] tested an aluminium 2024-T3 plate reinforced by carbon fibre reinforced polymer (CFRP) bonded with FM73 adhesive cured at 120°C . Two patch configurations were tested: a 4 and a 8 ply patch. FCG life and disbond growth have been measured. Obviously the plate reinforced by the 8-ply patch lived longer, although showed more extended adhesive failure.

What is interesting are the results of the models. The same modelling technique developed by Sun et al. in [82] was used. Disbond was modelled following observation of the experimental results. This time TRS were modelled. A thermal analysis was run with a temperature drop of -70°C . The actual temperature drop should have been closer to 100°C since the adhesive was cured at 120°C and room temperature is considered to be 20°C . The assumption of -70°C was justified by the fact that the actual temperature at which the adhesive hardens is not well known. The FCG life was computed by Paris’ equation (see section

2.3.2) by using either the maximum SIF for each crack length or the mean value of the SIF through the thickness or the RMS value. The lives computed by the maximum SIF resulted overconservative and the ones computed with the mean value over-predicted the real life. The best agreement with the experiments was obtained by the RMS of the SIF.

Although this paper is a leap forward in the study of bonded patch repair, some assumptions which reduce the accuracy of the analysis are still present. Firstly, disbond shape was modelled by observing the experiments. This means that a proper prediction of the FCG life can not be made but experimental tests are still necessary to build the model. Secondly, the effect of the TRS was considered in an approximate way. The residual SIF K_T should be summed to both the SIF at the maximum applied load $K_{M_{max}}$ and the SIF at the minimum applied load $K_{M_{min}}$ so that the effective SIF (ΔK_{eff}) range and R -ratio (R_{eff}) needed to compute the FCG life (see section 2.3) can be written as:

$$\Delta K_{eff} = (K_{M_{max}} + K_T) - (K_{M_{min}} + K_T) = K_{M_{max}} - K_{M_{min}} \quad (3.19)$$

and

$$R_{eff} = \frac{K_{M_{min}} + K_T}{K_{M_{max}} + K_T} \neq \frac{K_{M_{min}}}{K_{M_{max}}} = R \quad (3.20)$$

Klug et al. [83] studied a case where $K_{M_{min}}$ was null and consequently also the R -ratio. Since Paris' law was used in which the effect of the R -ratio is not taken into account, they rewrote the previous equations as:

$$\Delta K_{eff} = K_{M_{max}} + K_T \quad (3.21)$$

and

$$R_{eff} = \frac{K_{M_{min}}}{K_{M_{max}}} = 0 \quad (3.22)$$

so that the effect of the R -ratio disappears and Paris' law can be used.

Although this procedure is not completely correct, it actually is the only way to approximately take into account of TRS if the effect of R -ratio for the studied material is unknown.

In the same year (1999), Umamaheswar and Singh [89] studied different patch configurations. SIFs were obtained by both 2D and 3D models. Four different models were run to compare the SIF results and determine which one was the

most accurate one. The benchmark was a 3D model where 4 layers of brick elements were used for the substrate, 2 for the adhesive, and 4 for the patch. The 2D model was made of two layers of plate elements for substrate and patch and beams elements were used for the adhesive. Another model was made of 2D elements for substrate and patch and 3D elements for the adhesive. The last model was made of one layer of brick elements for substrate, adhesive, and patch. It is worth noticing that no constraint equations were used to connect substrate to adhesive and patch to adhesive in the models where substrate and patch were modelled by 2D elements. Consequently, for those models, the beams or 3D elements modelling the adhesive connected wrongly the midplane of the substrate to the bottom of the adhesive and the midplane of the patch to the top of the adhesive. Probably for that reason, the 2D models were considered unemployable to model single sided patch repair and the best model was declared to be the one that made use of only one layer of brick elements for each component of the assembly.

Parametric studies were also carried out in [89], but the life was computed by using the mean value of the SIF through the thickness instead of the RMS value as Klug et al. [83] had shown. For that reason the parametric study can be considered to have produced only qualitative results. Although under a qualitative point of view, they showed that boron fibre reinforced polymer (BFRP) patches are more effective in retarding the crack growth than aluminium and glass fibre reinforced polymer (GFRP) ones. Interesting observations emerging from Umamaheswar and Singh's paper [89] are that geometrical non-linear analyses are needed to study single-sided patch repair and that the propagating crack front in the substrate is not straight but curved.

With the increase of the computational power, modelling techniques moved more and more towards the use of 3D brick elements. Sabelkin et al. [90,91] used 3D models to study different configurations of single sided patch repairs. It was also proposed a new method to compute the temperature drop to apply to calculate the TRS. This value of the temperature drop was computed by matching the fatigue life obtained by models with different applied temperature drops to the one obtained by experiments. The obtained temperature drop was just $-22^{\circ}C$, even though the curing temperature of the adhesive was $120^{\circ}C$ and the test was carried out at room temperature (around $20^{\circ}C$). The actual temperature drop should have been closer to $-100^{\circ}C$. A temperature drop computed by com-

paring FCG lives obtained by models and test is not accurate because includes the scatter error of the FCG experimental lives in it. Good agreement between models and experiments was claimed but no graphs were presented.

More recently, efforts are towards creation of 3D models to take into account also of the curved crack front that develops during fatigue crack propagation for single-sided reinforced plates. The analysis of the evolution of the crack front shape has often been studied for surface cracks [92–94]. Lee et al. [95, 96] applied that technique for the patch repair problem. A successive 3D finite element analysis technique was developed to study the FCG life of patched plates taking into account that the crack front is not straight (as it has to be using a 2D FE model) but curved due to the asymmetric geometry and secondary bending. It was done considering a set of points along the crack front, computing the SIF for those points, and estimating the crack growth increment for each point using a Paris' law type equation, re-meshing the crack front and running a new analysis. Their numerical results are in excellent agreement with the experimental ones, even though disbond was not considered. In fact, disbond between patch and substrate develops during fatigue loading and a reduction of the bridging effect is caused. TRS were not modelled, but the paper does not say whether the adhesive was cured at elevated temperature or not.

Hosseini-Toudeshky et al. [97, 98] also produced a 3D modelling technique where the crack front shape can be predicted. In [97] the 3D FEM results were compared against experiments in terms of both FCG life and crack front. Although no explanation is given on the way they dealt with TRS and disbond, the results are in good agreement. In [98], Hosseini-Toudeshky et al. conducted two 3D FE analyses of curved and straight crack fronts. They found that the FCG life can be computed by the simpler model with straight crack front using an equivalent SIF, which, for each crack length, is a value of SIF in a position along the sample thickness, which depends on the elastic modulus of the plate and repair patch and also the plate thickness. That position was found to be between $0.32 \sim 0.37$ of the plate thickness from the un-patched side. This was done because the algorithms of re-meshing are tedious and time-demanding. For that reason successive re-mesh needs to be avoided.

3.1.5 Room for improvement for numerical modelling techniques

Many of the frequently used modelling techniques for patch repair have been reviewed. Although considerable progress have been made in the past 30 years toward an accurate and reliable modelling technique, some gaps are still present. These gaps of knowledge are summarised in the following list.

- **Progressive adhesive failure.** It has never been modelled interactively along with the substrate crack propagation. In most of the modelling technique reviewed before, the disbond shape is either imposed by the observation of the experiments [69, 72, 82–88] or completely neglected [89, 90, 90, 95–98], although, as a matter of fact, adhesive failure reduces the patch effect.
- **Secondary bending by 2D models.** A linear distribution of SIF through the crack thickness was assumed [82, 83, 88]. Whether the SIF through the thickness is linear or not has not been formally demonstrate, though. Moreover, a distribution of SERR through the thickness is supposed to be impossible to be computed by a 2D model [73, 77].
- **Curved crack front.** The secondary bending effect causes the substrate crack to grow faster on one side and slower on the other. Consequently, the crack front which starts as a straight line through the thickness, evolves to a curvature. This can be modelled by 3D FE models and re-meshing algorithm, but it is preferable to avoid re-meshing. The idea of Hosseini-Toudeshky et al. [97, 98] to find an equivalent point through the thickness where the SIF of a straight crack front is representative of an equivalent SIF of the curved crack front can be exploited by 2D models, but it has not been done yet.
- **Non-linearity.** It was shown in the literature [89, 95, 96] that geometrically nonlinear analyses are needed to study single-sided patch repairs because of the secondary bending. The use of a non-linear analysis makes it impossible to eliminate the dependance of the SIF on the applied stress and compute a geometric factor such as β (equation 2.2).
- **Thermal residual stress effect.** TRS were completely neglected in the most of the studies [72, 82, 84–89, 95–98]. Klug, Maley and Sun [83] were

the first ones to consider them. Unfortunately, they could not compare predicted TRS with experimental measurements. Moreover, the TRS effect was accounted into the maximum SIF instead of the effective R -ratio.

- **Redistribution of TRS.** When the crack propagates in the substrate the TRS caused by curing the adhesive will redistribute. To the author's knowledge this redistribution and its effect has never been modelled.
- **Interaction of TRS and mechanical load .** TRS causes secondary bending as well. The final deformed shape depends on both the external load and TRS, consequently the SIF caused by the secondary bending would also change if the two loads are applied together. This has not been mentioned in the literature.

The modelling technique developed by the author and presented in the next chapter deals with each of these problems and provide solutions to them.

3.2 Delamination and progressive adhesive failure modelling

Apart from the literature on repairs, some further literature review on the approaches to model delamination or adhesive failure is reported in this section. Delamination and disbond have been broadly studied in the literature for laminated composites and adhesive joints.

Before reviewing the literature it is important to distinguish delamination growing under static load from that under fatigue load. In the first case the load is increased step by step and the delamination grows. In the second case a fatigue load is applied to the laminate and the delamination grows. The ways to study the two loading conditions are different as it is different to study fracture under static or fatigue load. For that reason this part of literature review is divided into two subsections (3.2.1 and 3.2.2).

3.2.1 Static loading

There are essentially two methods to study delamination for composite materials subjected to static load. One makes use of the decohesion elements and the other uses an initiation criterion coupled with a failure criterion (Puck's law method + SERR).

Decoherence elements have been developed and applied by Needleman et al. to describe void creation from inclusions [99] and other problems [100–103]. This kind of elements are described by a peculiar, non-linear constitutive relations which connect the interfacial forces to the interfacial displacements (figure 3.5). These relations describe how the interfacial forces increase with the interfacial

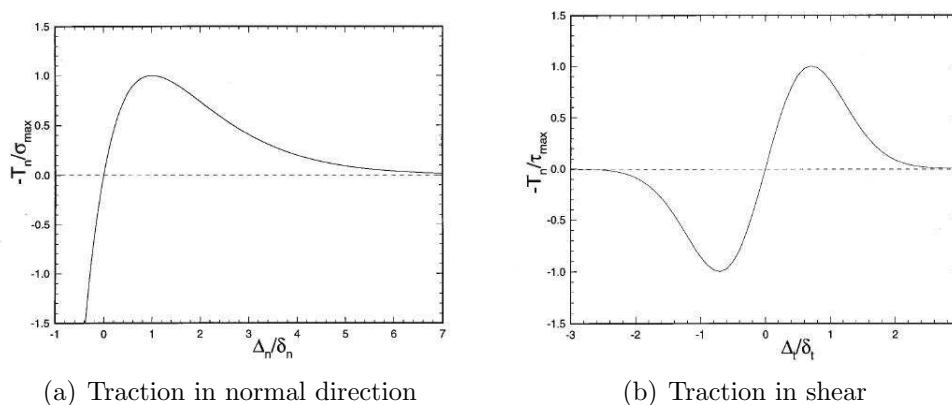


Figure 3.5: Decoherence element constitutive relations [99].

displacement, reach a maximum and then lower until complete separation is achieved and no forces are generated. These decohesion (also called cohesive) elements are described in details by Camanho et al. in [104, 105].

Many elements have been developed and implemented in commercial FE codes, such as ABAQUS and MSC MARC. They can have zero thickness and connect solid elements, or a finite thickness and connect plate elements, or just one dimension (line decohesion elements), or be spring elements connecting nodes [104]. In order to use decohesion element the interfacial response of the structure must be known. This can be described by 3 parameters (figure 3.6). The first is the stiffness of the interfacial element before failure (K_p), the second is the failure stress (σ_c), and the third is the critical strain energy release rate (G_c) that is the area of the constitutive relation.

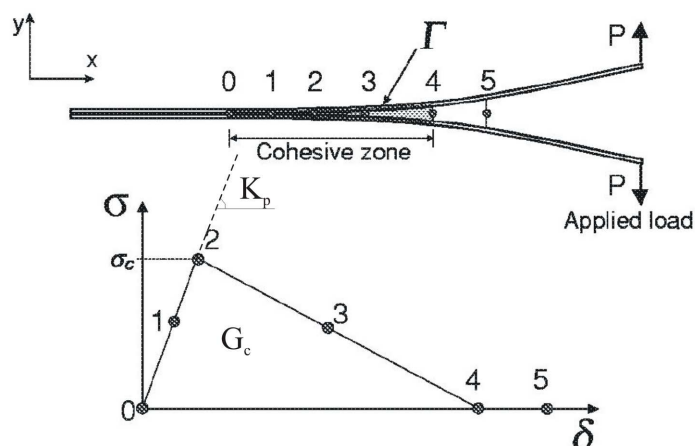


Figure 3.6: Cohesive zone response and parameters needed to characterise it [104].

In case of mixed mode loading, a mixed mode failure criterion is needed. The most used criterion is a interaction between the two modes [105]:

$$\left(\frac{G_I}{G_{Ic}}\right)^\alpha + \left(\frac{G_{II}}{G_{IIc}}\right)^\beta \geq 1 \tag{3.23}$$

where G_{Ic} and G_{IIc} are the critical SERR values for mode I and II respectively, and α and β fitting material coefficients.

The advantages in using these elements come from the fact that these elements are already implemented in some commercial FE codes and the initiation of delamination is taken care of by the element itself. Some disadvantages are also present. Firstly, the interfacial response must be known, since it can be different from case to case [106]. Secondly, some numerical problems could arise if the proper integration technique is not used. Thirdly, the failure law is based on the critical stress (σ_{cri}), consequently accurate stress computation is needed, thus very fine mesh in the delamination region.

A different approach to delamination study was taken by other researchers [107–112]. This approach uses the Puck’s law to compute the initiation of disbond propagation [107] and MVCCT (section 2.2.1) to compute the SERR along the disbond front. When the computed SERR is greater than the critical one (equation 2.13) disbond propagates. For mixed mode loading conditions equation 3.23 is used.

This approach to model delamination growth was also employed by Xie and Biggers [113,114]. A special finite element consisting of two 8-noded plate elements and three spring elements was implemented into the ABAQUS FE software. SERR was calculated by the modified virtual crack closure technique (MVCCT) inside the special element and the springs of this element are deleted when the mixed mode failure criteria described by equation (3.23) is satisfied. Therefore a moving delamination front can be modelled using a fixed mesh.

Schecker et al. [112] claimed that this method to model delamination is computationally more efficient than the use of decohesion elements.

3.2.2 Fatigue loading

When laminated composites and adhesive joints are subjected to fatigue loads, delamination happens at lower load levels than the static load case.

The work of many researchers [115–129] is based on the development or improvement of empirical laws. These laws link the disbond growth rate dl/dN to the SERR range (ΔG) using experimentally correlated material constants. They can be written in the general form as:

$$\frac{dl}{dN} = f(\Delta G) \quad (3.24)$$

Many different laws have been developed. In the 1980s, Paris' law type equations were developed and used where only region *II* of the crack propagation was modelled:

$$\frac{dl}{dN} = D(\Delta G)^n \quad (3.25)$$

where D and n are material constants.

Research has been done to include the effect of the stress R -ratio [117–119,122,124] and mixed mode loading conditions [115,116,118–120,124].

Mall et al. [119] showed that if $G_{TOT} = G_I + G_{II}$ is used in equation 3.25, mixed-modes can be studied. However, Wilkings et al. [115] and Wang et al. [116] showed that the material law changed as a function of the mixed-mode ratio in the problem. Like the FCG laws for metals are affected by the R -ratio and the loading condition (see section 2.3), the delamination propagation is also influenced by these factors.

In the 1990s, Kinloch et al. [125–127] developed a more comprehensive law.

This law describes also the threshold and the instable crack propagation regimes (regions *I* and *III*) in addition to the stable crack growth region (region *II*):

$$\frac{dl}{dN} = DG_{max}^n \frac{1 - \left(\frac{G_{th}}{G_{max}}\right)^{n_1}}{1 - \left(\frac{G_{max}}{G_c}\right)^{n_2}} \quad (3.26)$$

Where D , n , n_1 , n_2 are material parameters to be determined by fitting the experimental data. G_c is the critical strain energy release rate, G_{th} the threshold strain energy release rate, and G_{max} the cyclic maximum SERR at the delamination front. This equation is plotted in figure (3.7).

This material law was used to predict the life of bonded single-lap joints (loaded

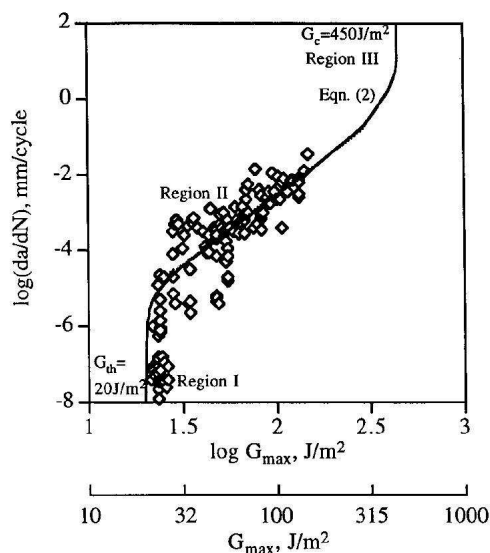


Figure 3.7: Example of delamination growth rate law [126, 127].

essentially in mode II) and also a “top-hat” section bonded to a base plate (loaded in mode I). The finite element method was used to calculate the strain energy release rate at the delamination front as a function of the delamination length ($G_{max} = f(l)$) and equation (3.26) was integrated to compute the FCG life of the joints and compared with experimental results. Good agreement is obtained for the ‘top-hat’ component but overconservative results were obtained for the lap joints. Although it was claimed that equation (3.26) could be used for mixed-modes, the results showed that when mode II is dominant an overconservative solution is obtained (see figures 16 and 17 in [126]). That may be due to the fact that the material coefficients used with the law were obtained from a tapered double cantilever beam test which is loaded in mode I.

Hadavinia et al. [128, 129] showed the effect of wet and dry environment on the coefficients of equation 3.26 showing that a wet environment causes a reduction of G_{th} . That law was used to compute the life of bonded lap joints [129]. Again the coefficients of the law were obtained by testing a tapered double cantilever beam that is in mode I and then applied to lap joint that are principally loaded in mode II. That produced again overconservative results.

Lately, the effect of the increase in fracture resistance with delamination growth is also studied [121, 123]. To the author's best knowledge, Shivakumar et al. [123] developed the most comprehensive law which includes all aforementioned effects in a single equation:

$$\frac{da}{dN} = D \left(\frac{G_{I_{max}}}{G_{IR}} \right)^m \frac{\left(1 - \left(\frac{G_{I_{th}}}{G_{I_{max}}} \right)^{D_1} \right)}{\left(1 - \left(\frac{G_{I_{max}}}{G_{IR}} \right)^{D_2} \right)} \quad (3.27)$$

Where D , m , D_1 , D_2 are fitting material parameters to be determined by fatigue test data, G_{Ic} the maximum cyclic strain energy release rate, G_{IR} the resistance value which depends on the delamination length and $G_{I_{th}}$ the threshold strain energy release rate. Detailed testing guidelines are given to obtain the coefficients. This material law was used to compute the delamination propagation of a GFRP laminate loaded in mode I and the results were in good agreement.

In the past five years Alderliesten et al. [130–136] have been studying fatigue crack propagation in GLARE fibre-metal laminates. They produced a fatigue delamination growth law as the function of the square root of the SERR:

$$\frac{dl}{dN} = C_d (\sqrt{G_{max}} - \sqrt{G_{min}})^{n_d} \quad (3.28)$$

where C_d and n_d are material fitting coefficients. It is worth noticing that the square root of the SERR is proportional to the SIF.

This law is again a Paris' law type equation where only region II is described and the effect of R -ratio is neglected. Although this law has been proved to be adequate to model delamination damage in the fibre-metal laminate GLARE, the effect of the R -ratio should not be neglected, nor should all the other effects accounted for in the aforementioned delamination laws (equations 3.26 and 3.27).

All these laws provide good tools to computed delamination growth under fatigue loads. It would be enough to compute the SERR in the delamination front and then integrate one of these laws to obtain the disbond or delamination propagation life.

Unfortunately, there are some drawbacks which limit the use of this approach. Firstly, a database of material constants for currently used adhesives is not yet available; it was proved that the coefficients of these material laws depend on many factors, such as wet or dry environments [128,129], temperature [131], adhesive and adherends materials, and surface treatments. If the scatter presented in experiments to compute static critical values of SERR for mode I and mode II load can be considered wide [137], the scatter in producing a fatigue delamination growth curve is much much broader [138]. Consequently, all those material fitting coefficients and respective laws can only be used for the very adhesive and adherends for which they were obtained.

Secondly, none of them can deal with disbond initiation. In fact, to predict the fatigue life of an adhesive joint, the critical SERR value for the onset of disbond initiation as function of cycle numbers [121] must be known; an other way to compute initiation is by either using a stress-based criterion or assuming the presence of initial defect in the adhesive interface [136]. In the first case, stress computation is required and the mesh size will influence the results. In the second case, over-conservative prediction could be obtained if the assumed initial flaw does not actually exist.

Thirdly, these Paris' law type equations were obtained from tests under single mode load conditions whereas, for the bonded crack retarder or repair problem, disbond usually propagates under mixed mode load.

Therefore, although there have been some success in modelling specific configurations of adhesively-bonded joints, these empirical laws are not yet ready for modelling bond strap reinforced structures.

3.3 Bonded crack retarders

As said before there is not much literature available on the bonded crack retarders concept.

The first to introduce the crack retarders concept (called "crack stoppers" in the original contest) was Schijve in 1990 [17]. Plates reinforced by either rivetted or

bonded straps (or strips) made of ARALL (ARamid Aluminium Laminates) or titanium alloy (Ti-6Al-4V) were tested as well as integral strips. It was shown how the integral strips only produce crack retardation until the crack reaches the first edge of the strips and after the strip crack retardation effect vanishes. On the other hand, plates reinforced by riveted and bonded crack retarders showed crack growth retardation also after the crack has passed the straps. It was shown that the retardation is larger for a strap of higher stiffness. Schijve concluded his study pointing out that “there are several interacting mechanisms, which are not easy to model in a quantitatively accurate way.”

CFRP reinforcements on steel plate were studied by Colombi et al. [18]. The CFRP straps were prestretched in order to cause a compressive stress in the substrate which promotes crack closure and slows the FCG rates. The three layer model introduced by Naboulsi and Mall [88] was used. SERR on the disbond front were calculated. Disbond shape was modelled by imposing the same shape observed during experiments. Disbond growth was not modelled. Parametric studies were carried out to show the influence of the elastic modulus, strap thickness and pretension level on the SERR at the disbond front.

Heinimann et al. [11] tested different strap configurations and materials (GLARE-1, aluminium 7075-T762, and CFRP based fiber metal laminate) on aluminum substrates. Wide panels with seven bonded GLARE-1 straps were tested. The grip ends of straps and substrate were pinned together during the bond cycle. In that way straps and substrate expand and compress at the same rate during the cure of the adhesive and the tensile TRS can be significantly reduced. The results were really promising in terms of crack growth retard; the thinnest test panels had the largest reinforcement volume fraction (28%) and achieved an average fatigue life improvement of more than 300%.

Zhang and Li [12] studied by numerical simulations integral stringer panels reinforced by either UD carbon-epoxy laminates or Ti-6Al-4V straps. Finite element method (FEM) was used to model crack growth and disbond failure. Based on the numerical modelling, the FCG life was significantly improved by both types of bonded straps.

Tests and finite element modelling were conducted by Colavita et al. [19] and Bowler [20] using CFRP straps on aluminium plate. They worked on carbon epoxy straps and showed how curing the adhesive at elevated temperature could actually reduce the life of the strapped integral structure compared to the unreinforced one due to the adverse effect of the thermal residual stresses.

Although some experimental work has been carried out on the subject, a complete modelling methodology has yet to be developed. Moreover, the effect of the strap material and dimension are still to be understood as well as all the other parameters which could influence the design of straps.

Chapter 4

Modelling methodology

This chapter presents the modelling technique which has been developed in this research programme to study integral panels reinforced by bonded straps.

Reality is complicated and it is often impossible to model each and every single mechanism; for that reason, it is important to identify the most relevant mechanisms involved in a problem before modelling it. This is done in section 4.1 where the most important mechanisms which act on the fatigue life of the bonded reinforced structure are identified and examined. In section 4.2 the 2D “two layer plus spring” modelling technique is described highlighting how each of the mechanisms have been taken into account and the problems associated with the calculation of FCG life solved. It closes by describing how this modelling technique has been implemented in a computer code interfacing the commercial NASTRAN FE package. Section 4.4 describes the 3D modelling technique used to assess the accuracy of the 2D “two layer plus spring” modelling technique.

4.1 Mechanisms

The mechanisms which affect crack propagation in strap reinforced integral panels are complex with multiple failure modes and many influential factors that also interact each other. An example of these kind of structures can be seen in figure 1.5. Under cyclic loads, four possible failure modes are identified, i.e. initiation and growth of a lead crack in the substrate, disbond failure in the adhesive interface between straps and substrate, delamination damage in composite straps,

and cracking in the straps. In order to model these failure modes and predict FCG life of reinforced structures, four primary mechanisms have been identified and need to be simulated.

- **Strap stiffening and bridging effect**

This is the only positive mechanism. The stiffening/bridging action reduces crack growth rates. Before the substrate crack enters the strapped region, the strap is already effective. It acts as a “stiffener” taking part of the load from the cracked substrate. This is the so-called stiffening effect. When the substrate crack enters and passes the strapped region, the traction forces exerted by the strap decrease the crack surface opening displacement and reduce the crack tip stress intensity factor; this action is called crack bridging. This scenario is shown in the first column of table 4.1.

- **Disbond failure**

The passing of the lead crack promotes disbond in the bonding interface. Disbond propagates under cyclic load reducing the effectiveness of the strap bridging effect.

- **Secondary bending**

Due to the unsymmetrical configuration of one-side strap, secondary bending is generated at the application of external load. This causes the substrate to bend producing higher tensile stresses at the un-reinforced side; consequently, different crack growth rates and curved through-thickness crack front are observed.

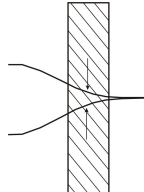
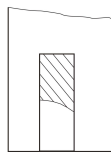


- **Thermal residual stresses (TRS)**

These arise from elevated temperature cure of adhesive bonds and are due to the difference in the coefficients of thermal expansion of the two adherends. For the strap materials used in this work, tensile stresses are produced in the substrate causing crack growth acceleration. TRS also causes secondary bending due to the unsymmetrical configuration.

These mechanisms, their effects on FCG rates, and the influential parameters are summarised in table 4.1.

It is worth adding that both the external load and TRS cause secondary bending, but in opposite directions. Secondary bending produces strong geometric nonlinear effect. Therefore, crack tip stress intensity factors due to the mechanical and thermal loads cannot be simply summed together; both loads must be considered simultaneously in one nonlinear FE analysis to determine the overall bending direction and magnitude for each crack length.

Table 4.1: Mechanisms involved in bonded strap reinforced structures.

	Positive effect	Negative effect		
Mechanism	<p>Stiffening & bridging</p> 	<p>Disbond</p> 	<p>Secondary bending</p> 	<p>Thermal residual stresses</p> 
Description	<p>Reduce crack tip stress and crack opening; slow down crack growth</p>	<p>Reduce the bridging effect</p>	<p>Cause higher crack growth rate and curved crack front</p>	<p>Tensile stresses accelerate crack growth rate</p>
Influential design parameter	<ul style="list-style-type: none"> • Strap stiffness: geometry and mechanical properties 	<ul style="list-style-type: none"> • Adhesive toughness and mechanical properties • Stiffness of strap and substrate 	<ul style="list-style-type: none"> • Stiffness of strap and substrate 	<ul style="list-style-type: none"> • Stiffness of strap and substrate • Coefficients of thermal expansion • Curing temperature

4.2 Two layer plus spring modelling technique

4.2.1 Employed finite elements

3D FE models are able to take account of all 3-dimensional actions present in the problem, but they are time and resource consuming. Moreover, the very thin adhesive layer leads to either element aspect ratio problem or extremely fine mesh, which will require even more computational effort. On the other hand, conventional 2D FE models take much less computing time, but it is more difficult to model effects such as the secondary bending and non-uniform crack profiles. Therefore a novel and enhanced 2D FE model has been developed to study bonded crack retarders taking into account of the aforementioned mechanisms and failure modes.

The modelling technique employs 2D plate elements for the substrate and 2D laminate or plate elements for straps made of composite or metallic materials. Adhesive is modelled by two rigid elements to represent the adhesive layer thickness and three coincident spring elements to mimic the interlaminar peeling and shear actions (figure 4.1). This adhesive model was developed by Tahmasebi [139] for analysis of bonded joints and it is used in this work to simulate the behaviour of the bond interface.

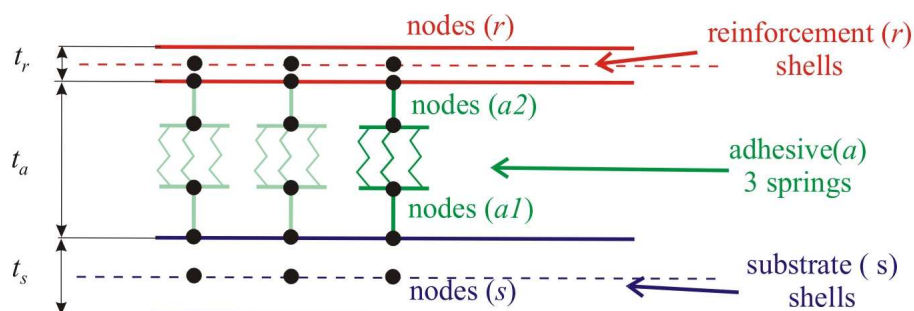


Figure 4.1: Diagram of employed finite elements for modelling the substrate plate, reinforcement strap and adhesive. Nodes connecting the “spring” elements are coincident in the model but are shown as detached here for clarity.

The stiffness of the spring elements (K_{az} , K_{ax} , and K_{ay}) along the three directions are calculated by the following equations:

$$K_{az} = \frac{A_a E_a}{t_a} \quad , \quad K_{ax} = K_{ay} = \frac{A_a G_a}{t_a} \quad (4.1)$$

where A_a is the area of the adhesive element (figure 4.2), E_a the adhesive elastic modulus, G_a the adhesive shear modulus, and t_a the adhesive thickness.

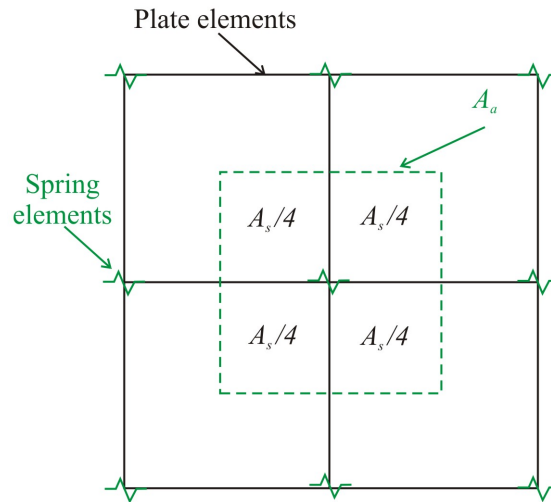


Figure 4.2: Area A_a for calculating the stiffness of the spring elements used to model the adhesive element in the centre of the picture.

In order to force the displacement continuity through the thickness, this model makes use of the multi-point constraint (MPC) equations. Based on the Midlin plate theory the i^{th} nodal displacements for a plate element can be written as:

$$u(z)_i = u_i^o + z\phi_i^y \quad , \quad v(z)_i = v_i^o - z\phi_i^x \quad , \quad w(z)_i = w_i^o \quad (4.2)$$

where u_i^o , v_i^o and w_i^o are the membrane nodal displacements in the x , y , and z direction respectively, ϕ_i^y nodal rotation around the y -axis, and ϕ_i^x nodal rotation around the x -axis (figure 4.3). Naming the nodes that belong to the substrate and need to be connected to the adhesive as *nodes s*, the nodes on the bottom of the adhesive as *nodes a1*, the nodes on the top of the adhesive as *nodes a2*, and the nodes that belong to the strap as *nodes r* (figure 4.1), the MPC equations

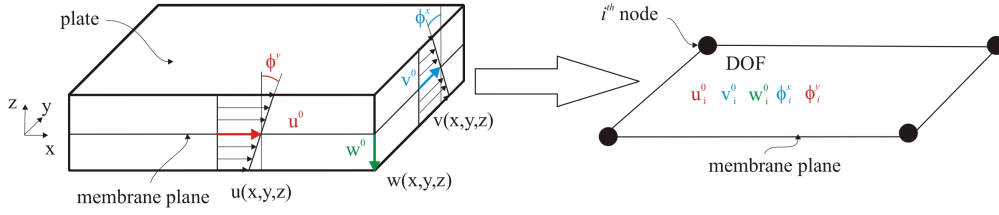


Figure 4.3: Diagram of plate modelling approximations: from real plate to plate finite element. Firstly the plate is modelled by the Midlin plate theory where the dependency of the displacements from the thickness position has been removed; secondly, the FE approximation is introduced where the dependency of displacements from the position on the plane has been removed by using the shape function. Every single node now has 5 degrees of freedom describing the displacements in any point of the plate.

can be written as:

$$\begin{aligned}
 u_{a1}^o &= u_s^o + \frac{t_s}{2} \phi_s^y & , & & v_{a1}^o &= v_s^o - \frac{t_s}{2} \phi_s^x & , & & w_{a1}^o &= w_s^o \\
 u_{a2}^o &= u_r^o - \frac{t_r}{2} \phi_r^y & , & & v_{a2}^o &= v_r^o + \frac{t_r}{2} \phi_r^x & , & & w_{a2}^o &= w_r^o
 \end{aligned} \tag{4.3}$$

where the subscripts s , $a1$, $a2$, r indicate the plane to which the nodes belong (figure 4.1), t_s and t_r the thickness of substrate and strap, respectively.

The use of the MPC allows modelling displacement continuity through the thickness of the assembly of substrate, adhesive and reinforcement. This is essential to correctly model the bending stiffness of the structure and take into account of the secondary bending and thermal residual stress correctly.

These MPC equations usually need to be input in the FE model node by node via the graphical user interface (GUI) of a pre-processing program, e.g. MSC PATRAN or FEMAP. This is time consuming when thousands of nodes need to be tied with MPC equations. A computer code has been written by the author in MATLAB language in order to automate the applications of the MPC equations node by node. This code asks as input four files containing the aforementioned four groups of nodes s , $a1$, $a2$, r (figure 4.1) and the NASTRAN input file (*.bdf) of the model without the MPC equations. The code computes the thickness of substrate and reinforcement and automatically writes the MPC equations in NASTRAN language and delivers a new *.bdf file where the equations are written. More details on how to build the finite element model and use the MPC computer program are reported in appendix D.

4.2.2 Stress intensity factor with secondary bending effect

Linear elastic fracture mechanics is used to calculate the principal parameter that governs the fracture failure. In order to study the lead crack in the substrate, the FE analysis results are used in the modified virtual crack closure technique (section 2.2.1) to compute the strain energy release rate¹ (noted as SERR or G). In the absence of bending, equation 2.15 is used and, for the substrate (s) it can be written as:

$$G_I = -\frac{1}{2\Delta a t_s} F_s^y \Delta v_s = -\frac{1}{\Delta a t_s} F_s^y v_s \quad (4.4)$$

where, Δa is the crack length increment, t_s the substrate thickness, F_s^y the constraint force at the crack tip node, and v_s the displacement at the node immediately behind the crack tip (figure 4.4(a)). From the SERR, the SIF can be computed by using equation 2.14.

Due to the secondary bending, a rotation and a constraint moment exist in the substrate (figure 4.4(b)), consequently, the SIF of the substrate crack varies along the thickness. Methods to obtain the SIF along the crack front for each crack length have been developed for patch repair problems (section 3.1). Wang et al. [73, 77] showed that a distribution of SIF along the crack front cannot be obtained by calculating the strain energy release rates. They argued that, from an energy point of view, only the total energy can be computed (G_I) from the two components of the SERR, one due to traction (G_{I_F}) and the other due to bending (G_{I_M}). Applying the MVCCT to the lead crack in the substrate the total SERR can be written as:

$$G_{I_{tot}} = G_{I_F} + G_{I_M} = -\frac{1}{\Delta a t_s} (F_s^y v_s^0 + M_s^x \phi_s^x) \quad (4.5)$$

where, v_s^0 and ϕ_s^x are nodal displacement and rotation, F_s^y and M_s^x nodal constraint force and moment, t_s the thickness of substrate, and Δa the crack extension size necessary to apply the MVCCT (figure 4.4(b)). From the total strain energy release rate, only the root mean square (RMS) value of the SIF ($K_{I_{RMS}}$) can be calculated:

$$K_{I_{RMS}} = \sqrt{G_{I_{tot}} E_s^*} \quad (4.6)$$

¹Since this subsection concerns the substrate only, for clarity, subscript (s) is omitted for SERR (G) and SIF (K).

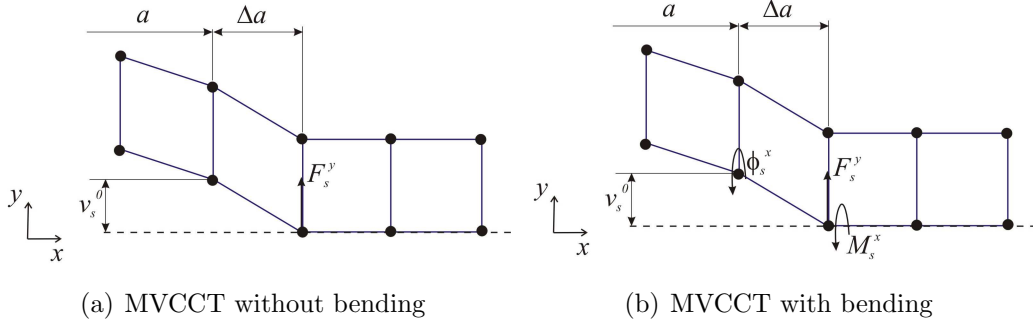


Figure 4.4: Schematic of the modified virtual crack closure technique (MVCCT) for the lead crack in substrate.

Sun et al. [80–83] used a different approach and calculated the two SIF components from the corresponding SERR components (G_{I_F} and G_{I_M} , equation 4.5):

$$K_{I_F} = \sqrt{G_{I_F} E^*} \quad , \quad K_{I_M} = \sqrt{3G_{I_M} E^*} \quad (4.7)$$

They then assumed a linear distribution of SIF along the crack front (through the thickness) and obtained:

$$K_I(z) = K_{I_F} + \frac{2z}{t} K_{I_M} \quad (4.8)$$

Thus, a distribution of SIF along the crack front can be calculated by the energy method and, according to the assumption, the distribution is linear.

The method developed in this work is different from the aforementioned two approaches. Here we attempt to demonstrate that a distribution of SERR and SIF along the crack front can be calculated by using the Mindlin plate theory (equations 4.2) to obtain the constraint force $F_s(z)$ and displacement $v_s(z)$ variations along the crack front (figure 4.4(b)). The vertical displacement v_z can be obtained by equation 4.2 for the substrate (s):

$$v_s(z) = v_s^0 - z\phi_s^x \quad (4.9)$$

The constraint force distribution is a linear function of the position through the thickness:

$$F(z) = mz + c \quad (4.10)$$

where c is the intercept and m the slope. The nodal constraint force (F_s^y) can be connected to the force distribution in this way:

$$F_s^y = \frac{1}{t_s} \int_{-\frac{t_s}{2}}^{\frac{t_s}{2}} F_s(z) dz \quad (4.11)$$

substituting equation 4.10 into 4.11 the intercept c can be found:

$$F_s^y = \frac{1}{t_s} \int_{-\frac{t_s}{2}}^{\frac{t_s}{2}} (mz + c) dz = c \quad (4.12)$$

consequently

$$c = F_s^y \quad (4.13)$$

The nodal constraint moment (M_s^x) can be compute as:

$$M_s^x = -\frac{1}{t_s} \int_{-\frac{t_s}{2}}^{\frac{t_s}{2}} F_s(z) z dz \quad (4.14)$$

where the minus sign is due to the reference system and sign convention shown in figure 4.3. Substituting equation 4.10 into 4.14 the slope m can be found:

$$M_s^x = -\frac{1}{t_s} \int_{-\frac{t_s}{2}}^{\frac{t_s}{2}} (mz + c) z dz = -m \frac{t_s^2}{12} \quad (4.15)$$

consequently:

$$m = -\frac{12M_s^x}{t_s^2} \quad (4.16)$$

Substituting equations 4.13 and 4.16 into equation 4.10 the distribution of constraint force through the thickness is obtained:

$$F_s(z) = F_s^y - z \frac{12M_s^x}{t_s^2} \quad (4.17)$$

The the SERR distribution through the thickness can now be obtained by simply substituting equations 4.9 and 4.17 into the general MVCCT equation 4.4:

$$G_I(z) = -\frac{1}{\Delta at_s} F_s(z) v_s(z) = -\frac{12M_s^x \phi_s^x}{\Delta at_s^3} z^2 + \left(\frac{12M_s^x v_s^0}{\Delta at_s^3} + \frac{\phi_s^x F_s^y}{\Delta at_s} \right) z - \frac{F_s^y v_s^0}{\Delta at_s} \quad (4.18)$$

The SIF can be computed by using the following equation:

$$K_I(z) = \sqrt{G_I(z)E^*} = \sqrt{\left[-\frac{12M_s^x \phi_s^x}{\Delta a t_s^3} z^2 + \left(\frac{12M_s^x v_s^0}{\Delta a t_s^3} + \frac{\phi_s^x F_s^y}{\Delta a t_s} \right) z - \frac{F_s^y v_s^0}{\Delta a t_s} \right] E^*} \quad (4.19)$$

This leads to a parabolic distribution of SERR along the crack front; thus SIF is a square root of the parabola.

It is worth noting that the mean value of the SERR through the thickness ($G_{I_{mean}}$), which can be computed by integrating equation 4.18, is actually equal to the so-called “total” SERR ($G_{I_{tot}}$) that was calculated by Wang et al. [73, 77] and reported in equation 4.5:

$$G_{I_{mean}} = \frac{1}{t_s} \int_{-\frac{t_s}{2}}^{\frac{t_s}{2}} G_I(z) dz = -\frac{1}{\Delta a t_s} (F_s^y v_s^0 + M_s^x \phi_s^x) = G_{I_{tot}} \quad (4.20)$$

Moreover, it can be shown that by using the total or mean SERR with equation 2.14 and making use of equation 4.20, the RMS value of the SIF is obtained:

$$K_I = \sqrt{G_{I_{tot}} E^*} = \sqrt{\frac{1}{t_s} \int_{-\frac{t_s}{2}}^{\frac{t_s}{2}} G_I(z) E^* dz} = \sqrt{\frac{1}{t_s} \int_{-\frac{t_s}{2}}^{\frac{t_s}{2}} K_I(z)^2 dz} = K_{I_{RMS}} \quad (4.21)$$

This means that the RMS SIF has an actual physic meaning, i.e. it is the SIF obtained from the “total” (or through-thickness mean) SERR.

This methodology for calculating the SIF along the crack front is validated against a 3D FE model in section 5.2.2.

4.2.3 Disbond failure modelling

In this modelling methodology disbond growth is modelled interactively with the growing crack in substrate. In most of the papers in the open literature on selective reinforcement or patch repair problems, disbond is either not considered [89, 90, 90, 95–98] or modelled based on prescribed disbond shape and size as a function of the substrate crack length based on experimental observations [69, 72, 82–88].

The laws available in the literature to study delamination or disbond under fatigue load have been reviewed in section 3.2.2. These laws link the disbond growth rate dl/dN to the SERR range (ΔG) using experimentally correlated

material constants and can be written as a Paris law type equation:

$$\frac{dl}{dN} = f(\Delta G) \quad (4.22)$$

Although the rigorous way to study disbond growth would be through the use of those laws, that could not be done for the following reasons:

- a database of material constants for currently used adhesives is not available and the sensitivity of analysis results to these constants is unknown; consequently all those laws can only be used for the adhesive and adherends that they were specifically developed for;
- none of these laws can deal with disbond initiation. In fact, to predict the total fatigue life of an adhesive joint, the critical SERR value for the onset of disbond initiation as function of cycle numbers must be counted (a sort of S-N curve for adhesives); otherwise an initial disbond damage is assumed to exist in the model and over-conservative life prediction could be obtained;
- these Paris law type equations were obtained from tests under a single load mode, whereas for the bonded crack retarder problem disbond usually propagates under mixed mode load.

These problems could have been explored and solved by experimental investigation. However it was not in the project scope and objectives determined by the project consortium (section 1.2).

The alternative methodology to study disbond growth herein used is based on the same idea of Xie and Biggers' [113, 114] (section 3.2.1). The main difference is that conventional finite elements (plate and spring elements) are used instead of a special finite element. The procedure to model disbond failure can be split into three steps.

1. Individuation of a disbond front. This is done by checking how many nodes in an element of substrate (or strap) still have adhesive groups² attached. If an element has only one or two adhesive groups, those groups

²Assembly of three springs and two rigid elements.

are considered as candidate elements for disbond (figure 4.5) and the next steps are repeated for each of the candidate elements.

2. Calculation of three SERR components for the candidate elements (figure 4.5) by the MVCCT (section 2.2.1):

$$\begin{aligned} G_I &= -\frac{F_{az}(w_{a2} - w_{a1})}{2\Delta lb_a} \quad , \quad G_{II} = -\frac{F_{ay}(v_{a2} - v_{a1})}{2\Delta lb_a} \\ G_{III} &= -\frac{F_{ax}(u_{a2} - u_{a1})}{2\Delta lb_a} \end{aligned} \quad (4.23)$$

where, F_{az}, F_{ay}, F_{ax} are the forces in the springs, w, v, u the displacements of the nodes immediately behind the crack tip, and $\Delta lb_a = \Delta A$ the area of crack extension in which the crack-tip nodes are released to computed the SERR.

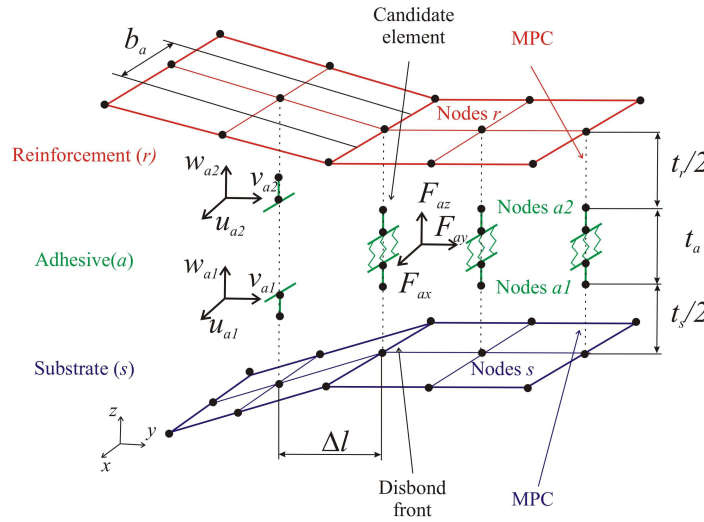


Figure 4.5: Schematic of MVCCT for computing the strain energy release rate for candidate spring elements along the disbond front.

3. Identification of the failing adhesive groups. The mixed mode failure criterion introduced in section 3.2.1 is used to identify the failing candidate joint elements:

$$\left(\frac{G_I}{G_{Ic}}\right)^\alpha + \left(\frac{G_{II}}{G_{IIc}}\right)^\beta \geq 1 \quad (4.24)$$

The candidate adhesive groups that meet the failure criterion are deleted from the FE model to simulate adhesive disbond growth. The disbond front will be updated and another FE analysis is required to compute the SERR along the new disbond front. Again, the failing candidate adhesive

groups will be deleted. This interactive analysis goes on until no spring element fails, i.e. the final disbond shape is found for the given substrate crack length. Eventually, disbond growth and its effect on the SIF of the substrate crack are calculated for the entire crack length range.

The main advantage of this method is that re-meshing can be avoided. In fact, the failed spring elements can be easily removed from the NASTRAN input file without affecting the remaining mesh. This method could be called a “quasi-static” delamination growth analysis, since it does not model the effect of fatigue loads. It must be said, though, that disbond growth in patch repair and bonded crack retarders is often or mostly caused by the high local stresses in the substrate crack tip region due to the “stress singularity” effect rather than fatigue loads. Disbond initiation is considered by assuming an initial defect in the adhesive interface. This defect is positioned on the boundaries of the reinforcement strap (figure 4.6) so that two advantages can be gained. First, the MVCCT can be applied to model disbond since it requires to release the crack tip node to compute the SERR (section 2.2.1). Second, the adhesive failure will be triggered by the passing crack since, due to the symmetrical constraints on the mid plane, the displacements are null until the crack makes the nodes on the mid plane open (figure 4.6). The initial defect size is equal to one element size along the strap sides.

Predicted disbond shapes are validated against experimental measurements and reported in section 5.2.3.

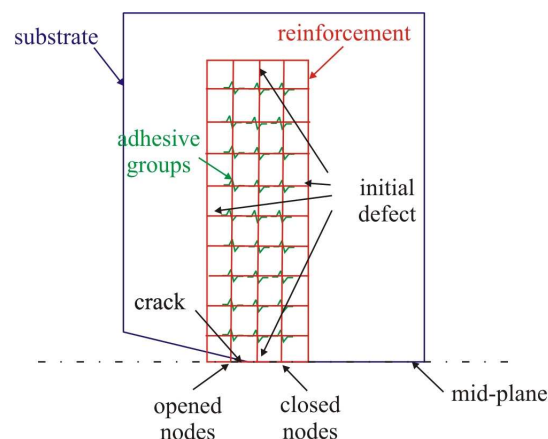


Figure 4.6: Example of introduction of adhesive defect to model adhesive failure initiation.

4.2.4 Thermal residual stress (TRS) calculation

First, it is necessary to understand how these TRS are generated. In the case of two plates bonded at elevated temperature, the two adherends become bonded when the adhesive is completely polymerised at the curing temperature T_C . This temperature is usually referred to as the stress free temperature $T_C = T_o$, since before reaching the temperature the two adherends are still free to expand and slide over each other. When the assembly is cooled down to room temperature T_R (i.e. the test temperature), the two adherends will try to contract to the original size, but displacement compatibility has to be maintained at the bond interface. If the adherends have different coefficients of thermal expansion (CTE), they will contract differently during the temperature drop and that generates the TRS. For an assembly of two different adherends of same dimensions and made of isotropic materials subjected to a temperature rise ($\Delta T > 0$) or temperature drop ($\Delta T < 0$), a 1D closed-form solution to compute the TRS in the substrate can be derived.

From figure 4.7, by neglecting the adhesive layer since its stiffness is much smaller than that of substrate and reinforcement, the following equation of equilibrium can be written:

$$\sigma_s t_s w_s + \sigma_r t_r w_r = 0 \Rightarrow \sigma_s t_s + \sigma_r t_r = 0 \quad (4.25)$$

and compatibility:

$$\varepsilon_s = \varepsilon_r \Rightarrow \alpha_s \Delta T + \frac{\sigma_s}{E_s} = \alpha_r \Delta T + \frac{\sigma_r}{E_r} \quad (4.26)$$

where ε_s and ε_r are the strains and α_s and α_r the CTE of substrate (s) and reinforcement (r).

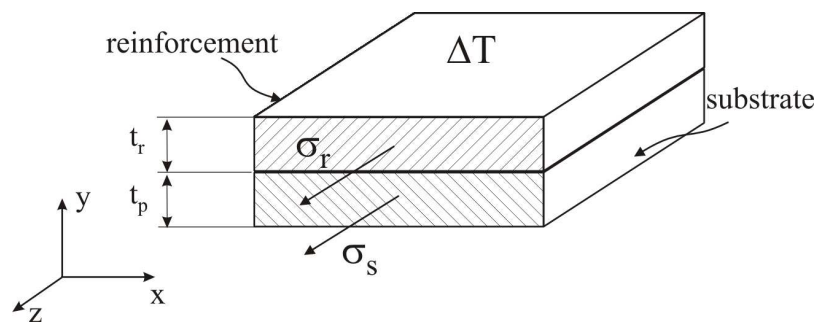


Figure 4.7: Cross section of two bonded plates subjected to a temperature load ΔT .

From the compatibility equation 4.26 the stress in the substrate can be extracted:

$$\sigma_s = (\alpha_r - \alpha_s)E_s\Delta T + \frac{E_s}{E_r}\sigma_r \quad (4.27)$$

From the equilibrium equation 4.25 the stress in the reinforcement can be obtained:

$$\sigma_r = -\frac{t_s}{t_r}\sigma_s \quad (4.28)$$

Substituting equation 4.28 into equation 4.27 the stress in the plate, i.e. the residual stress in the plate caused by the temperature load ΔT can be obtained:

$$\sigma_{s_{res}} = \frac{t_r E_r E_s (\alpha_r - \alpha_s) \Delta T}{t_r E_r + t_s E_s} \quad (4.29)$$

ΔT is the difference between the final temperature and the stress-free temperature T_o . In the case of bonding two structures, the stress free temperature is the temperature at which the two plates are actually bonded together; this temperature is very close to the curing temperature T_C . The final temperature is the one at which the experiment is carried out, i.e. room temperature T_R for this study. Consequently, the temperature drop is:

$$\Delta T = T_R - T_C \quad (4.30)$$

This temperature load is on the bonded structure for all its service life. In the presence of a crack the geometry of the structure changes, thus the TRS will redistribute. Equation 4.29 is used in [66] to estimate the TRS for patch repair, although no demonstration of the equation is given. This equation is useful to understand the influential parameters. These are:

1. mismatch of CTE between substrate and reinforcement $\alpha_r - \alpha_s$; the higher it is, the higher the TRS;
2. elastic moduli of substrate and reinforcement; the stiffer they are, the higher the TRS;
3. geometry of the substrate and reinforcement; the thicker the substrate, the lower the TRS, and the thicker the reinforcement, the higher the TRS; the effect of the width can not be seen in equation 4.29 because it is obtained from a 1D model where the widths of the two adherends are equal; it can be deduced that the effect of the width is similar to that of the thickness.

Equation 4.29 can not be used to accurately predict the TRS of complex geometries. In those cases a thermal load FE analysis is necessary.

In this modelling technique, thermal load FE analyses are performed for each strap configuration by inputting the temperature drop given by equation 4.30. Care should be taken in modelling the curing process and residual stress redistribution during crack propagation for two reasons. First, thermal and mechanical stresses must be applied simultaneously for reasons explained in the next section 4.3.1. Second, to perform the mechanical load analysis the FE model must be supported as it is in the fatigue test machine. However, if the thermal load analysis is conducted under this boundary condition, thermal residual stresses (TRS) will be generated in the support boundaries of the substrate, i.e. where the specimen is clamped. These TRS are not physically there, since the substrate and reinforcement strap have already reached the equilibrium condition at the end of the curing process before being fitted on to the test machine. In order not to generate these unrealistic TRSs, it is necessary to calculate an equivalent CTEs for the reinforcement (α_r^*) and substrate (α_s^*) as follows:

$$\alpha_r^* = \alpha_r - \alpha_s \quad , \quad \alpha_s^* = \alpha_s - \alpha_s = 0 \quad (4.31)$$

Therefore the substrate does not get unrealistic deformation and the relative CTE between the substrate and reinforcement is maintained. In this way the effect of temperature can be totally taken into account without the influence of boundary conditions. Moreover, the temperature drop will be kept there when applying the mechanical load for each crack length and in this way the redistribution of TRS with a growing crack can be modelled. Predicted TRS and their redistribution are validated against test results in section 5.2.4.

In this study the substrate is made of an aluminium alloy and the straps are made of one of the following materials: carbon fiber reinforced plastics (CFRP), glass fiber reinforced plastics (GFRP), titanium alloy Ti-6Al-4V (Ti-6-4), and fibre-metal laminate GLARE. In each case the CTE of the reinforcement material (α_r) is smaller than that of the substrate (α_s). This difference generates tensile residual stresses in the substrate that promotes crack opening, thus accelerates crack propagation.

4.3 Fatigue crack growth prediction

Two challenges arise for predicting crack growth rates in bonded structures. The first is caused by the geometric non-linearity of one-side strap configuration; the other is due to the fact that although a distribution of SIF along the crack front can be obtained by the 2D model, only one SIF value is needed for each crack profile for calculating the FCG rate and life.

4.3.1 Geometric non-linearity effect

Secondary bending presents on application of the mechanical and thermal loads; it leads to nonlinear force-displacement relation.

In the linear elastic case, to compute the SIF range only one FE analysis is needed for each crack length, for example at the maximum load. Then from the stress ratio $R = \sigma_{max}/\sigma_{min}$, SIF at the minimum load $K_{min} = RK_{max}$ and SIF range $\Delta K = (1 - R)K_{max}$ can be found. This cannot be done when the problem is geometrically nonlinear because:

$$R = \frac{K_{min}}{K_{max}} \neq \frac{\sigma_{min}}{\sigma_{max}} \quad \text{and} \quad \frac{K_{app}}{\sigma_{app}} \neq \frac{K_{max}}{\sigma_{max}} \neq \frac{K_{min}}{\sigma_{min}} \quad (4.32)$$

This means that a normalised or dimensionless SIF, usually named as the β factor (section 2.1.1), which is a function of the geometry only, does not exist due to the nonlinearity effect.

In this study, this problem is solved by performing a so-called ‘‘alternate analysis’’ of the SIF at the maximum and minimum applied stresses; thus K_{max}^{tot} and K_{min}^{tot} are calculated for the cyclic maximum and minimum stresses. This leads to an effective R ratio, which is different to the nominal stress ratio, and an effective SIF range ΔK . This alternate analysis was applied in [140] by the authors for a composite patch repair problem without the TRS effect. In the presence of TRS the problem is more complicated.

First of all, in order to understand the difficulties introduced by the non-linearity of the problem, it is worth describing how the problem is usually dealt with for the TRS in welded joints, in which the classic superposition method [141] is used. It consists of carrying out a mechanical load analysis to compute the SIF (K^M) and a thermal one to compute the residual SIF (K^T). Those two SIF are

completely independent, consequently can be computed separately and summed. Thus, the classic method rules that ΔK is not affected by TRS:

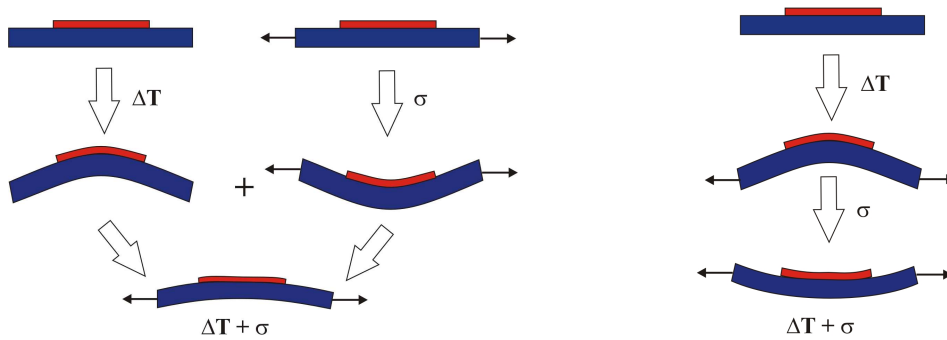
$$\Delta K_{eff} = K_{max}^M + K^{\mathcal{P}} - (K_{min}^M + K^{\mathcal{P}}) = K_{max}^M - K_{min}^M = \Delta K_M \quad (4.33)$$

and the effective R ratio (R_{eff}) is:

$$R_{eff} = \frac{K_{min}^M + K_T}{K_{max}^M + K_T} \quad (4.34)$$

In many cases, e.g. the study of welded joints, no secondary bending is involved, thus the problem is geometrically linear and superposition can be applied.

In the case of single-sided bonded reinforcements, secondary bending is caused by both mechanical load and TRS. If the superposition is applied, the two bending effect would be considered separately and then summed (figure 4.8(a)). In fact, the mechanical load is not applied to an undeformed structure, but to a deformed configuration after curing of the adhesive. That would completely change the final deformed shape of the structure, stress distribution, and consequently the SIF value (figure 4.8(b)).



(a) Linear superposition of thermal and mechanical load analyses.

(b) Non-linear analysis of thermal and mechanical loads

Figure 4.8: Side view sketch of a reinforced plate showing the difference in applying the superposition rule and non-linear analysis when secondary bending and non-linearity are involved in the problem; the final deformed shapes are different, although the applied thermal and mechanical load are equal.

Consequently, due to the nonlinearity of the problem and coupling effect, superposition of the mechanical load caused SIF (K^M) and thermal residual SIF (K^T) cannot be used:

$$K^{M+T} \neq K^M + K^T \quad (4.35)$$

A total SIF (K^{tot}), which includes the interaction between the mechanical and thermal stress fields, must be computed at the maximum and minimum applied load separately. This method, developed in this research project, is referred to as the "alternate analysis". The effective SIF range (ΔK_{eff}) and effective ratio (R_{eff}) are calculated as:

$$\Delta K_{eff} = K_{max}^{tot} - K_{min}^{tot} \quad \text{and} \quad R_{eff} = \frac{K_{min}^{tot}}{K_{max}^{tot}} \neq \frac{\sigma_{min}}{\sigma_{max}} \quad (4.36)$$

where K_{max}^{tot} and K_{min}^{tot} include the mechanical, thermal, and coupling SIF at the maximum and minimum applied load, respectively. The magnitude of the interaction between mechanical and thermal stress fields is demonstrated through some examples in section 5.2.5.

Observing figure 4.8(b), it may be noticed that there could be a particular applied loads at which the bending caused by the applied load and the TRS cancel themselves. Although that may be true for one particular crack length, balancing the two effects to cancel global bending is an impossible task. This is because when the crack propagates the neutral axis changes its position and TRS redistributes; both will change the global bending direction and magnitude.

It is also worth noticing that in this section only the geometric non-linearity of the structure has been analysed so far. Material non-linearity, such as plasticity is also addressed in the modelling techniques for metallic straps. An elastic-perfectly plastic constitutive relation is used for the metallic straps to account of the limitation in the bridging effect caused by yielding (section 6.1.1). The substrate is considered to be elastic so that linear elastic fracture mechanics theory can be applied.

4.3.2 Equivalent stress intensity factor: weight function

Although the through-thickness distribution of SIF along the crack front can be found by equation 4.19, only one SIF value is required for each crack profile in the NASGRO equation [61] or any similar empirical crack growth laws (section 2.3). Obvious candidates included the mean, the maximum and RMS values of the SIF. The RMS is directly connected to the total strain energy release rate (equation 4.21). Moreover, as mentioned in the literature review (section 3.1.4),

Klug, Maley and Sun [83] showed that the best agreement with experiments was obtained using the RMS value. Instead, the maximum SIF value, i.e. SIF on the un-reinforced side, could give overly conservative life prediction since the influence of other SIF values through the thickness is neglected.

In fact, the major problem of finding a meaningful average value is that the crack front in the substrate evolves from straight to curved during propagation [142]. The most accurate way to model it would be using a 3D finite element model and successive re-meshing the crack front, which could be extremely computational expensive and an alternative solution was sought.

The alternative solution employed in this 2D modelling technique is based on the idea of Hosseini-Toudeshky and Mohammadi [98]. Two 3D FE analyses of curved and straight crack fronts (the latter can be studied by 2D model) were conducted to study the single-sided patch repair problem (section 3.1.4). They found that the FCG life can be computed by the simpler model with straight crack front using an equivalent SIF, which, for each crack length, is a value of SIF in a position along the sample's thickness. This position depends on the elastic modulus of the plate and repair patch and also the plate thickness. It was found to be between $0.32 \sim 0.37$ of the plate thickness from the unpatched side. In a similar way, a weight function is developed in this work to take account of the fact that the crack length at the un-reinforced side is dragged back by all other shorter crack lengths, and vice versa for the crack length at the reinforced side. This weight function is based on the argument that the crack front, which by a 2D model has to be a straight line, is actually parabolic (for single-sided patch repair [95, 96, 98] and also single-sided strap reinforced structures [142]). This 3D effect can be considered by a suitable weight function. Imposing the parabola vertex at the un-reinforced side with the value of 1 and prescribing the value on the reinforced side as 0, a weight function ($W(z)$) to describe the parabola is obtained:

$$W(z) = -\frac{1}{t_s^2}z^2 - \frac{1}{t_s}z + \frac{3}{4} \quad (4.37)$$

where, $-t_s/2 \leq z \leq t_s/2$. Using the weight function (equation 4.37) and SERR distribution through the thickness (equation 4.18), a weighted SERR (G_{Iw}) can be computed:

$$G_{Iw} = \frac{\int_{-t_s/2}^{t_s/2} W(z)G_I(z)dz}{\int_{-t_s/2}^{t_s/2} W(z)dz} = -\frac{9}{10} \frac{M^0\phi}{\Delta at} - \frac{1}{8} \left(\frac{12M^0v^0}{\Delta at^2} + \frac{\phi F^0}{\Delta a} \right) - \frac{F^0v^0}{\Delta at} \quad (4.38)$$

Similarly, a weighed SIF (K_{Iw}) can be calculated:

$$K_{Iw} = \sqrt{E^* \left[-\frac{9}{10} \frac{M^0 \phi}{\Delta at} - \frac{1}{8} \left(\frac{12M^0 v^0}{\Delta at^2} + \frac{\phi F^0}{\Delta a} \right) - \frac{F^0 v^0}{\Delta at} \right]} \quad (4.39)$$

A computer program as been developed to compute the RMS and weighted values of SIF for each crack length as well as the distribution through the thickness. A user's guide is attached in appendix D.4.

4.3.3 Integration and FCG life prediction

Fatigue crack growth rates and lives are predicted by using the material law that is the crack growth rate vs. the SIF range for different R -ratios. These curves can be expressed by either empirical equations, e.g the Paris law or NASGRO equation, or tabular form on point-by-point basis (section 2.3). This curves are numerically integrated with calculated stress intensity factor range (ΔK) and effective SIF ratio (R) as a function of the crack length (a) for each study case to compute the fatigue crack growth (FCG) life (section 2.3.5).

The computer code AFGROW [61] is commonly used to carry out the integration. For this problem though, it cannot be used since the effective R ratio cannot be input as a function of the crack length. The way that AFGROW deals with residual stress effect is by inputting the residual stress field first and then calculating the residual stress intensity factors by either the Gaussian integration or a weight function and then use the superposition method to determine the effective R ratio within the code. As described in section 4.3.1, for one-side bonded structures, the mechanical and thermal stress fields interact each other to produce the so-called effective SIF and effective R ratio; hence both stress fields must be considered together to deliver the effective SIF and R ratio values for each crack length.

For this reason a computer subroutine, which can take as input ΔK , R , and a , was included in the main computer code (LICRA) with which the modelling technique is implemented. This subroutine uses either a tabular form of the material law associated with the Harter T-method or NASGRO equation to compute the FCG life of the structure. The numerical integration is carried out by using the Runge-Kutta algorithm [143] of the fifth order. A user's guide is attached in appendix D.4.

The only drawback of this code is that can only integrate constant amplitude load cases.

The integral stringer panels reinforced by bonded straps that are reported in chapter 7 were subjected to variable amplitude loads, consequently, in order to be able to use AFGROW to carry out the integration, some tricks were used as explained below.

The first problem was that AFGROW accepts as input a β solution and not ΔK . This problem was simply solved by computing an equivalent β solution that, although is not load independent due to the non-linearity problems (section 4.3.1), can be input into AFGROW and makes it compute the right ΔK :

$$\beta_{eff} = \frac{\Delta K_{eff}}{\Delta \sigma \sqrt{\pi a}} \quad (4.40)$$

The second problem is that the effective R -ratio can not be input. To solve this problem an equivalent residual SIF must be computed from the known values K_{max}^{tot} and K_{min}^{tot} . This is accomplished by assuming that the coupling between thermal and mechanical load is equal at the maximum and minimum load³:

$$K_{max}^C = K_{min}^C = K^C \quad (4.41)$$

thus, the effective SIF can be written as:

$$\Delta K_{eff} = K_{max}^{tot} - K_{min}^{tot} = \left(K_{max}^M + \cancel{K^T} + \cancel{K^C} \right) - \left(K_{min}^M + \cancel{K^T} + \cancel{K^C} \right) \quad (4.42)$$

then:

$$\Delta K_{eff} = K_{max}^M - K_{min}^M \quad (4.43)$$

The R_{eff} is known from the analysis, thus:

$$R_{eff} = \frac{K_{min}^{tot}}{K_{max}^{tot}} = \frac{K_{min}^M + K^T + K^C}{K_{max}^M + K^T + K^C} \quad (4.44)$$

The applied R ratio is another known parameter which, under the approximation of equal coupling effect and neglecting the mechanical non-linearity, can be written as:

$$R = \frac{\sigma_{min}}{\sigma_{max}} = \frac{K_{min}^M}{K_{max}^M} \quad (4.45)$$

³This is not true since the non-linearity of the problem (section 4.3.1). It is however a necessary approximation to find a solution. This method is used only for variable amplitude load cases.

Simultaneously solving equations 4.43, 4.44, 4.45 for K_{max}^M , K_{min}^M , and $K^T + K^C$ the the equivalent residual SIF (K_{eq}^T) states:

$$K_{eq}^T = K^T + K^C = \frac{\frac{\Delta K}{1-R} (R_{eff} - R)}{1 - R_{eff}} \quad (4.46)$$

This equivalent residual SIF (equation 4.46) can be input in AFGROW along with the equivalent β solution (equation 4.40) to compute the life for variable amplitude load cases.

4.3.4 Life Increment Crack Retarders Analysis (LICRA) computer code

A computer program (LICRA) interfacing the commercial package MSC/NASTRAN has been developed to implement the aforementioned modelling techniques taking into account the effects present in bonded crack retarders. LICRA algorithm is described by the following steps:

1. FE model of the structure is built and a NASTRAN input file (*.bdf) exported from a pre-processor (such as PATRAN or FEMAP). This model must be built by following the instructions in appendix D.1.
2. LICRA reads the FE model from the NASTRAN input file and applies the MPC equations to the adhesive nodes and produces a *.mesh file where only the mesh of the model is written without any analysis option (instructions in appendix D.2).
3. The analysis options are input by the graphical user interface (GUI) of the code. Now a NASTRAN input file (*.nas) which includes the NASTRAN analysis options as well as the mesh file (*.mesh) is produced (instructions in appendix D.3).
4. This file is submitted by LICRA to NASTRAN to solve the FE analysis and deliver stresses, strains, and displacements needed to study disbond propagation.
5. LICRA reads the NASTRAN results and computes the SERR along the disbond front. It checks whether any adhesive element has failed.

6. If any adhesive element has failed, it updates the mesh file and starts again from step 4. Steps 4-6 are repeated until no adhesive elements fails, i.e. the disbond front has stabilised. When it has, LICRA proceeds to the next step.
7. A node on the substrate crack path is released to apply the MVCCT.
8. A NASTRAN analysis at the maximum applied load is run to compute the SIF values through the thickness.
9. A NASTRAN analysis at the minimum applied load is run to compute the SIF values through the thickness.
10. The substrate crack is incremented by a given Δa and steps 4-10 are repeated until the substrate crack length is longer than a given maximum. When it is, LICRA proceeds to the next step.
11. The RMS and weighted values of the SIF, SIF range and effective R-ratio are calculated for each crack length.
12. FCG rates and lives are calculated by integrating the material law.

LICRA program flow chart can be seen in Figure 4.9. LICRA user's guide is given in appendix D.

4.4 3D modelling technique

Although this thesis is about developing a 2D finite element technique, 3D models are necessary to validate the 2D FE results for the through thickness effects. For the 3D modelling technique, 8-noded brick elements are used to model substrate, adhesive, and strap. Due to the small thickness of the adhesive a fine mesh is needed or element aspect ratio problems can be encountered.

A MATLAB code (3D-VCCT) has been written to automatically compute the SIF along the crack front for different crack lengths. The model is input in 3D-VCCT program and the SERR and SIF distribution on the crack front are computed by applying the MVCCT on the crack front (see figure 2.8 and equation 2.17). Subsequently, the crack length is automatically incremented by a constant value along the crack front and the new SIF distribution is computed. A flow

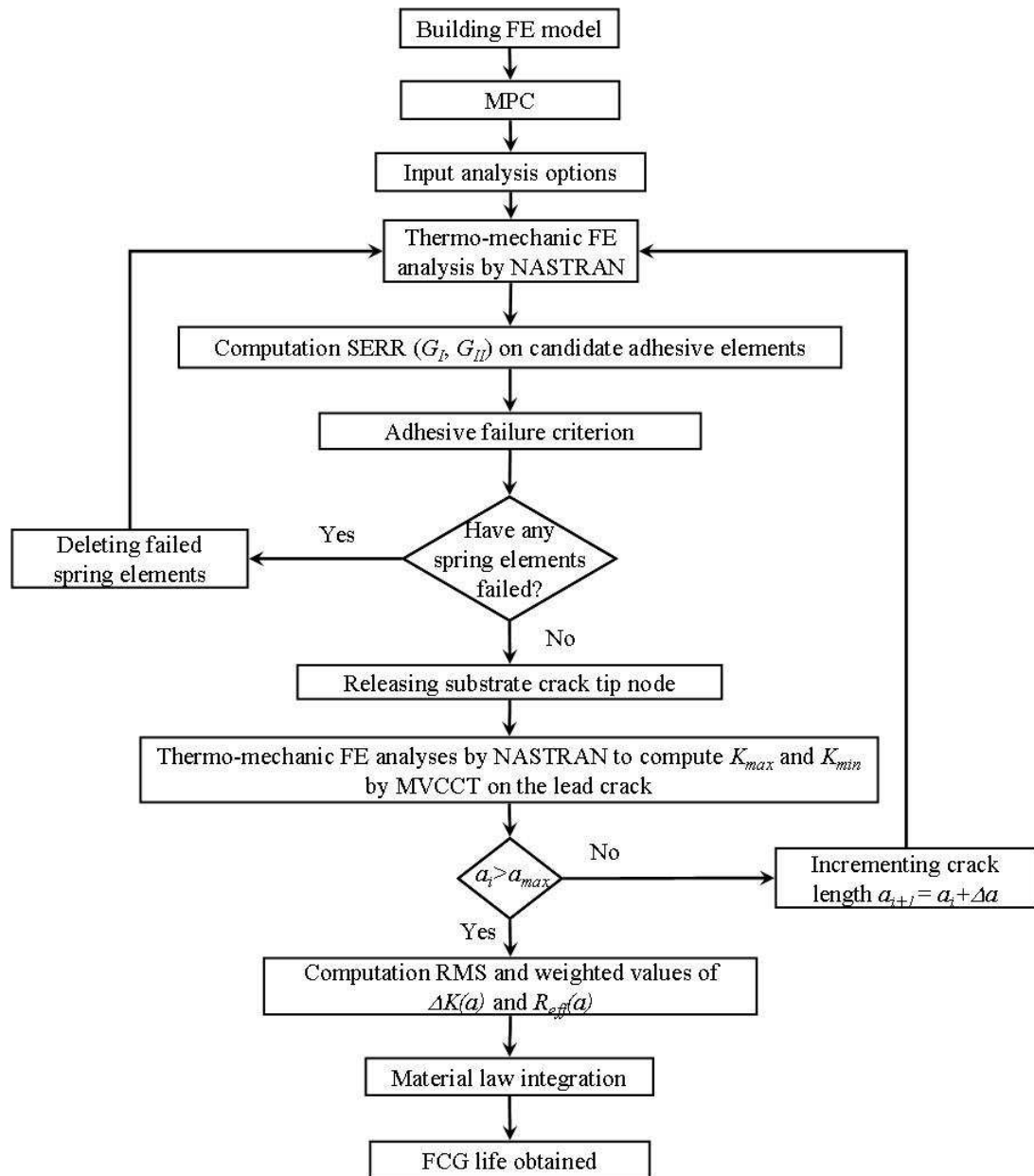


Figure 4.9: Flow chart diagram showing procedures for predicting fatigue crack growth life of structures reinforced by bonded crack retarders. Author developed LICRA computer code which interfaces the NASTRAN commercial code.

chart of the computer program can be seen in figure (4.10). The user's manual for the 3D-VCCT code is reported in appendix E.

A comparison between the SERR and SIF computed by the 3D and 2D modelling techniques can be found in section 5.2.2.

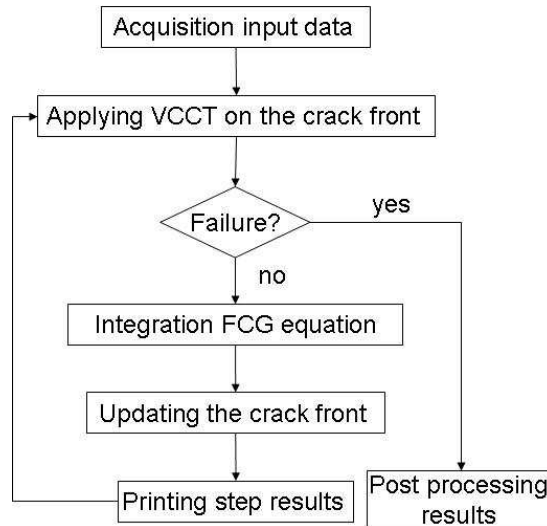


Figure 4.10: Flow diagram of 3D-VCCT computer code to computed distribution of SIF through the thickness by 3D FE models.

Chapter 5

Validation: test coupon level

In this chapter the 2D modelling methodology which has been described in chapter 4 is validated against analytical solutions, 3D FE models, and experimental measurements.

Initially un-reinforced plates are studied (section 5.1). Four different geometries are used to assess the mesh convergence, the accuracy of the MVCCT calculated SIF and predict FCG lives. Those are compared to experiments for validation. After assessing and validating the models for un-reinforced plates, the modelling methodology to study bonded reinforced plates is validated (section 5.2). The sample material and geometries are listed in section 5.2.1. The secondary bending study and methodology to compute the SERR through the thickness by 2D plate elements is validated against 3D FE results in section 5.2.2. In section 5.2.3 disbond progression modelling is validated against experiments. Calculated TRS and their redistribution with crack propagation are validated against experiments in section 5.2.4. The effect of the non-linearities caused by the secondary bending and the coupling of thermal and mechanical loads are demonstrated in section 5.2.5 along with the errors which would be made if neglected.

At this point each single mechanism involved in the problem has been validated. The final and most important validation is the prediction of FCG lives. In the last section of this chapter, the predicted FCG lives are compared against experimental ones. The errors made in the predictions are gathered in a table so that the accuracy of the modelling technique can be assessed.

5.1 Un-reinforced plates

5.1.1 Mesh convergence

It is important to know the FE mesh sensitivity before applying the MVCCT to complex structures. In order to assess the mesh convergency a simple middle crack tension M(T) plate is studied (figure 5.1).

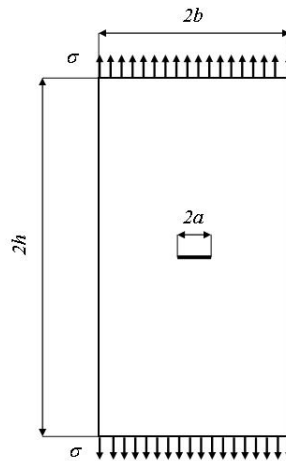


Figure 5.1: M(T) sample geometry

The plate is 320 mm wide ($2b$) and 1600 mm high ($2h$) giving an h/b ratio equal to 5. 2D 4-noded plate elements are used to model the plate. The mesh is regular along the crack path. Four different square element sizes are used to study the convergence: 1 mm, 2 mm, 4 mm, and 8 mm.

The FE results are compared with the known finite-width correction, SIFC:

$$SIFC = \sqrt{\frac{1}{\cos\left(\frac{\pi a}{2b}\right)}} \quad (5.1)$$

The results can be seen in figure 5.2(a).

As aforementioned in table 2.1, the MVCCT is not strongly mesh dependent but still the mesh effect can be seen. The errors made by the FE analyses are shown in figure 5.2(b). By using a mesh with a characteristic dimension of 1 mm the error made is less than 1% for short crack lengths and grows to a maximum 2% for longer ones. The 2 mm mesh also gives accurate result giving an error

of about 2%. It can be concluded that a mesh with a characteristic element dimension (m) over half width (b) less or equal to 1/80 is suitable to obtain accurate β solutions.

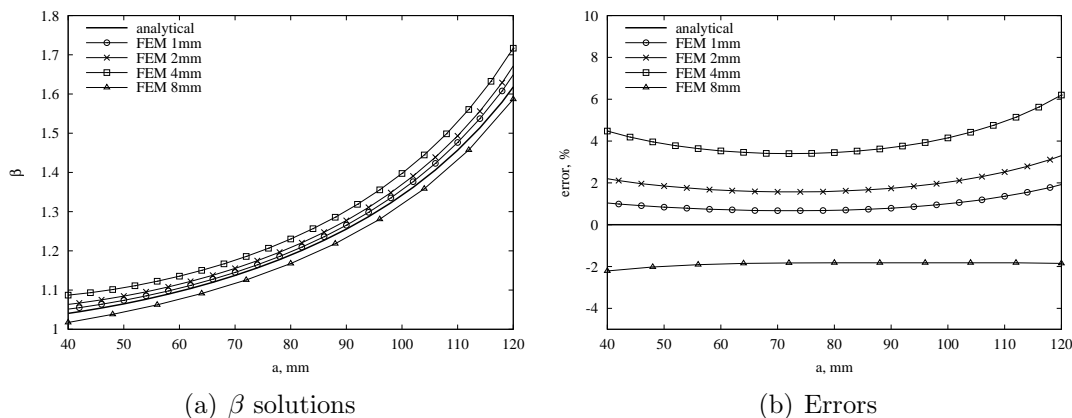


Figure 5.2: Mesh convergence test for a un-reinforced M(T) plate.

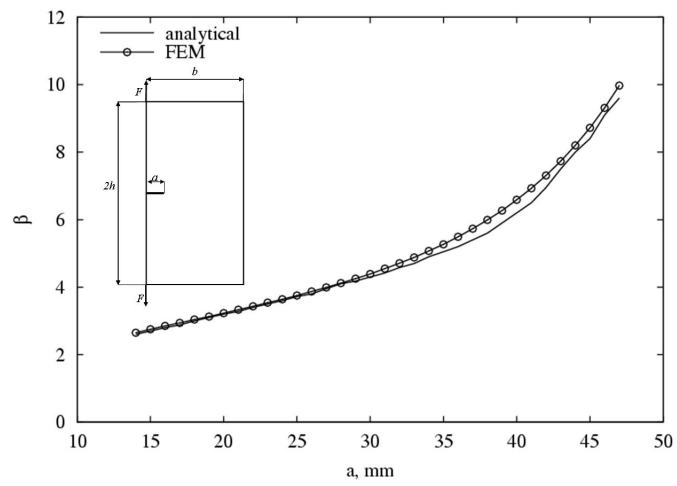
5.1.2 β solution accuracy

The MVCCT was also used to compute the β solution of different sample geometries to assess the reliability of the method. Three different geometries are used (inserts of figure 5.3): compact tension C(T), single edge notch tension SENT, and cracks at hole. The dimensions are shown in table 5.1.

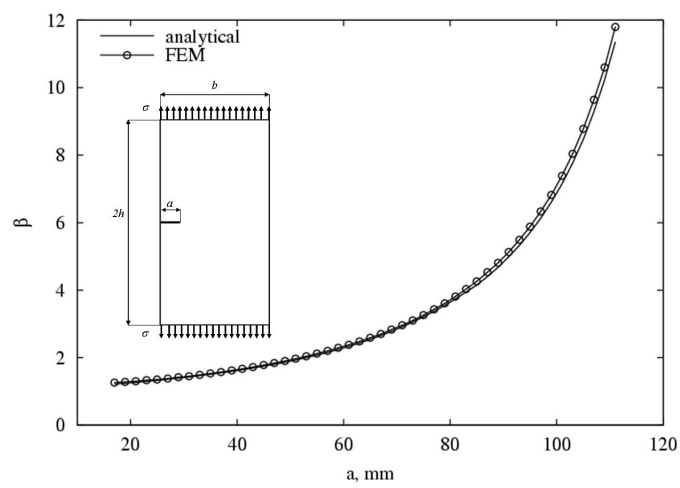
Geometry	b mm	h or R mm
C(T)	70	35
SENT	140	200
Cracks at hole	50	12.5

Table 5.1: Sample dimensions

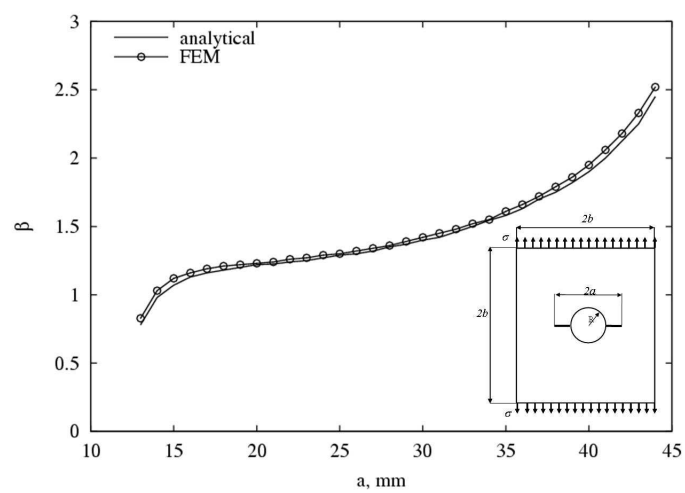
The β solutions found by the FE analyses and MVCCT are compared against analytical β solutions found in Rooke and Cartwright’s compendium of SIF [31]. The results are shown in figure 5.3. FE results are in good agreement with analytical showing that the mesh of the model and the method to compute the SIF are suitable to study more complicated problems.



(a) CT



(b) SENT



(c) Crack at hole

Figure 5.3: Validation of β solutions against analytical solutions [31].

5.1.3 FCG validation

Three un-reinforced aluminium plates were examined. They were: a single edge notch tension SENT plate made of Aluminium Alloy 7085-T7651 10 mm thick, a “wide” middle crack tension M(T) plate made of Aluminium Alloy 2024-T3 1.6 mm thick, and a “narrow” M(T) plate 10 mm thick also made of Aluminium 7085-T7651. The geometry of the plates and the mechanical properties of the materials can be seen in figure 5.4 and table 5.2. NASGRO equation (section 2.3.3) was used to describe the crack growth rate material law for AA 2024-T3, where the material coefficients were found in NASGRO material database implemented in AFGROW [61]. C and n coefficients (equation 2.21) were modified following the findings in [20] and the values are reported in table 5.2. On the other hand, AA 7085-T7856 is a relatively new material and no coefficients are available in the NASGRO database [61], thus, some experimental tests were conducted in [142] for two different R -ratios (0.1 and 0.6) to characterise it. The other curves for different R -ratios were interpolated by using Harter T-method (section 2.3.4). The obtained material law for AA7085-T7856 is shown in figure 5.5.

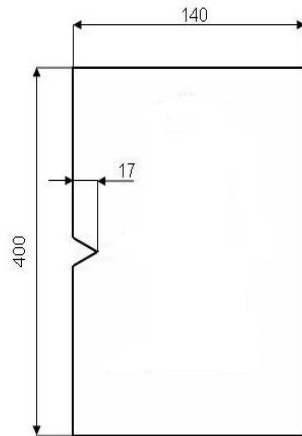
Table 5.2: Mechanical properties of aluminum alloys used in this study.

Material	AA 2024-T3*	AA 7085-T7651†
t (mm)	1.6	10
E (MPa)	73000	71000
ν	0.33	0.33
ρ (g/cm^3)	2.77	2.77
α ($\mu^\circ C^{-1}$)	23.6	23.6
C	1.1×10^{10}	See figure 5.5
n	2.601	

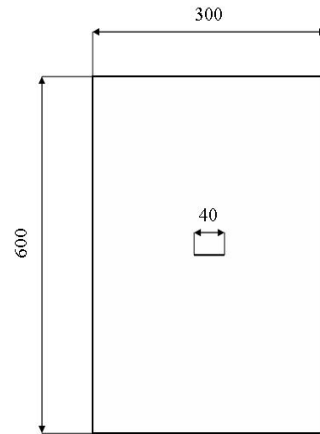
* Values from [20].

† Values from [142]

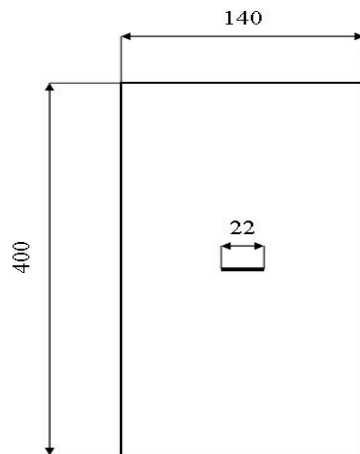
In figures 5.6(a) and 5.6(b) the numerical prediction of FCG rate and life for the SENT plate subjected to a constant amplitude load spectrum ($\sigma_{max} = 18.57 MPa$ and ratio $R = 0.1$) are compared with experiments. This relatively low load level was decided by the consortium essentially to reduce problems of in-plane bending and consequent crack turning showed by this geometry and material.



(a) AA 7085-T7651 single edge notch tension (SENT)



(b) AA 2024-T3 middle crack tension M(T) specimen (wide)



(c) AA 7085-T7651 middle crack tension M(T) specimen (narrow)

Figure 5.4: Dimension and geometry of the specimens without straps. (Sketches not to scale)

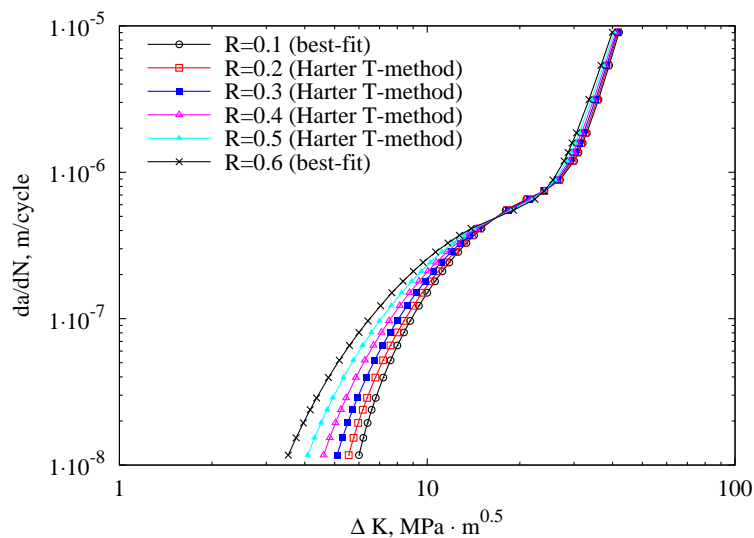
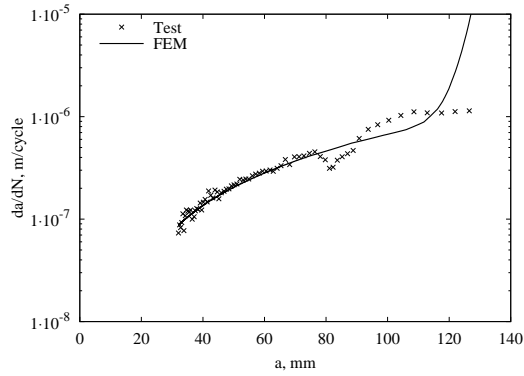


Figure 5.5: Material law of fatigue crack growth rate for aluminium alloy 7085-T7651. Curves for $R = 0.1$ and 0.6 are best-fitted lines of the test results from [142] and the others are obtained by using the Harter T-method [61].

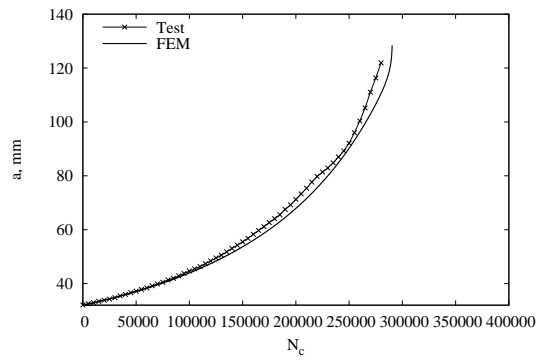
Good agreement is shown by prediction and test up to a crack length of $a = 80\text{mm}$. At this crack length, crack turning was observed during the experiment and, since the electric potential method [142] was used to measure the crack length, the actual crack length was different from the measured one causing discrepancy between test and model.

In figures 5.6(c) and 5.6(d) the calculated FCG rate and life for the wide M(T) plate tested at $\sigma_{max} = 70\text{MPa}$ and $R = 0.1$ is compared with experiments from [19, 20]. Also in this case a good agreement in terms of final FCG life is obtained (figure 5.6(d)) although some discrepancies can be observed in terms of FCG rate (figure 5.6(c)). Since the β -solution for this geometry is well known [31], the reason of the discrepancy can only be found in the used material law, which, as it was pointed out in section 2.3.6, is subjected to considerably wide scatter.

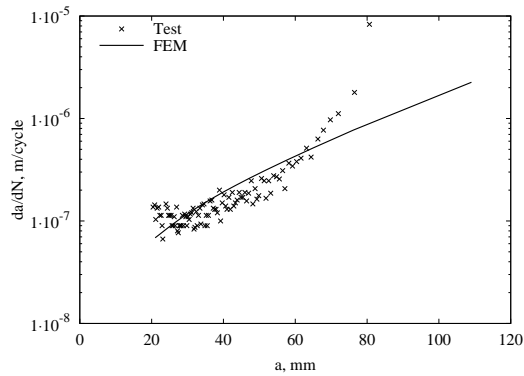
Figures 5.6(e) and 5.6(f) show FCG rate and life for the narrow M(T) plate subjected to $\sigma_{max} = 26\text{MPa}$ and $R = 0.1$. This experimental test was used to obtain the crack growth properties of AA7085-T7651 at $R = 0.1$ that will be used for all the predictions in this thesis (figure 5.5). This prediction is in perfect agreement with the test since the material law obtained by this test was simply integrated. The only approximation introduced in this numerical analysis is the computed β -solution that showed to be in agreement with the exact analytical solution available for this geometry.



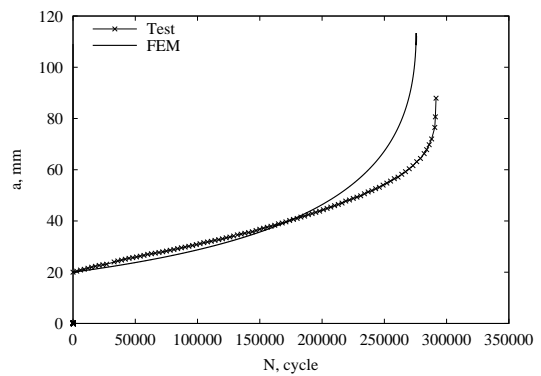
(a) FCG rate, SENT



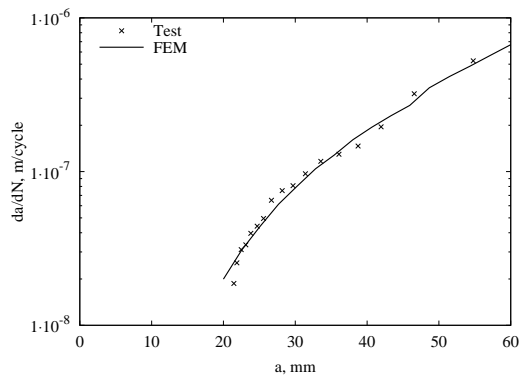
(b) FCG life, SENT



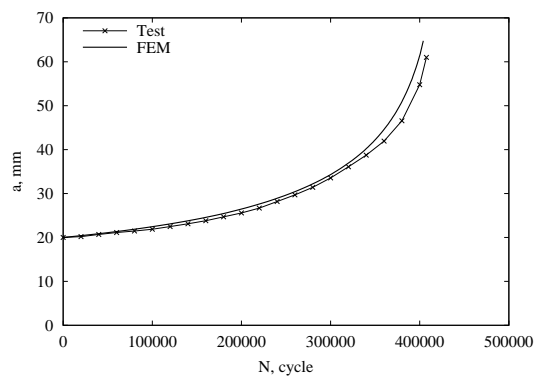
(c) FCG rate: wide M(T)



(d) FCG life: wide M(T)



(e) FCG rate: narrow M(T)



(f) FCG life: narrow M(T)

Figure 5.6: Validation of FCG rate and life against test results for un-reinforced SENT and M(T) samples. Test results from [20, 142].

5.2 Reinforced plates

5.2.1 Specimen geometries and materials

To validate the modelling technique described in chapter 4, experimental data reported in [142, 144–150] are used. No tests were conducted directly by the author and each validation case is taken from either the literature or internal reports given by members of the same research consortium.

The samples used for the validation are a single edge notch tension (SENT) and a middle crack tension M(T) samples of 7085–T7651 aluminium alloy (mechanical properties can be found in table 5.2 and geometries in figure 5.7). The material law of fatigue crack growth rate for 7085–T7651 is shown in figure 5.5 where the curves for R ratio of 0.1 and 0.6 were obtained by best fitting test results found in [142], and curves for other R ratios were obtained by using the Harter T-method [61]. The test samples are 10 mm thick and were clamped at both ends for 65 mm leaving a net length of 270 mm.

Straps are bonded to the substrate as shown in figure 5.7. They are made of four different materials. These are glass fibre reinforced polymer (GFRP), carbon fibre reinforced polymer (CFRP), titanium alloy Ti-6AL-4V (Ti-6-4), and the GLARE I 3/2 (GLARE). The straps were bonded to the substrate either using FM 94 adhesive cured at 120°C or Redux 810 cured at room temperature. The mechanical properties of the strap and substrate materials, used as input to the predictive models, are given in table 5.3. Strap dimensions were variable. A notation is used in this work to describe the strap dimensions. The notation is defined as $wXXdYYtZZlSSS$, where w is the strap width, d the distance between strap edge and initial crack tip, t the strap thickness, and l the strap total length. For example, $w20d2.5t4.4l180$ defines a strap of 20 mm wide, 2.5 mm from the initial crack tip, 4.4 mm thick, and 180 mm long.

The specimens are loaded by a constant amplitude spectrum load with stress ratio $R = 0.1$ and maximum applied stress equal to either $\sigma_{max} = 18.57$ MPa, 26.38 MPa, or 60 MPa.

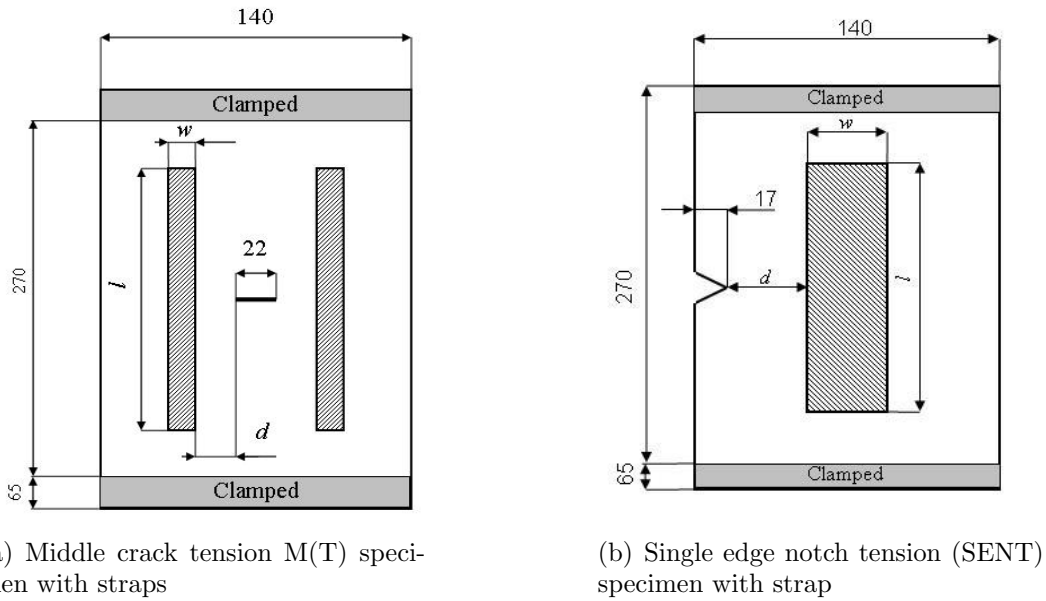


Figure 5.7: Geometry and dimension of two test specimens. Strap dimensions are variable. Sketches not to scale.

5.2.2 SIF distribution through the plate thickness

The first step of methodology validation was to compare the through-thickness distribution of SERR and SIF obtained by the 2D model with those by a 3D FE model.

The SENT sample in figure 5.7(b) is used for this purpose with an initial crack length of 32 mm reinforced by a titanium strap of dimensions $w20d5t2l200$. The analysis is conducted at $\sigma_{max} = 18.57$ MPa. Neither the thermal residual stress nor adhesive disbond is considered in this analysis in order to focus on validating the method of using 2D plate finite elements with multi-point constraint (MPC) to take account of the secondary bending effect. SERR and SIF are calculated for each crack length.

Firstly, calculated SERR through-thickness distributions are shown in figure 5.8 for three crack lengths. The so-called top surface is where the strap is bonded ($z = 10$ mm). SERR obtained by the 2D model (noted as $G_I 2D$) is in good agreement with that obtained by the 3D model ($G_I 3D$). A parabolic fitting curve is also plotted ($G_I 3D$ par) to show that it fits perfectly with the result by the 3D model with exception at the top and bottom surfaces of the plate. This confirms that the SERR distribution has a parabolic shape. The discrepancy at the top and bottom faces may be explained by the crack tip stress singularity; when a

Table 5.3: Mechanical properties of substrate, strap and adhesive materials.

Material	Adhesive ^b	Adhesive [†]	CFRP	GFRP
Type	Redux 810	FM 94	Cycom 919HF-42%-HS	Hexcel 913
E_1 (GPa)	1.90	1.90	135.0 [‡]	46.0 [‡]
E_2 (GPa)	1.90	1.90	9.65 [‡]	5.5 [#]
G_{12} (GPa)	0.62	0.62	4.55 [‡]	3.8 [#]
ν_{12}	0.52	0.52	0.3 [‡]	0.28 [#]
α_{11} ($\mu^\circ C^{-1}$)	/	/	-0.3 [*]	7 [*]
α_{22} ($\mu^\circ C^{-1}$)	/	/	30 [*]	21 [*]
ρ (g/cm^3)	1.1	1.1	1.8 [*]	2 [*]
G_{Ic} (J/m^2)	300	600	/	/
G_{IIc} (J/m^2)	1200	2500	/	/
T_C $^\circ C$	20	120	/	/

Material	Titanium [§]	GLARE I 3/2 [§]	
Type	Ti-6Al-4V	Aluminium 7475-T761	glass epoxy S2
E_1 (GPa)	113.8	70.3	48.9
E_2 (GPa)	113.8	70.3	5.5
G_{12} (GPa)	42.4	26.43	5.5
ν_{12}	0.342	0.330	0.330
α_{11} ($\mu^\circ C^{-1}$)	8.6	23.2	6.10
α_{22} ($\mu^\circ C^{-1}$)	8.6	23.2	2.62
ρ (g/cm^3)	4.51	2.81	1.95

* Generic properties.

^b Data sheet www.hexcel.com, access date Jan 2009. Critical values of SERR have been assessed by disbond comparison of tests and models.

[†] In the absence of published mechanical properties for this adhesive, the mechanical properties of Hexcel Redux 810 are used as typical values. Critical values of SERR have been assessed by disbond comparison of tests and models.

[‡] Values from [151].

[‡] Generic CFRP www.composite.about.com/library/data/blc-t300-934-1.htm, access date April 2008.

[#] Generic GFRP www.composite.about.com/od/data/l/blg_eg epoxy.htm, access date April 2008.

[§] Titanium alloy grade 5 www.asm.matweb.com/search/SpecificMaterial.asp?bassnum=MTP641, access date April 2008.

[§] Courteously from Erik J. Kroon, GTM-advanced structures.

crack intersects with a free surface, the order of stress singularity differs from the inverse-square-root singularity of a 2D (through-thickness) crack problem described by the Westergaard stress function, thus 3D cracks at the plate surface cannot be characterised by the SIF [152].

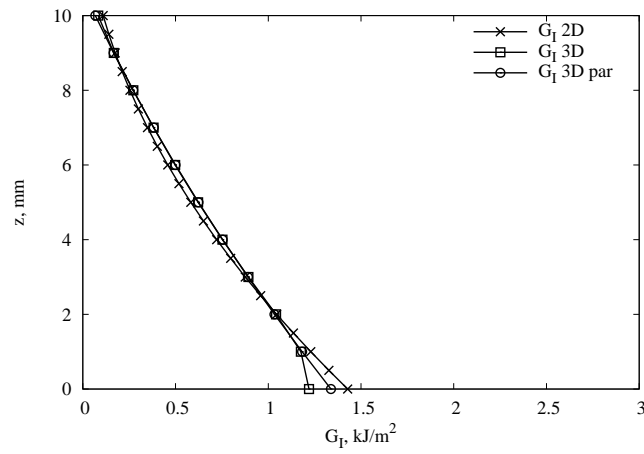
The corresponding SIF through-thickness distribution are shown in figure 5.9. Again 2D (K_I 2D) and 3D (K_I 3D) results are in good agreement. A fitting line (K_I 3D lin) is plotted to extrapolate the SIF values to the top and bottom faces of the plate; it does not fit the results as well as the parabolic fit does for the SERR. This is because that SIF is not strictly a straight line, but the square root of a parabola.

In figure 5.10 the SERR and SIF at the top (reinforced side) and bottom faces are plotted against crack length (a) and compared with the mean SERR and its corresponding SIF (root mean square value) obtained by the 2D and 3D analyses. Good agreement is archived between the two models for each crack length. Therefore the 2D model is validated in terms of through-thickness SERR and SIF distributions by taking into account of the secondary bending effect.

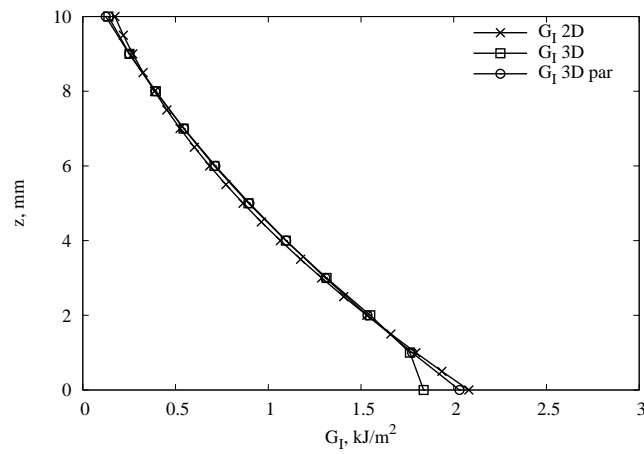
5.2.3 Progressive disbond failure

Another failure mode in bonded crack retarder problem is the progressive disbond of adhesive that reduces the effectiveness of the strap. This progressive damage should be adequately modelled in order to achieve good prediction of FCG life. Both the SENT and M(T) specimens (figure 5.7) are used in this analysis. The SENT has an initial crack length (a_o) of 32 mm and is reinforced by a titanium strap of $w20d5t2l200$. Applied cyclic stress is $\sigma_{max} = 18.57$ MPa, $R = 0.1$. The M(T) has an initial half crack length (a_o) of 11 mm and is reinforced by a GFRP strap of dimensions $w20d2.5t4.4l180$. Applied cyclic stress is $\sigma_{max} = 60$ MPa, $R = 0.1$.

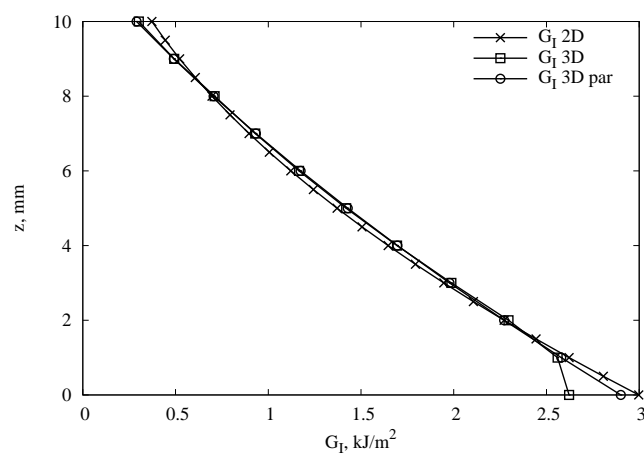
Predicted final disbond shape and area are compared with the experimental measurements reported in [144,146]. Before discussing the comparisons, the meaning of final disbond damage needs some clarification. In the experimental test, disbond grows progressively and two failure modes can be observed when substrate crack reaches its critical length, i.e. either one side of the strap (divided by the crack growth path) debonds completely from the substrate and the experiment stops, or the broken substrate (in two pieces separated by the crack) are kept



(a) Crack length $a = 52$ mm



(b) Crack length $a = 72$ mm



(c) Crack length $a = 92$ mm

Figure 5.8: SERR through-thickness distribution: SENT sample with titanium strap $w20d5t2l200$.

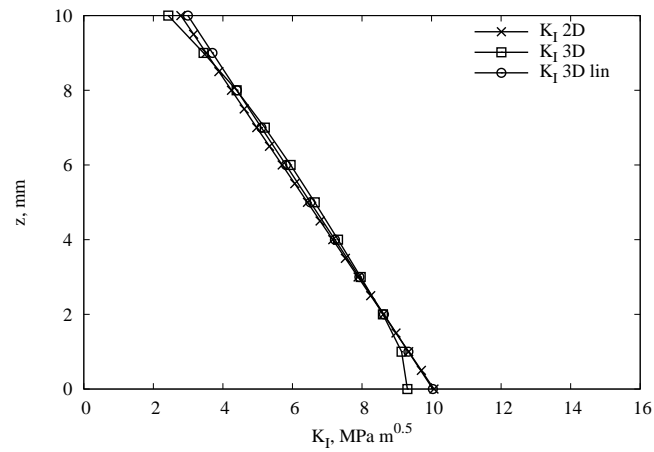
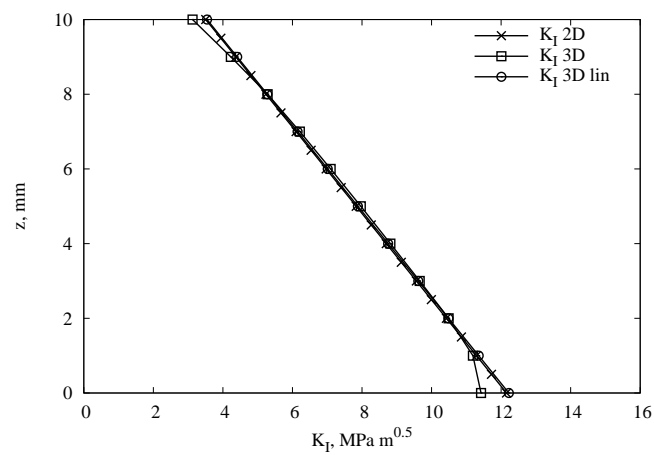
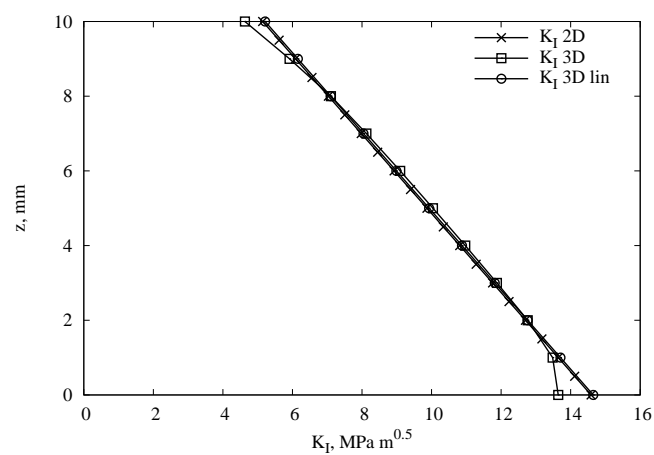
(a) Crack length $a = 52$ mm(b) Crack length $a = 72$ mm(c) Crack length $a = 92$ mm

Figure 5.9: SIF through-thickness distribution: SENT sample with titanium strap $w20d5t2l200$.

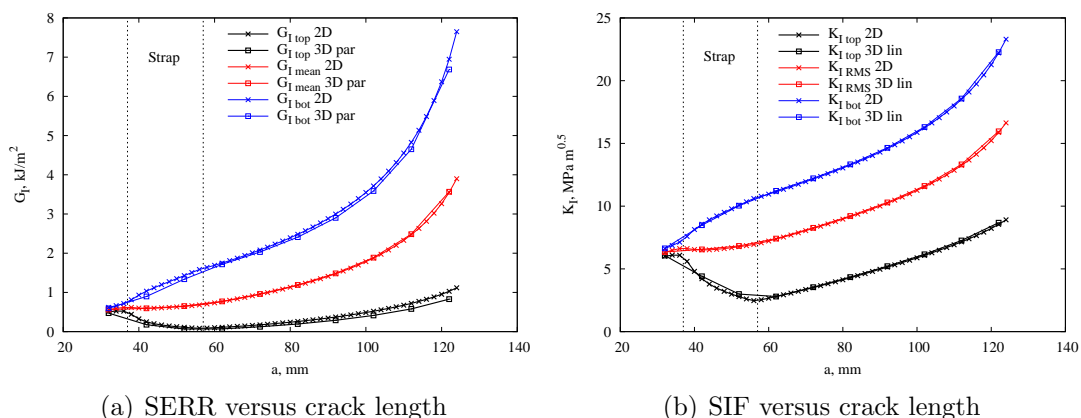


Figure 5.10: Comparison of 2D and 3D model calculated SERR and SIF values in two different thickness positions: “top” means reinforced face, “bot” means un-reinforced face. SENT sample with titanium strap $w20d20t2l200$.

connected by the strap and the test machine keeps running even though the substrate has broken into two pieces. In the second case, although the structure can still bear the load, the test is considered finished since the substrate has failed. During the experiments it is often difficult to decide if the strap has debonded completely and, subsequently, the sample has failed, or the substrate has failed before the strap has debonded completely on one side of the crack because the adhesive is unable to transfer the load to the strap. Conventionally the final disbond area is defined as the adhesive failure area obtained at the end of the test, i.e. when the reinforced plate fails due to either of the two failure modes. If one side of the strap is completely debonded, then the area on the other side is taken as final disbond damage extent. From the modelling point of view, final disbond area is obtained by one of the following definitions: 1) when strap debonds from substrate completely; 2) the disbond area at the critical crack length in the substrate.

Figure 5.11(a) shows the comparison of calculated and measured final disbond shape for a titanium strap reinforced SENT sample. In the figures only the lower half of the strap is shown and the disbond and bonded areas are indicated. Substrate crack growth path is from the upper left corner to the right as indicated. Predicted and measured final disbond shape and area are in good agreement. Disbonds in an M(T) plate reinforced by two GFRP straps are shown in figure 5.11(b). The agreement between the predicted and measured [144, 146] disbond areas is also acceptable. For this case, the actual disbond damage has two dis-

bond fronts: one was close to the substrate crack (upper part in the figure) and the other started from the bottom corner of the strap (strap end edge). The model did not find this second disbond front because disbond initiation is driven by the passing substrate crack. However, by analysing the shear stresses in the adhesive (section 6.1.4) it is found that, for an un-cracked substrate, the maximum shear stress is actually developed at the strap ends (bottom corner in figure 5.11(b)), that is likely to cause a second disbond front.

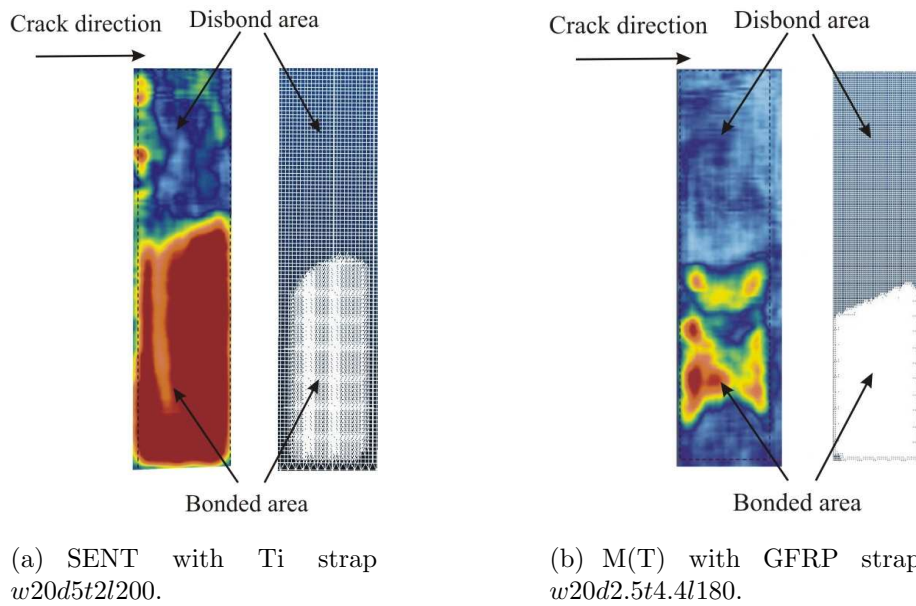


Figure 5.11: Final disbond shapes: modelling (right) vs. measurement (left) [144, 146]. Only half strap is illustrated. Dimensions in figure 5.7

5.2.4 Thermal residual stresses and redistribution

Thermal residual stresses (TRS) are caused by curing adhesive at elevated temperature. Their influence on FCG rate is important and ought to be considered in predictive models. TRS can be experimentally measured, but testing is time and money consuming. For this reason a modelling technique has been developed in section 4.2.4 and is herein validated.

In this section predicted thermal residual stresses in the SENT sample (figure 5.7(b)) reinforced by straps of different dimensions and materials are presented to demonstrate the robustness of the methodology. The used adhesive is the FM94 cured at 120 °C. The analysis is composed of two steps: the first is to determine

the initial residual stress distribution after curing process; the second is to model a series of stress re-distribution during crack propagation. Calculated residual stresses are plotted across the sample width in three different thickness positions (figure 5.12). Predictions are compared with the experimental measurements of the titanium straps reported in [148] and other material straps reported in [149]. Calculated initial TRS distribution is plotted against experiments in figure 5.13 for different strap materials, widths and thicknesses. For each strap configuration, the calculated and measured TRS are in good agreement. Discussions for each strap configuration follows.

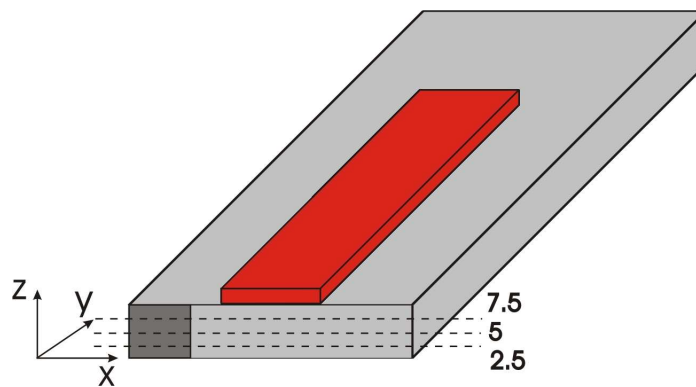


Figure 5.12: Definition of lines along which the TRS were calculated for the SENT specimens.

Figures 5.13(a) and 5.13(b) show the initial stress distributions for two titanium strap cases, $w20d20t2l200$ and $w20d20t4l200$. Although the cure temperature, the elastic modulus and coefficient of thermal expansion (CTE) are all the same for the two cases, TRS produced by the thicker (4 mm) strap are much higher. This is because that a thicker strap is also stiffer, consequently when the temperature drops to the room temperature the strap does not contract with the substrate as much as the thinner strap (2 mm) and the displacements compatibility between strap and substrate is achieved at a higher stress level in the substrate. It is also worth noting the stress concentration spot beneath the strap, i.e. the “bump” feature in the graphs. This feature is related to the titanium strap; the reason will be discussed in the next paragraphs.

Strap width effect can be seen by comparing figure 5.13(a) with 5.13(d) ($w20d20t2l200$ vs. $w100d20t2l200$) and 5.13(b) with 5.13(c) ($w20d20t4l200$ vs. $w60d20t4l200$), where TRS caused by titanium straps of different widths are plotted. Peak stress values for the wider straps are higher due to the higher

stiffness. Therefore, the stiffer the strap, the higher the TRS peak values. Stresses caused by straps of the same dimensions ($w20d20t2l200$) but different materials are plotted in figures 5.13(a), 5.13(e), and 5.13(f), respectively for the titanium, GFRP, and CFRP straps. TRS are strongly influenced by material's CTE and elastic modulus. Observation from these results is: the stiffer the strap and the lower the longitudinal CTE, the higher the TRS. The CFRP strap produces the highest TRS (figure 5.13(f)), followed by the titanium strap (figure 5.13(a)) and then the GFRP (figure 5.13(e)); GFRP has the lowest longitudinal elastic modulus.

Neither the CFRP nor the GFRP straps produce the distinct “bump” feature around the strap region as the titanium strap does 5.13(a). The “bump” is caused by the isotropic property of titanium alloy. Since the CTE of the titanium ($8.6 \mu^{\circ}C^{-1}$) is much lower than that of the aluminium ($23.6 \mu^{\circ}C^{-1}$), the strap does not contract in the transverse direction (x -direction) at the same rate as the aluminium substrate during the temperature drop. This causes tensile residual stress also in the x -direction that due to the Poisson's effect will make the substrate contract in the y -direction adding extra residual stress to what caused by the y -direction contraction. However, since the substrate and strap have to satisfy the displacement compatibility requirement, there is an increase in the σ_{yy} around the strap region. No “bumps” for GFRP and CFRP reinforced cases because the CTE in the transverse direction (x -direction) of these two polymer composites (respectively 30 and $21 \mu^{\circ}C^{-1}$) is very close to that of the aluminium substrate ($23.6 \mu^{\circ}C^{-1}$); consequently, in the x -direction, these straps contract at the same rate of the aluminium substrate during the temperature drop causing no further increase in the y -direction stresses.

When the crack propagates, TRS will re-distribute, that will in turn influence the crack growth rate. The SENT sample reinforced by a titanium strap ($w20d20t2l200$) is used to demonstrate the analysis for four growing crack lengths. Figure 5.14 shows the predicted TRS at two thickness positions (see figure 5.12) and comparison with the experimental measurements reported in [150]. Good agreement is achieved for each crack length. Figure 5.14(a) shows the TRS distribution for crack length $a = 29$ mm, i.e. just before the crack tip enters the strap. The peak stress value is not really meaningful due to the dependence on the model mesh size. Figure 5.14(b) shows the TRS when the crack is beneath the strap ($a = 47$ mm) and figures 5.14(c) and 5.14(d) show the stresses when

crack has just passed the strap ($a = 69$ mm) and far beyond the strap ($a = 90$ mm).

From these analysis, it can be concluded that the distribution and magnitude of the TRS due to the curing process and their subsequent redistribution during crack propagation can be determined by the modelling method presented in chapter 4.

5.2.5 Influence of geometric nonlinearity and thermo mechanical load coupling

It is mentioned in section 4.3.1 that a dimensionless stress intensity factor (β) that is only a function of the geometry does not exist for this bonded structures due to the geometric nonlinearity. It is demonstrated in this section that changing of the applied load magnitude or the presence of TRS will change the value of β . There are two reasons for this. First, the magnitude of secondary bending is a function of the applied load; second, extent of disbond damage also depends on the applied load and different disbond area causes different geometric effect to β .

In this study, the root mean square (RMS) value of the through-thickness SIF range, ΔK , is determined by the alternate analysis method described in section 4.3.1. An effective β factor (equation 4.40) is computed and plotted to demonstrate that a classical β factor dependent only on the geometry as described in section 2.1.1 does not exist for this kind of problems.

In figure 5.15(a) β factor versus crack length is plotted for two SENT plates reinforced by titanium strap of dimension $w20d20t2l200$ (geometry in figure 5.7(b)). One sample was cured at the room temperature and the other at 120°C . Therefore, just the effect of the TRS on the secondary bending is seen in the β solution. Initial crack length was $a_o = 17$ mm and applied stress was $\sigma_{max} = 18.57$ MPa and $R = 0.1$, referred to as the “low load” case in this work. The curves can be split into two parts according to the crack length. When $a \leq 50$ mm, β value is lower for the sample cured at elevated temperature (low load + TRS), because the TRS try to bend the plate in the opposite direction to that caused by the secondary bending due to the applied load; this reduces the overall bending and consequently the β factor. When $a \geq 50$ mm, the difference in β solution is caused by the difference in disbond area. When there are TRS, adhesive is more

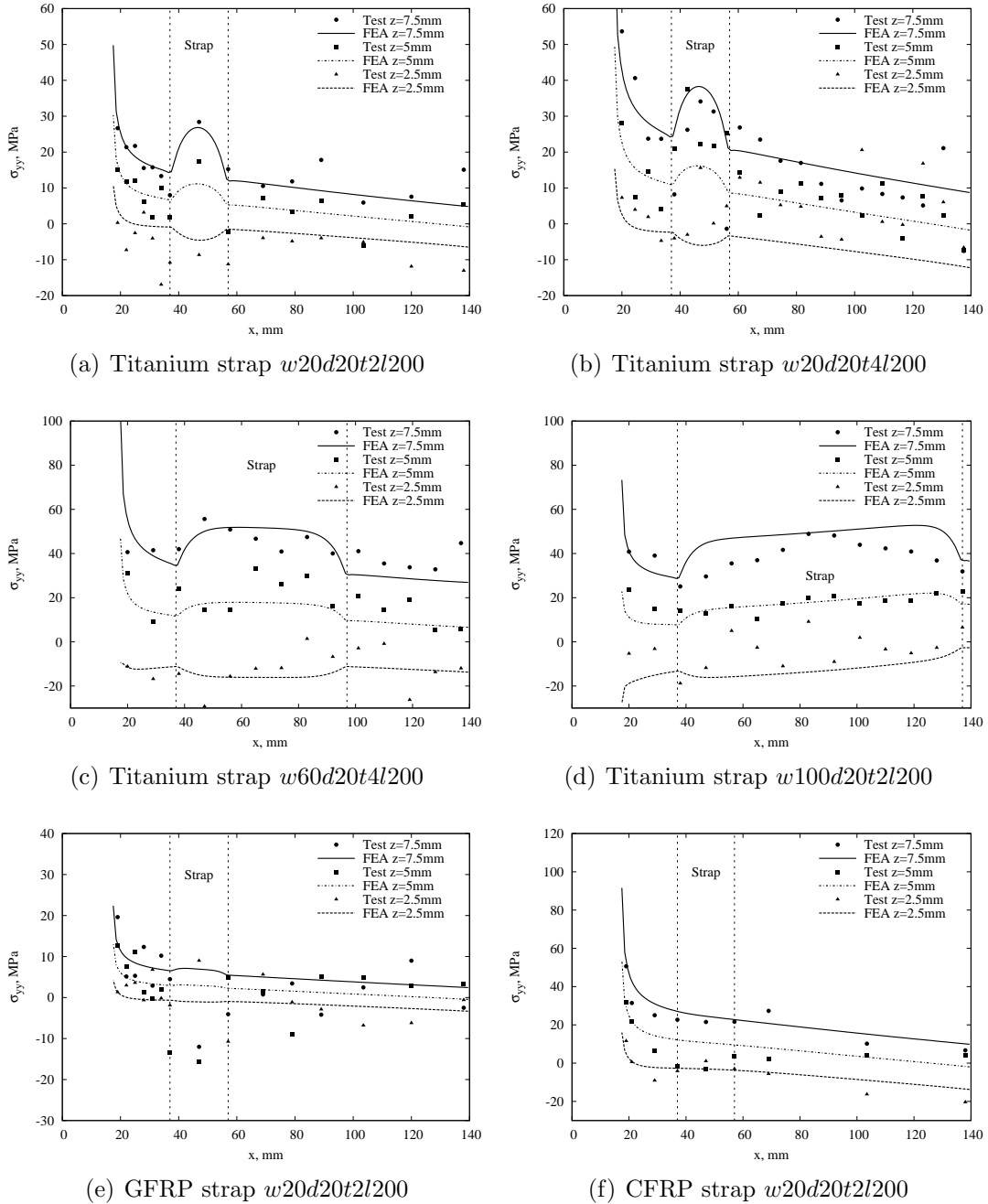


Figure 5.13: Initial distributions of residual stresses in the longitudinal direction in the SENT bonded with various straps: modelling vs. measurement [148, 149].

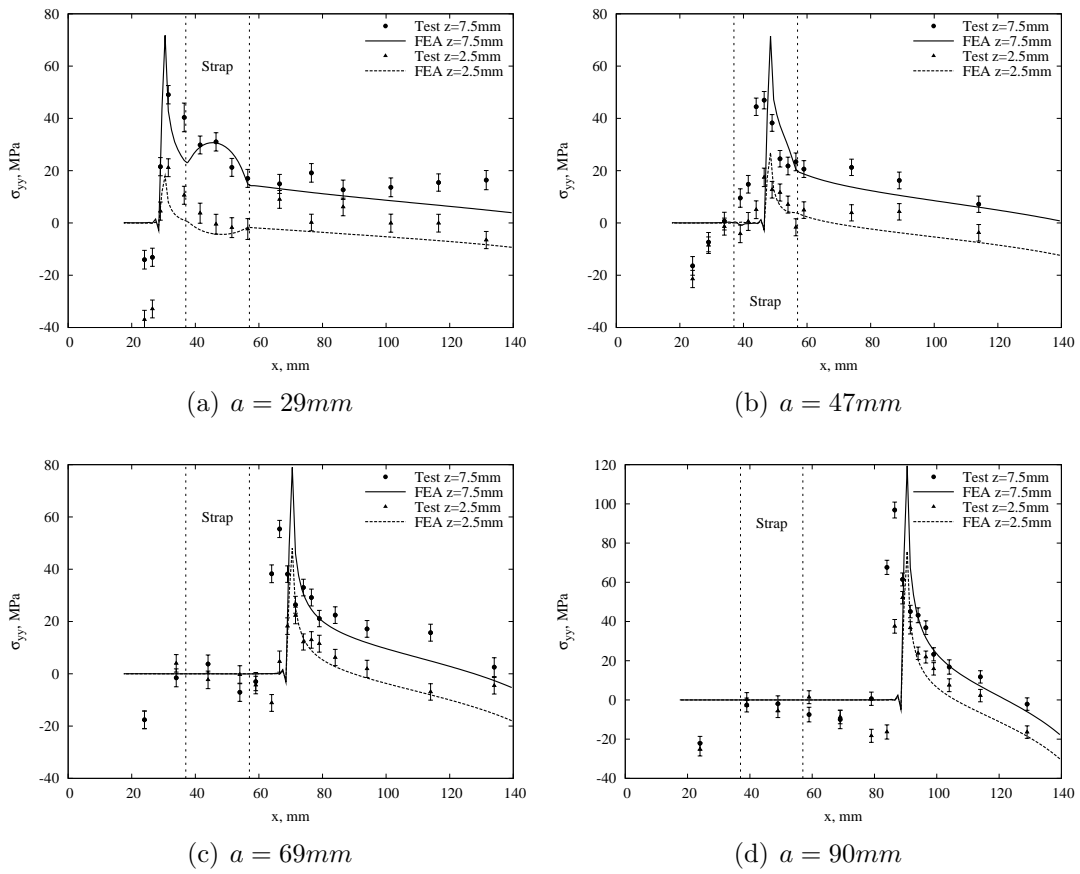


Figure 5.14: Redistribution of TRS with crack propagation: modelling vs. measurement [150]. SENT sample with titanium strap $w20d20t2l200$.

stressed and the disbond damage is larger and β is higher. It is known in the literature that the effects of TRS should be equal at the maximum and minimum applied loads and consequently should not affect the SIF range. This is true when there is no secondary bending involved, e.g. welded joints or cold worked samples (equation 4.33). However, in this case, TRS affect the bending direction and magnitude, and consequently they will influence the SIF range. Therefore, β solution by normalisation with applied load does not exist.

Another comparison is shown in figure 5.15(b) where the SENT plate is subjected to the “high load” ($\sigma_{max} = 60$ MPa) and “low load” ($\sigma_{max} = 18.57$ MPa). Therefore the effect of the applied load on β solution can be seen. Again the curves can be split into two regions separated by crack length $a = 40$ mm. In the first region ($a < 40$ mm) only the effect of the load on the secondary bending can be seen because the adhesive has not yet started debonding. Higher load causes more bending, thus higher β factor. In the second region ($a > 40$ mm) adhesive is failing and higher load cause more adhesive disbond and consequently higher β values.

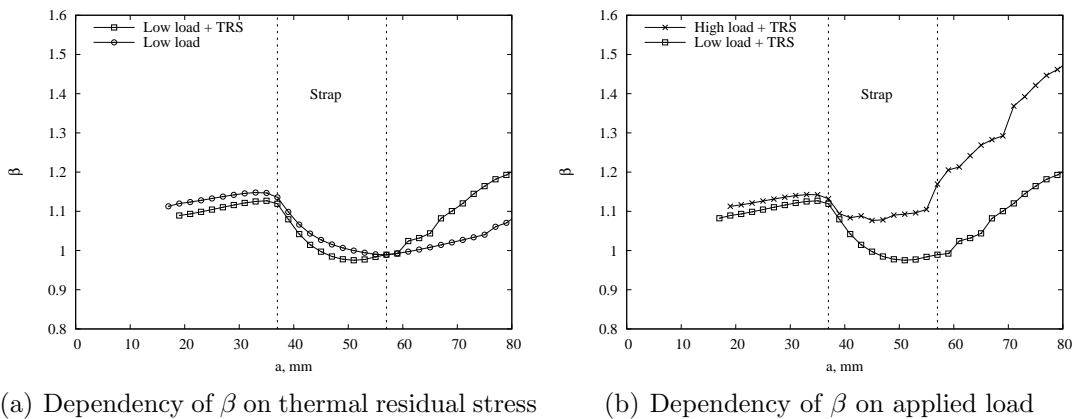


Figure 5.15: Influence of geometric nonlinearity on the dimensionless SIF (β) due to different magnitude of secondary bending and disbond. SENT sample with titanium strap $w20d20t2l200$.

Another important factor mentioned in section 4.2.4 is that the mechanical and thermal loads must be applied at the same time and the stress intensity factor computed by a single FE analysis. This is due to the interaction between the mechanical and thermal loads; consequently, superposition of two separate analysis results may lead to erroneous solutions. In fact, each load causes bending in opposite directions; hence the overall deformed shape affects the SIF and should

be determined by considering both stress fields in one single analysis. To demonstrate this effect, a SENT plate with titanium strap is studied at the low stress case (18.57 MPa). Calculated SIF values due to the mechanically applied stress (indicated by M), thermal stress (T), summed SIF by adding the separate solutions from the applied and thermal stresses (M+T), and the total SIF obtained by a joint thermo-mechanical analysis (M+T+coupling) are plotted against crack length (a) in figure 5.16(a). It can be seen that the coupling effect of the thermal and mechanical loads is not negligible. Errors generated by summing the two separate solutions is also shown in the same figure. It is between -12% and $+20\%$. The same analysis was performed for the higher applied stress (60 MPa) and the results are shown in figure 5.16(b). The error by superposition is slightly smaller (between -4% and $+8\%$), but still not negligible. This is due to the fact that higher applied load means higher applied SIF, then the contribution of residual SIF to the total SIF is relatively smaller, thus smaller error.

This analysis has demonstrated that, due to the influence of secondary bending and adhesive disbond, the β solution is also function of the applied load. Thus the SIF range must be computed case by case and a solely geometric solution β no longer exists. Moreover, the coupling effect of thermal and mechanical loads on secondary bending requires both load fields being taken into account simultaneously in one FE analysis to compute the overall SIF. If the superposition method is applied, one might encounter errors up to 20%.

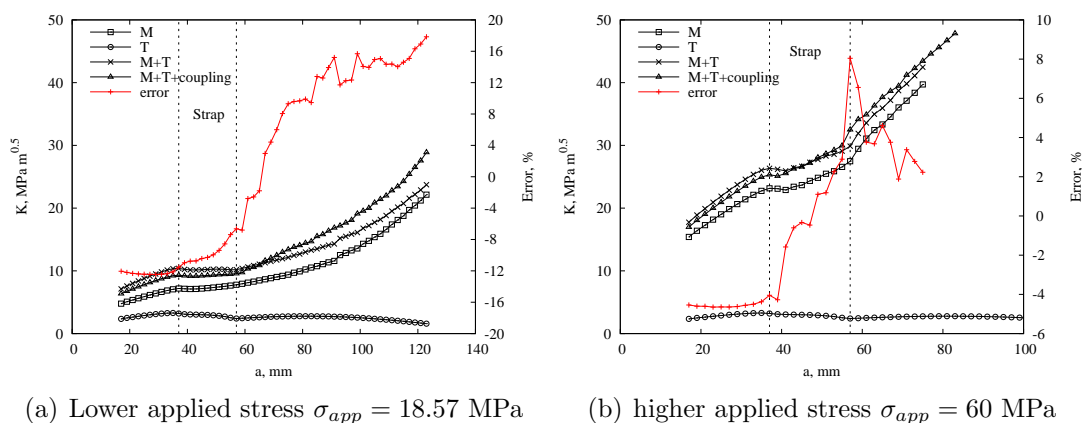


Figure 5.16: Interaction of mechanical and thermal loads at low and high applied load. SENT sample with titanium strap $w20d20t2l200$.

5.2.6 FCG life predictions

Each previously examined mechanism influences the crack growth driving force SIF, and hence the accuracy in fatigue crack growth life prediction. Therefore, the ultimate validation test is to compare predicted FCG rates and lives with test results. Example samples are reinforced by straps made of the titanium, CFRP, GFRP, Aluminium and GLARE material; the mechanical properties used in the predictive models are given in table 5.3. Some of the best and worst predictions are shown in figures 5.17-5.21 and discussed in this section. The rest of the validation cases are reported in appendix B for information.

The first validation analysis involves the SENT plate reinforced by a titanium strap of dimension $w20d5t2l200$ (figure 5.7(b)). The initial crack length a_o is 32 mm and the applied stress $\sigma_{max} = 18.57$ MPa, $R = 0.1$. The specimen was cured at high temperature (HT, $T_C = 120^\circ C$). Predicted FCG rate and life are compared with the test results found in [144] in figures 5.17(a) and 5.17(b). Both root mean square (RMS) and weighted (w) values of the SIF range are used for the prediction. Good agreement is achieved by the weighted solution in terms of the FCG rate before the crack tip has passed the strap. After that point calculated crack growth rate using the weighted SIF is slightly faster giving a conservative prediction of FCG life (error -17.1%). The RMS SIF produced a slightly lower crack growth rate at the beginning and faster at the end giving a final value of number of cycle really close to the measured one (error $+0.42\%$).

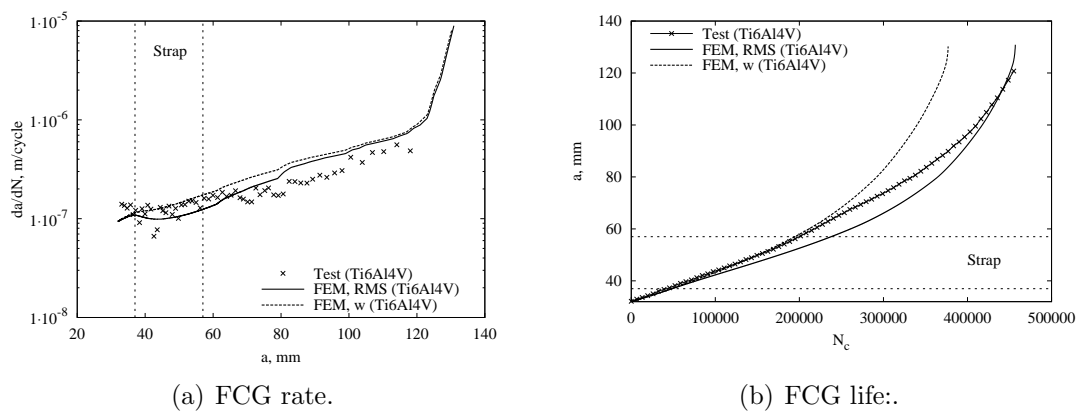


Figure 5.17: Validation of FCG rate and life against test results [144]: SENT, Ti6Al4V strap $w20d5t2l200$, HT cure.

The second validation case is for the SENT plate reinforced by a CFRP strap of dimension $w20d5t2l200$ (figure 5.7(b)). The initial crack length a_o is 32 mm and the applied stress $\sigma_{max} = 18.57$ MPa, $R = 0.1$. The specimen was cured at high temperature (HT). FCG rate and life predictions are compared against experiments from [142] in figure 5.18. Although from the observation of the FCG rate (figure 5.18(a)) it looks like the predictions are in agreement with the experiments, this is one of the least accurate predictions. The errors made by the weighted and RMS are +19.9% and +45.1% respectively. These errors could be due to an underestimated material law for high R ratio. Refereing to figure 5.5, it can be seen that only the material laws for $R=0.1$ and $R=0.6$ are obtained from experimental tests. All the other curves are interpolated by the Harter T-method. The effective R -ratio (R_{eff}) for this specimen are between 0.3 – 0.4 which are the further curves from the actual experimental data. It might be that the real curves for R -ratio 0.3 and 0.4 are actually higher than the interpolated ones. If so, prediction accuracy could be improved.

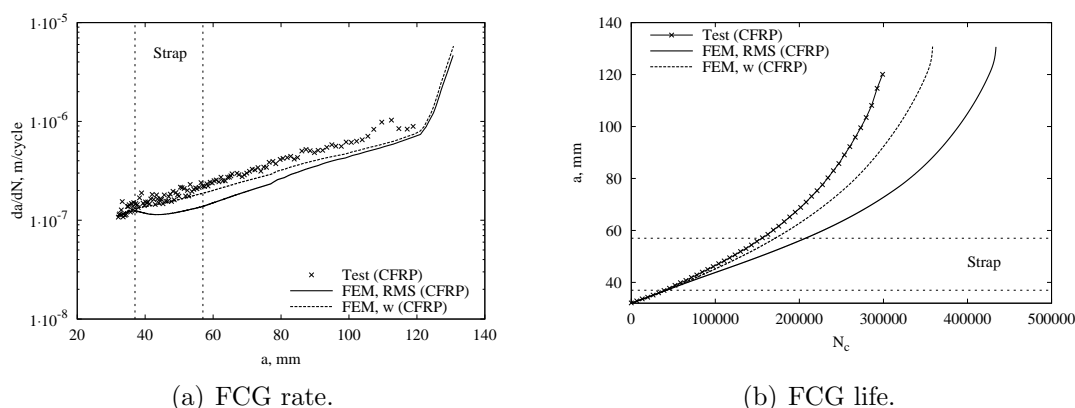


Figure 5.18: Validation of FCG rate and life against test results [142]: SENT, CFRP strap $w20d5t2l200$, HT cure.

The third case is an M(T) plate reinforced by GFRP straps of dimension $w20d2.5t4.4l180$ (figure 5.7(a)). The initial half crack length a_o is 11 mm and applied stress $\sigma_{max} = 60$ MPa, $R = 0.1$. The specimen was cured at high temperature (HT). The experimental results can be found in [146]. The prediction results are shown in figures 5.19. The weighted solution is in good agreement with the test until the crack approaches the end of the strap and, after that, the crack growth rate is slightly overestimated causing an error of -15.5% in the final FCG life. The RMS solution produces lower crack growth rate at the

beginning and higher at the end resulting in a prediction error of 0.5%.

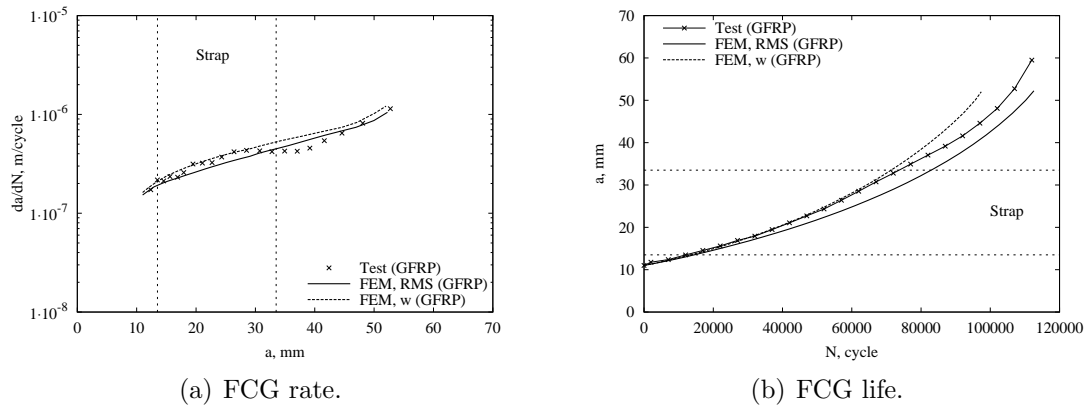


Figure 5.19: Validation of FCG rate and life against test results [146]: M(T), GFRP strap $w20d2.5t4l180$, HT cure.

The fourth case is an M(T) plate reinforced by aluminium alloy straps (7085-T7651) of dimension $w20d2.5t5l180$ (figure 5.7(a)). The initial half crack length a_o is 11 mm and applied stress $\sigma_{max} = 60$ MPa, $R = 0.1$. The specimen was cured at high temperature (HT) but there are no TRS since substrate and strap are made of the same material. The experimental results can be found in [142]. The FCG rate and life are shown in figure 5.20. The predictions are in good agreement with the test results until the crack approaches the end of the strap. At that point the crack growth slows down in the test and this effect is not caught by the modelling technique. The final errors produced by the weighted and RMS SIF are -41.7% and -29.5% respectively. The reason of this out of trend and large error are associated with the relatively thick strap (5 mm). A thick strap behaves more like a stringer and decrease the crack growth rate when the crack is passing it. This effect is not considered in this model technique since the strap is modelled by 2D plate elements parallel to the substrate. It must also be added that the strap has a width over thickness ratio equal to 4 that is considerably small to be modelled with plate elements.

The last validation case is also an M(T) plate but reinforced with GLARE straps of dimension $w10d8t5.4l180$ (figure 5.7(a)). The initial half crack length a_o is 20 mm and the applied stress $\sigma_{max} = 26.38$ MPa, $R = 0.1$. The specimen was cured at room temperature (RT), thus no TRS in the substrate. The experimental

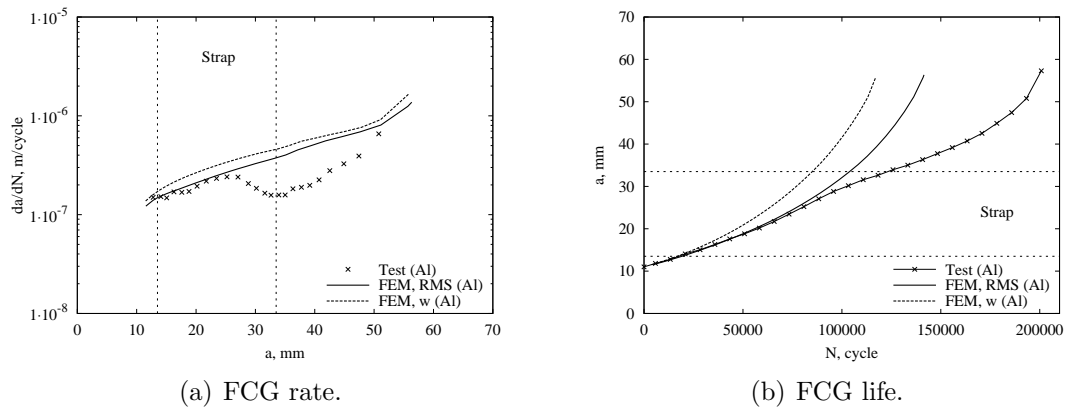


Figure 5.20: Validation of FCG rate and life against test results [142]: M(T), Al strap $w20d2.5t5l180$, HT cure.

results are taken from [142]. Predicted FCG rate and life are showed in figures 5.21(a) and 5.21(b), respectively. Again both weighted and RMS SIF values are used for the prediction. FCG rate calculated by the weighted SIF solution is in excellent agreement with the test results for crack lengths $a > 30$ mm. However, since at the beginning of crack propagation the calculated FCG rate is slightly higher than the experimental measured, the predicted life is conservative (error -13.5%). The RMS solution is in good agreement up to crack length of 30 mm but after that, it underestimates the FCG rate resulting error of $+9.3\%$ in the final life.

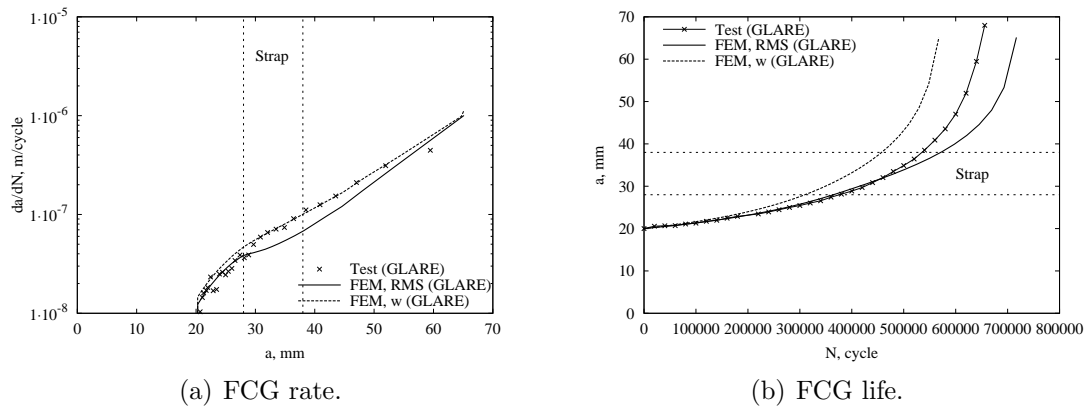


Figure 5.21: Validation of FCG rate and life against test results [142]: M(T), GLARE strap $w10d8t5.4l180$, RT cure.

A summary of FCG life predictions and errors is given in table 5.4. It can be seen that the weighed SIF value predicts FCG lives that are consistently conservative.

While marginally more accurate results can be archived by using the RMS SIF value although predicted lives are not always conservative. The mean error is computed for both RMS and weighted predictions. It can be seen that for the RMS value the mean error is close to 0% whereas the weighted value produces a -15% of error. A more meaningful parameter is the mean absolute error. This value is computed by averaging the absolute errors. It can be see in table 5.4 that these errors are around 20% for both the RMS and weighted predictions. This error lies well within the scatter range in the experimental tests.

It seems that when a conservative solution is needed the weighed SIF value should be used for life prediction. However, both the weighed and RMS values can be used to find the FCG life range.

Prediction errors are also graphicly represented in figure 5.22 by showing the difference between predicted and experiential life divided by the experimental life, $(N_{FEM} - N_{test})/N_{test}$ for each validation case.

From the results presented in figure 5.17-5.21, in appendix B, table 5.4 and figure 5.22 the methodology to compute FCG life of bond strap reinforced plates is considered to be validated for different substrate geometries, strap materials and geometries, and applied load levels.

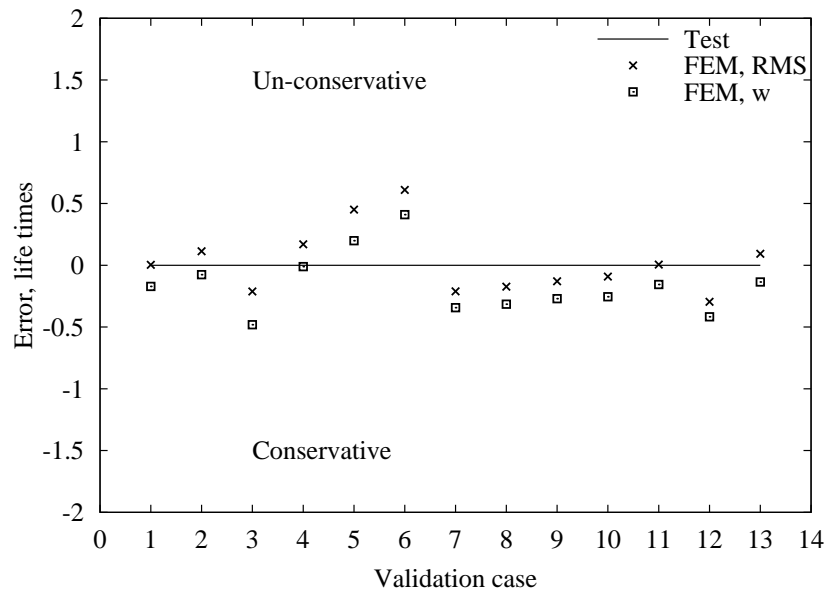


Figure 5.22: Summary of the prediction errors.

Table 5.4: Predicted FCG lives and error ranges in comparison with test results (life in cycles).

Specimen+strap, strap geometry, cure temp, load	Test	Prediction		Figure
		K RMS (error %)	K w (error %)	
SENT+Ti6-4, <i>w20d5t2l200</i> , HT, $\sigma = 18.57$	455000	456900 (+0.42 %)	377000 (-17.1 %)	5.17
SENT+Ti grade 2, <i>w20d5t2l200</i> , HT, $\sigma = 18.57$	404000	449900 (+11.4 %)	373300 (-7.6 %)	B.1
SENT+GFRP, <i>w20d5t2l200</i> , RT, $\sigma = 18.57$	595000	469200 (-21.1 %)	308650 (-48.1 %)	B.2
SENT+GFRP, <i>w20d5t2l200</i> , HT, $\sigma = 18.57$	358000	418900 (+17.0 %)	354000 (-1.11 %)	B.3
SENT+CFRP, <i>w20d5t2l200</i> , HT, $\sigma = 18.57$	299000	433900 (+45.1 %)	358500 (+19.9 %)	5.18
SENT+GLARE, <i>w20d5t1.8l200</i> , HT, $\sigma = 18.57$	262000	422000 (+61.1 %)	369400 (+40.1 %)	B.4
SENT+GLARE, <i>w20d5t5.4l200</i> , HT, $\sigma = 18.57$	619000	488700 (-21.1 %)	406800 (-34.3 %)	B.5
SENT+GLARE, <i>w30d5t3.6l200</i> , HT, $\sigma = 18.57$	601500	497600 (-17.3 %)	411900 (-31.5 %)	B.6
SENT+GLARE, <i>w60d5t1.8l200</i> , HT, $\sigma = 18.57$	557000	485100 (-12.9 %)	406400 (-27.0 %)	B.7
SENT+GLARE, <i>w100d5t1.8l200</i> , HT, $\sigma = 18.57$	620000	563600 (-9.10 %)	461900 (-25.5 %)	B.8
M(T)+GFRP, <i>w20d1.5t4.4l180</i> , HT, $\sigma = 60$	112000	112600 (+0.54 %)	94550 (-15.5 %)	5.19
M(T)+Al, <i>w20d2.5t5l180</i> , HT, $\sigma = 60$	200800	141500 (-29.5 %)	117100 (-41.7 %)	5.20
M(T)+GLARE, <i>w10d8t5.4l180</i> , RT, $\sigma = 26.38$	656000	717000 (+9.30 %)	567400 (-13.5 %)	5.21
Mean error		+2.6 %	- 15.6 %	/
Mean absolute error		+19.7 %	+ 24.1 %	/

note: "HT" means curing at elevated temperature of 120°C

σ is the maximum applied stress; $R = 0.1$ for all cases.

5.3 Modelling technique critique: strong and weak points

It has been demonstrated that in most cases the modelling technique developed and described in this thesis is able to accurately predict the FCG lives of strap reinforced samples. Following this validation study the capabilities and limitations of the modelling technique are assessed in this section.

This modelling technique, although uses 2D plate elements, is capable of calculating the secondary bending effect on the through-thickness distribution of SIF and the result is as accurately as a more computational intensive 3D FE model. The progressive adhesive failure is also modelled and predicted final disbond shape and area agree with the experimental measurement.

Thermal residual stresses and their redistributions with crack propagation are calculated for different strap materials and dimensions. Good agreement with the measured values is achieved for each strap configuration.

The “alternate analysis” method has been developed to obviate the fact that it is impossible to derive a non-dimensional load-independent SIF, i.e. the β factor, due to the secondary bending and its dependency on the applied load and disbond area.

The coupling between the thermal and mechanical load has also been assessed and dealt with by applying both loads simultaneously to the structure. For the cases presented in this chapter, neglecting the thermal-mechanical coupling effect leads to an error in SIF of up to 20 %.

FCG lives of a wide range of sample geometries, applied loads, strap geometries and materials and curing temperatures have been predicted and compared to experiments. The average absolute error in the predicted lives ($\sim 20\%$) shows the capability of the predictive model.

Unfortunately, although accurate in most of the cases, this modelling technique is still a numerical approximation of reality and, as such, has got some limitations.

The first limitation lies in modelling “thick” straps. When the width to thickness ratio of a strap is less or equal to 4 the strap actually behaves like a stringer and 2D plate elements are not able to accurately model it. This limitation is stronger

for stiff strap materials where a substantial deceleration in crack growth just after when the crack passes the strap is shown in the experiments. This effect is not caught by the modelling technique and results in an overconservative FCG live prediction.

Another limitation is intrinsic of the problem and due to the nonlinearity. Since the amount of bending is a function of the load, also the through-thickness distribution of the SIF is affected by it. As long as the structure is subjected to constant amplitude variable loads, the alternate analysis solves the problem. In the case of variable amplitude loads, a FE analysis should be run for each load level and the load history influences not only the substrate crack propagation rates but also the adhesive failure. These mechanisms are not accounted for by this modelling technique. In those cases, the maximum applied load range in the spectrum may be applied to the model to compute the effective β solution that, although approximated, could be used for any load levels in the spectrum.

The last limitation of the modelling technique is due to the disbond progression algorithm. Firstly, the quasi-static disbond criterion is not able to completely compute the amount of disbond which grows under fatigue. In this modelling technique, the disbond growth is triggered by the passing substrate crack more than the fatigue loading. In reality some disbond will grow even before the crack approaches the strap. This is more true for low applied variable load, i.e. low SIF at the substrate crack. In these cases, the crack takes longer to reach the strap but the stresses in the adhesive might, nevertheless, be elevated due to the stiffness or geometry of the strap and consequently, disbond growth might appear under pure fatigue loads without any help from the substrate crack. This kind of disbond growth is not predicted by this modelling technique. Secondly, the iterative procedure to compute disbond growth substantially increases the computational time. Excessive computing time is needed when this methodology is applied to structures with multiple straps.

These drawbacks can be eliminated or reduced in various ways but, due to the limited time of the project, implementation of possible solutions has to be part of future work (section 8.4).

Bearing in mind the capabilities and limitations of this modelling technique, parametric studies are carried out to understand the most important strap parameters which influence the performance of the reinforced structures in the next chapter.

Chapter 6

Parametric Studies

This chapter describes the influences of strap materials, strap dimension, adhesive properties, and the TRS on the performance of the bonded straps. The aim is to find the most important design parameters and provide guidelines to the design of bonded strap reinforced integral structures.

In first section, TRS are not considered by studying structures which are bonded at room temperature. This is to simplify the problem and avoid the interaction between bridging and TRS effects, both are influenced by the stiffness of the strap. The effects of the strap material and dimension are so studied, followed by a FCG life sensitivity analysis on elastic modulus of the strap and adhesive properties.

Once the importance of the strap material and dimension choice are established without the influence of the TRS, the TRS effect is included (section 6.2). Firstly a parametric study on the TRS distribution in the substrate is carried out; secondly the influence of strap material and dimension choice on the FCG life is studied.

Due to the interactions between the various factors, design of an effective strap is a complicated task. In order to simplify the problem, a method to find the lightest strap geometry for a given life target is produced: the design graph (section 6.3).

This chapter closes (section 6.4) with a list of guidelines for the design of strap based on the experience and knowledge of the problem acquired during this research project.

6.1 Room temperature cure: no TRS

6.1.1 Strap material

6.1.1.a Constant strap weight analysis

Different strap materials are studied by keeping the weight of the strap constant (4.5 g), i.e. by changing the strap thickness for a specific strap width ($w20d25l200$). A selection of strap materials are used to reinforce the M(T) specimen made of aluminium 2024-T3 (properties in table 5.2). Geometry and dimension of the plate can be found in figure 5.4(b). Mechanical properties of the strap materials and thicknesses are in table 6.1. Redux 810 cured at room temperature is used for bonding (properties in table 5.3). The maximum applied stress is $\sigma_{max} = 75$ MPa and stress ratio $R = 0.1$.

Firstly, different laminate stacking sequences are examined for the CFRP straps (same considerations can be made for GFRP), then the best lay-up configurations are compared with straps made of titanium alloy and GLARE.

Table 6.1: Mechanical properties of the strap materials and adhesive employed in the constant weight analysis.

Material	CFRP [‡]	GFRP [†]	GLARE [‡]	Titanium [§]
Type	M21/T800	generic	1	generic
Lamination	$\theta_1/\theta_2/\theta_2/\theta_1$	$\theta_1/\theta_2/\theta_1$	2/1	
t[mm]	4×0.125	$0.125/0.2/0.125$	0.36	0.2
E_1 [MPa]	171000	43000	66000	110000
E_2 [MPa]	17200	8900	54000	110000
G_{12} [MPa]	5100	4500	16000	41353
ν_{12}	0.42	0.27	0.31	0.33
ρ [g/cm^3]	1.8	2	2.52	4.51

[‡] Values from [20].

[†] <http://composite.about.com/library/data/blg-sgepoxy.htm>, access date Dec 2006.

[‡] Values from [153].

[§] Generic properties.

Results for different lay-ups of the carbon-epoxy straps are shown in figure 6.1. Figure 6.1(a) shows that the UD straps provide the lowest crack growth driving force in terms of β , and consequently the longest life (figure 6.1(b)). However, by using the UD straps, disbond failure happens earlier than other strap lay-ups and

in a sudden manner, i.e the strap debonds completely before the substrate fails¹. If a complete strap/substrate disbond is considered as a failure criterion, then the UD strap can not be employed. However, if it is considered that the substrate is able to carry load after disbond until final failure, then UD would be the best stacking sequence (the reasons of complete disbond will be examined later). Similar ranking of stacking sequences are obtained for the glass-epoxy straps. Examining figure 6.1 it can be said that CFRP or GFRP angle-ply laminates are not suitable to effectively retard the crack growth. The best material, if complete disbond is considered unacceptable, is the cross-ply CFRP laminate. However, if complete disbond is tolerated, then the unidirectional CFRP laminate is the best one.

After having studied the CFRP straps, other strap materials are examined and comparisons made among the four candidate materials. Figure 6.2 shows the comparisons in terms of the crack growth driving force coefficients β and the predicted FCG lives. The best one seems to be the CFRP cross ply (CP). In fact, the CFRP UD had already been eliminated because of the largest disbond caused by high stiffness mismatch. It can be seen in figure 6.2(b) that the other good straps are made of GLARE and the titanium alloy.

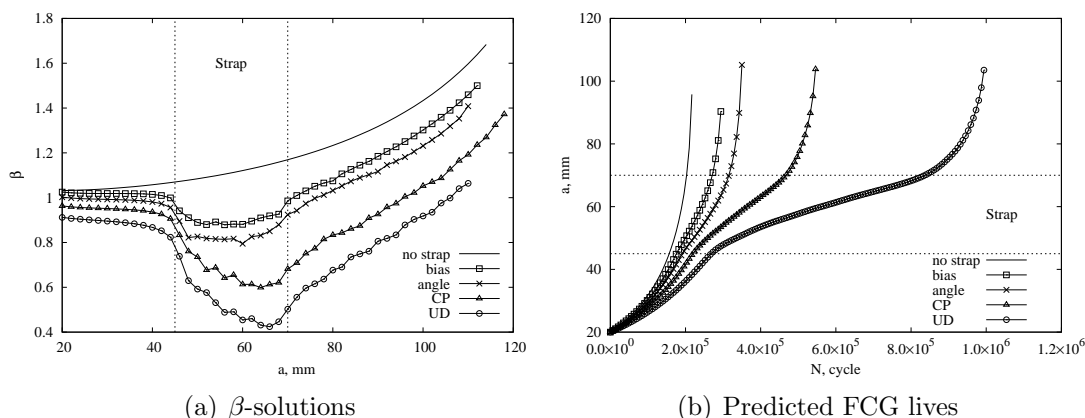


Figure 6.1: M(T) sample with CFRP straps; comparison of different lay-ups: unidirectional (UD) $[0]_4$, cross-ply (CP) $[90/0]_s$, angle $[30/60]_s$, bias $[-45/45]_s$.

This results show that in the absence of TRS the most important mechanical property of the straps is the elastic modulus, and in this constant weight analysis, the ranking is proportional to the specific elastic modulus of the materials. Still two phenomena need to be taken into account in the selection of the strap

¹Disbond is a function of the load and the considerations hereby made are valid for the load examined

material: firstly the cause of critical disbond failure as function of the strap stiffness, secondly the influence of plastic deformation in the straps.

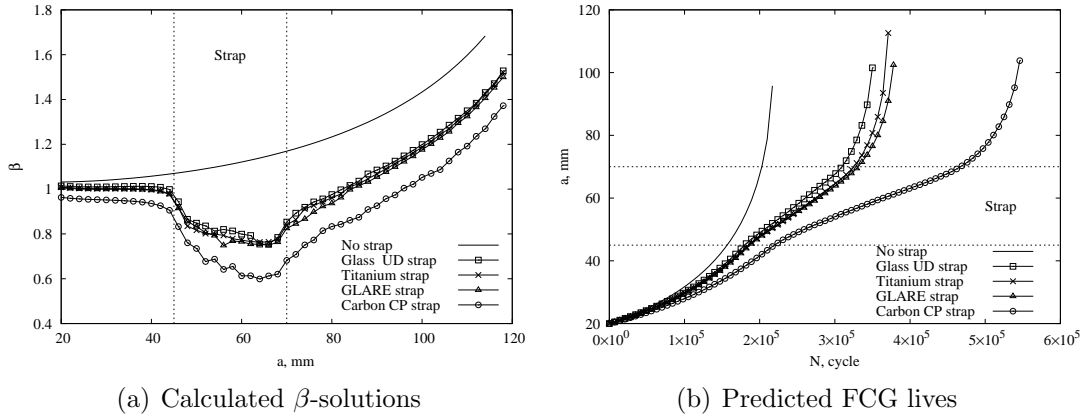


Figure 6.2: Comparison of different strap materials. M(T) sample.

6.1.1.b Critical disbond analysis

The complete disbond shown by the UD CFRP materials is further studied in order to find the causes. The same plate configuration of the previous problem was employed. Two UD CFRP straps of different thickness ($t = 0.25$ mm and 0.5 mm) and one cross-ply strap ($t = 0.5$ mm) are examined under different applied loads. The results are shown in fig.(6.3).

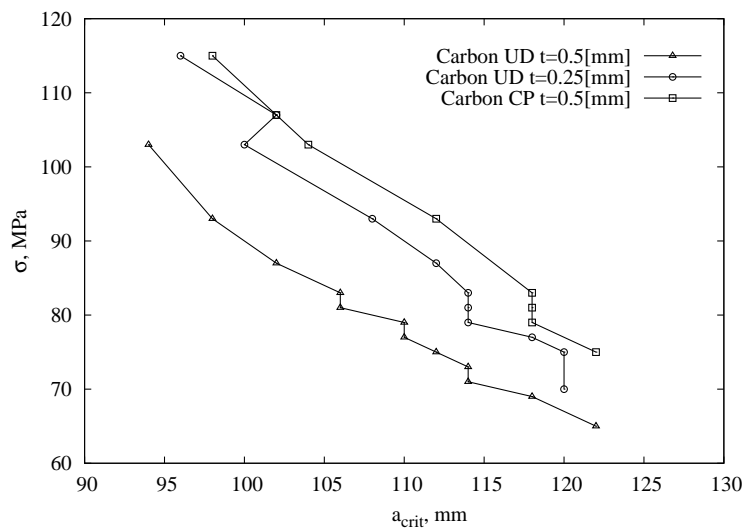


Figure 6.3: Crack length of complete disbond for three different strap configurations under different load values.

For each given maximum applied stress (σ), the critical crack length (a_{crit}) at which the strap complete disbond failure occurs can be found. Intuitively the complete disbond would depend on the mismatching between the stiffness of the aluminum substrate and the strap. Surely, the stiffer the strap, the more load is transferred from the substrate to the reinforcement through the adhesive and, consequently, the adhesive fails earlier. This observation can be demonstrated by calculating the membrane stiffness of the laminates \mathbf{A} as follows [154]:

$$\mathbf{A} = \sum_{k=1}^{k=N_l} \int_{t_{k-1}}^{t_k} \mathbf{C}^k dz = \sum_{k=1}^{k=N_l} \mathbf{C}^k (t_k - t_{k-1}) dz \quad (6.1)$$

where N_l is the number of layers, \mathbf{C}^k the material matrix for the k^{th} -layer, and t_k the thickness of the k^{th} -layer. The value of this matrix in MPa m for the three strap thicknesses and lay-ups yields:

$$\mathbf{A}_{UD0.5} = \begin{bmatrix} 87044 & 3677 & 0 \\ 3677 & 8755 & 0 \\ 0 & 0 & 25590 \end{bmatrix}, \quad \mathbf{A}_{UD0.25} = \begin{bmatrix} 43522 & 1838 & 0 \\ 1838 & 4377 & 0 \\ 0 & 0 & 1275 \end{bmatrix} \quad (6.2)$$

$$\mathbf{A}_{CP0.5} = \begin{bmatrix} 47900 & 3677 & 0 \\ 3677 & 47900 & 0 \\ 0 & 0 & 2550 \end{bmatrix}$$

where $\mathbf{A}_{UD0.5}$, $\mathbf{A}_{UD0.25}$, $\mathbf{A}_{CP0.5}$ are respectively the membrane stiffness for the unidirectional 0.5 mm thick, unidirectional 0.25 mm, and cross ply 0.5 mm laminates.

It must be noted that the stiffest material is the UD ($t = 0.5 \text{ mm}$), but even though a thicker cross ply carbon-epoxy ($t = 0.5 \text{ mm}$) is slightly stiffer than a thinner UD ($t = 0.25 \text{ mm}$), critical disbond happens later for the former than the latter, under the same load. It can be said that critical disbond does not only depend on the longitudinal stiffness of the straps but also on the difference between values A_{11} and A_{22} of its membrane stiffness. This means that in terms of complete disbond, cross-ply or fabric laminates should behave better than unidirectional ones but, on the other hand, more plies are necessary for the CP to obtain similar stiffness as the UD laminate. To summarise, UD composites should be employed to obtain a life target but if they suffer from complete disbond under the given load and geometry then, cross-ply or fabric laminate should be employed to achieve that life target without critical disbond failure.

6.1.1.c Metallic straps: effect of plastic deformation

Initially in the project, the plan was to use commercial grade 2 titanium instead of aeronautical titanium alloy Ti 6Al-4V (commercial grade 5). The main difference in mechanical properties between these two materials is the different yield strength (table 6.2).

Table 6.2: Mechanical properties of titanium alloy straps.

Material	Titanium Grade 5, ELI, Annealed Ti 6 Al 4 V	Titanium Grade 2 CP Titanium
t [mm]	0.2	0.2
E_1 [MPa]	113800	105000
G_{12} [MPa]	42400	38300
ν_{12}	0.342	0.37
ρ [g/cm ³]	4.43	4.51
σ_y [MPa]	790	275
σ_{uts} [MPa]	860	344

Source: www.aerospacemetals.com/titanium.html

For the same configuration of the previous problem and under the same cyclic load, the two straps are studied by using an elasto-plastic FE analysis to take into account of yielding. The straps are modelled as elastic-perfectly plastic materials. The β -solution and FCG life are shown in figure 6.4.

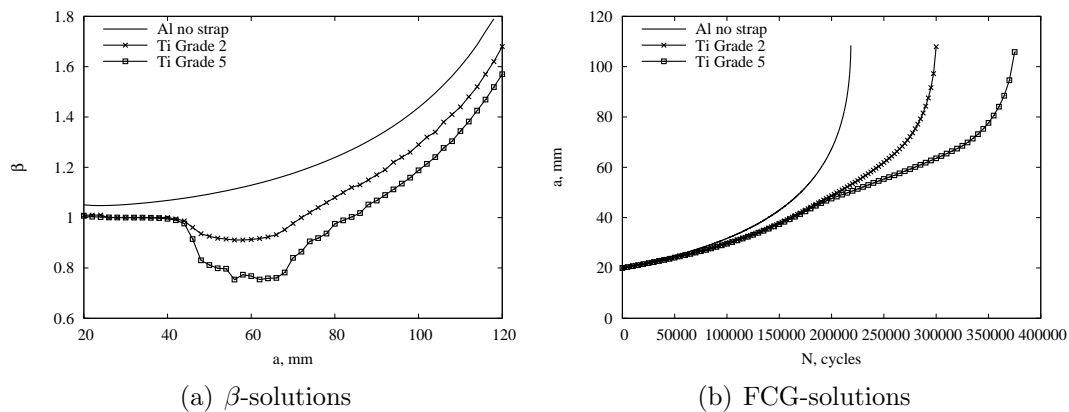


Figure 6.4: Comparison of grade 5 titanium and grade 2 titanium straps.

Grade 5 titanium is more effective in retarding crack propagation. This is because it can carry more load compared to the grade 2 titanium. By observing figure 6.5 it can be seen that grade 5 titanium reaches a von Mises stress of 550 MPa

on most of the strap whereas the grade 2 titanium strap cannot carry more than its yielding stress 275 MPa. This means that its bridging effect is limited to its yield stress. Moreover, it is very likely that the grade 2 titanium strap breaks under low-cycle fatigue. From this analysis it can be deduced that high strength material are better straps.

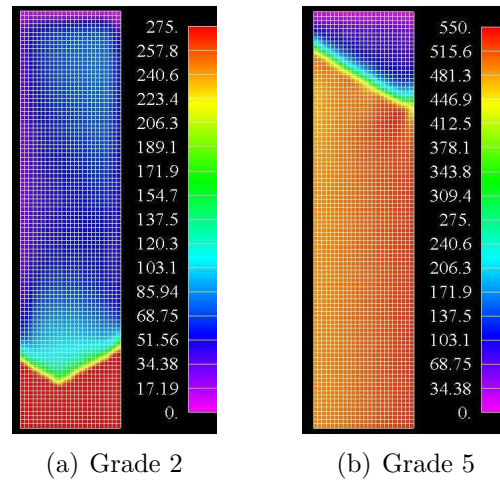


Figure 6.5: Comparison von Mises stress in titanium straps for a crack length $a = 124$ mm

6.1.2 Strap dimension

Different strap dimensions and positions are studied for the cross ply CFRP strap on the SENT specimen showed in figure 5.7(b) made of aluminium alloy 7085-T7651 (table 5.2) with thickness of 10 mm. The maximum applied stress $\sigma = 53.57$ MPa and the stress ratio $R = 0.1$. In order to classify the different strap configurations, the notation defined in section 5.2.1 is used. The goal is to maximise the number of cycles to failure (N_c), compared to that of the unreinforced plate (N_{Al}), and minimise the strap weight (m) by working on the strap width (w), distance (d) and thickness (t). A parameter (e) is proposed. It indicates the percentage of life improvement with respect to the plain panel per unit of strap mass.

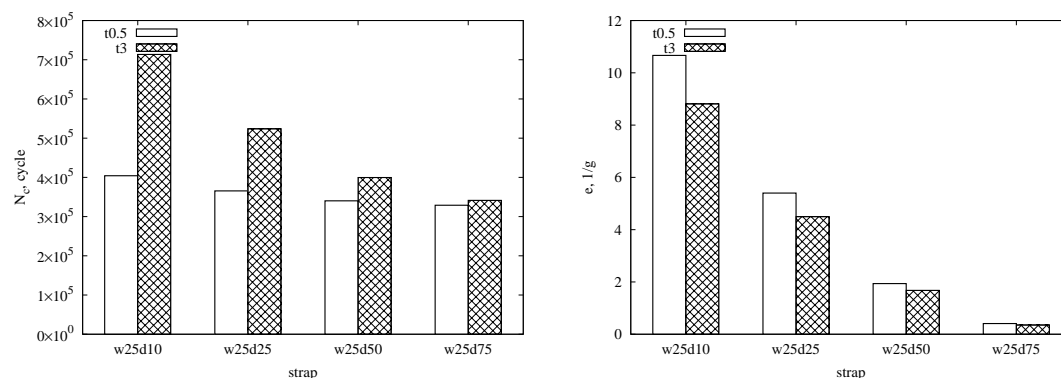
$$e = \frac{\frac{N_c - N_{Al}}{N_{Al}} 100}{m} \quad (6.3)$$

To limit the interactions between the different parameters and truly understand their effect on the FCG life, each design variable has been studied by keeping

the others constant. The distance d is the simplest and clearest parameter. The results are shown in figure 6.6. Examining figures 6.6(a) and 6.6(b) it can be seen that the closer the strap is to the crack tip the better it behaves in terms of both e and N_c . Obviously, having a strap very close to the crack tip would require short gap between one strap and the others, i.e. small strap pitch in the wing box.

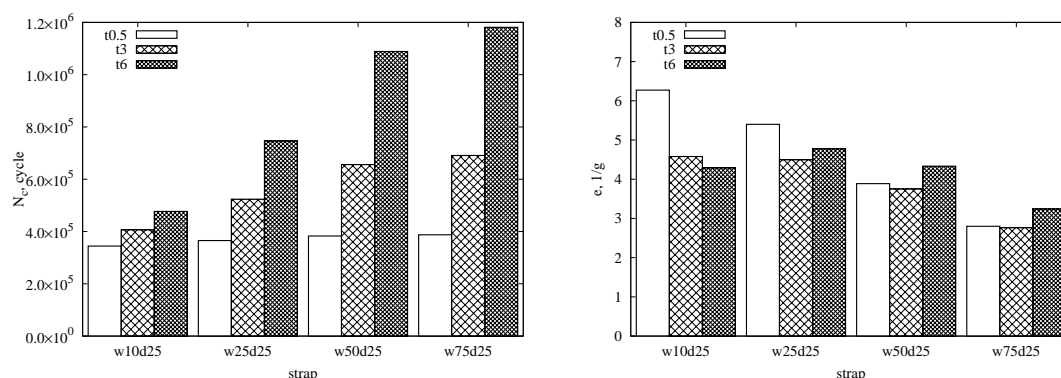
Having assessed the effect of the distance, it is decided to keep it constant at 25 mm from the crack tip and study the other two parameters.

The effects of strap thickness t and width w are more complicated. Figures 6.6(c) and 6.6(d) show that e and N_c are in an opposite trend.



(a) FCG life for different strap distances (d)

(b) e for different strap distances (d)



(c) FCG life for different strap widths (w) and (d) e for different strap widths (w) and thicknesses (t)

Figure 6.6: Influence of different strap positions and dimensions. SENT sample.

That means that although increasingly wider and thicker straps produce a longer FCG life (N_c), the “efficiency” of the straps decrease, i.e. the percentage of life increment for unit of strap mass (e) decreased. Thus, this analysis demonstrates that by increasing the strap dimensions the FCG life of the structure keeps improving. Unfortunately, the weight of the strap also increases and an optimum

in terms of maximum life increment and minimum weight can not be found. The problem must be reformulate in order to find a meaningful solution. The question is: what is the lightest strap dimension which can make the structure reach a given life target? This question is addressed in section 6.3 by the design graph.

6.1.3 Stiffness ratio

From the above results it can be inferred that the important design parameter is the stiffness of the strap in the direction perpendicular to the substrate crack propagation. The stiffness of a strap is associated with the product of the Young's modulus (E) and the cross section area. In fact, a stiffer strap is able to reduce the crack-tip SIF (or β) when the crack enters the strap region and propagates under the strap, the so-called strap stiffening effect. This phenomenon is similar to the crack growth in a skin-stringer panel, in which case the stiffness of the stringer (riveted to the skin sheet) makes the β function reduce. For example the relative stiffness S is defined as the ratio of the in-plane extensional stiffness of the stiffener and the skin sheet and is given by [31]:

$$S = \frac{AE_2}{btE_1} \quad (6.4)$$

where, A is the cross-section area of the stiffener, t the thickness of the skin sheet, b the stiffener pitch, E_1 and E_2 the Young's modulus of the sheet and stiffener material, respectively. In a similar way, a parameter to quantify the stiffening effect of the strap was defined by Schjive [17] for bonded reinforced plates:

$$\mu = \frac{\sum_{i=1}^n E_r^i A_r^i}{E_s A_s + \sum_{i=1}^n E_r^i A_r^i} \quad (6.5)$$

where E_r , E_s , A_r , A_s correspond to the longitudinal Young's modulus and cross section area of reinforcement strap and substrate respectively, n is the total number of straps. The stiffening effect can be seen in figures 6.1(a) and 6.2(a); when the crack tip is before and under the strap the β solution is lower than the un-reinforced plate. Another positive effect is the so-called bridging effect. When the crack tip has passed the strap region, the strap will produce a bridging (or traction) force to reduce the crack opening displacement, thus a reduction in the β value (refer to figures 6.1(a) and 6.2(a)). This effect can also be characterised by the stiffness ratio (equation 6.5).

Stiffness also contributes to other mechanisms involved in bonded structures as summarised in table 4.1. For example, disbond failure at the interface due to shear load transfer. A stiffer strap will cause a bigger stiffness mismatch with the substrate material and hence a larger disbond, due to the fact that more stress will be transferred from the substrate to the strap. A trade-off between strap stiffness and adhesive toughness is necessary during the selection of the strap materials.

6.1.4 Sensitivity analysis

6.1.4.a Strap stiffness

The sensitivity strap stiffness on the stiffening effect is firstly analysed. A way to quantify the stiffening effect is by checking the substrate stresses. For this study the SENT plate shown in figure 5.7(b) without the notch is used. The strap geometry is $w20t2l200$. Three different strap material elastic moduli are analysed: 40, 80 and 140 GPa. The respective stiffness ratio is $\mu = 0.012$, 0.039 and 0.058. TRS are not consider in order not to interfere with the bridging effect.

Results of the analysis are showed in figure 6.7. The stress reduction in the substrate is proportional to the stiffening ratio.

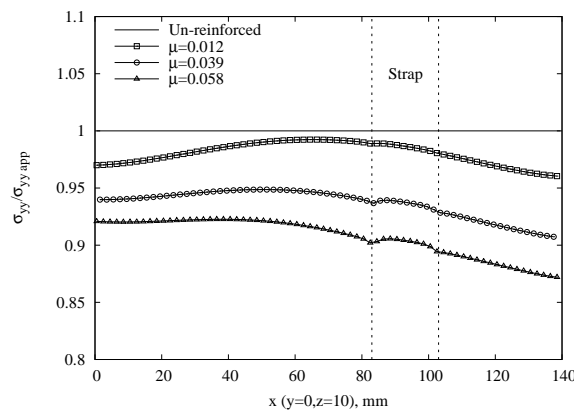


Figure 6.7: σ_{yy} stress in the substrate as a function of the strap stiffness: stiffening effect.

It is also interesting to check the stress in the straps. σ_{yy} stress distribution is plotted along the strap length for different strap moduli in figure 6.8(a). Again the load carried by the strap is directly proportional to the stiffening ratio.

Looking at the stress contour (figure 6.8(b)) in the strap, it is interesting to notice how the stress goes to zero towards the upper free edge of the strap. This suggest that the use of tapered straps would be a good solution in terms of weight and stresses.

The stresses in the adhesive layer are also computed for the same strap elastic moduli. The shear stress in the adhesive is shown in figure 6.9.

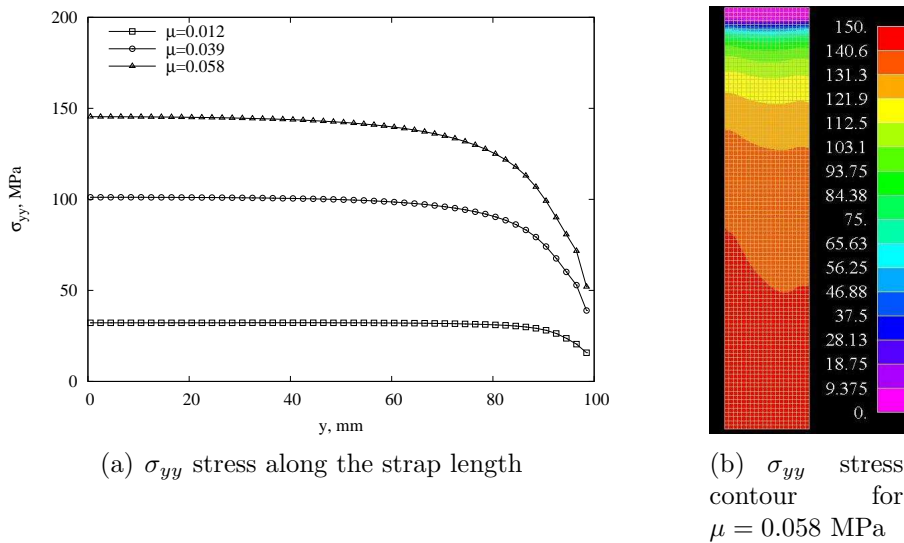


Figure 6.8: Stress carried by the strap as a function of the stiffening ratio. Applied stress 70 MPa.

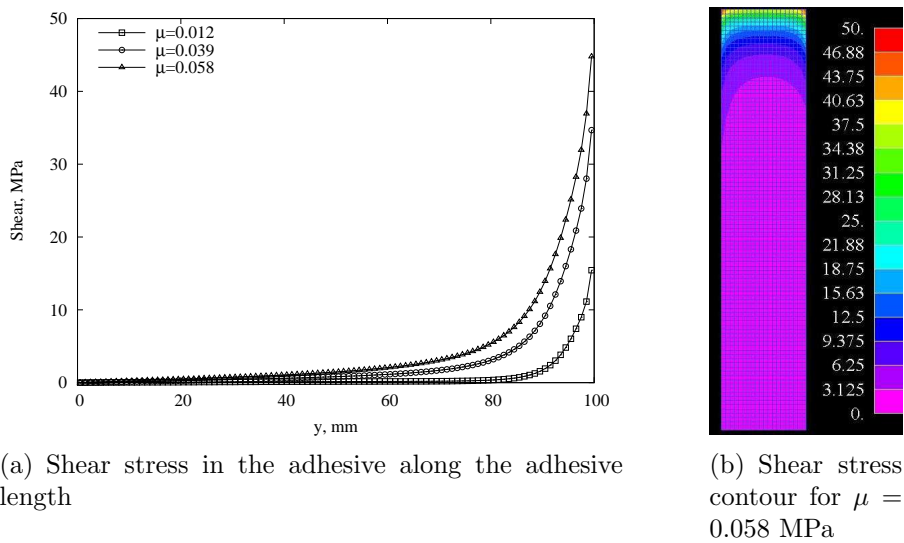


Figure 6.9: Shear stress in the adhesive as a function of the stiffness ratio. Applied stress 70 MPa

Firstly it can be observed that increasing the stiffness ratio not only increases the bridging and stiffening effect but also the shear stress in the adhesive, i.e. promote delamination. It is also interesting to note that the highest shear stress is reached at the top corners of the straps in the case of an un-cracked substrate. This explains the second disbond front shown by some of the experimental tests (e.g. figure 5.11(b)). This also confirms the fact that a stiffer strap material is more efficient to retard crack propagation, but the adhesive shear stresses is higher and it is necessary to compromise between strap stiffness and adhesive strength in order not to incur in premature and sudden failure of the adhesive.

The sensitivity of the FCG life to the strap elastic modulus is also important. For this study the M(T) plate showed in figure 5.7(a) is used. The strap dimensions are $w20d2.5t5l180$. Three different strap elastic moduli are used: 40, 70 and 140 GPa. The maximum applied stress is 60 MPa. This effect is shown in figure 6.10. The FCG life of the reinforce panel is improved of 56 %, 79 % and 122 % respectively by the 40, 70 and 140 GPa straps. It seems that life is not strongly sensitive to the elastic modulus of the straps. This is true, though, just for this maximum applied load (60 MPa).

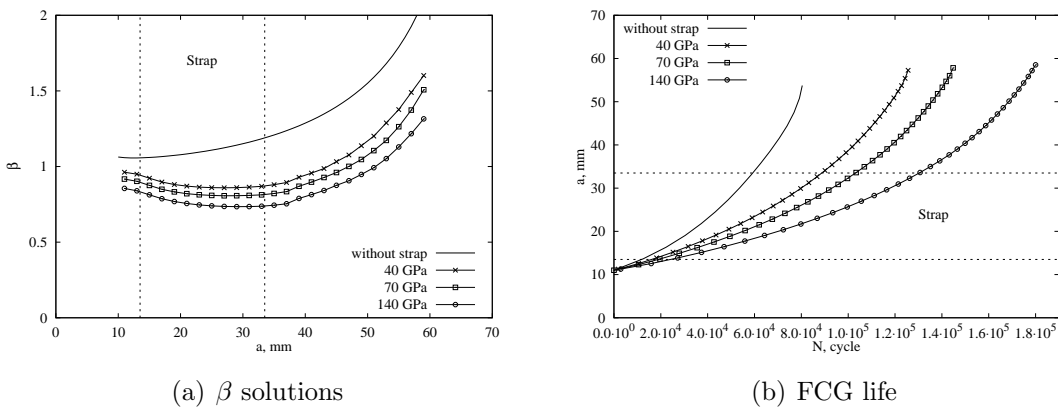


Figure 6.10: Effect of strap elastic modulus on the FCG live. Strap dimension $w20d2.5t5l180$. No TRS. Applied stress $\sigma_{max} = 60$ MPa.

In figure 6.11 the FCG life versus the strap elastic modulus for two different maximum applied loads (30 MPa and 60 MPa) is shown. Two things are worth noticing. Firstly at “low” applied load FCG life is more sensitive to the strap elastic modulus. Secondly, bonded straps are more efficient at “low” applied load. In fact the same strap dimension and stiffness cause a larger life increment

when the applied maximum load is “lower”².

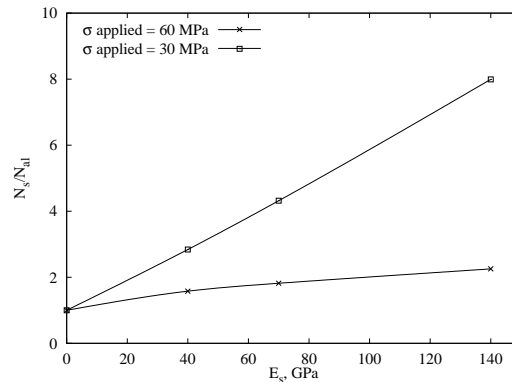


Figure 6.11: Effect of strap elastic modulus on the FCG live for different applied stresses.

6.1.4.b Influence of adhesive properties

The mechanical properties of the adhesive also influence the FCG life of the structure.

The effect of the critical strain energy release rate in mode II (G_{IIc}) is shown in figure 6.12 for the specimen geometry studied in the previous section at a maximum applied stress of 60 MPa. It can be seen that in terms of FCG life the difference caused by different toughness is not very important. This is true for this applied load, for a lower applied load the effect is bigger. In fact, a difference in β -solution is more important when the applied load is low since it acts for more life cycles.

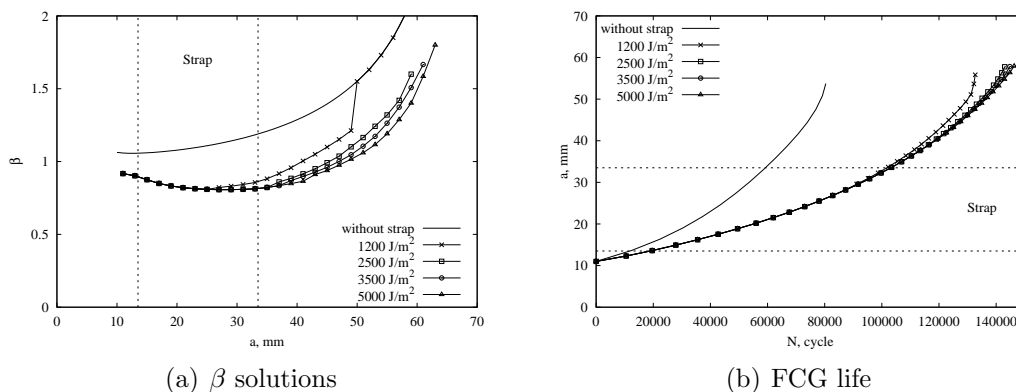


Figure 6.12: Effect of adhesive toughness (G_{IIc}) on FCG life. Strap dimension $w20d2.5t5l180$. no TRS. Applied stress $\sigma_{max} = 60$ MPa.

²More correctly relatively low SIF instead of load (refer to section 6.2.2)

In figure 6.13 FCG lives are plotted against G_{IIc} . It shows that the effect of the adhesive toughness is more important for small values.

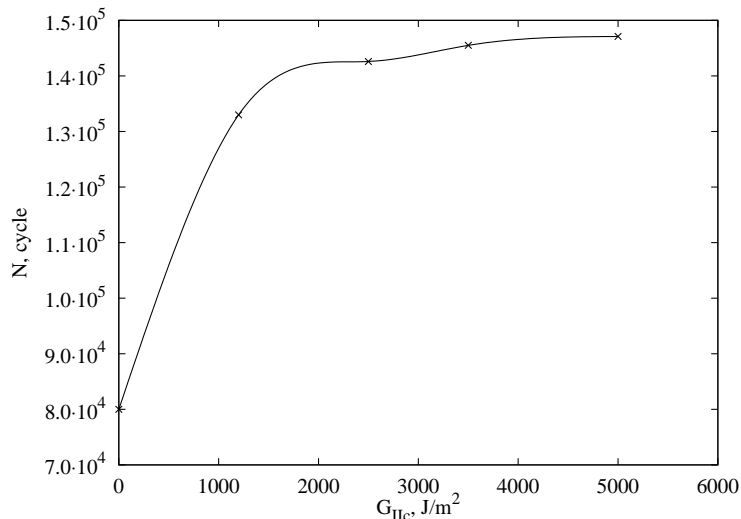


Figure 6.13: Effect of the critical strain energy release rate of the adhesive on the FCG life

In order to understand the physical limits due to the adhesive choice, FCG calculated by using mechanical properties of an ideal adhesive at low and high applied load and for two different strap stiffness are plotted in figure 6.14. The ideal adhesive is represented as a rigid link between strap and substrate which is not subjected to failure.

Two important observations can be made by analysing the graphs in figure 6.14.

1. Comparing figure 6.14(a) with 6.14(b) and figure 6.14(c) with 6.14(d) it is confirmed that the effect of the adhesive properties is more important at low applied load.
2. Comparing figure 6.14(a) with 6.14(c) and figure 6.14(b) with 6.14(d) it can be seen that the effect of the adhesive is more important when stiffer straps are used.

Consequently tough and stiff adhesive are more suitable to bond selective reinforcements. The life improvement brought by this ideal adhesive is not substantial for low stiffness strap and elevated applied loads but it is increasingly higher for stiffer strap and low applied load.

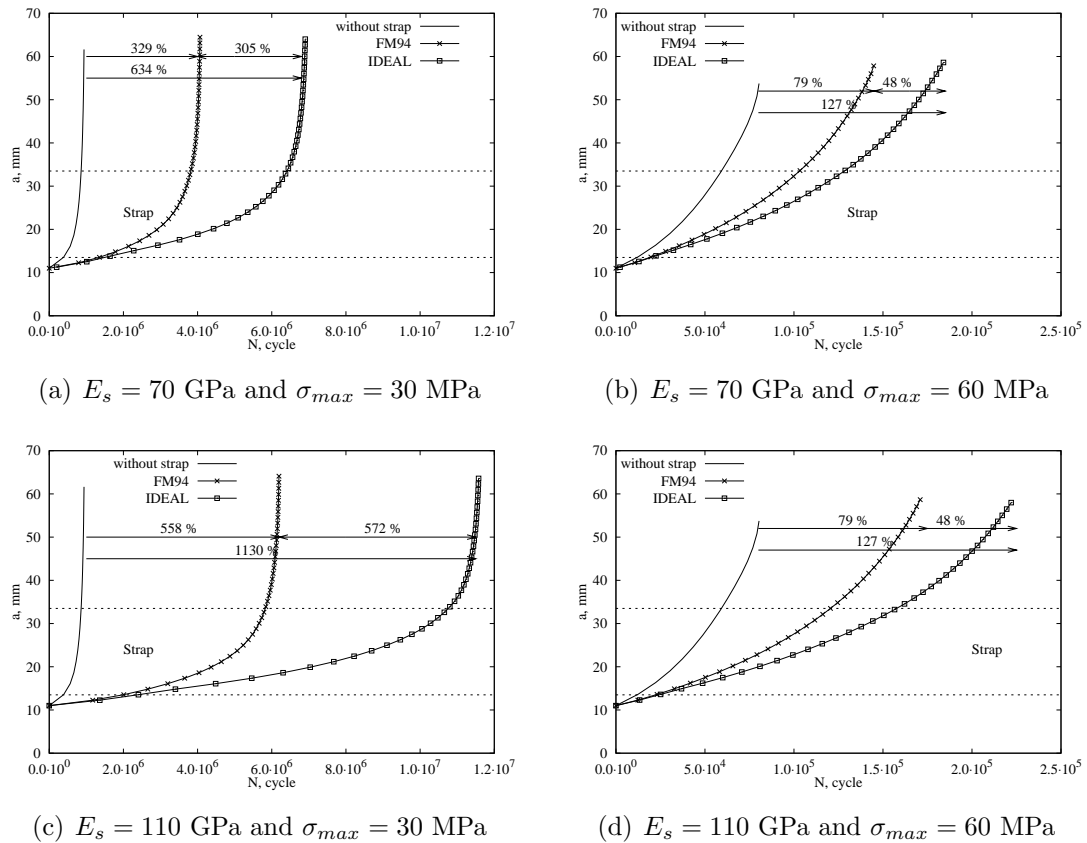


Figure 6.14: FCG lives due to ideal adhesive ($G_{IIc} = \infty$) at low and high applied load $\sigma_{max} = 30$ and 60 MPa for two different strap stiffness $E_s = 70$ and 110 GPa. Strap dimension $w20d2.5t5l180$. No TRS.

6.2 Elevated temperature cure

In this section firstly the effect of the TRS on the FCG life is analysed, then parametric studies to find a way to reduce TRS are carried out. In the following analyses each of the mechanisms described in table 4.1 influences the life and interacts with the other, making result interpretation difficult.

6.2.1 TRS effect

The SENT plate shown in figure 5.7(b) was reinforced by a GFRP strap of dimension $w20d5t2l200$. Two analysis are carried out: adhesive cured at room temperature (no TRS are generated) and adhesive cured at elevated temperature.

The maximum applied stress is $\sigma_{max} = 18.57$ MPa.

The TRS in the substrate are shown in figure 5.13(e). Although they are low the effect on the FCG life of the structure can be seen in figure 6.15. The fact that tensile TRS reduce the life is known from the literature and it is not the main observation of this analysis. From figure 6.15(a) it can be seen how TRS are more harmful at the beginning of the crack propagation than near to the end. This effect was also found in the experimental test and confirmed by many analyses [142]. The reason of this effect are explained in the next section.

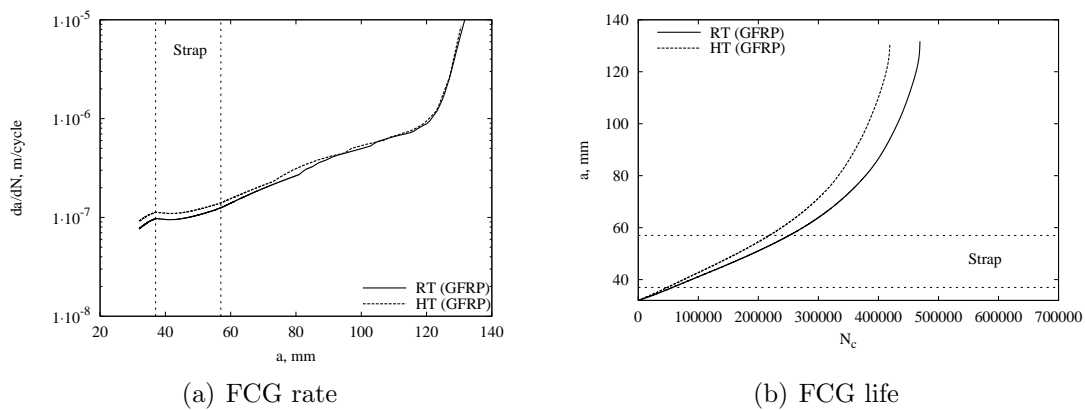


Figure 6.15: Effect of TRS for a GFRP strap of dimension $w20d5t2l200$ loaded at $\sigma_{max} = 18.57$ MPa

6.2.2 Effect of TRS at high and low applied load

The SENT plate shown in figure 5.7(b) was reinforced by a titanium strap of dimension $w20t2d20l200$. The structure was cured at elevated temperature with the TRS distribution being shown in figure 5.13(a). This structure was load by two different load spectra: $\sigma_{max} = 60$ MPa (high load) and 18.57 MPa (low load), $R = 0.1$.

Figure 6.16 shows the SIF ranges and effective R-ratios. For the higher applied load cases the effective R-ratio is lower because the TRS are a relatively smaller percentage of the applied load than for the low applied load case.

In figures 6.17 the FCG rate versus the crack length is plotted for the two cases compared with the respective case without TRS. It is worth noticing that the effect of the TRS is much stronger at the lower applied load where the difference in FCG rate between no TRS and TRS cases is large. Vice versa, at higher applied load level the effect of TRS is almost non existent.

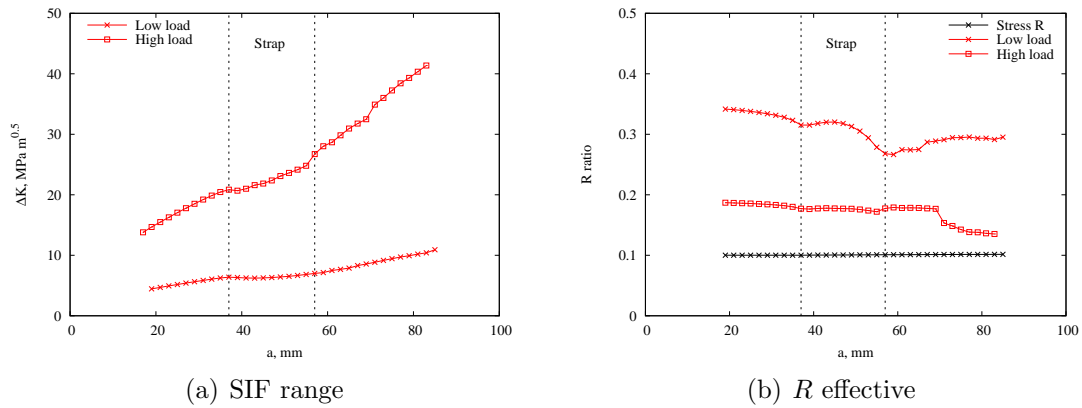


Figure 6.16: Comparison of SIF ranges and R ratios at low and high applied load for a SENT plate reinforced by titanium strap of $w20t2d5l200$ strap cured at elevated temperature.

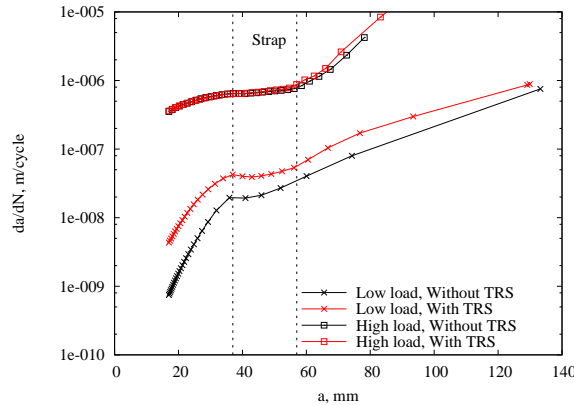


Figure 6.17: Effect of the TRS on FCG rates at low and high applied load, with and without TRS.

This could be explained by a lower effective R -ratio in the high load case, but it is not enough to explain the complete disappearance of TRS effect.

The real reason dwells in the FCG rate material law of the substrate. At low applied load, the SIF is between $5 - 10 \text{ MPa}\sqrt{m}$. From figure 5.5, this SIF range falls in slow crack growth (section 2.3). This region of the material law is also where the effect of R -ratio is important. The SIF range for the high load case is between $15 - 40$ then it falls in the region II or the so-called Paris regime where the effect of the R -ratio is small. What is important then to define whether the TRS are harmful or not, it is not the applied load, but more properly, the SIF range values at which the structure is subjected.

At low applied ΔK the material law shows large sensitivity to the R -ratio and the curves for the same R -ratio are more steep than that in region II. The R -ratio

sensitivity is to blame for the larger effect of the TRS at lower applied load and at the beginning of the FCG life (section 6.2.1). The slope of the curve influences the sensitivity of the FCG life to the strap stiffness at low or high applied load (or more correctly low and high SIF range) as shown in section 6.1.4.

These considerations are important in the design of the strap and the material law of the substrate should be taken into account as a design factor.

6.2.3 Effect of strap dimension on TRS

The effect of strap dimensions on the TRS is analysed by studying the SENT plate (figure 5.7(b)) reinforced by a titanium strap. For each configuration, TRS (σ_{yy}) at $z = 7.5$ mm from the bottom of the plate (figure 5.12) for the initial crack length of 17 mm and residual SIF (K_{res}) versus crack length are plotted. The latest takes into account of TRS redistribution.

The strap thickness effect ($w20d20t2, 4, 6l200$) is shown in figure 6.18. The thicker the strap is the higher the TRS are. It should be noted that, although between 2 and 4 mm the TRS are considerably higher, between 4 and 6 mm their increment is marginal.

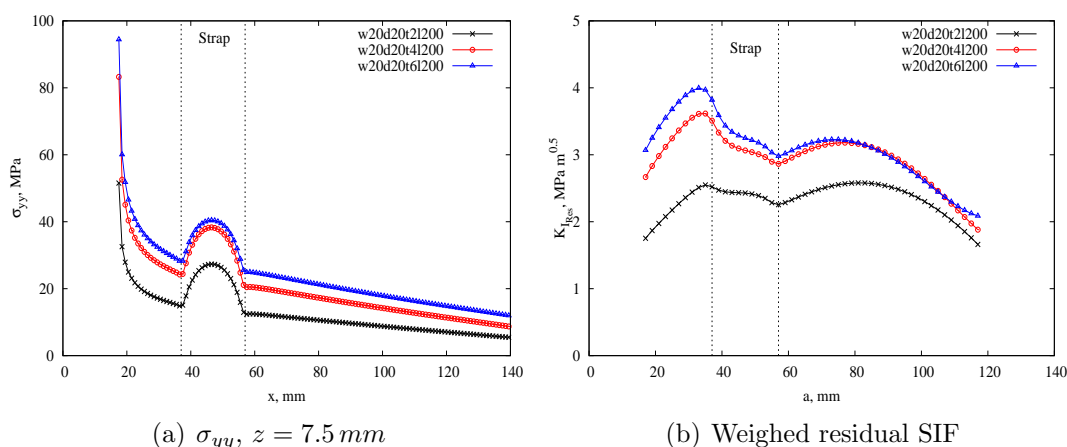


Figure 6.18: Comparison of TRS and residual SIF for straps of different thicknesses $t = 2, 4, 6$ mm.

In figure 6.19 the width effect ($w20, 60, 100d20t2l200$) is shown. The wider the strap is, the higher the TRS are, but the difference in terms of residual SIF is really small between $w60$ and $w100$.

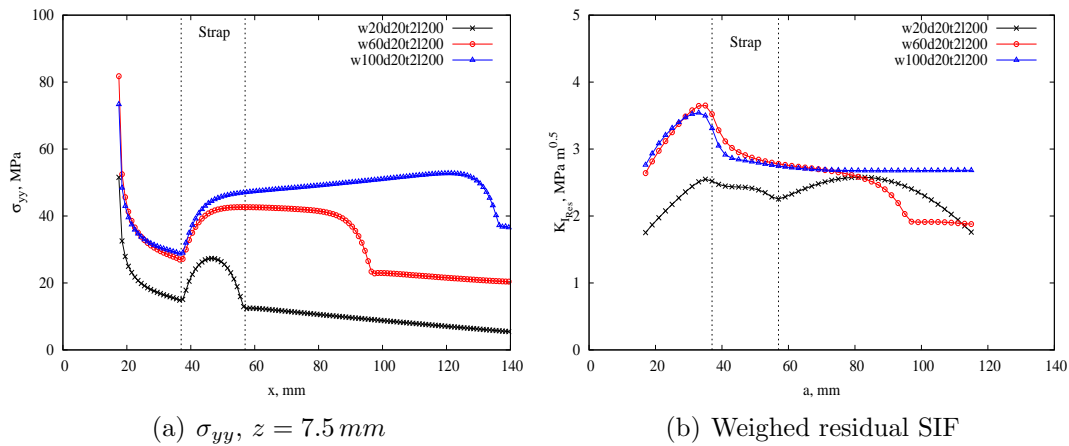


Figure 6.19: Comparison of TRS and residual SIF for straps of different widths $w = 20, 60, 100 \text{ mm}$.

The effect of strap length ($w20d20t2l200, 160, 90$) is examined in figure 6.20. The strap length does not influence the TRS much, although a decrease in SIF can be seen for the shortest length 90 mm.

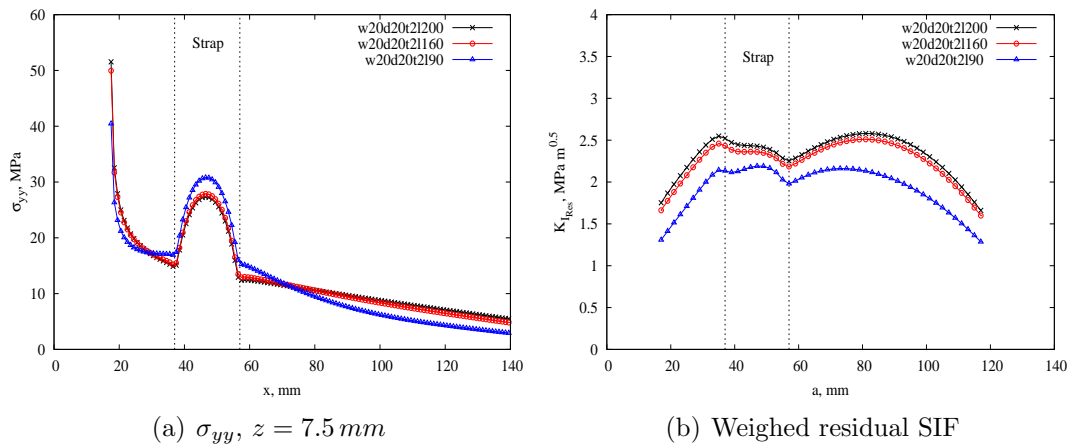


Figure 6.20: Comparison of TRS and residual SIF for straps of different lengths $l = 200, 160, 90 \text{ mm}$.

In figure 6.21 three different strap geometries are examined by keeping the strap cross section area constant. Since the material is the same, the strap stiffness is the same. It can be seen that, in terms of residual SIF, the wider and thinner the strap is, the lower the SIF. This consideration is true for TRS effect, but it might not be true in terms of FCG life where all the involved mechanisms (table 4.1) must be taken into account.

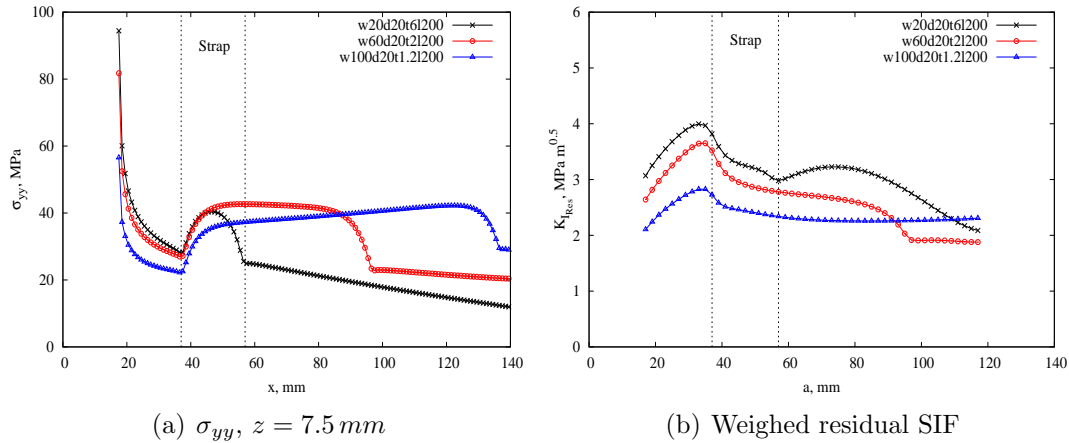


Figure 6.21: Comparison of TRS and residual SIF by keeping the strap cross section area constant.

6.2.4 Strap material

Four candidate strap materials are studied as reinforcement for the SENT plate (figure 5.7(b)). The mechanical properties of plate and strap materials can be found in tables 5.2 and 5.3. The applied maximum stress is 18.57 MPa and R -ratio 0.1. The straps are all of the same dimensions $w20t2d5l200$. In figure 6.22, FCG rate and life are plotted.

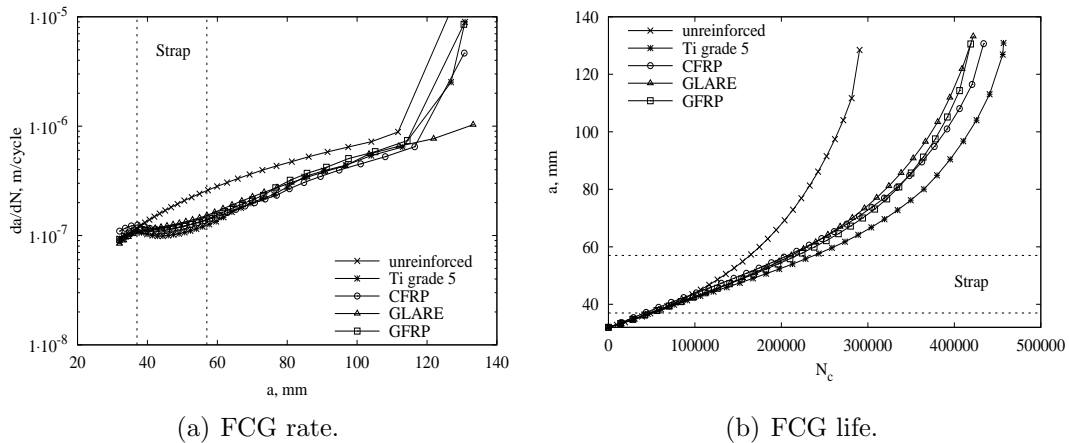


Figure 6.22: Comparison of FCG rate and life for different strap materials with the same dimension $w20t2d5l200$. Applied maximum stress 18.57 MPa, $R = 0.1$. Adhesive cured at 120°C .

The best strap material from this analysis is titanium. It should be said though that titanium is also one of the heaviest strap.

CFRP³ is instead penalised by the high TRS generated in the substrate. GLARE and GFRP, although generate the lowest TRS, are less effective than titanium since they have a lower elastic modulus.

This material ranking is true only for the considered specimen geometry and applied stress level. Due to the several interactions between all the effects specific analysis should be carried out case by case to find the best strap material.

6.2.5 Strap dimension

The same configuration of the previous section is used in this study. The used strap material is GLARE.

The effect of different strap widths ($w_{20, 60, 100}$) is showed in figure 6.23. In the presence of TRS, the wider the strap is, the longer the life.

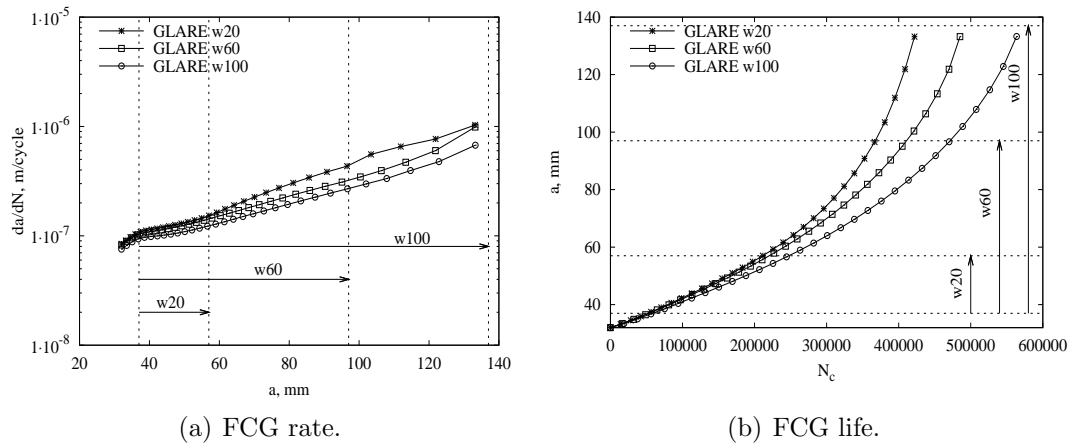


Figure 6.23: Effect of strap width in the presence of TRS. GLARE strap $w_{20, 60, 100}$. Applied maximum stress 18.57 MPa, $R = 0.1$. Adhesive cured at $120^\circ C$.

In figure 6.24 the FCG rate and life obtained by 3 different GLARE straps with the same cross section area (same stiffness ratio) is shown. The life improvements obtained by the three strap geometries are almost identical because the stiffness ratio is identical and TRS effect is small for GLARE straps. Analysing the crack propagation in detail, it can be seen that the narrow and thick strap ($w_{20}t_{5.4}$)

³Although CFRP results to be the second best from this numerical analysis, the experimental life was actually shorter than the predicted one. If the experimental life is considered, CFRP performed worse than GLARE

shows the higher crack retardation at the beginning but then, extensive disbond reduces the crack retardation. Consequently, the final life of the structure is shorter than the one obtained by the $w30t3.6$ strap. The wide and thin strap solution ($w60t1.8$) shows the smallest life improvement.

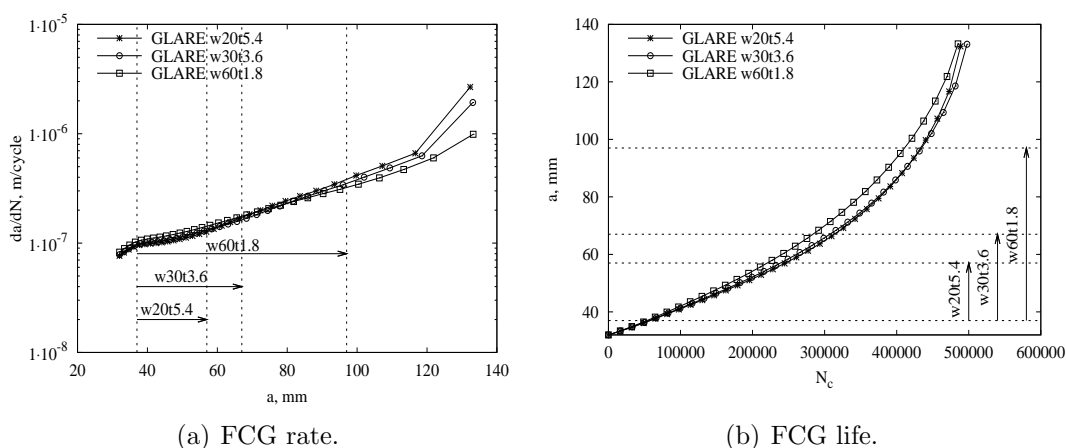


Figure 6.24: Comparison of FCG rate and life for constant cross section area GLARE straps. GLARE straps $w20t5.4d5l200$, $w30t3.6d5l200$, and $w60t1.8d5l200$. Applied maximum stress is 18.57 MPa and R -ratio 0.1. Adhesive cured at high temperature.

Again this results are true only for the considered specimen geometry, strap material and applied load spectrum. Due to the several interactions between all the effects, specific analysis should be carried out case by case to find the best strap material. In the next section a method to find the best strap dimension and material is described.

6.3 Design graph

The design graph is a diagram showing the relation between strap dimension variables and fatigue life and can lead the designers to the best strap choice for a given life target. Figure 6.25 is an example.

The x -axis shows the width ratio (w_r/w_s =strap width/ substrate width). It has two y -axes. The left one shows the percentage of life increment ΔN (Eq. 6.6),

and the right gives the percentage of mass increment Δm (eq. 6.7).

$$\Delta N = \frac{N_r - N_s}{N_s} \times 100 \tag{6.6}$$

$$\Delta m = \frac{(m_r + m_s) - m_s}{m_s} \times 100 = \frac{m_r}{m_s} \times 100 \tag{6.7}$$

where N_r is the FCG life of the reinforced plate, N_s the FCG life of the substrate without strap, m_r the weight of the strap and m_s the weight of the substrate.

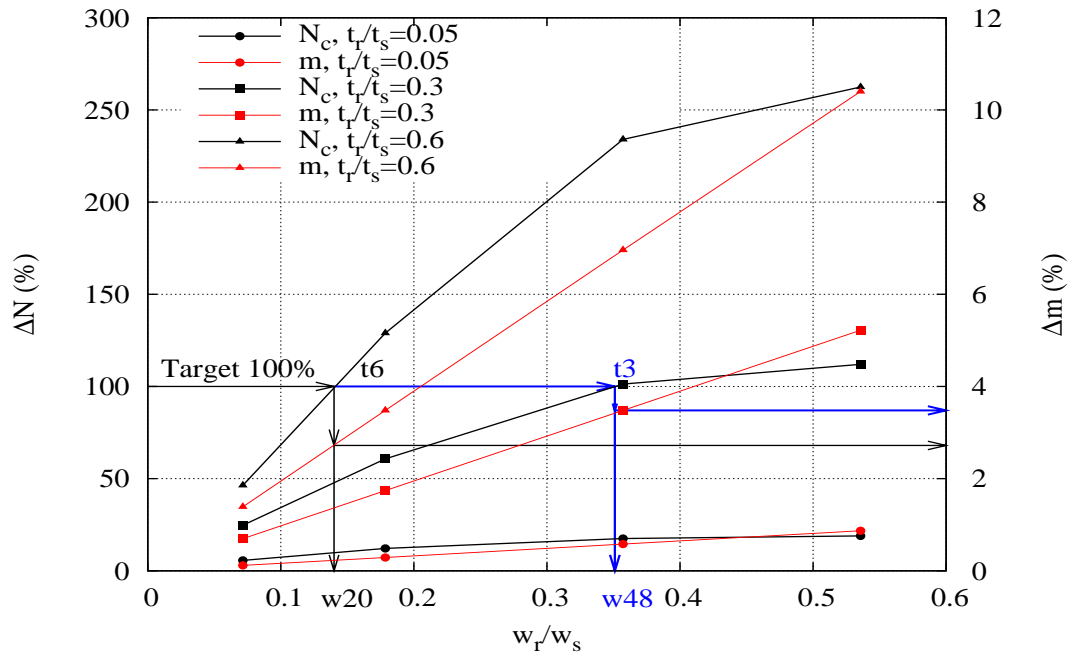


Figure 6.25: Example of using the design graph to find strap geometry (CFRP cross ply)

In the graph there are three pairs of curves. Each pair refers to a specific thickness ratio (t_r/t_s =strap thickness / substrate thickness) and is indicated by a different symbol (triangles, squares, circles). Each pair has two curves, the black line refers to the life increment and is read on the left axis; the red line refers to the mass increment and is read on the right axis.

The example shown in figure 6.25 is for a CFRP strap bonded to a SENT plate (figure 5.7(b)) under a maximum applied stress of 18.57 MPa and $R = 0.1$. The adhesive is cured a room temperature and there are no TRS in the substrate. This example is explained as follows. If a life increment of 100% is sought, two solutions can be found, i.e. $w20d25t6$ and $w48d25t3$ (see arrows in figure 6.25). Between these two solutions the lighter one is immediately identified,

i.e. *w20d25t6* with a weight gain of 20g, or nearly 3% weight increment. It is interesting to notice that for this analysis a narrow & thick strap shows to be more effective than a wide & thin one.

To summarise, using the design graph the lightest strap dimension to reach a life target can be found. If a design graph is build for each candidate strap material, the lightest strap configuration for each material can be found. Then, by comparing the weights of the optimums for each material, the lightest strap material and dimension to achieve a given life target is found.

6.4 Design guidelines

Building the design graph for each candidate strap material is time consuming. In this section some design guidelines for the straps are given so that, depending on the structure and applied load spectrum, only the design graphs for the most promising materials and strap dimensions need to be built. These guidelines are based on the observation of the parametric and sensitivity study results presented in the previous sections.

In designing a strap reinforced structure the following points should be considered:

- Stiffer strap materials offer higher bridging effect.
- The coefficient of thermal expansion of the strap material should be as close as possible to that of the substrate material.
- High strength materials make better straps.
- Fatigue insensitive materials make more durable straps.
- Tough and stiff adhesives cured at the lowest possible temperature are more suitable for these strap reinforced structures.
- The FCG rate law of the substrate material should be considered for the choice of the strap material and dimensions; in the case of *AA7085-T7651* substrate where the effect of the *R*-ratio is small in region II and III⁴ (figure 5.5), the strap material should be chosen also based on the applied load

⁴Many materials show a weak dependency on the *R*-ratio in the region II or Paris region; that is the reason why Paris law does not include the *R*-ratio effect.

spectrum. For low applied SIF range, the effect of TRS is more important so the choice of the material should be based on that criterion. For high applied SIF range, TRS effect is small so materials with lower CTE and higher stiffness can be used. In this analysis the effect of ground-air-ground thermal load cycles is neglected.

Following these guidelines the best strap material is the GLARE thanks to its high CTE, medium stiffness, and the excellent fatigue properties. Aluminium straps are also good but they are fatigue sensitive and without a validated predictive tool to predict failure of the strap under fatigue, its use is unadvisable. Another good material for medium range applied SIF values is titanium alloy despite its weight penalty.

For what concerns the best strap dimensions, the following guidelines might help in the design:

- The wider and thicker the straps are, the larger the life increment.
- The closer the straps are to the initial crack tip, the better; unfortunately that impose a short strap pitch, thus higher weight penalty.
- Narrow and thick straps are usually better than wide and thin if they are applied at the same distance from the initial crack tip when TRS are not present. If there are TRS, TRS effect is lower for wide and thin straps since the tensile stresses are redistributed further away from the crack tip. Consequently, it is important to establish wheatear TRS are really harmful or not for the used substrate material, under the applied load spectrum and for the chosen strap material.

These are guidelines for pre-selection of strap materials and dimensions. In order to find the best strap material, it is advisable to produce the design graph for each of the candidate strap material, under the given load spectrum.

It should be also acknowledged that fatigue crack growth life is not the only sizing criterion for aircraft structures, and as a result some of the best solutions for improved crack growth may not be feasible for real design applications. For example, galvanic corrosion is a concern for long-term durability when bonding

CFRP composites to aluminium structures. Another important design criterion is the notch strain to failure limit. Since there may be holes in the aluminium structure as well as in the reinforcement straps, the realistic maximum strain of a metallic wing box at ultimate load is about 2–2.5%. The maximum notch strain to failure of carbon fibre composites is around 0.8–1.0%. Hence if we use a strap that has a blunt notch strain to failure much below that of the metallic structure, we could either risk the failing of strap before reaching the structure ultimate load or have to limit the maximum design strain (and therefore maximum stress) allowable for the metallic structure resulting in very conservative design [155].

Chapter 7

Large-scale integral skin-stringer panels

7.1 From samples to large scale structures

Only small scale samples have been examined and analysed in the previous chapters. This is because tests and models of small scale structures are quicker, simpler, and very useful in identify the mechanisms involved in a phenomenon.

Those tests and models were firstly used to develop a modelling procedure for the problem and secondly to validate the procedure. In fact, in order to validate this technique, a multitude of tests and models were needed and small scale samples offered quick and reliable results.

After validation, parametric studies on samples were carried out to understand which ones are the most important strap design variables, their influence on FCG life improvement, and to narrow down the possible choices of strap materials and dimensions to use on the large scale stringer panels. In fact, a test for a coupon lasts 1 day, while it take more than 1 months for a reinforced large scale stringer panel to break, this makes large number of tests on stringer panels unpractical. Moreover, in terms of modelling time (time to build the model plus time to run it), samples were much less demanding.

The modelling procedure and results obtained on samples are still valid for reinforced large scale panels for the following two reasons:

1. If the SIF of coupons could be accurately computed so that an accurate life

prediction could be obtained (table 5.4), the SIF of larger structures can be computed as well. The accuracy of the SIF is not affected because the principal mechanisms which influence crack propagation (and retardation) are the same (section 4.1).

2. Since the SIF can be computed, for the similitude principle, i.e two structures made of the same material and subjected to the same SIF behave in the same way independently from the dimensions (section 2.3), the life of an integral large scale stringer panel can be computed as well.

Moreover, for the similitude principle, the design guidelines given in section 6.4, obtained by the analysis of coupons, are valid for real structures as well.

The parametric studies presented in the previous chapter helped in selecting the most promising strap materials for the large scale stringer panels, i.e. GLARE and aluminium.

Although the modelling procedure developed, validated, and employed for samples is capable of computing the FCG life of this panel, an accurate FE model needed to be built. The first part of this chapter covers modelling of the un-reinforced configuration (section 7.2). Firstly, the geometry of the panel and the failure scenario are described along with the applied variable amplitude load spectrum. Secondly, the approach to building an accurate and yet simple 2D FE model is described. Stresses and displacements obtained by the 2D model are compared with a 3D FE model to assess the accuracy. Once the 2D FE model is validated, fracture mechanics analysis is carried out. The β solution is computed and the predicted FCG life is validated against experiments.

The second part of this chapter reports the study of the reinforced panels (section 7.3). Four different strap configurations are studied. Stress analyses of the panels at the maximum applied load are carried out to understand how the stresses and secondary bending change by adding the straps and define the stiffening effect due to the straps. Thermal residual stresses are also computed for the two panels reinforced by GLARE straps. Finally FCG life of one of the reinforced panels is predicted and validated against experimental test life.

This chapter closes with a comparison of the four different studied strap configurations investigated in this project in terms of FCG life.

7.2 Un-reinforced panel

7.2.1 Geometry, material and applied load

The panel was designed by the industrial partners in the consortium. Engineering drawings are in appendix C. A cross section sketch is shown in figure 7.1 to define the geometric parameters.

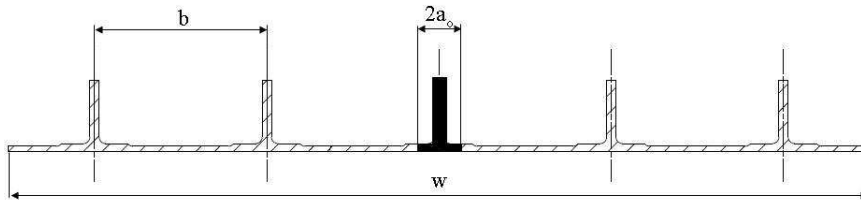


Figure 7.1: Cross section sketch of the integral panel.

A complete sketch of assembly for fatigue testing is given in figure 7.2. The panel has five integral “blade” stringers. The skin thickness is $t = 4$ mm and the doublers are 6 mm. The panel width is $w = 650$ mm and the stringer pitch $b = 130$ mm. The stringer area is $A_{st} = 436 \text{ mm}^2$ and the stringer to skin area ratio is $A_{st}/bt = 0.838$. The panel is made of AA 7085-T7651. The mechanical properties of the panel can be found in table 5.2 and the FCG material law in figure 5.5.

The end fitting is designed to annihilate the secondary bending effect by loading the panel on its neutral axis when in pristine condition. The panel is loaded

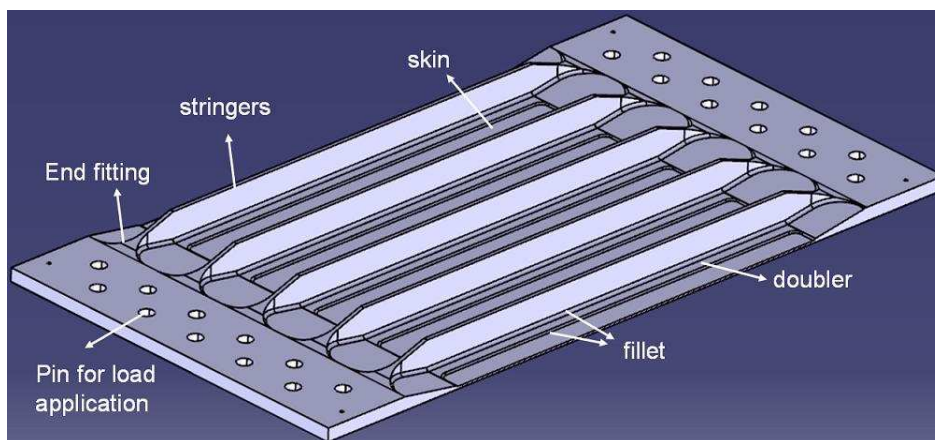


Figure 7.2: Sketch of the un-reinforced large-scale integral skin-stringer panel

through the pin-holes and connected to the fatigue testing machine by two support plates for each side (figures C.2 and C.3). The two plates are loaded by a thick steel pin.

The initial damage scenario is an initial crack length $2a_0 = 22$ mm under a broken central stringer (figure 7.1).

The maximum applied stress is $\sigma_{max} = 49.72 MPa$ corresponding to an applied load $F_{max} = 237$ kN. The normalised spectrum is plotted in figure 7.3. It contains 54246 cycles and is mostly composed by compressive to compressive loads since it simulates an upper wing load condition¹.

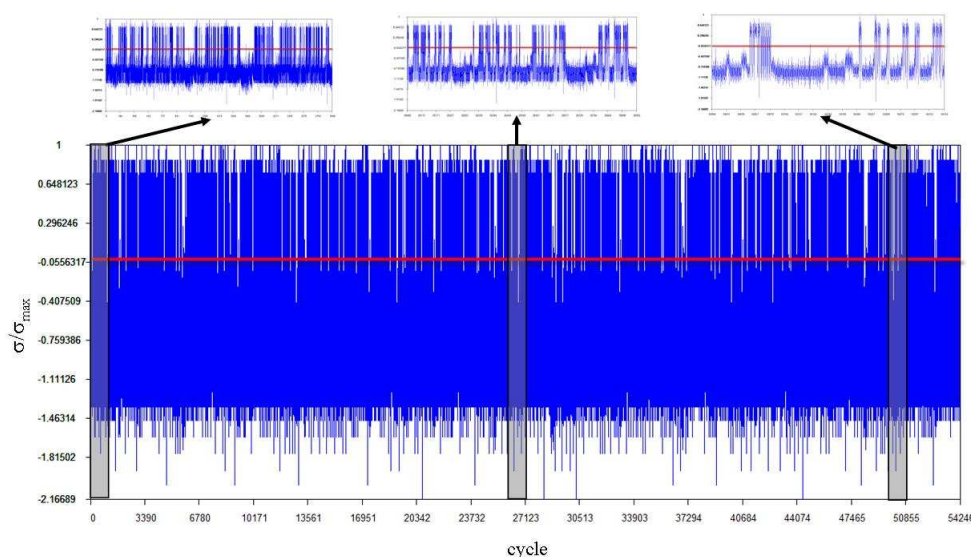


Figure 7.3: Applied variable amplitude load spectrum.

It is important to consider that accurate predictive models for crack growth under predominantly compressive loads are not yet available in the literature [156]. It is known that compressive cycles accelerate crack propagation but this effect is not included in any predictive models. Retardation models, such as FASTRAN [157], have been developed to consider the overload effect on the FCG rates, but not compressive-compressive cycle crack acceleration [158]. For this reason the compressive-compressive cycle effect has been neglected for the integration of the FCG and only the compressive-tensile and tensile-tensile cycles are considered to contribute to the crack propagation. A summary of three possible situation is represented in figure 7.4.

¹Due to the high numbers of cycles composing the spectrum, a table with the values cannot be included in the thesis.

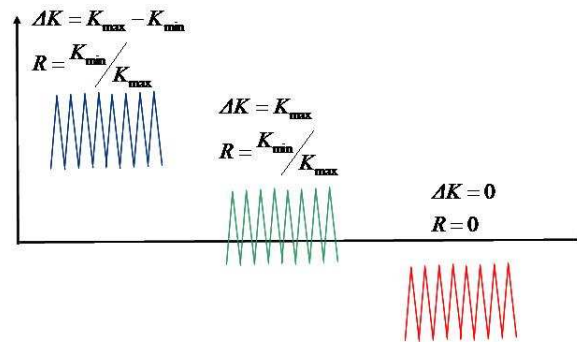


Figure 7.4: Summary of the possible fatigue load cycles and their contribution to the FCG.

7.2.2 FE model simplifications: meshing, stress and secondary bending analysis

Due to the complicated geometry of the panel, a 3D FE model was built to assess and validate a simpler 2D FE model. Only a quarter of the panel is modelled by making use of the symmetry constraints.

The 3D model uses 152438 CTRETA elements with 247631 nodes. The characteristic mesh size is 5 mm. This size was chose as a compromise between computational time and conformity of the mesh to the geometry. The mesh is shown in figure 7.5.

The load was applied to the pin holes by rigid elements to simulate the contact

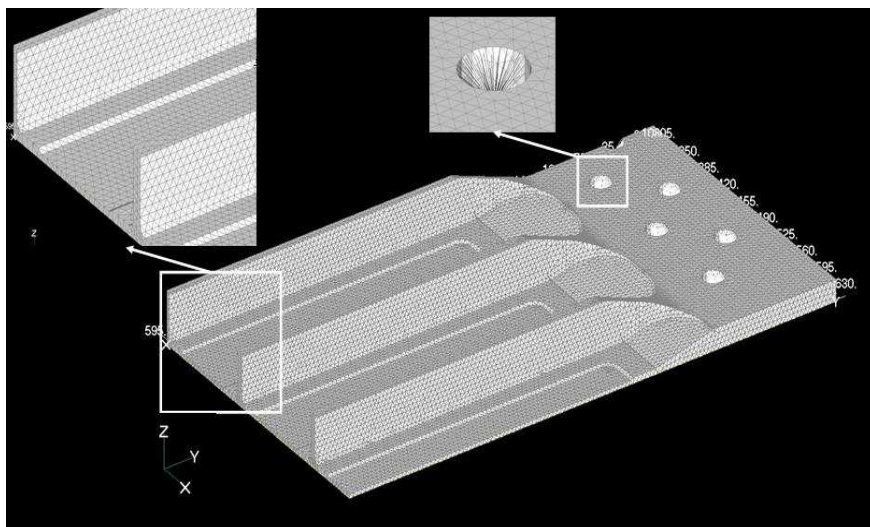


Figure 7.5: Un-reinforced panel: 3D FE model.

between the pins and the panel in the simplest way. In fact, we are not interested in the stress concentrations at the pin holes, but just the way the load is distributed in the panel. Focus is given to the bending and stresses generated in the $X - Z$ plane of the panel where the crack propagates.

The 2D FE model was built by modelling the mid plane surface of the panel (figure 7.6). The simplifications introduced are summarised as follows:

- Filets have not been modelled;
- The stringer curved end (figure 7.6) designed to allow even transfer of load from the end fitting to the stringers has been neglected. This could cause locally higher stress concentration where the stringers join the end fitting;
- The triangular end fitting section (figure 7.6) of the real panel was modelled by using constant thickness 2D elements (mean thickness of the test panel) placed on the geometrical mid plane;
- The doublers present at the base of the stringers are thicker than the skin (6 mm instead of 4 mm); that means that the mid planes should be offset by 1 mm; this characteristic was also neglected and the two planes are placed at the same position but the used elements have different thickness; this would cause stress discontinuities but cannot be avoided since the effect of the doublers in the crack propagation must not be neglected.

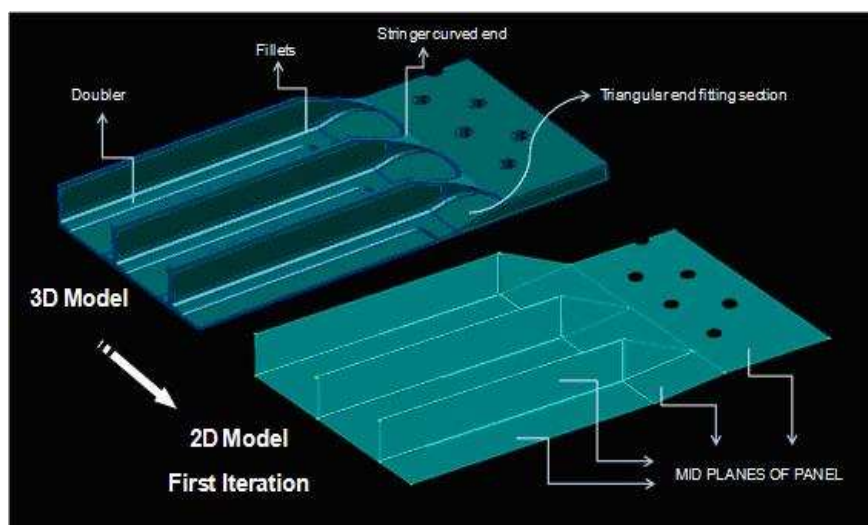


Figure 7.6: 3D FE model to 2D FE model simplification.

Although the possibility of using 2D elements with variable thickness to model variable thickness parts present in the test panel, the simpler option of constant thickness elements was preferred to avoid stress discontinuities that would be generated and keep the model simple. The use of offset for the 2D elements was also avoided since, although not commonly known, NASTRAN neglects it for non-linear analysis (solver 106 or NLSTATIC).

The 2D FE model can be seen in figure 7.7. The model is made of 94211 elements composed by 94896 nodes. The mesh dimension on the crack propagation path (y -symmetry plane) and the strap region is uniform 1×1 mm. A mesh transition to 4×4 mm elements is used to limit the number of elements of the model. The load is applied at the pin holes. There is no interest in an accurate prediction of the stresses near the holes thus, contact is not modelled. Rigid elements are used to transfer the load instead.

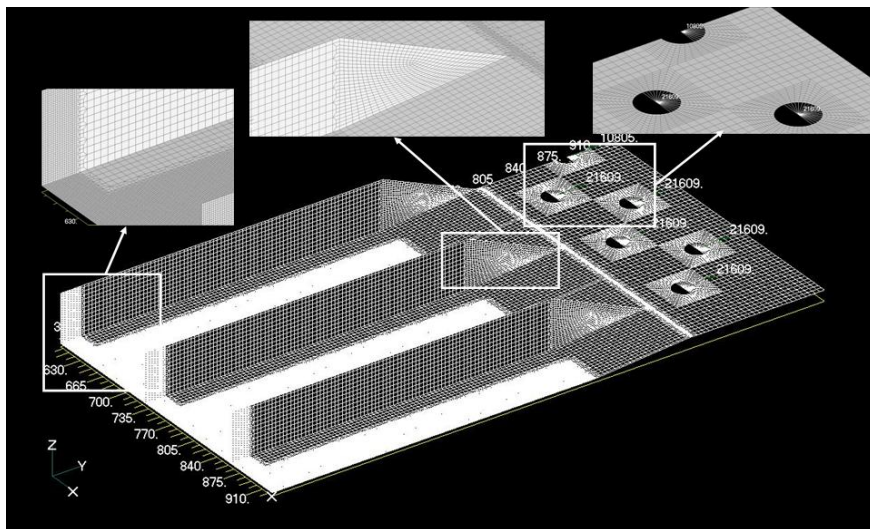
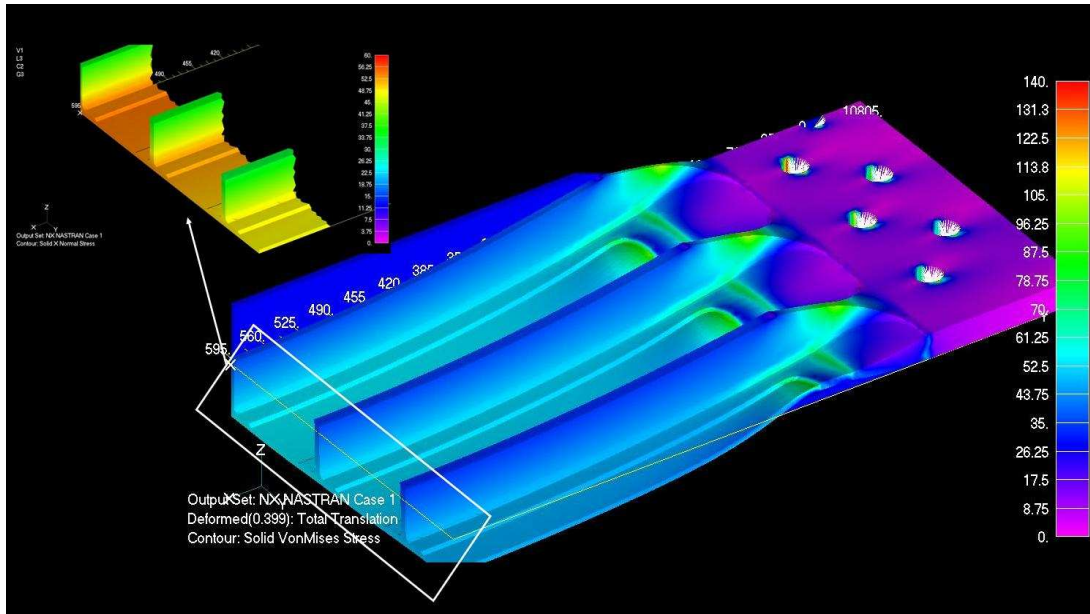
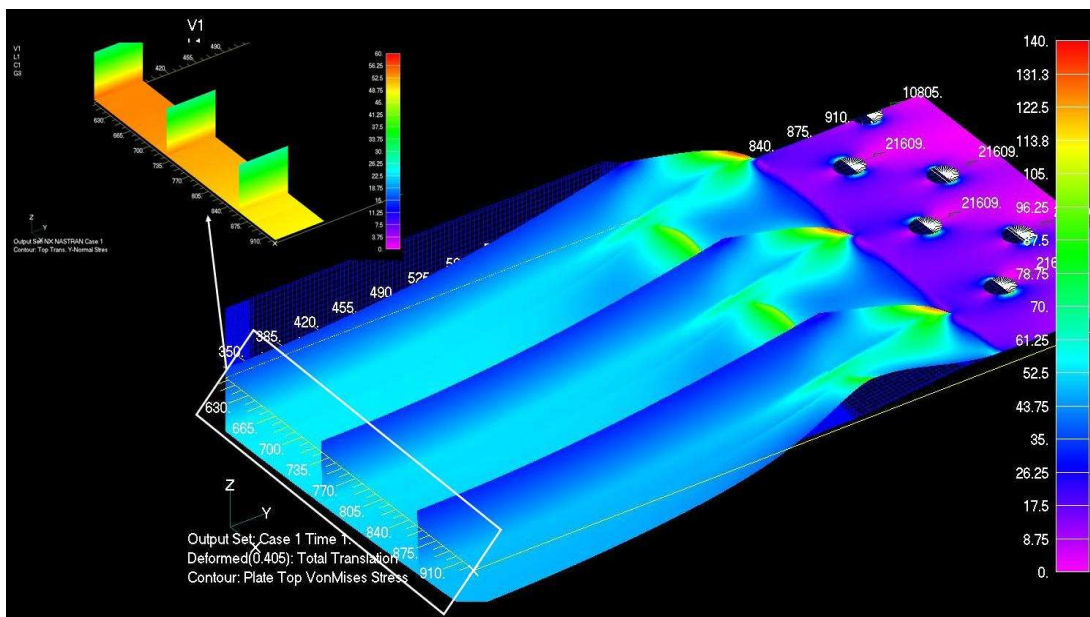


Figure 7.7: Un-reinforced panel: 2D FE model.

The two models were run with the non-linear NASTRAN solver (solver 106 or NLSTATIC) to accurately predict secondary bending. The von Mises stress and deformed shape obtained by the 3D and 2D FE models are compared in figure 7.8. The same stress scale is used in both models. By comparing the colours of the contour maps it can be seen that the two models are in good agreement in terms of von Mises stress (figures 7.8(a) and 7.8(b)). Displacements along crack propagation path (y -symmetry plane) are compared in figure 7.9. The vertical solid lines shown the position of the stringers and the dashed lines the position of the doublers. The results are in good agreement.



(a) 3D FE model.



(b) 2D FE model.

Figure 7.8: Stresses contour and and deformed shape by 2D and 3D FE models. Inserts show detailed stress contour maps on the future crack region.

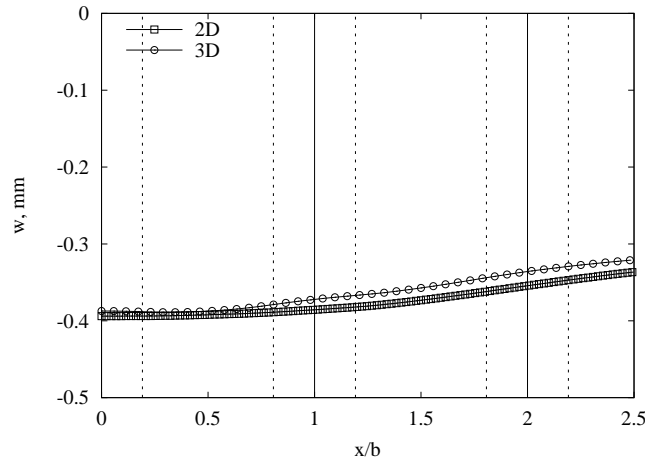


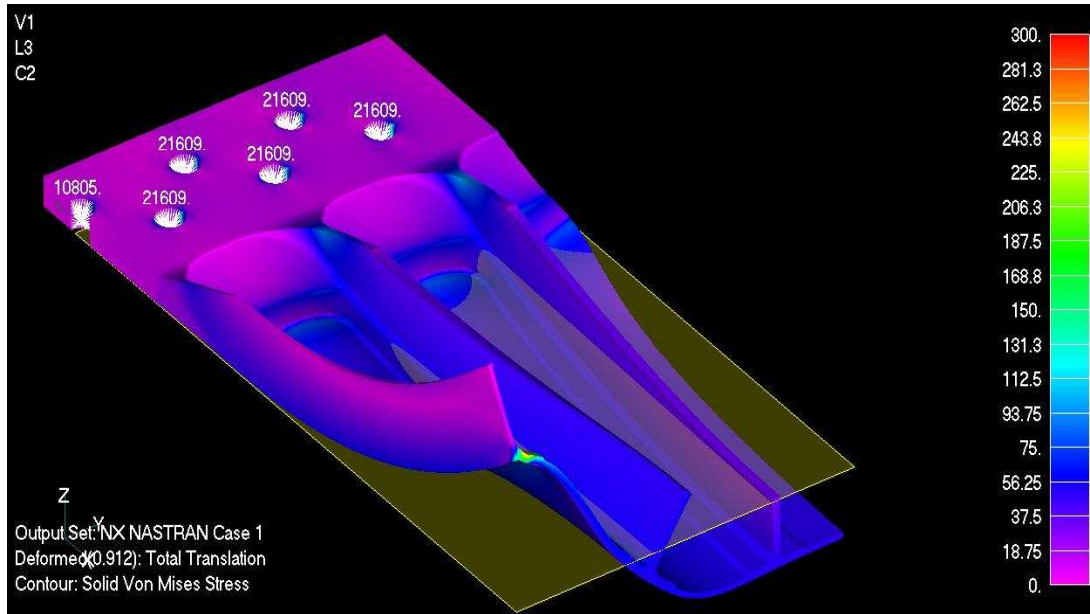
Figure 7.9: Out-of-plane displacement (w): comparison of 3D and 2D FE models.

The stress analysis was also carried out for broken central stringer failure scenario with initial crack length $2a_0 = 22$ mm. The stress contour and deformed shape obtained by 3D and 2D FE are shown in figure 7.10. Good agreement between the two models is achieved. It is worth noticing how the secondary bending direction changes along the width of the panel. In the centre, the broken central stringer causes the neutral plane to shift below the load application plane and the panel bends upwards. Beyond the central part, the outer stringers are still intact and the panel bends downwards. This shows how the neutral plane position varies with the crack length and the panel bending direction changes with crack propagation and progressive stringer failure, and on the other hand, bending direction influences the crack growth. For this reason the modelling of the secondary bending needs to be accurate.

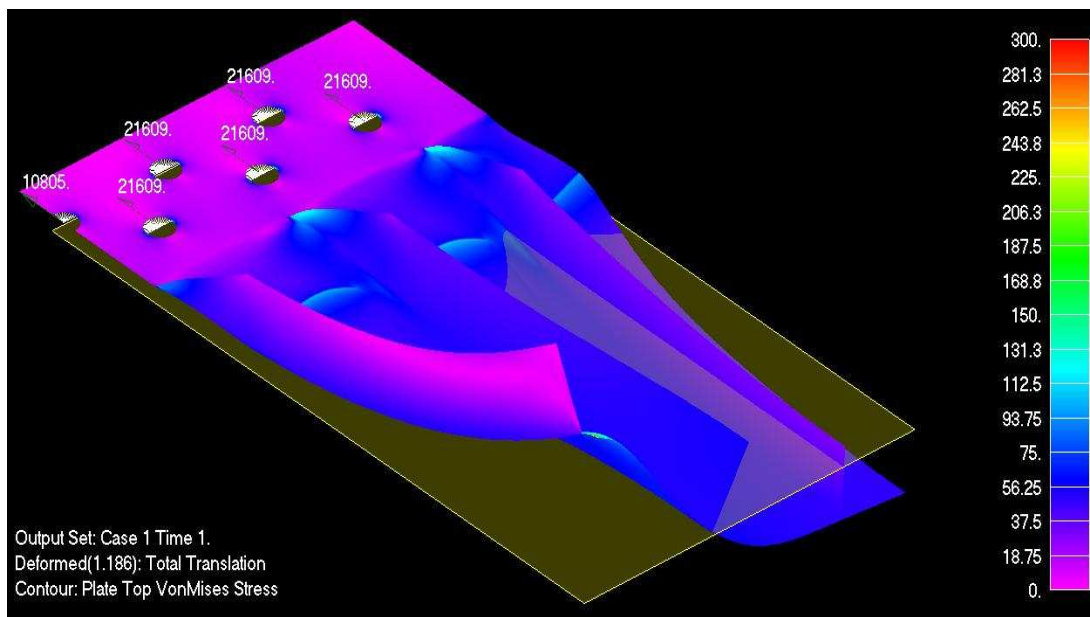
Stress and deformation analyses have shown that this 2D FE model results to be adequately accurate to compute displacements and stresses despite the simplifications introduced and thus it is used in the next section to conduct the fracture mechanics analysis.

7.2.3 β solution and FCG life validation

Before computing the equivalent β solution (equation 4.40) for the un-reinforced stinger panel, the way that the crack propagates in the stringers was studied. The correct way to model crack propagation in the stringer should be by also computing the stress intensity factor of the stringer crack and let it propagate



(a) 3D FE model.



(b) 2D FE model.

Figure 7.10: Stresses contour and and deformed shape of the cracked panel: comparison of 2D and 3D FE models.

independently from the substrate crack, i.e. integrating the skin and stringer SIF separately. That would require re-meshing the stringer for each crack propagation step. This procedure can be avoided by assuming the crack growth in the stringer as a function of the crack in the skin, i.e. the crack in the stringer can grow 0.5, 1, 2, 3 or 4 times faster than the crack in the skin (see appendix D.3 for the program instructions). In this analysis, the crack in the stringer grows at the same rate of the crack in the substrate (figure 7.11).

The equivalent β solutions (section 4.3.3) are computed by using the modelling

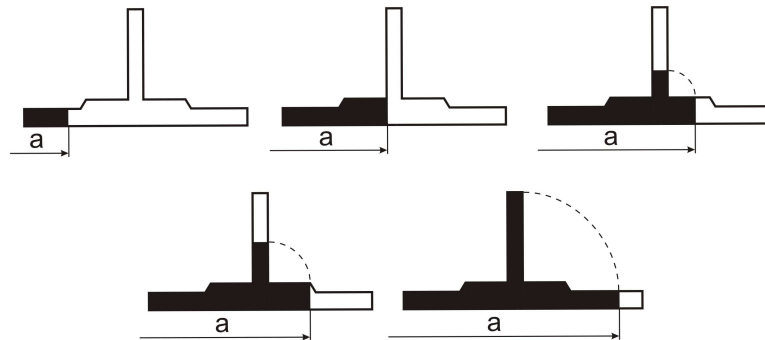


Figure 7.11: Model of crack growing into the stringer till stringer failure.

technique (section 4.2) and the computer code LICRA (appendix D) developed by the author. The solutions are shown in figure 7.12. Those solutions are compared with a solution found in [142] obtained by using a commercial 3D FE program called STRESS CHECK which can predict the propagating crack front shape by re-meshing. It can be seen that the 2D solution is very close to the 3D. The predicted FCG rate and life of the panel are shown in figure 7.13 along with

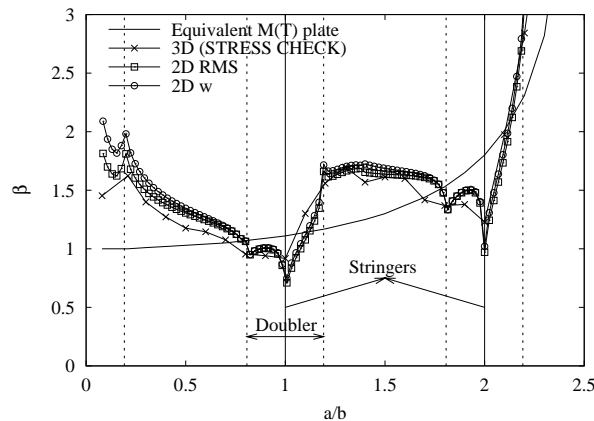


Figure 7.12: RMS and weighted β solutions for the un-reinforced stringer panel compared with a 3D solution obtained by a commercial code STRESS CHECK using 3D FE [142].

the test results reported in [142]. There is good agreement between prediction and test life till the crack reaches the end of the first doubler. After the failure of

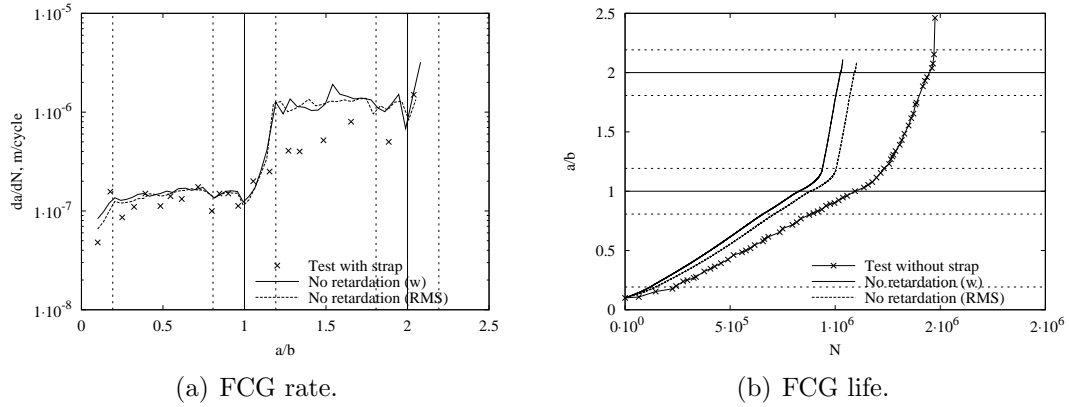


Figure 7.13: Validation of FCG rate and life against test results: un-reinforced integral stringer panel; experiments from [142].

the first stringer has been reached in the model, the prediction trends away from the experimental result. A postmortem analysis of the test showed a peculiar crack behaviour in the stringer during the experiment. The crack propagated till half of the stinger height and then turned 90° and run in the parallel direction of the load (longitudinal direction of the stringer, figure 7.14).

Before analysing the possible reasons for this crack turning, let us understand

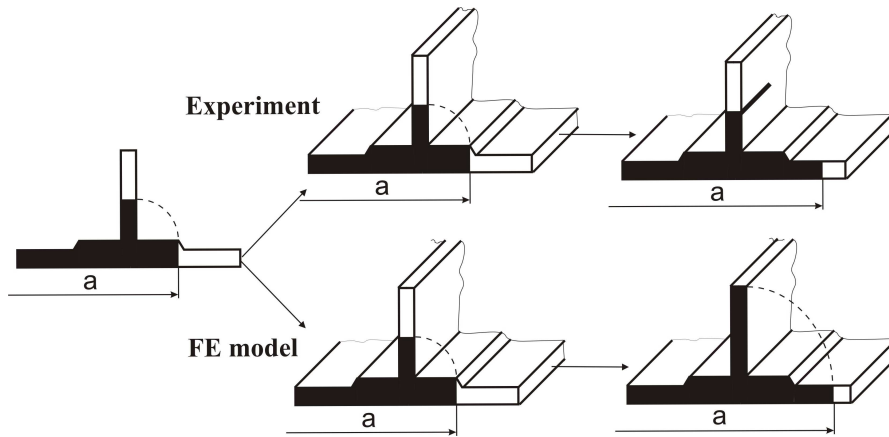


Figure 7.14: Difference between modelling of crack propagating in the stringer and real situation.

the consequences. Due to the crack deviation, the upper part of the stringer remains intact and provides some force to bridle the skin crack, which results in a lower crack growth rate. In fact the FE model shows higher crack growth acceleration after the modelled failure of the first stringer than the experimental

result (figure 7.13, $a/b = 1.2$). Although crack turning in the stringer was not modelled, the prediction is quite in good agreement with the experiment (errors: $\text{RMS} = -25\%$ and $w = -29\%$). The final prediction error is limited because the model is accurate when the crack growth in the first stringer bay and the error is built up essentially during crack growth in the second bay where the crack growth rate is already elevated.

The reasons of crack turning might be several. Firstly an asymmetric grip condition could cause some torsion in the panel which would promote crack turning. Another reason could be that the shift in the neutral plane caused by the growing crack produces some torsion in the stringers (figure 7.10). The last reason could be related to the mechanical properties of AA 7075 and the manufacturing processes of the panel. This panel was machined from a single block of material; the mechanical properties through the thickness of the block change and consequently the integral stringer panel fabricated may not be fully isotropic. Crack turning like this was already observed in tests carried out by Alcoa on integral panels and blamed on the last reason. It is believed that the cause of crack turning in this specific situation was produced by the interaction of the three aforementioned causes.

7.3 Reinforced panel

7.3.1 Strap geometries and materials

Four different strap configurations are used to reinforce the integral skin-stringer panel analysed in the previous section. The choice of using just four configurations is due to time and cost problems. By running a quick numerical analysis of the panel and considering that the testing machine can work at a maximum frequency of 1 Hz under that spectrum, the test was estimated to last 1-2 months², consequently only a limited number of tests could be run. The candidate strap material strap materials are the following four: GFRP, CFRP, Titanium 6-4, GLARE and for each material a multitude of dimensions and configurations could be chosen.

The choice of strap materials and dimensions to be used for the test comes from

²In reality the test on the reinforced panel lasted more than 3 months since the testing machine broke down twice

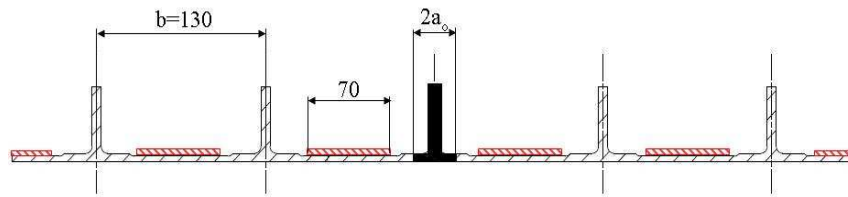
the considerations gathered by the coupon tests and numerical analyses presented in chapter 6 and design guidelines given in section 6.4. In fact, the load spectrum used for this analysis has many low amplitude cycles. It was found that TRS are more harmful at low applied stresses (section 6.2.2), thus strap materials should have coefficients of thermal expansion close or equal to that of the substrate. For this reason GLARE and AA 7085-T7651 materials were chosen. Now two strap geometries needed to be selected for each material.

The choice of the strap dimensions is again based on the considerations presented in chapter 6. In fact it was found that the most important variable in the design of a strap is the stiffness ratio (section 6.1.3, equation 6.5). For this reason then the 4 strap configurations were designed to provide constant stiffness ratio, $\mu = 0.2$.

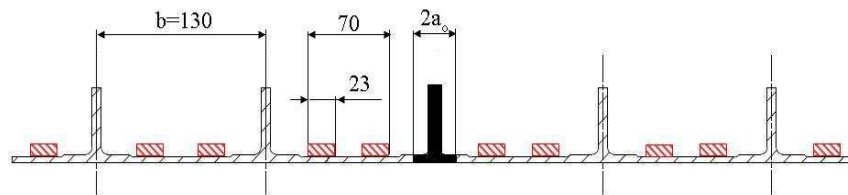
The chosen strap configurations are:

- **GLARE wide straps.** One wide and thin strap per bay, straps dimensions $w70t3.8l685$ and half width strap is used in the last bay. The mesh used for the model is shown in figure 7.16(a). It consists of 389529 elements and 446426 nodes.
- **GLARE narrow straps.** Two narrow and thick straps per bay, straps dimensions $w23t5.4l685$ and only one strap is used in the last bay. The mesh used for the model is shown in figure 7.16(b). It uses 322243 elements and 286774 nodes.
- **Aluminium wide straps.** One wide and thin strap per bay (AA 7085-T7651), straps dimensions $w70t3.25l685$. Strap position and mesh are equal to the GLARE wide strap configuration.
- **Aluminium narrow straps.** Two narrow and thick straps per bay (AA 7085-T7651), straps dimensions $w23t4.55l685$. Strap position and mesh are equal to the GLARE narrow strap configuration.

Constant stiffness ratio for the two different strap materials is obtained by changing the thickness of the straps. The aluminium narrow straps are thinner than the GLARE ones; the same for the wide straps. For the same strap material, the two different strap geometries (wide & thin and narrow & thick) are designed to give again a constant stiffness ratio. The choice of using a wide & thin strap is based on the findings presented in section 6.2.3, i.e. a thin & wide strap produces



(a) Wide strap configuration.



(b) Narrow strap configuration.

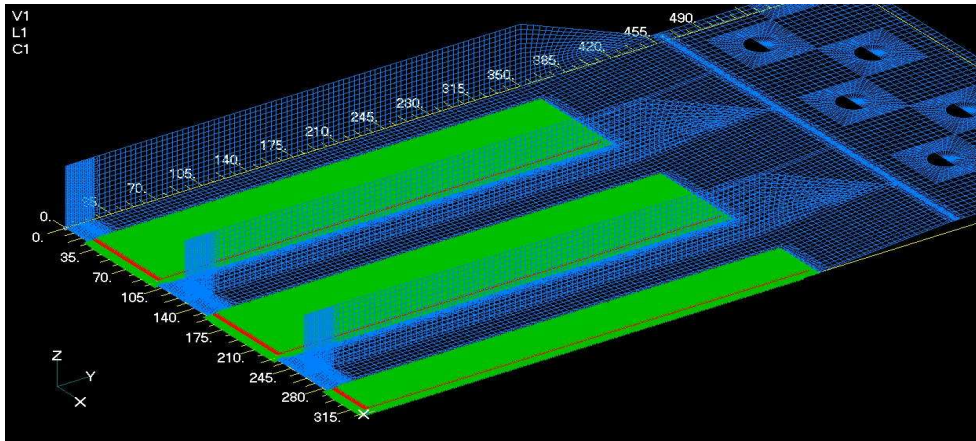
Figure 7.15: Cross section sketch of the reinforced integral panels.

lower TRS. The narrow & thick configuration was chosen as comparison with the wide & thin because it was found that a thicker strap, in the absence of TRS, produces higher bridging effect and crack retardation (section 6.1.2 and 6.3). All the straps are bonded with the adhesive FM94 and cured at 120 °C. Mechanical properties of adhesive and strap material can be found in table 5.3.

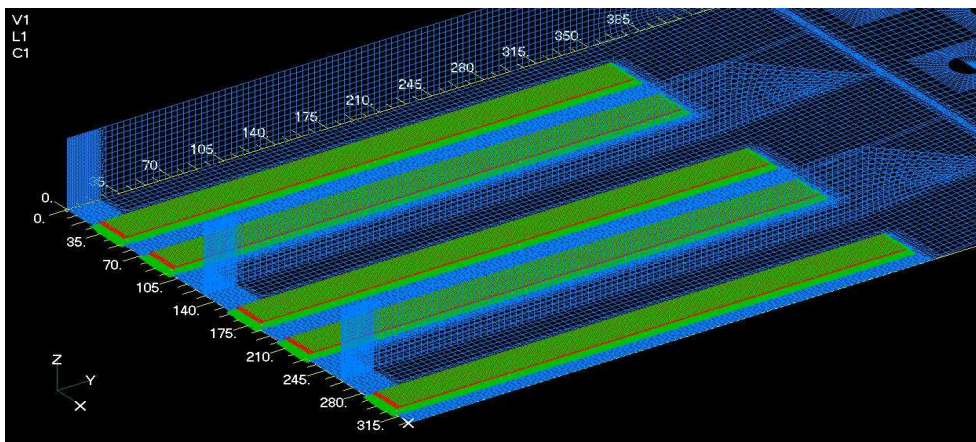
7.3.2 Stiffening effect

Before analysing the enhanced damage tolerance capability of these panels, stress analysis at the maximum applied load ($\sigma_{max} = 49.72 MPa$, $F_{max} = 237$ kN) is carried out. In order to show the stiffening effect, the panel are studied in pristine condition.

The von Mises stress contour on the substrate for the four strap configurations compared with the un-reinforced case are shown in figure 7.17. The plots use the same stress scale. These plots show that the stress in the substrate decrease for the aluminium wide and narrow straps (figures 7.17(b) and 7.17(c)). This is due to the stiffening effect introduced by the straps. Observing figures 7.17(d) and 7.17(e), which show the stresses for the GLARE strap configurations, it can be



(a) Wide strap configuration.



(b) Narrow strap configuration.

Figure 7.16: Reinforced panels: 2D FE mesh.

seen that the stresses in the substrates are very close to that of the un-reinforced panel. It seems like there is no stiffening effect brought by the GLARE straps. This is because there are also tensile TRS in the substrate for the GLARE strap configurations.

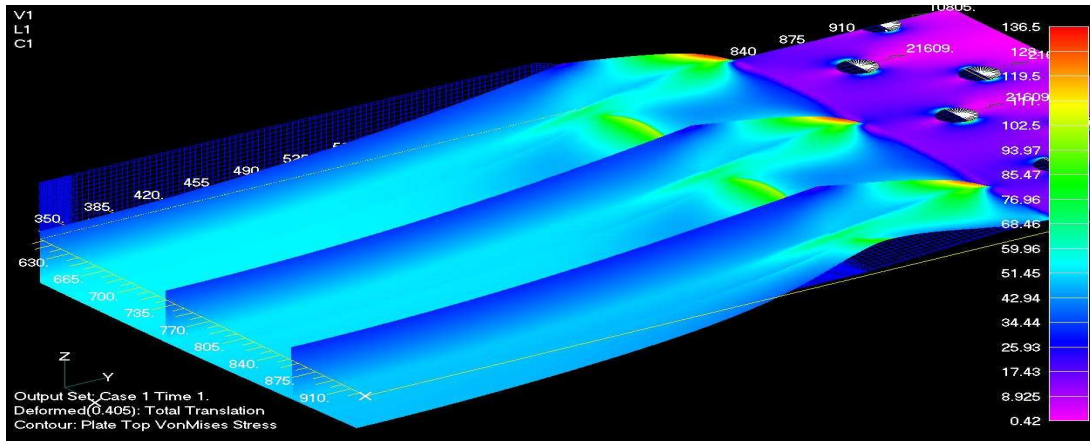
If the TRS effect is neglected, the same amount of stiffening effect will be obtained by the four strap configurations (figures 7.17(b), 7.17(c), 7.17(f), and 7.17(g)). The loading direction stress σ_{yy} in the substrate along crack propagation path (y -symmetry plane) are plotted in figure 7.18. It can be seen that the stresses in the substrate for all four cases have decreased by about 20% due to the stiffening effect; that is equal to the stiffness ratio of the straps (equation 6.5).

As a consequence of this analysis it was agreed by the consortium to test the reinforced panels at a 20% higher applied load so that the stresses in the substrate are equal for the un-reinforced and reinforced panels. Thus, the new maximum applied stress to the reinforced structures is $\sigma_{max} = 59.67MPa$ corresponding to a machine load $F_{max} = 284$ kN.

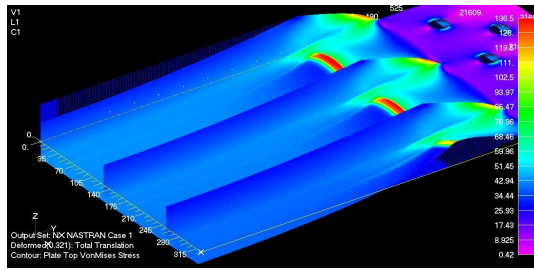
This means that, if the bonded straps enhance the damage tolerance capability of the panel at the same substrate stress level (higher applied stress), it would be possible, instead of adding the strap to the structure as it was done in this case, to remove material/weight from the substrate and use it as straps to make lighter and safer structures.

7.3.3 Stress analysis of the straps

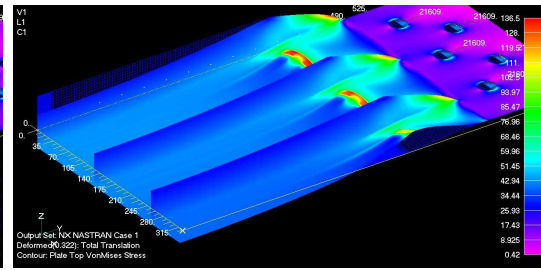
The von Mises stress in the straps is also examined for the pristine reinforced panel. In figure 7.19, the top surface stress contour maps for the aluminium strap configurations are shown. It is worth noticing how the stress decreases towards the end of the straps (top of the figure), thus a tapered strap would be a good solution. Figure 7.20 shows the von Mises stress in the top aluminium layer of the GLARE straps in the absence of TRS. Also in this case the stress decrease and goes to zero at the end of the straps. By comparing figures 7.19 and 7.20 it can be seen that the level of stress carried by the straps is equal for all the four cases (figures all plotted in the same scale). This is because the stiffening effect and the stress in the straps is only dictated by the stiffness ratio. The stiffness ratio for these for cases is constant, thus the stress levels are equal.



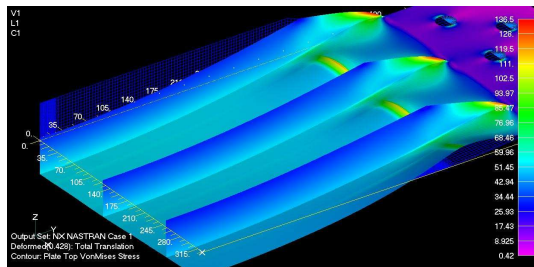
(a) Un-reinforced panel (substrate stress, $\sigma_{sub} = 50MPa$)



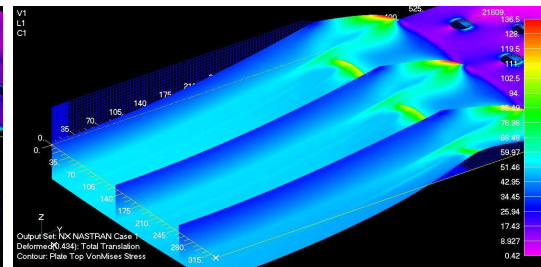
(b) Aluminum wide strap ($\sigma_{sub} = 40MPa$)



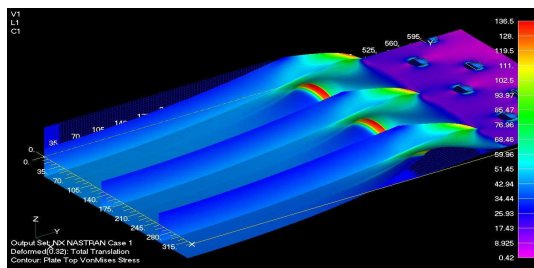
(c) Aluminum narrow strap ($\sigma_{sub} = 40MPa$)



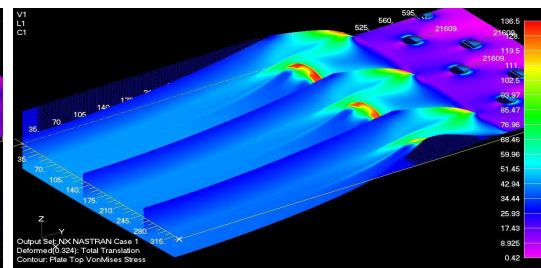
(d) GLARE wide strap with TRS
($\sigma_{sub} = 47MPa$)



(e) GLARE narrow strap with TRS
($\sigma_{sub} = 47MPa$)



(f) GLARE wide strap without TRS
($\sigma_{sub} = 40MPa$)



(g) GLARE narrow strap without TRS
($\sigma_{sub} = 40MPa$)

Figure 7.17: Comparison of von Mises stresses in the substrate at the maximum applied load ($\sigma_{max} = 49.72$) for the different strap configurations. Same stress scale is used for each case.

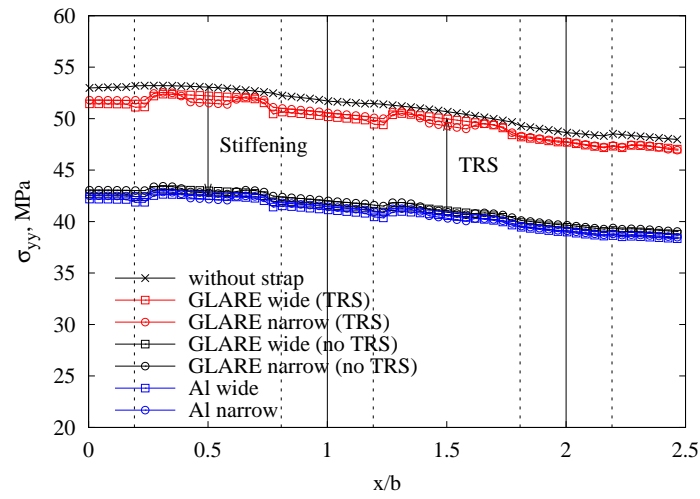
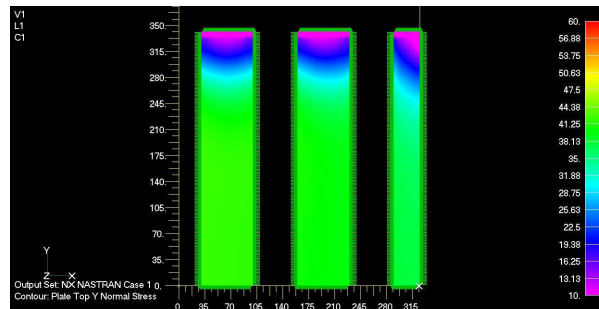
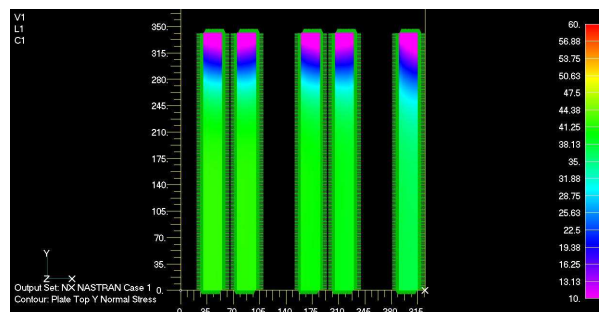


Figure 7.18: Stiffening effect: σ_{yy} stress in the substrate.

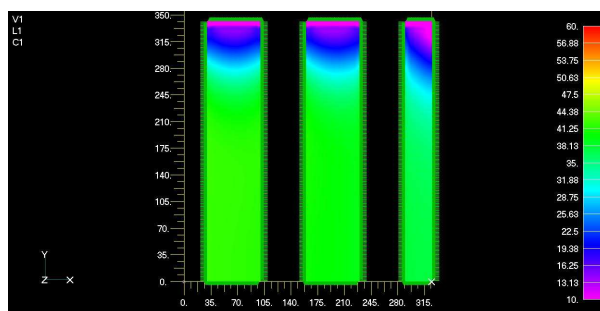


(a) Wide strap

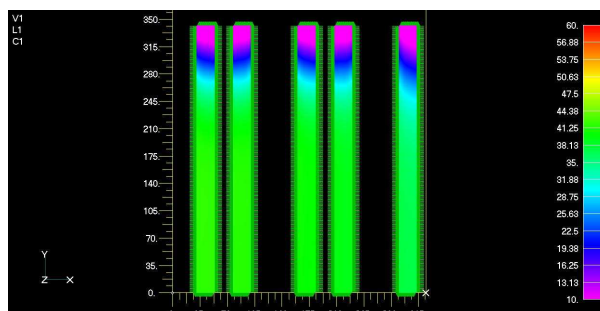


(b) Narrow strap

Figure 7.19: Aluminium strap configurations: von Mises stresses in the straps



(a) Wide strap



(b) Narrow strap

Figure 7.20: GLARE strap configurations: von Mises stress in the straps in the absence of TRS effect.

7.3.4 Thermal residual stress analysis

Tensile TRS in the substrate accelerate crack propagation rate and are important in the prediction of FCG life. For the studied cases, TRS are important since they cause major differences between the GLARE and aluminium strap configurations. Fortunately, TRS produced by the GLARE straps are relatively low when compared to other materials such as CFRP or titanium alloy, thus they should not penalise it too much.

The substrate TRS contour maps for the pristine panel are shown in figure 7.21 for both wide and narrow strap configurations. It can be seen that TRS are slightly higher beneath the straps and the maximum stress value is about 10 MPa.

TRS distributions at the top, middle and bottom of the substrate along the panel width (x -axis) is shown in figure 7.22. The maximum value is about 10 MPa. It is interesting to notice that the bending direction is different from the coupon plates in which TRS cause the coupons to bend upwards. In this case the panel bends downwards and the stress at the top of the plate is lower than the bottom one (figure 7.22). This is because the neutral plane of the panel (with the

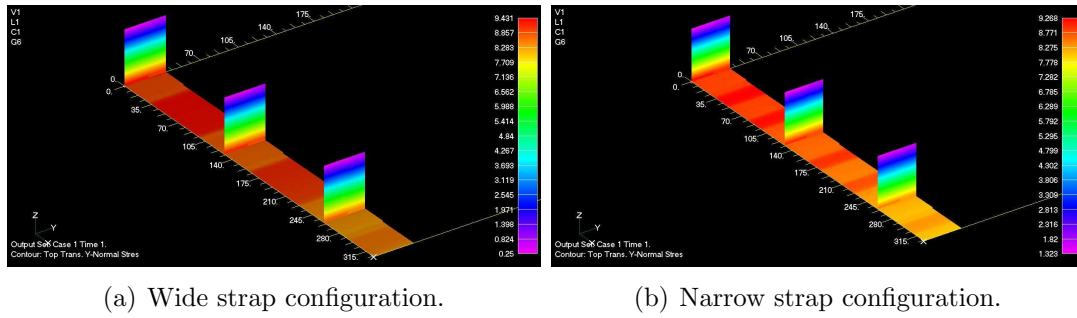


Figure 7.21: TRS comparison between wide and narrow GLARE strap configuration: σ_{yy} at the top of the substrate.

stringers) is above the surface of application of the TRS, i.e. the top of the skin. Locally, instead, the TRS try to bend the substrate/skin upwards increasing the stress at the top of the substrate and decreasing the one at the bottom (see figure 7.22).

Comparing wide and narrow strap configurations, it can be seen that the level of TRS is almost identical. The reason is due to the same stiffness ratio of the two configurations. It should be noticed though that, for the narrow configuration, between the two straps, i.e. in the middle of the bay, the TRS are slightly higher. The residual stress intensity factors for the two panel were computed and shown in figure 7.23 to understand which configuration is better. Firstly, it can be observed that the values of residual SIF are relatively low. Secondly, the narrow strap configuration shows a peak of SIF in the middle of the bay which is not the case of the wide one. Thus, the narrow strap configuration is slightly worse than the wide one, although these values of SIF are too low to considerably affecting the performance of the narrow strap configuration.

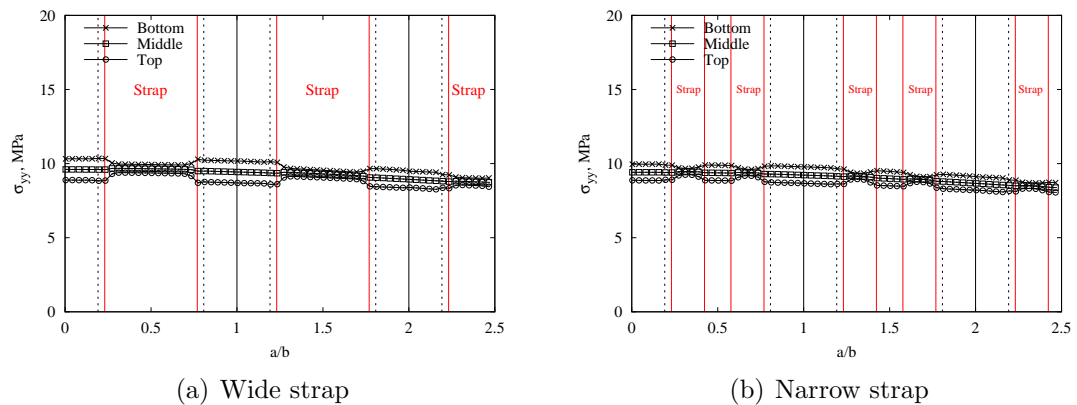


Figure 7.22: Comparison of TRS between the two GLARE strap configurations.

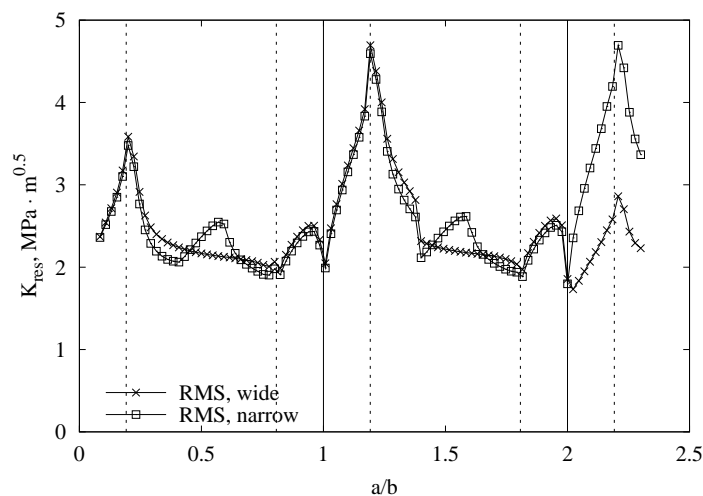


Figure 7.23: Residual SIF for the wide and narrow GLARE strap configurations.

7.3.5 FCG life validation: GLARE wide

Only the experimental results for the GLARE wide configuration are available at the time of this thesis.

The effective weighted β -solution (equation 4.40) obtained by FEA using computer code LICRA (appendix D) is shown in figure 7.24. Two things should be noticed by observing figure 7.24. Firstly, the bridging and stiffening effect provided by the straps results in a strong reduction of β . Secondly, adhesive failure does not influence the β -solution much when the crack is in the first bay, although when it approaches the second bay, the β value increase due to the reduced bridging and stiffening effect.

This β -solution was used to calculate FCG life by the Harter T-method (section 2.3.4) and the equivalent residual stresses intensity factor (section 4.3.3) with AFGROW program since LICRA can not integrate variable amplitude load spectrum. The predicted FCG rate and life are compared with experiments in figure 7.25.

The reinforced panel test was stopped at a crack length of $a = 1.2b$ due to time constraint [142]. The prediction, instead, shows the FCG life till failure of the panel. Prediction and experiment are in good agreement. Crack growth deceleration when entering the first strap and acceleration approaching the first stringer are correctly predicted by the modelling technique and the computer code LICRA. It is important to notice that the GLARE wide straps can almost triple

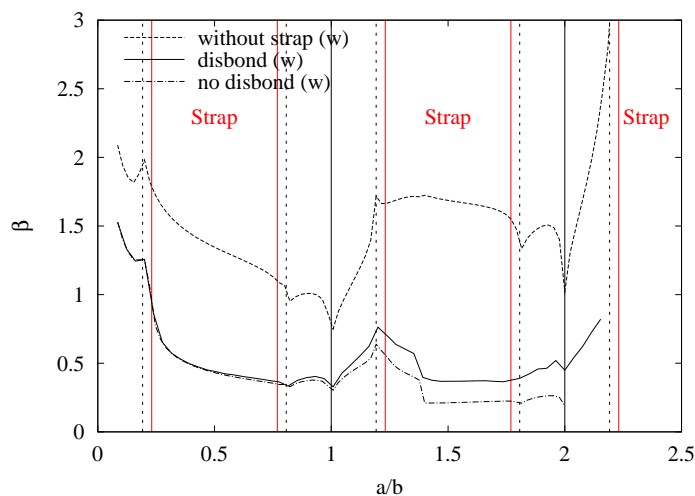
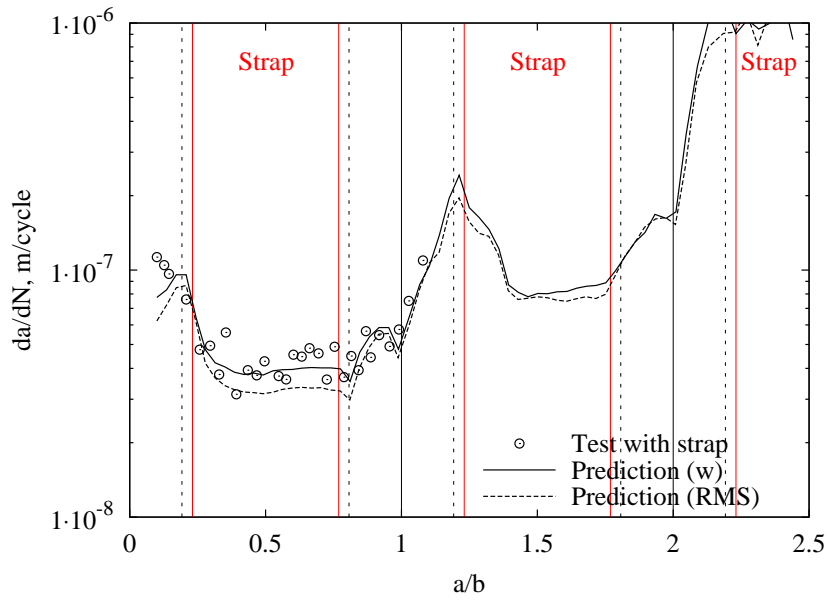


Figure 7.24: GLARE wide strap configuration: β solutions.

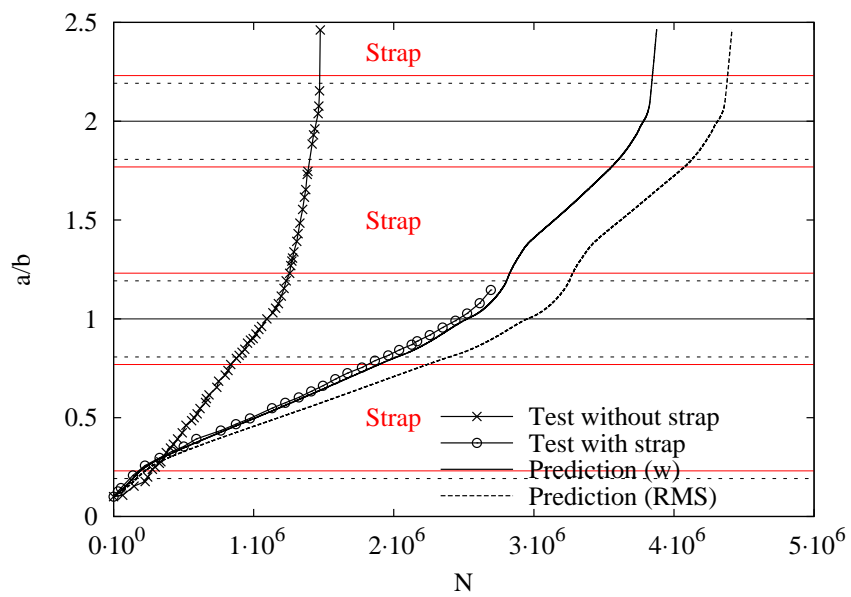
the life of the baseline unenforced panel at a 20% higher load.

Stress analysis of the straps with substrate crack propagation is also carried out. Figure 7.26 shows von Mises stress in the first layer of GLARE (aluminium layer) for different crack lengths. Figure 7.26(a) is for a crack length of 100 mm, i.e. the crack tip has just passed the strap. The stress in the strap is very high (about 300 MPa) because disbond is limited. In fact disbond front can be seen from the stress contour map and it is identified as the line where the stress suddenly changes. For longer cracks, the disbond area increases but the stress decrease to about 150 MPa. So high stress levels in the strap are very likely to cause strap failure. Fortunately, on top of the aluminium layer there is a GFRP layer which limits the failure of the strap in the first aluminium layer so that the bridging effect of the strap is not affected and the life of the structure improved. At this point disbond growth would move to the weakest interface that is the aluminium/GFRP within GLARE itself. This observations have been confirmed by the experimental tests reported in [142].

Strap failure analysis is still not implemented in the LICRA code, thus stress analysis of the straps needs to be carried out manually. Although a rigorous method would be to use the S-N curve along with the Miner rule to compute the fatigue life of the straps, it cannot be done manually because the stress in the straps changes for each crack length. Consequently, engineering common sense is used instead. If the stress in the straps is close to yielding, then the straps will very likely fail under fatigue. For the validation cases shown in chapter 5



(a) FCG rate.



(b) FCG life.

Figure 7.25: GLARE wide strap configuration: FCG rate and life validation against experiments [142].

this method was used for the GLARE straps. LICRA is run once to compute the disbond, stresses, and life with supposedly pristine straps, then the stresses are checked manually and if necessary a new model is run with imposed failure of the first layer of aluminium in GLARE and disbond interface set to be the aluminum /GFRP interface in GLARE itself.

In this case, due to excessive computational time required to run the large-scale panel model, only the case of perfect straps is run. This justifies the fact that the supposedly conservative weighted SIF solution is, in this case, slightly un-conservative.

Bonded straps are demonstrated to be very efficient in improving the FCG life of large-scale integral skin-stringer panels for this compressive load dominated spectrum. Moreover, the modelling procedure developed in this thesis and implemented in LICRA has been demonstrated to be able to predict the FCG life of a bonded reinforced large scale skin-stringer integral panel. This modelling procedure is used in the next section to predict the life of the other three chosen strap configurations.

7.3.6 Strap configuration comparison

Having validated the predicted FCG life for the GLARE strap reinforced integral skin-stringer panel, a comparison between the four strap configurations is done by FE modelling.

The effective weighted β -solutions (equation 4.40) are computed for all four configurations by FEM using LICRA computer code (appendix D). Due to the multiple disbond fronts and the large number of elements in the model the computational time required to model disbond propagation is considerably excessive. Firstly, an analysis without disbond modelling is carried out to understand the differences between the four configurations. The results are shown in figure 7.27. It can be seen that the only difference between the four configurations is in the gap between the two narrow straps. In fact, the β solution does not show the effect of TRS and disbond is not considered, the results of the four strap configurations are quite similar since the same stiffness ratio is used.

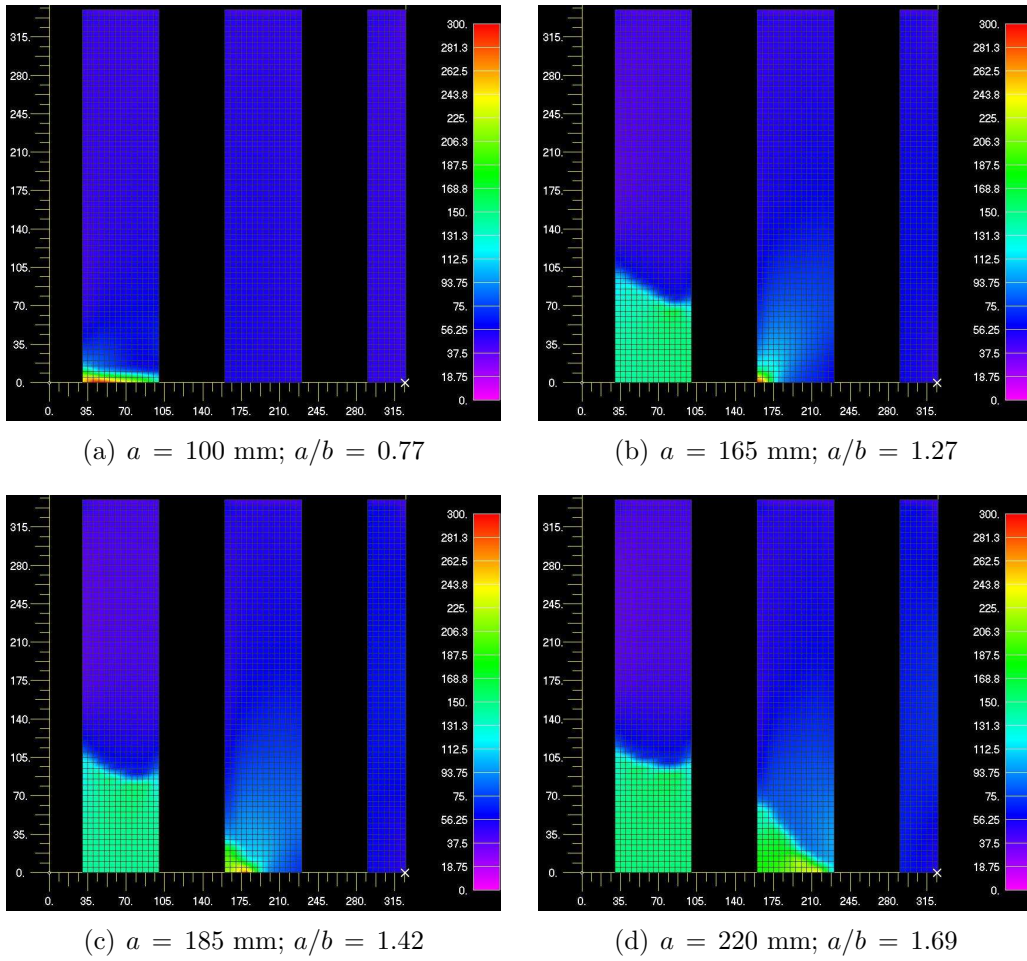


Figure 7.26: GLARE wide strap configuration: von Mises stress contours on the bottom ply (nearest to substrate and most stressed) as a function of the substrate crack length.

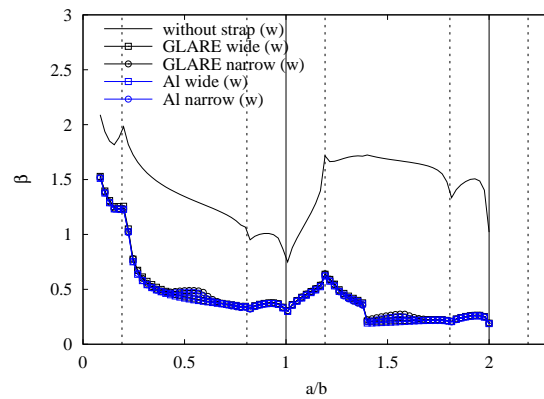
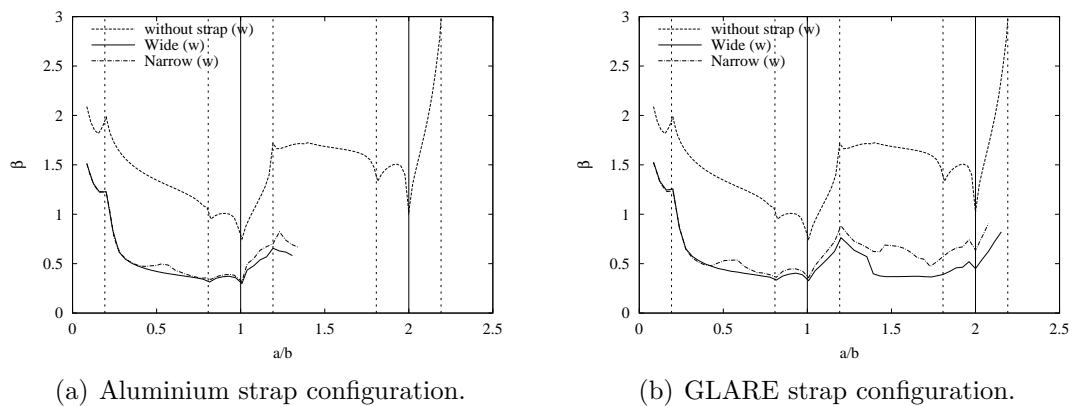


Figure 7.27: β solutions for the different strap configurations without modelling disbond failure.

Since the test was stopped when the crack was in the second bay, also the models were run up to a crack length of $a = 170$ mm. The life in the first bay is the most important part, in fact, when the crack approaches the second bay, the boundaries of the panel influence the crack propagation. At this point, the panel does not behave as a real wing panel anymore; the latter is much wider and supported.

The equivalent weighted β solutions are shown in figure 7.28.

For both strap materials, it can be seen that the narrow strap configurations



(a) Aluminium strap configuration.

(b) GLARE strap configuration.

Figure 7.28: β solutions for the different strap configurations with disbond analysis.

produce a higher β in the middle of the first bay than the wide strap configurations. Moreover, when the crack approaches the first stringer the β solutions of the narrow strap configurations are again higher than the wide configurations. This is because that narrow straps show more disbond.

Predicted FCG rate and life of the four strap configurations are shown in figure 7.29.

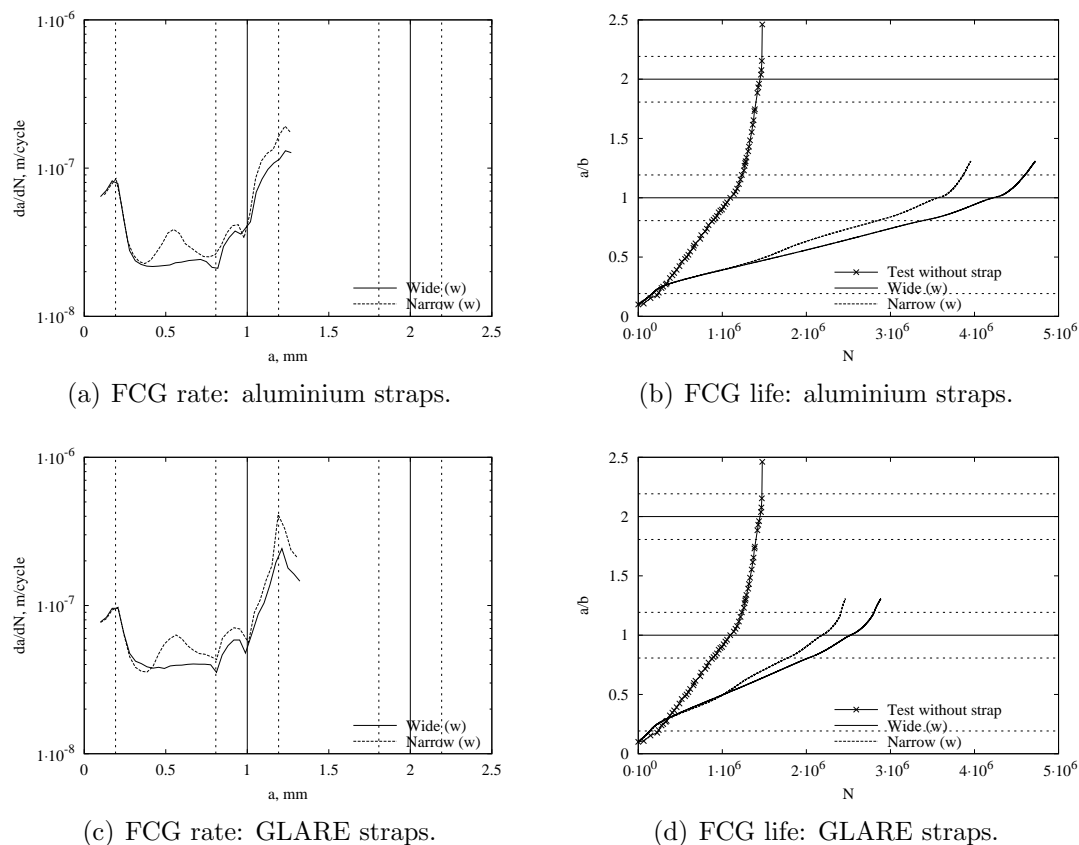


Figure 7.29: FCG rate and life comparisons for the four strap configurations: GLARE and aluminium, wide and narrow

The following considerations can be made based on the predicted FCG lives:

- **Wide straps perform better than narrow straps.** This seems to be in contradiction to the results in section 6.3 where it was found that narrow and thick straps perform better. In fact, it is not. In this case, the stiffness of the wide strap was split in two separate narrow straps where the second strap is considerably more distant from the initial crack tip than the wide one. The difference in the coupon sample analyses is that one wide and thin strap was substituted by one narrow and thick strap of the same stiffness ratio and both straps were placed at the same distance from the intimal crack tip. Increasing the distance from the initial crack tip was seen to be one of the factor which reduces the effectiveness of the straps (section

6.1.2). This is the reason why the wide and thin strap configurations are better than the narrow and thick. Unfortunately though, it is not certain that this wide and thin strap configuration is the lightest one among all strap geometries able to obtain the same life improvement. The use of the project graph (section 6.3) is the best way to obtain the optimum strap geometry for a given life target.

- **Aluminium straps are better than GLARE straps if they do not fail under fatigue.** The reasons of this finding are essentially three. Firstly, aluminium straps do not generate TRS in the substrate, thus increase the FCG life more than any other material. This shows even more in this case since the spectrum is composed of many low stress amplitude cycles and, as shown in section 6.2.2, TRS are more harmful than in elevated stress conditions. Secondly, aluminium to aluminium adhesive bond is stronger, thus disbond grow is slower than for other bonding interfaces. Thirdly, since aluminium is stiffer than GLARE, same stiffness ratio can be achieved by using aluminium with a thinner strap. This means a reduction of secondary bending, that, although small in terms of SIF, make a difference when it is integrated throughout the entire life of the structure. Although aluminum straps are very promising, they present a major drawback. Aluminium is a fatigue sensitive material, thus possible failure of the straps has to be taken into account. Many aluminium strap failures have been reported on sample tests [142] as well as for large scale panels [11]. In figure 7.30, the stress contour maps in the straps for a crack length of $a = 165$ are shown. The von Misses stress is around 170MPa . At that maximum symmetric cyclic stress an aluminium 7XXX series survives for about 10^4 cycles [159]. Although the stress shown in figure 7.30 is at the maximum applied load, it is very unlikely that the straps could survive for a life with an order of magnitude 10^6 . If aluminium straps are to be used, validated numerical tools are required to accurately estimate the fatigue life of the straps and, possibly, the crack propagation in the straps. Although it is part of the future work, LICRA does not predict fatigue life of the straps, thus aluminium straps are not recommended.

The result of these analyses shows that wide and thin GLARE straps are the most suitable to improve the damage tolerance capability of this panel under this spectrum load.

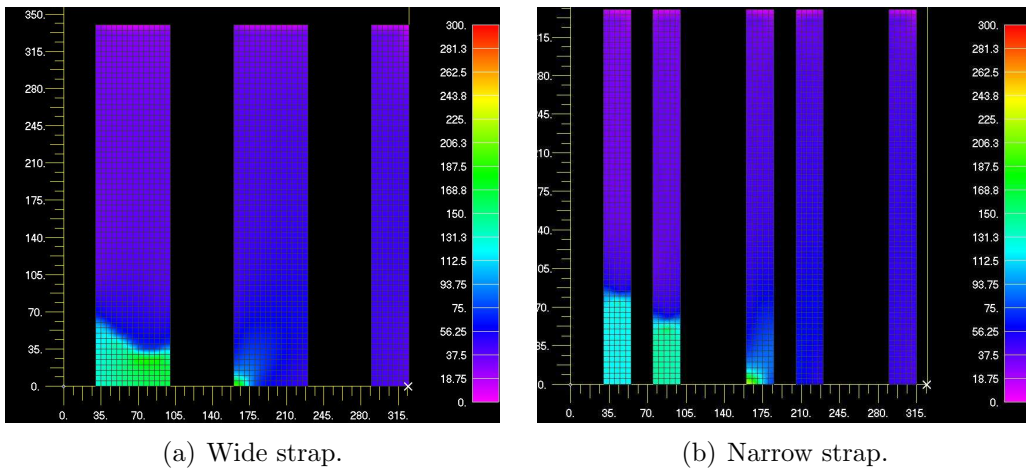


Figure 7.30: Von Mises stress contours for a substrate crack $a = 165$ mm for aluminium strap configurations.

Chapter 8

Conclusions and future studies

8.1 Predictive model development

A two-dimensional finite element modelling methodology has been developed to calculate the stress intensity factors (SIF) and predict the fatigue crack growth (FCG) life of bonded strap reinforced structures. The novel aspects introduced in this methodology are:

1. Through-thickness distribution of strain energy release rate (SERR) and SIF can be computed by 2D finite elements.
2. An average through-thickness SIF value is determined by a parabolic weight function to model typical curved crack front in thick substrate with one-side strap reinforcement.
3. Adhesive disbond and progressive damage growth are modelled throughout the life of the lead crack in the substrate.
4. Thermal residual stresses (TRS) and their redistribution due to crack growth are computed and their effect is taken into account in the stress intensity factor calculation.
5. Effect of secondary bending produced by both mechanical and thermal stresses is computed and considered in the through-thickness SIF distribution. Geometric nonlinearity is dealt with by using the “alternate analysis”

method which also takes into account of the nonlinear interaction between the mechanical and thermal stress fields.

This modelling methodology has been implemented into a computer program, which has been called LICRA (Life Increment Crack Retarders Analysis). LICRA interfaces NASTRAN commercial program to conduct the FE analysis.

This modelling methodology has been validated against a wide range of experimental tests and given good fatigue crack growth life predictions. It has also been used to demonstrate the effectiveness of bonded straps in enhancing the damage tolerance capability of integral metallic structures.

8.2 Design parameter studies

Extensive parametric studies of different crack retarders (materials, adhesives, dimension and positions) have been conducted by LICRA to find the key variables which influence the effectiveness of the straps. Main conclusions on strap performance, influential design variables, and their interactions are:

1. Strap stiffness plays an important role in decreasing crack propagation rate. Higher material elastic modulus and larger strap cross-section area increase the strap performance.
2. Tensile thermal residual stress (TRS) arising from elevated temperature cure increase crack propagation rate. Tensile TRS can be reduced by decreasing the cure temperature of the adhesive and/or the mismatch of coefficients of thermal expansion between the strap and substrate. This makes straps more effective.
3. Tougher adhesives reduce disbond propagation. Stiffer adhesives increase the crack bridging effect but also interlaminar shear stresses. The ideal adhesive should be as tougher and stiffer as possible.
4. Based on the analysis of reinforced M(T) samples, under constant amplitude load, with adhesive being cured at room temperature, the studied strap materials are ranked from best to worst as: CFRP, GLARE, Ti-6Al-4V, and GFRP (based on same strap weight).

5. Based on the analysis of reinforced SENT samples, under constant amplitude load, with adhesive cured at 120°C , the studied strap materials are ranked from best to worst as: Ti-6Al-4V, CFRP, GLARE, and GFRP (based on same strap dimension). It must be said that the life improvement offered by CFRP straps was overestimated by the modelling technique.
6. The magnitude of the TRS effect on FCG is affected by applied stress levels and substrate material crack growth rate law. At higher SIF ranges, the stiffness of the strap is the most influential variable and the TRS effect is limited, thus strap material choice should be based on the elastic modulus. At lower SIF ranges, the TRS effect can strongly reduce or even cancel the stiffening and bridging effect, thus strap material selection should be based on the coefficients of thermal expansion.
7. The best strap material should offer balanced properties in terms of stiffness, weight, coefficient of thermal expansion, compatibility with the aluminium substrate and fatigue properties. The fibre metal laminate GLARE seems to possess these characteristics.

FCG rates are sensitive to many factors, such as applied stress, TRS stress, crack tip position in the residual stress field, secondary bending, bridging effect, and adhesive failure. For this reason the best strap material and dimensions for any structure cannot be given. General guidelines to the design of the straps have been given, although, for any given structure, the use of the design graph (presented in section 6.3) is recommended.

LICRA computer code can be used to create the design graphs needed to find the best strap design (material, dimensions and weight) to achieve a given life target. This is the searched, fully operational and validated, numerical tool to design efficient selective reinforcements.

8.3 Contributions to knowledge

1. The effectiveness of bonded straps has been demonstrate for large-scale integral skin-stringer panels under a variable amplitude load spectrum which is dominated by compressive loads.
2. The most important strap design variables and their sensitivity on the FCG

propagation have been identified. A way to find the lightest strap material and geometry for a given life target has been developed and described.

3. The developed modelling methodology includes all known mechanisms which influence crack propagation in bonded structures. It includes the following novelties: computation of through-thickness SERR and SIF distribution by 2D finite elements, a weight function to average the through-thickness SIF by considering a curved crack front, modelling of progressive adhesive failure, prediction of TRS distribution and redistribution with crack propagation, and the so-called “alternate analysis” developed to consider the geometric non-linearity due to the secondary bending and thermal mechanical coupling into the SIF range and effective R-ratio.

This technique is automatised in a computer program and applicable for bonded strap reinforced structures as well as bonded patch repair problems and integral panels with bonded stringers.

8.4 Recommended future studies

1. Modelling adhesive disbond propagation under fatigue load by a Paris' law type equation instead of the quasi-static disbond method used in this methodology.
2. Modelling damage accumulation for composite straps.
3. Modelling fatigue initial damage life and fatigue crack propagation in metallic straps.
4. Effect of ground-air-ground thermal cycles on the fatigue crack growth life of bonded strap reinforced structures.
5. Modelling of stringer crack growth independently from the substrate crack by computing the stringer crack stress intensity factor and coupling the two crack growth integrations.
6. Due to the fact that a β -solution for the structure cannot be found, in the case of variable amplitude load spectrum, the analysis is carried at the maximum applied load in order to obtain a conservative result; this ap-

proximation should be removed and a way to take into account of different load cycles in the stress intensity factor should be found.

7. Analysis, modelling and design of smart straps; sensor-actuator straps which could produce crack closure forces in the substrate and, in the meantime, monitor disbond propagation and the health of the structure.

References

- [1] H. J. Schmidt and B. Schmidt-Brandecker. Damage tolerance design and analysis of current and future aircraft structure. In *AIAA/ICAS International Air and Space Symposium and Exposition: the next 100 years*, Dayton, Ohio, July 2003. AIAA 2003-2784.
- [2] J. Munroe, K. Wilkins, and M. Gruber. Integral airframe structures (ias) validated feasibility study of integrally stiffened metallic fuselage panels for reducing manufacturing costs. Technical Report NASA/CR-2000-209337, Boeing Commercial Airplane Group, Seattle, Washington, May 2000.
- [3] E. Carrera and M. Boscolo. Classical and mixed finite elements for static and dynamic analysis of piezoelectric plates. *International journal for numerical methods in engineering*, 70:1135–1181, 2007.
- [4] E. Carrera, M. Boscolo, and A. Robaldo. Hierarchic multilayered plate elements for coupled multifield problems of piezoelectric adaptive structures: Formulation and numerical assessment. *Archives of computational methods in engineering*, 14:383–430, 2007.
- [5] E. Carrera, A. Robaldo, M. Boscolo, and C. Fagiano. Mixed elements for accurate vibration of piezo-electric plates. In *Proceedings 2nd ECCOMAS thematic conference on smart structures and materials*, Lisbon, Portugal, July 2005.
- [6] E. Carrera, M. Boscolo, C. Fagiano, and A. Robaldo. Mixed finite elements for piezoelectric plates based on unified formulation. In *XVII Congresso AIMETA di Meccanica Teorica e Applicata*, Florence, Italy, September 2005.

- [7] E. Carrera, M. Boscolo, C. Fagiano, and A. Robaldo. Unified formulation to assess multilayered plate analysis of thermo-mechanical problems. In *XVIII Congresso nazionale AIDAA*, Volterra(PI), Italy, September 2005.
- [8] M. Pacchione and J. Telgkamp. Challenges of the metallic fuselage. In *25th ICAS conference*, Hamburg, 2006.
- [9] H. J. Schmidt, C. Voto, and J. Hansson. Tango metallic fuselage barrel validation of advanced technologies. In J. Rouchon, editor, *Proceedings of the 21st Symposium of the International Committee on Aeronautical Fatigue, ICAF*, pages 273–288. Cepadues Editions, 2001.
- [10] S. Bansal. Finite element analysis of stress intensity factor of integrally stiffened panels. Master’s thesis, Cranfield University, United Kingdom, 2008.
- [11] M. B. Heinemann, R. J. Bucci, M. Kulak, and M. Garratt. Improving damage tolerance of aircraft structures through the use of selective reinforcement. In *Proceedings 23rd Symposium of International Committee on Aeronautical Fatigue (ICAF)*, pages 197–208, Hamburg, June 2005.
- [12] X. Zhang and Y. Li. Damage tolerance and fail safety of welded aircraft wing panels. *AIAA Journal*, 43(7):1613–1623, 2005.
- [13] G. I. Nesterenko. Comparison of damage tolerance of integrally stiffened and rivetted structures. In *ICAS congress*, 2000.
- [14] G. I. Nesterenko. Damage tolerance of integrally stiffened and riveted stiffened structures. In *ICAF congress*, 1999.
- [15] G. I. Nesterenko. Service life of airplane structures. In *ICAS congress*, 2002.
- [16] G. I. Nesterenko and B. G. Nesterenko. Ensuring structural damage tolerance of Russian aircraft. *International Journal of Fatigue*, 2008. In press.
- [17] J. Schijve. Crack stoppers and arall laminates. *Engineering Fracture Mechanics*, 37(2):405–421, 1990.
- [18] P. Colombi, A. Bassetti, and A. Nussbaumer. Delamination effects on cracked steel members reinforced by prestressed composite patch. *Theoretical and Applied Fracture Mechanics*, 39:61–71, 2003.

- [19] M. Colavita, A. Bowler, X. Zhang, and P. E. Irving. Adhesively bonded CFRP straps as fatigue crack growth retarders on AA2024-T3. In *SAMPE 2006*, Long Beach, April 2006.
- [20] A.J. Bowler. Crack stoppers and fail safety in integral metal aircraft structure. Master's thesis, Cranfield University, United Kingdom, 2005.
- [21] <http://www.aiqnet.com/aml/archives2007/4a%20al%20products%20for%20aero%20jboselli.pdf>. Internet page. Accessed January 2009.
- [22] D. Broek. *Elementary engineering fracture mechanics*. Marinus Nijhoff Publishers, 4 edition, 1986.
- [23] T. L. Anderson. *Fracture mechanics: fundamentals and applications*. CRC Press, 1995.
- [24] E. E. Gdoutos. *Fracture mechanics. An introduction*. Springer, 2 edition, 2005.
- [25] www.owl.net.rice.edu/~msci301/fuchs%20fig4.8.jpg. internet page. Accessed September 2007.
- [26] A. A. Griffith. The phenomena of rupture and flow in solids. *Philosophical Translation Royal Society London*, A221:163–197, 1921.
- [27] G. R. Irwin. Onset of fast crack propagation in high strength steel and aluminium alloys. *Sagamore Research Conference Proceedings*, 2:289–305, 1956.
- [28] G. R. Irwin. *Fracture, Handbuch der Physik VI*. Springer-Verlag, 19 edition, 1958.
- [29] D. Broek. *Elementary engineering fracture mechanics*, chapter 5 The energy principle, pages 123–149. Marinus Nijhoff Publishers, 4 edition, 1986.
- [30] E.F. Rybicki and M.F. Kanninen. A finite element calculation of stress intensity factors by a modified crack closure integral. *Engineering Fracture Mechanics*, 9:931–938, 1977.
- [31] D. P. Rooke and D. J. Cartwright. *Compendium of Stress Intensity Factors*. Her Majesty's Stationery Office, London, 1976.
- [32] Y. Murakami. *Stress intensity factors handbook*. Pergamon, 1987.

- [33] H. M. Westergaard. Bearing pressures and cracks. *Journal of Applied Mechanics*, 6:49–53, 1939.
- [34] P. C. Paris and G.C. Sih. Stress analysis of cracks. *ASTM STP*, 381:30–81, 1965.
- [35] J. R. Rice. Some remarks on elastic crack-tip stress fields. *International Journal of Solids and Structures*, 8:751–758, 1972.
- [36] J.D. Eshelby. Calculation of energy release rate. In *Conference on Prospects of Advanced Fracture Mechanics*, pages 69–84, Delf, 1974.
- [37] D. J. Cartwright and D. P. Rooke. Methods of determining stress intensity factors. Technical Report 73031, RAE, 1973.
- [38] D. R. J. Owen and A. J. Fawkes. *Engineering fracture mechanics: Numerical methods and applications*. Pineridge Press, 1983.
- [39] D.M. Tracey. Finite elements for determination of crack tip elastic stress intensity factor. *Engineering Fracture Mechanics*, 3:255–266, 1971.
- [40] W.S. Blackburn. Calculation of stress intensity factors at crack tips using special finite elements. In *The Mathematics of Finite Elements*, pages 327–336, 1973.
- [41] J.E. Akin. The generation of elements with singularities. *International Journal of Numerical Methods in Engineering*, 10(1):1249–1260, 1976.
- [42] S.E. Benzley. Representation of singularities with isoparametric finite elements. *International Journal of Numerical Methods in Engineering*, 8(3):537–545, 1974.
- [43] R.S. Barsoum. On the use of isoparametric finite elements in linear fracture mechanics. *International Journal of Numerical Methods in Engineering*, 10(1):25–37, 1976.
- [44] R.D. Henshell and K.G. Shaw. Crack tip elements are unnecessary. *International Journal of Numerical Methods in Engineering*, 9:495–509, 1975.
- [45] P.R. Heyliger. On conventional and quarter point mixed elements in linear elastic fracture mechanics. *Engineering Fracture Mechanics*, 31:157171, 1988.

- [46] V.B. Watwood. The finite element method for prediction of crack behavior. *Nuclear Engineering and Design*, 11:323–332, 1969.
- [47] T. K. Hellen. On the method of virtual crack extension. *International Journal of Numerical Methods in Engineering*, 9:187–207, 1975.
- [48] D. M. Parks. A stiffness derivative finite element technique for determination of crack tip stress intensity factors. *International Journal of Fracture*, 10:487–502, 1974.
- [49] D. M. Parks. The virtual crack extension method for nonlinear material behaviour. *Computer Methods in Applied Mechanics and Engineering*, 12:353–364, 1977.
- [50] D. M. Parks. Virtual crack extension: A general finite element technique for j-integral evaluation. *Numerical Methods in Fracture Mechanics*, pages 464–479, 1978.
- [51] J.R. Rice. A path independent integral and the approximate analysis of strain concentration by notches and cracks. *Journal of Applied Mechanics*, 35:379–386, 1968.
- [52] I.S. Raju. Calculation of strain energy release rate with higher order and singular finite elements. *Engineering Fracture Mechanics*, 28:251–274, 1987.
- [53] J.T. Wang and I.S. Raju. Strain energy release rate formulae for 3d finite element. *Engineering Fracture Mechanics*, 54:211–228, 1995.
- [54] R. Krüger, M. König, and T. Schneider. Computation of local energy release rates along straight and curved delamination fronts of unidirectionally laminated dcb- and enf- specimens. In *Proceedings of the 34th AIAA/ASME/ASCE/AHS/ASC SSDM Conference*, pages 1332–1342, La Jolla, CA, 1993.
- [55] R. Krueger. The virtual crack closure technique: history, approach and applications. Report No. 2002-10 NASA/CR-2002-211628, ICASE, ICASE Mail Stop 132C NASA Langley Research Center Hampton, 2002.
- [56] P.C. Paris and F. Erdogan. A critical analysis of crack propagation laws. *Journal of Basic Engineering, Translation ASME, Series D*, 85(3):528–534, 1963.

- [57] R.G. Forman, V.E. Kearney, and R.M. Engle. Numerical analysis of crack propagation in cyclic-loaded structures. *Journal of Basic Engineering*, 89:459–464, 1967.
- [58] J. A. Harter. Modgro user manual, version 1.2, technical memorandum. Technical Report AFWAL-TM-88-157-FIBE, AFWAL Flight dynamics laboratory, July 1994.
- [59] K. Walker. The effect of stress ratio during crack propagation and fatigue for 2024-t3 and 7075-t6 aluminum. Technical Report ASTM STP 462, ASTM, 1970.
- [60] R.G. Forman and S.R. Mettu. Behavior of surface and corner cracks subjected to tensile and bending loads in ti-6al-4v alloy. In *Fracture mechanics 22nd Symposium*, 1992. ASTM STP 1131.
- [61] J.A. Harter. *AFGROW users guide and technical manual*. Air Vehicles Directorate, afrl-va-wp-tr-2006-xxxx edition, June 2006.
- [62] D. Broek. *Elementary engineering fracture mechanics*, chapter 17.7 Safety Factors, pages 470–471. Marinus Nijhoff Publishers, 4 edition, 1986.
- [63] A. A. Baker. Repair of cracked or defective metallic aircraft components with advanced fibre composites - an overview of australian work. *Composite Structures*, 2:153–181, 1984.
- [64] A. A. Baker. A summary of work on applications of advanced fibre composites at the aeronautical research laboratories, Australia. *Composites*, 9(1):11–16, 1978.
- [65] A. A. Baker. Evaluation of adhesives for fibre composite reinforcement of fatigue cracked aluminium alloys. *SAMPE Journal*, 15:10–17, 1979.
- [66] A. A. Baker. Fibre composite repair of cracked metallic aircraft components - practical and basic aspects. *Composites*, 18(4):293–308, 1987.
- [67] A. A. Baker. Bonded composite repair of fatigue-cracked primary aircraft structure. *Composite Structures*, 47:431–443, 1999.
- [68] A.A. Baker, L.R.F. Rose, and R. Jones. *Advanced in the bonded composite repair of metallic aircraft structure*. Elsevier, 2002.

- [69] R.J. Callinan, L.R.F. Rose, and C.H. Wang. Three dimensional stress analysis of crack patching. In *Proceedings 9th International conference on fracture*, pages 2151–2158, April 1997.
- [70] M. Heller and R. Kaye. Shape optimisation for bonded repairs. In Baker, F. Rose, and R. Jones, editors, *Advances in the bonded composite repairs of metallic aircraft structures*, pages 269–291. Elsevier, 2002.
- [71] A. A. Baker, M. J. Davis, and G. A. Hawkes. Repair of fatigue cracked aircraft structures with advanced fibre composites: residual stress and thermal fatigue study. In *Proceedings 10th International Committee on Aeronautical Fatigue (ICAF)*, page paper 4.3, 1979.
- [72] M. M. Ratwani. Analysis of cracked adhesively bonded laminated structures. *AIAA Journal*, 17(9):988–994, 1979.
- [73] C. H. Wang, L. R. F. Rose, and R. Callinan. Analysis of out-of-plane bending in one-sided bonded repair. *International Journal of Solids and Structures*, 35(14):1653–1675, 1998.
- [74] L. R. F. Rose. An application of the inclusion analogy for bonded reinforcements. *International journal of Solids and Structures*, 17(2):135–144, 1981.
- [75] L. R. F. Rose. A cracked plate repaired by bonded reinforcements. *International Journal of Fracture*, 18(2):135–144, 1982.
- [76] L. R. F. Rose and C. H. Wang. Analytical methods for designing composite repairs. In Baker, F. Rose, and R. Jones, editors, *Advances in the bonded composite repairs of metallic aircraft structures*, pages 137–175. Elsevier, 2002.
- [77] C. H. Wang and L.R.F. Rose. On the design of bonded patches for one-sided repair. In *Proceedings 11th International conference on composite materials*, pages 347–356, Gold Coast, Australia, July 1997.
- [78] C. H. Wang, L. R. F. Rose, R. Callinan, and A. A. Baker. Thermal stresses in a plate with a circular reinforcement. *International Journal of Solids and Structures*, 37:4577–4599, 2000.

- [79] C. H. Wang and L.R.F. Rose. A crack bridging model for bonded plates subjected to tension and bending. *International Journal of Solids and Structures*, 36:1985–2014, 1999.
- [80] M.J. Young and C. T. Sun. On the strain energy release rate for cracked plate subjected to out-of-plane bending moment. *International Journal of Fracture*, 60:227–247, 1993.
- [81] C. Arendt and C. T. Sun. Bending effects of unsymmetric adhesively bonded composite repairs on cracked aluminum panels. In *Proceedings of the FAA/NASSA symposium on advanced integrity methods for airframe durability and damage tolerance, Pt. 1*, pages 33–48, Hampton, VA, 1994.
- [82] C. T. Sun, J. Klung, and C. Arendt. Analysis of cracked aluminium plates repaired with bonded composite patches. *AIAA Journal*, 34(2):369–374, 1996.
- [83] J. Klug, S. Maley, and C. T. Sun. Characterization of fatigue behavior of bonded composite repairs. *Journal of Aircraft*, 36(6):1016–1022, 1999.
- [84] R. Jones and R. J. Callinan. On the special crack tip elements in cracked elastic sheets. *International Journal of Fracture*, 13:51–54, 1977.
- [85] R. Jones and R. J. Callinan. Finite element analysis of patched cracks. *Journal Structural Mechanics*, 7:107–130, 1979.
- [86] R. Jones and R. J. Callinan. A design study on crack patching. *Fibre Science Technology*, 14:99–111, 1981.
- [87] R. Chandra and K. Guruprasad. Numerical estimation of stress intensity factors in patched cracked plates. *Engineering Fracture Mechanics*, 27(5):559–569, 1987.
- [88] S. Naboulsi and S. Mall. Modelling of a cracked metallic structure with bonded composite patch using the three layer technique. *Composite Structures*, 35:295–308, 1996.
- [89] T.V.R.S. Umamaheswar and R. Singh. Modelling of a patch repair to a thin cracked sheet. *Engineering Fracture Mechanics*, 63:267–289, 1999.

- [90] V. Sabelkin, S. Mall, and J.B. Avram. Fatigue crack growth analysis of stiffened cracked panel repaired with bonded composite patch. *Engineering Fracture Mechanics*, 73:1553–1567, 2006.
- [91] V. Sabelkin, S. Mall, M.A. Hansen, R.M. Vandawaker, and M. Derriso. Investigation into cracked aluminium plate repaired with bonded composite patch. *Composite Structures*, 79:55–56, 2007.
- [92] X. B. Lin and R. A. Smith. Finite element modelling of fatigue crack growth of surface cracked plates. Part I: The numerical technique. *Engineering Fracture Mechanics*, 63:503–522, 1999.
- [93] X. B. Lin and R. A. Smith. Finite element modelling of fatigue crack growth of surface cracked plates. Part II: Crack shape change. *Engineering Fracture Mechanics*, 63:523–540, 1999.
- [94] X. B. Lin and R. A. Smith. Finite element modelling of fatigue crack growth of surface cracked plates. Part III: Stress intensity factor and fatigue crack growth life. *Engineering Fracture Mechanics*, 63:541–556, 1999.
- [95] Woo-Yong Lee and Jung-Ju Lee. Fatigue behavior of composite patch repaired aluminum plate. *Journal of Composite Materials*, 39(16):1449–1463, 2005.
- [96] Woo-Yong Lee and Jung-Ju Lee. Successive 3d fe analysis technique for characterization of fatigue crack growth behavior in composite-repaired aluminum plate. *Composite Structures*, 66:513–520, 2004.
- [97] H. Hosseini-Toudeshky, B. Mohammadi, G. Sadeghi, and H.R. Daghyani. Numerical and experimental fatigue crack growth analysis in mode-i for repaired aluminum panels using composite material. *Composites Part A: applied science and manufacturing*, 38:1141–1148, 2007.
- [98] H. Hosseini-Toudeshky and B. Mohammadi. A simple method to calculate the crack growth life of adhesively repaired aluminum panels. *Composite Structures*, 79:234–241, 2007.
- [99] A. Needleman. Continuum model for void nucleation by inclusion debonding. *Journal of applied mechanics*, 32:525–531, 1987.

- [100] A. Needleman and A. J. Rosakis. Effect of bond strength and loading rate on the conditions governing the attainment of intersonic crack growth along interfaces. *Journal of the Mechanics and Physics of Solids*, 47(12):2411–2449, 1999.
- [101] A. Needleman. An analysis of intersonic crack growth under shear loading. *Journal of Applied Mechanics, Transactions ASME*, 66(4):847–857, 1999.
- [102] A. Needleman and V. Tvergaard. An analysis of ductile rupture modes at a crack tip. *Journal of the Mechanics and Physics of Solids*, 35(2):151–183, 1987.
- [103] H. H. M. Cleveringa, E. Van Der Giessen, and A. Needleman. Discrete dislocation analysis of bending. *International journal of plasticity*, 15(8):837–868, 1999.
- [104] P. P. Camanho, C. G. Dàvila, and D. R. Ambur. Numerical simulation of delamination growth in composite materials. Technical Report TP-2001-211041, NASA, August 2001.
- [105] P. P. Camanho and C.G. Dàvila. Mixed-mode decohesion finite elements for the simulation of delamination in composite materials. Technical Report TM-2002-211737, NASA, June 2002.
- [106] M. A. Crisfield, H. B. Hellweg, and G. A. O. Davies. Failure analysis of composite structures using interface elements. In *Proceedings of the NAFEMS conference on application of finite elements to composite materials, volume 1-4*. 1997.
- [107] A. Puck and H. Schurmann. Failure analysis of frp laminates by means of physically based phenomenological models. *Composites Science and Technology*, 58(7):1045–1067, 1998.
- [108] C. Schuecker, D. H. Pahr, and H. E. Pettermann. Accounting for residual stresses in fem analyses of laminated structures using the puck criterion for three-axial stress states. *Composites Science and Technology*, 66(13):2054–2062, 2006.
- [109] C. Schuecker and H. E. Pettermann. A continuum damage model for fiber reinforced laminates based on ply failure mechanisms. *Composite Structures*, 76(1-2):162–173, 2006.

- [110] C. Schuecker and H. E. Pettermann. Fiber reinforced laminates: Progressive damage modeling based on failure mechanisms. *Archives of Computational Methods in Engineering*, 15(2):163–184, 2008.
- [111] C. Schuecker and H. E. Pettermann. Constitutive ply damage modeling, fem implementation, and analyses of laminated structures. *Computers and Structures*, 86(9):908–918, 2008.
- [112] G. Wimmer, C. Schuecker, and H. E. Pettermann. Numerical simulation of delamination onset and growth in laminated composites. In *Proceedings of the CDCM 2006 - Conference on Damage in Composite Materials*. Stuttgart, Germany, September 2006.
- [113] D. Xie and S.B. Jr. Biggers. Strain energy release rate calculation for moving delamination front of arbitrary shape based on the virtual crack closure technique. part i: Formulation and validation. *Engineering Fracture Mechanics*, 73:771–785, 2006.
- [114] D. Xie and S.B. Jr. Biggers. Strain energy release rate calculation for moving delamination front of arbitrary shape based on the virtual crack closure technique. Part II: Sensitivity study on modeling details. *Engineering Fracture Mechanics*, 73:786–801, 2006.
- [115] D. J. Wilkins, J.R. Eisenmann, R.A Camin, W.S. Margolis, and R.A Benson. Characterising growth in graphite-epoxy. In *Damage in composite materials*, pages 168–183, 1982. ASTM STP 775.
- [116] A.S. Wang, M. Slomiana, and R.B. Buncinel. Delamination crack growth in composite laminates. In *Delamination and debonding of materials*, page 135167, 1985. ASTM STP 876.
- [117] C. Bathias. Delamination threshold and loading effect in fiber glass epoxy composites. In *Delamination and debonding of materials*, page 21737, 1985. ASTM STP 876.
- [118] C. Gustafson and M. Hojo. Delamination fatigue crack growth in unidirectional graphite/epoxy laminates. *Journal of Reinforced Plastic and Composite*, 6:36–52, 1987.

- [119] S. Mall and W.S. Johnson. Characterization of mode i and mixed-mode failure of adhesive bonds between composite adherents. In *Composite materials: testing and design 7th conference*, page 322334, 1986. ASTM STP 893.
- [120] T.K. O'Brien. Towards a damage tolerance philosophy for composite materials and structures. Technical Report 1059, ASTM Special Technical Publication, 1990.
- [121] A. J. Vinciquerra, B.D. Davinson, J.R. Schaff, and S. L. Smith. Determination of mode ii fatigue delamination toughness of laminated composites. *Journal of Reinforced plastics and composites*, 21(07):663–677, 2002.
- [122] J. Andersons, M. Hojo, and S. Ochiai. Empirical model for stress ratio effect on fatigue delamination growth rate in composite laminates. *International Journal of Fatigue*, 26:597–604, 2004.
- [123] K. Shivakumara, H. Chena, F. Abalib, Dy Leb, and C. Davis. A total fatigue life model for mode i delaminated composite laminates. *International Journal of Fatigue*, 28:33–42, 1995.
- [124] G.A. Kardomateas, A.A. Pelegri, and B. Malik. Growth of internal delamination under cyclic compression in composite plates. *Journal of the Mechanics and Physics of Solids*, 43(6):847–868, 1995.
- [125] A. J. Kinloch and S. O. Osiiyemi. Predicting the faigue life of adhesively-bonded joints. *Journal of adhesion*, 43:73–90, 1993.
- [126] A. J. Curley, H. Hadavinia, A. J. Kinloch, and A. C. Taylor. Predicting the service-life of adhesively-bonded joints. *International Journal of Fracture*, 103(1):41–69, 2000.
- [127] A. J. Kinloch and A. C. Taylor. The use of fracture mechanics techniques to predict the service life of adhesive joints. In D. R. Moore, editor, *The application of fracture mechanics to Polymers, adhesives and composites, volume 33*, pages 187–192.ESIS publications, 2003.
- [128] H. Hadavinia, A. J. Kinloch, M. S. G. Little, and A. C. Taylor. The prediction of crack growth in bonded joints under cyclic-fatigue loading. Part I. Eperimental studies. *International Journal of Adhesion and Adhesives*, 23:449–461, 2003.

- [129] H. Hadavinia, A. J. Kinloch, M. S. G. Little, and A. C. Taylor. The prediction of crack growth in bonded joints under cyclic-fatigue loading. Part II. Analytical and finite element studies. *International Journal of Adhesion and Adhesives*, 23:463–471, 2003.
- [130] D. J. Shim, R. C. Alderliesten, S. M. Spearing, and D. A. Burianek. Fatigue crack growth prediction in glare hybrid laminates. *Composites Science and Technology*, 63(12):1759–1767, 2003.
- [131] R. C. Alderliesten. Effect of elevated temperature and moisture on fatigue delamination in the fiber metal laminate glare. In *9th joint FAA/DoD/NASA conference on aging aircraft*, Atlanta, March 2006. http://www.agingaircraftconference.org/all_files/30/30d/35_doc.pdf.
- [132] R.C. Alderliesten, J. Schijve, and S. van der Zwaag. Application of the energy release rate approach for delamination growth in glare. *Engineering Fracture Mechanics*, 73:697–709, 2006.
- [133] R. C. Alderliesten and J. J. Homan. Fatigue and damage tolerance issues of glare in aircraft structures. *International Journal of Fatigue*, 28(10 SPEC. ISS.):1116–1123, 2006.
- [134] R. C. Alderliesten. On the available relevant approaches for fatigue crack propagation prediction in glare. *International Journal of Fatigue*, 29(2):289–304, 2007.
- [135] R. C. Alderliesten. Analytical prediction model for fatigue crack propagation and delamination growth in glare. *International Journal of Fatigue*, 29(4):628–646, 2007.
- [136] R. C. Alderliesten. Damage tolerance of bonded aircraft structures. *International Journal of Fatigue*, 2008. Article in Press.
- [137] P. Davies, H. H. Kausch, J. G. Williams, A. J. Kinloch, M. N. Charalambides, A. Pavan, D. R. Moore, R. Prediger, I. Robinson, N. Burgoyne, K. Friedrich, H. Wittich, C. A. Rebelo, A. Torres Marques, F. Ramsteiner, B. Melve, M. Fischer, N. Roux, D. Martin, P. Czarnocki, D. Neville, I. Verpoest, B. Goffaux, R. Lee, K. Walls, N. Trigwell, I. K. Partridge, J. Jausaud, S. Andersen, Y. Giraud, G. Hale, and G. McGrath. Round-robin interlaminar fracture testing of carbon-fibre-reinforced epoxy and peek composites. *Composites Science and Technology*, 43(2):129–136, 1992.

- [138] I. Partridge. Internal meetings and communications.
- [139] F. Tahmasebi. Software tools for analysis of bonded joints. Technical Report 542, NASA/GSFC, 2001.
- [140] Marco Boscolo, Giuliano Allegri, and Xiang Zhang. An enhanced 2D modelling technique for single-sided bonded patches. *AIAA Journal*, 2009. In press.
- [141] D. V. Nelson. Effects of residual stress on fatigue crack propagation. Technical Report STP 776, ASTM, 1982.
- [142] D. Figueroa-Gordon. Bonded crack retarders internal reports and documentations. unpublished data. Cranfield University.
- [143] J. C. Butcher. *Numerical differential equation methods*, chapter Numerical methods for ordinary differential equations, pages 45–121. John Wiley & Sons, 2004.
- [144] X. Zhang, D. Figueroa-Gordon, M. Boscolo, G. Allegri, and P. E. Irving. Improving fail-safety of aircraft integral structures through the use of bonded crack retarders. In *Proceedings 24th Symposium of International Committee on Aeronautical Fatigue (ICAF)*, Naples, May 2007.
- [145] X. Zhang, M. Boscolo, D. Figueroa-Gordon, G. Allegri, and P. E. Irving. Fail-safe design of integral metallic aircraft structures reinforced by bonded crack retarders. *Engineering Fracture Mechanics*, , 76:114–133, 2009.
- [146] P. E. Irving, D. Figueroa-Gordon, X. Zhang, and M. Boscolo. Bonded crack retarders for enhanced fail safety and damage tolerance in aircraft structures. In *Proceedings of 1st International Conference of Engineering Against Fracture (ICEAF)*, Patras, May 2008.
- [147] P. E. Irving and D. Figueroa-Gordon. Routes to improved damage tolerance; prediction of damage tolerant performance of high strength and hybrid structures. In *Proceedings of 1st International Conference on Damage Tolerance of Aircraft Structures (DTAS)*, Delft, September 2007. <http://www.dtas2007.nl> accessed on September 2008.
- [148] C. D. M. Liljedahl, M. E. Fitzpatrick, and L. Edwards. Distortion and residual stresses in structures reinforced with titanium straps for improved

- damage tolerance. *Materials Science and Engineering A*, 486:104–111, 2008.
- [149] C. D. M. Liljedahl, M. E. Fitzpatrick, and L. Edwards. Residual stresses in structures reinforced with adhesively bonded straps designed to retard fatigue crack growth. *Composite Structures*, 86:344–355, 2008.
- [150] C. D. M. Liljedahl. Bonded crack retarders internal reports and documentations. unpublished data. Open University.
- [151] M. Samprovalakis. Fatigue crack growth rate reduction in aircraft using bonded crack retarders. Master’s thesis, Cranfield University, United Kingdom, 2007.
- [152] X. B. Lin and R. A. Smith. Finite element modelling of fatigue crack growth of surface cracked plates. Part I: The numerical technique. *Engineering Fracture Mechanics*, 63:503–522, 1999.
- [153] G. Wu and J. Yang. The mechanical behavior of glare laminates for aircraft structures. *JOM*, 57(1):72–79, 2005.
- [154] J.N. Reddy. *Mechanics of laminated composite plates and shells: theory and analysis.*, chapter 3, Classical and first-order theories of laminated composite plates, pages 109–164. CRC Press, 1997.
- [155] M. B. Heinimann. Internal meetings and communications.
- [156] James A. Harter. Comparison of contemporary fcg life prediction tools. *International Journal of Fatigue*, 21(1):181 – 185, 1999.
- [157] J. C. Newman. FASTRAN II - fatigue crack growth structural analysis program. Technical Report TM-104159, NASA, Febraury 1992.
- [158] M. B. Heinimann and J. C. Newman. Internal communications.
- [159] Military handbook 5: Metallic materials and elements for aerospace vehicle structures, 1998.

Appendix A

List of publications

Journal papers

Papers on my PhD subject

1. M. Boscolo and X. Zhang. A modelling technique for calculating stress intensity factors for structures reinforced by bonded straps. Part I: Mechanisms and formulation. *Engineering Fracture Mechanics*, 2009. Submitted Jan 2009.
2. M. Boscolo and X. Zhang. A modelling technique for calculating stress intensity factors for structures reinforced by bonded straps. Part II: Validation. *Engineering Fracture Mechanics*, 2009. Submitted Jan 2009.
3. M. Boscolo, G. Allegri, and X. Zhang. An enhanced 2D modelling technique for single-side patch repairs. *AIAA Journal*, 2009. Accepted for publications Jan 2009.
4. X. Zhang, M. Boscolo, D. Figueroa-Gordon, G. Allegri, and P. E. Irving. Fail-safe design of integral metallic aircraft structures reinforced by bonded crack retarders. *Engineering Fracture Mechanics*, 2009. 76:114-133, 2009.
5. M. Boscolo, G. Allegri, and X. Zhang. Design and modelling of selective reinforcements for integral aircraft structures. *AIAA Journal*, 46(9):2323–2331, 2008.

Papers on other subjects

6. J. Cheng, M. Boscolo, L. Lin, X. Zhang, J. Ma, L. Zhang. Comparison of biomechanical property of cerebral and mesenteric small arteries of simulated microgravity rats. Submitted Dec 2008.
7. E. Carrera, M. Boscolo, and A. Robaldo. Hierarchic multilayered plate elements for coupled multifield problems of piezoelectric adaptive structures: Formulation and numerical assessment. *Archives of Computational Methods in Engineering*, 14(4):383–430, 2007.
8. E. Carrera and M. Boscolo. Classical and mixed finite elements for static and dynamic analysis of piezoelectric plates. *International Journal for Numerical Methods in Engineering*, 70:11351181, 2007.

Conference papers

Papers on my PhD subject

9. P.E. Irving, D. Figueroa-Gordon, X. Zhang, and M. Boscolo. Bonded crack retarders for enhanced fail safety and damage tolerance in aircraft structures. In *1st International Conference of Fatigue Against Fracture, ICEAF*, Patras, Greece 2008.
10. Marco Boscolo, Giuliano Allegri, and Xiang Zhang. An enhanced 2D modelling technique for single-sided bonded patches. In *49th AIAA/ASME/ASCE/AHS/ASC Structures, Structural Dynamics, and Materials Conference*, Schaumburg, IL, USA, April 2008.
11. X. Zhang, D. Figueroa-Gordon, M. Boscolo, G. Allegri, and P. E. Irving. Improving fail-safety of aircraft integral structures through the use of bonded crack retarders. In *Proceedings 24th Symposium of International Committee on Aeronautical Fatigue, ICAF 2007*, Naples, May 2007.
12. Marco Boscolo, Giuliano Allegri, and Xiang Zhang. Design and modelling of selective reinforcements for integral aircraft structures. In *48th*

AIAA/ASME/ASCE/AHS/ASC Structures, Structural Dynamics, and Materials Conference, pages 4980–4993, Waikiki, Honolulu, Hawaii, April 2007.

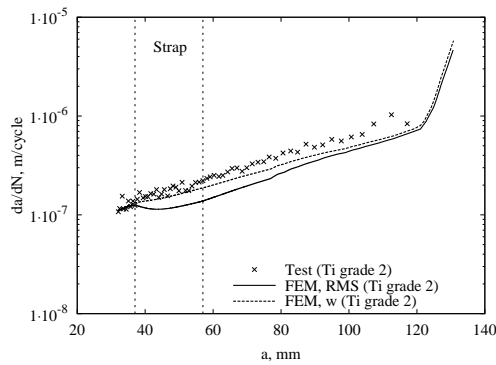
Papers on other subjects

13. E. Carrera, M. Boscolo, C. Fagiano, and A. Robaldo. Mixed finite elements for piezoelectric plates based on unified formulation. In *XVII Congresso AIMETA di Meccanica Teorica e Applicata*, Florence, Italy, September 2005.
14. E. Carrera, M. Boscolo, C. Fagiano, and A. Robaldo. Unified formulation to assess multilayered plate analysis of thermo-mechanical problems. In *XVIII Congresso nazionale AIDAA*, Volterra(PI), Italy, September 2005.
15. E. Carrera, M. Boscolo, C. Fagiano, and A. Robaldo. Mixed elements for accurate vibration of piezo-electric plates. In *II ECCOMAS Thematic Conference on Smart Structures and Materials*, Lisbon , Portugal, July 2005.

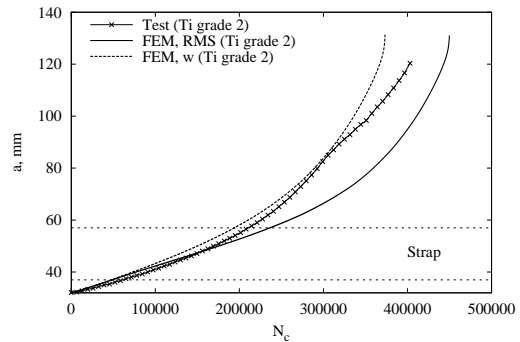
Appendix B

Validation of predicted FCG rates and lives

Plots of FCG rates and life for each validation case. Specimen geometries are shown in figure 5.7 and material properties in table 5.3. Strap dimension notation is defined in section 5.2.1. Both high temperature (HT) and room temperature (RT) cure cases are studied. FCG rates and life validation plots follow.

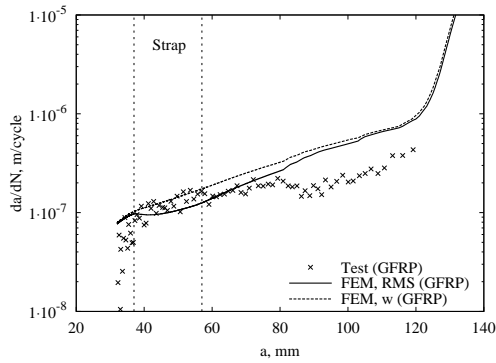


(a) FCG rate.

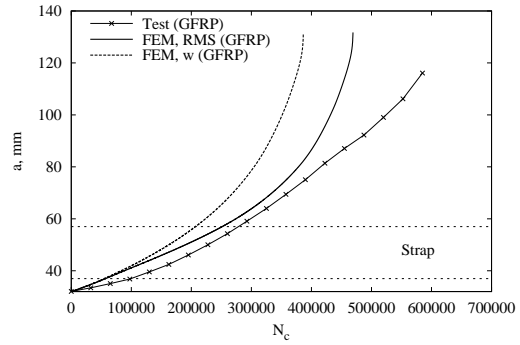


(b) FCG life:.

Figure B.1: Validation of FCG rate and life against test results: SENT, Ti grade2 strap *w20d5t2l200*, HT cure; Experiments from [142].

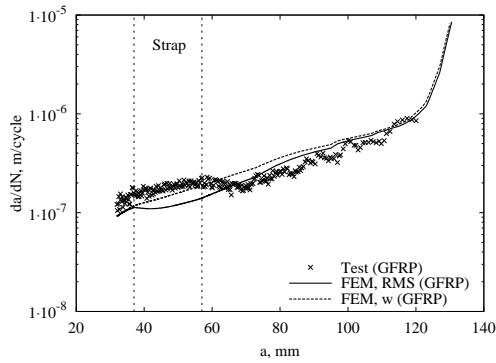


(a) FCG rate.

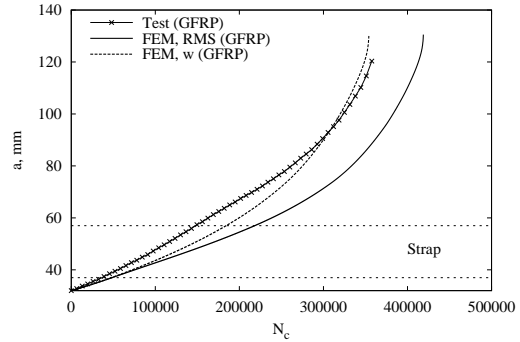


(b) FCG life:.

Figure B.2: Validation of FCG rate and life against test results: SENT, GFRP strap $w20d5t2l200$, RT cure; Experiments from [142].

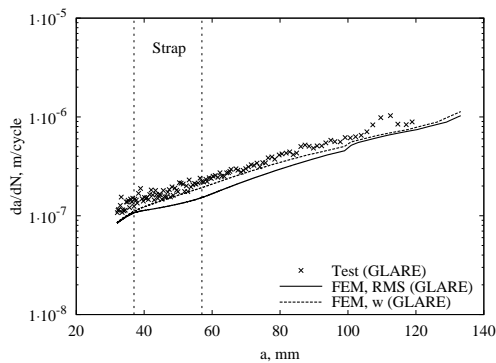


(a) FCG rate.

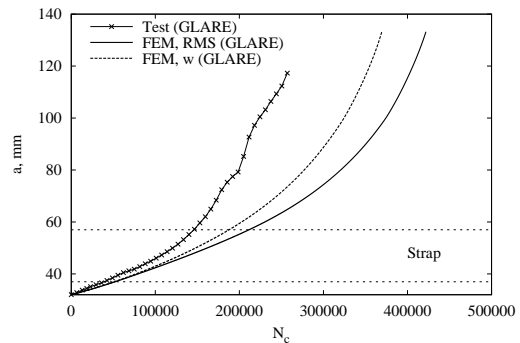


(b) FCG life:.

Figure B.3: Validation of FCG rate and life against test results: SENT, GFRP strap $w20d5t2l200$, HT cure; Experiments from [142].

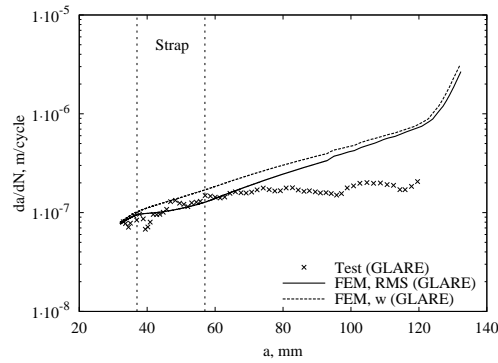


(a) FCG rate.

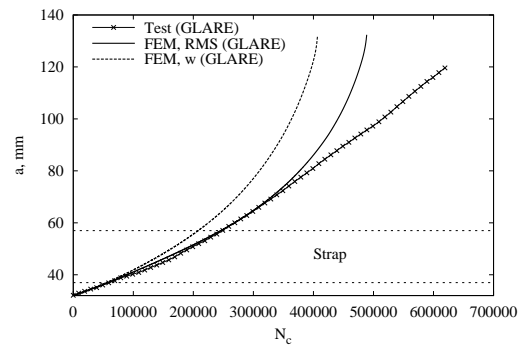


(b) FCG life:.

Figure B.4: Validation of FCG rate and life against test results: SENT, GLARE strap $w20d5t1.8l200$, HT cure; Experiments from [142].

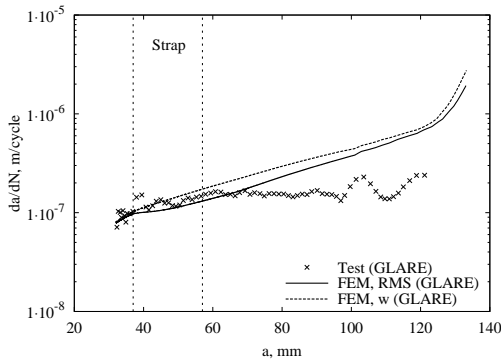


(a) FCG rate.

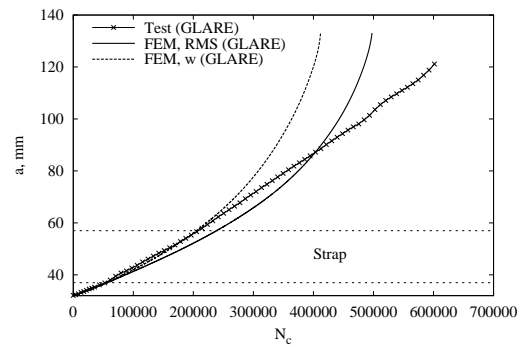


(b) FCG life:.

Figure B.5: Validation of FCG rate and life against test results: SENT, GLARE strap *w20d5t5.4l200*, HT cure; Experiments from [142].

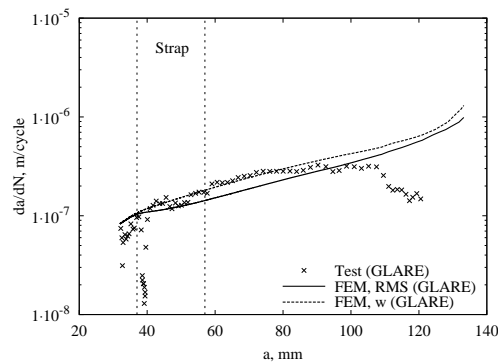


(a) FCG rate.

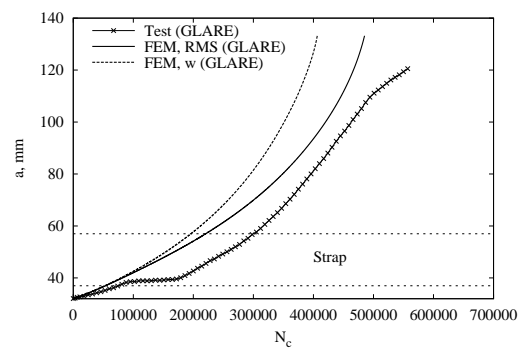


(b) FCG life:.

Figure B.6: Validation of FCG rate and life against test results: SENT, GLARE strap *w30d5t3.6l200*, HT cure; Experiments from [142].



(a) FCG rate.



(b) FCG life:.

Figure B.7: Validation of FCG rate and life against test results: SENT, GLARE strap *w60d5t1.8l200*, HT cure; Experiments from [142].

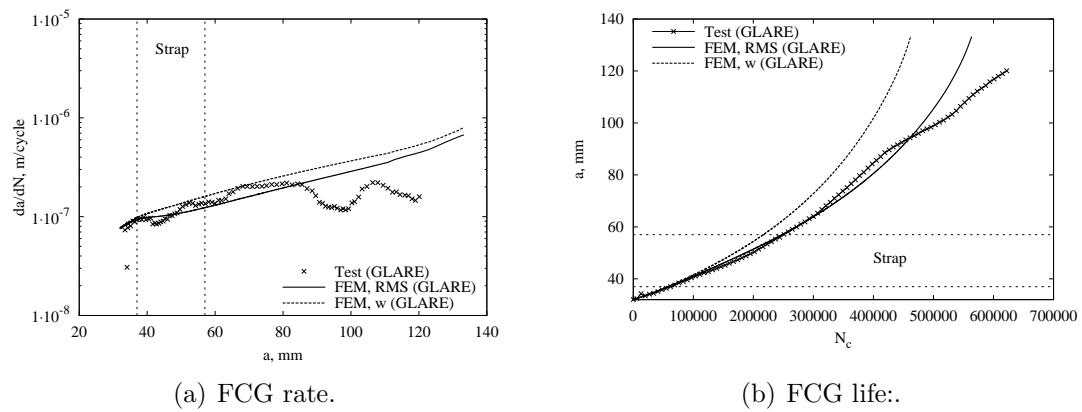


Figure B.8: Validation of FCG rate and life against test results: SENT, GLARE strap $w100d5t1.8l200$, HT cure; Experiments from [142].

Appendix C

Large panel: technical drawings

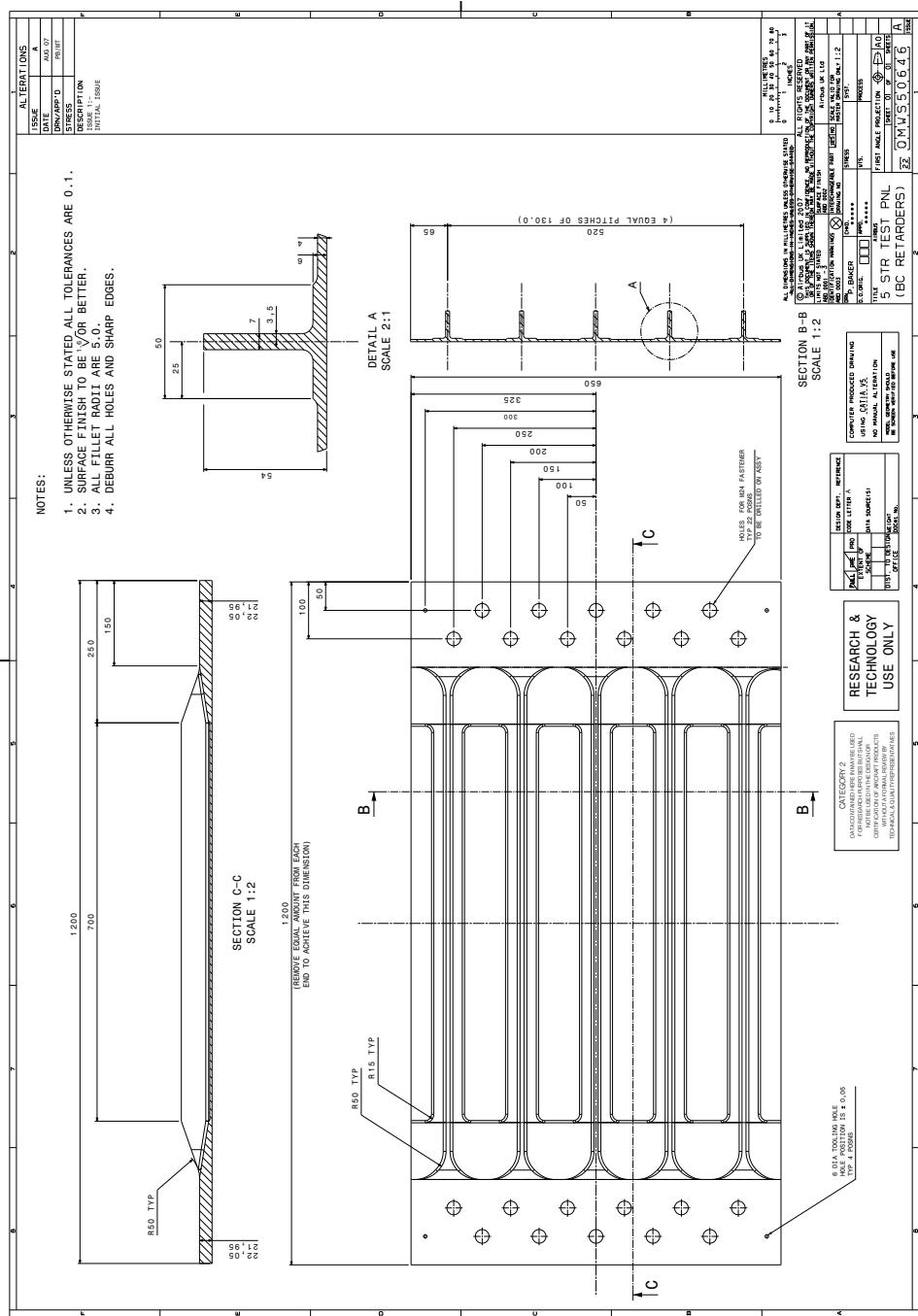


Figure C.1: Technical drawing of the un-reinforced large-scale integral skin-stringer panel. The drawing was provided courteously by Airbus.

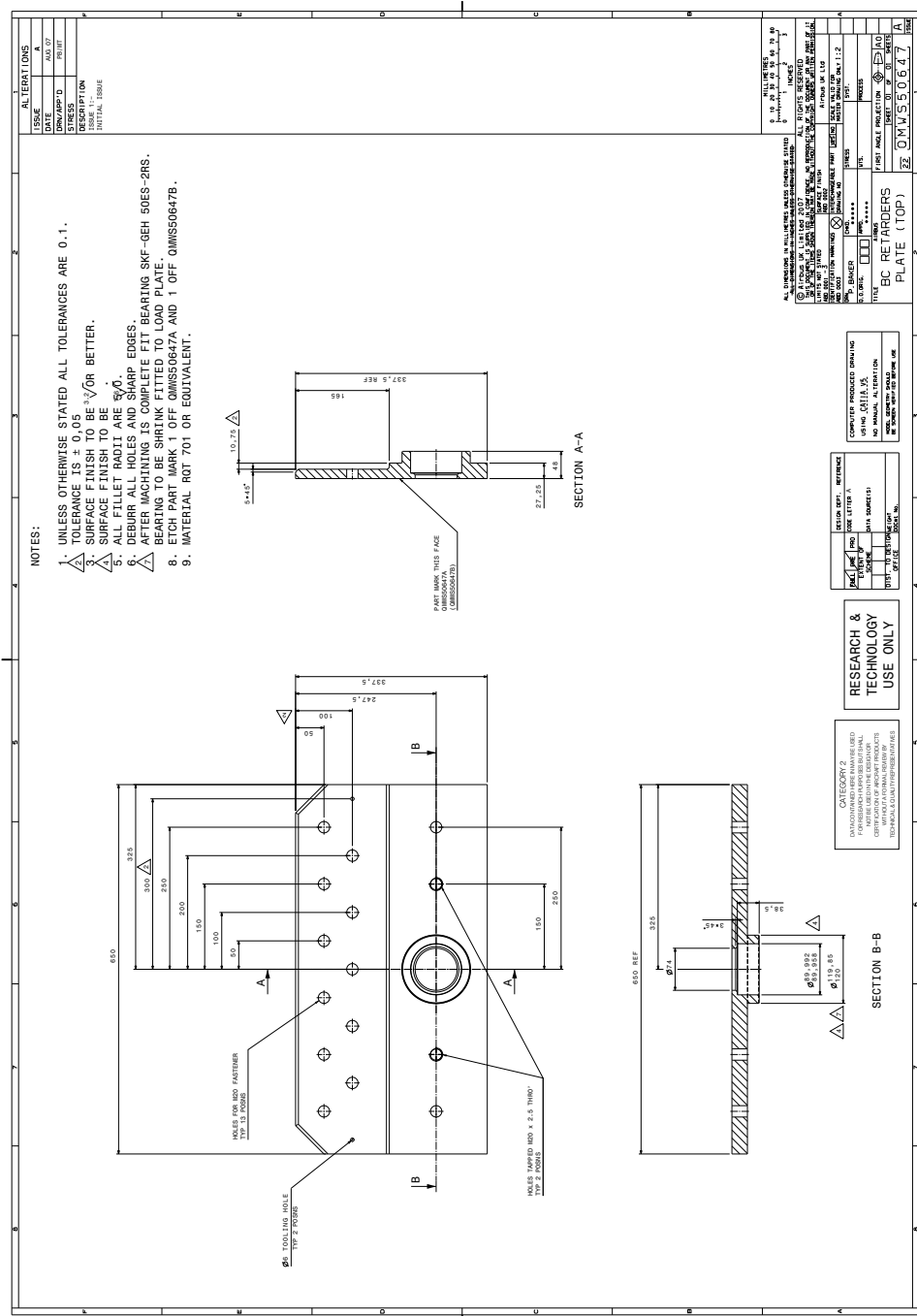


Figure C.2: Technical drawing of the top plate of the end fitting. The drawing was provided courteously by Airbus.

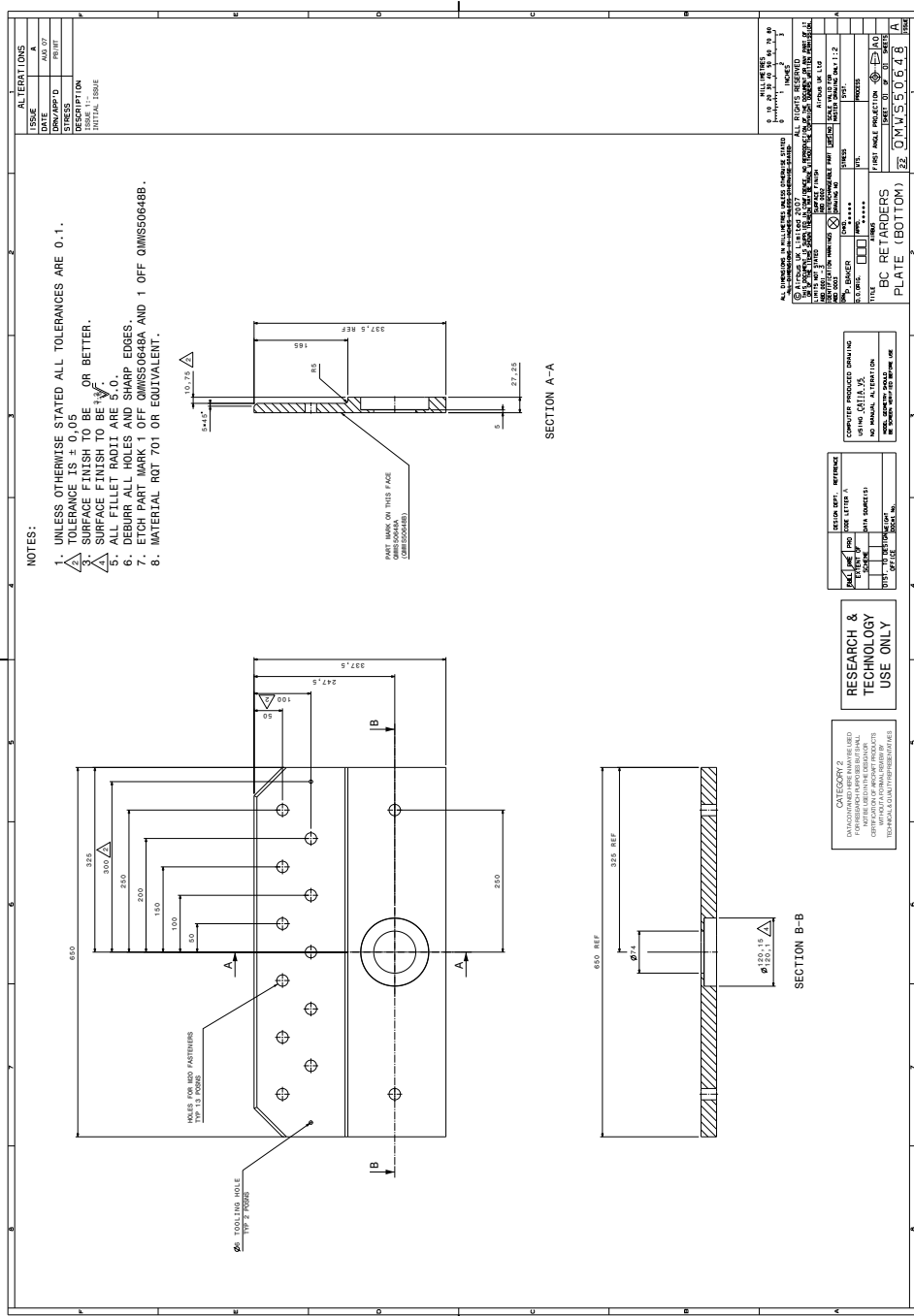


Figure C.3: Technical drawing of the bottom plate of the end fitting. The drawing was provided courtesy by Airbus.

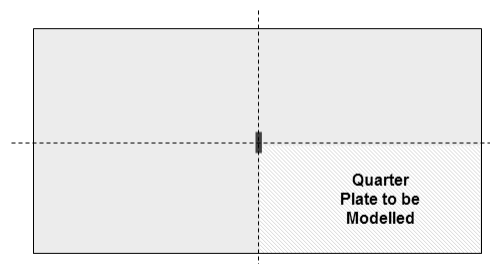
Appendix D

LICRA package user's instructions

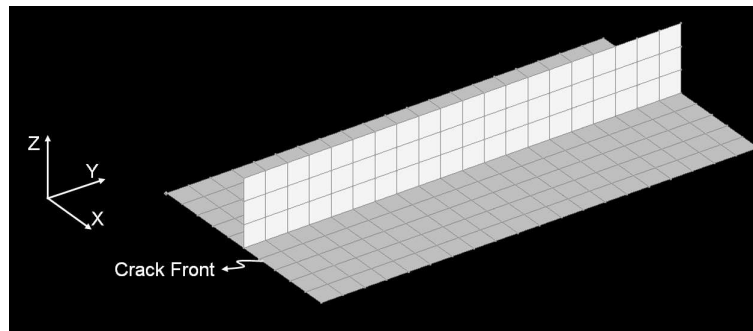
D.1 How to build the FE model

D.1.1 Geometry and orientation

Step 1. Only one quarter or half of the model should be modelled. The code can only study configuration with one crack front in the model, thus symmetric constrain should be used to reduce the structure to a simple model with only one crack front.



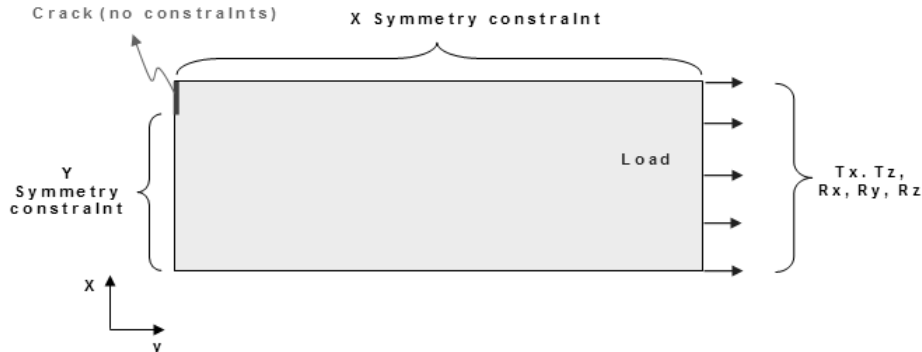
Step 2. It is necessary to use the right orientation of the panel. This is important for the code to work correctly, as it is designed for a specific orientation. As shown in the figure below the crack side must be on the X axis, the panel length on Y and the height of the panel or the depth on Z .



D.1.2 Meshing and boundary conditions

Step 3. Mesh must be regular on the crack front and beneath straps if presents. Constant width elements must be used on the crack propagation line. Square elements must be used for the substrate below the straps and the straps. .

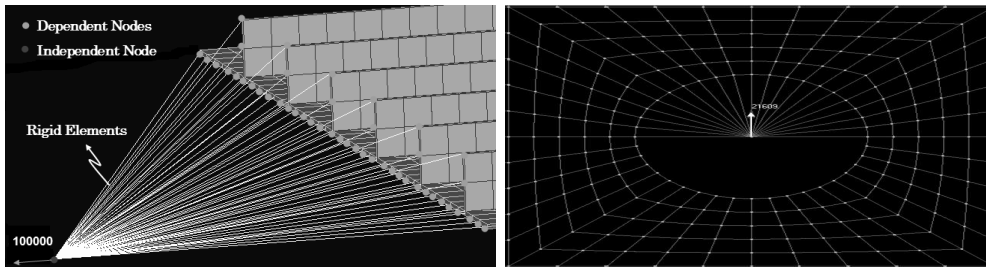
Step 4. The boundary conditions to use are shown in the figure shown next.



D.1.3 Load Application

Step 5. Rigid elements should be used to connect the nodes on the load end of the panel to an independent node as shown below in the first figure. However, if the end fitting section is modelled then the pin can be simplified as shown in the second figure. Here a node is created in the centre of the hole and all the nodes on half the edge of the hole are connected to it with all directions constrained. Further, the load to be applied by the pin is applied of the independent node in the centre.

In the case of strap analysis rigid elements cannot be used for the load application because will be misunderstood by the code has adhesive elements. This problem can be solved by using really stiff beam elements.



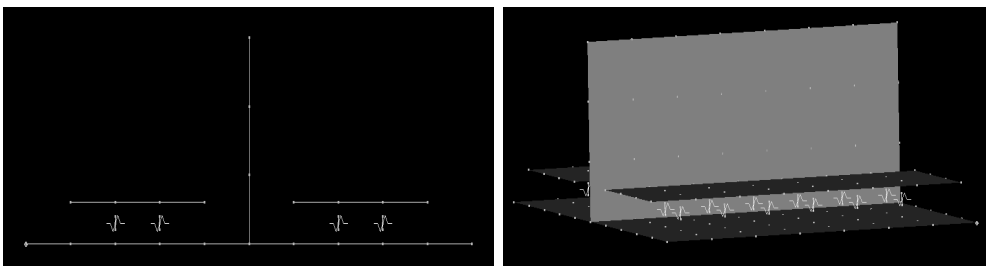
D.1.4 Strap modelling and adhesive modelling

This section is meant for analysis for bonded crack retarder panels only and should be skipped for un-reinforced panels.

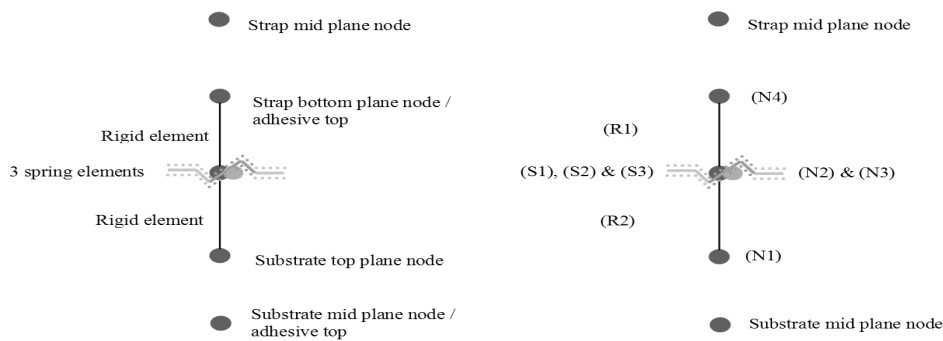
This will show the procedure to model straps and adhesive on the previous model. The properties are to be calculated as shown in chapter 4. Only modelling aspects are discussed here.

Step 6. The strap is modelled using 2D shell elements. Please note that the mid plane of the strap is to be modelled. Moreover, the elements on the strap should be of same size and geometry as the elements on the panel just below it.

The adhesive layer has to be made in between the panel and the strap. An adhesive group has to be build for each single substrate node corresponding to a strap node. An initial disbond defect is included in the model. One element size all around the strap needs to be disconnected from the substrate and no adhesive group should be built there. Following figure shows a strap which has four nodes but the outer nodes are disconnected.



The first step for creating the adhesive is to create the nodes. The figure below shows the details of the nodes and elements needed to create the adhesive bond. The figure on the left shows the elements created and its purpose while the figure on the right is to be referred to for further steps. Abbreviation “N” stands for nodes, “R” for rigid elements and “S” for spring elements. **The order of steps is very important for this section and is to be followed very precisely for successful run using LICRA.**



Step 7. Create node N1 above the panel substrate node at a height corresponding to half the thickness of the panel under the strap. This is a node representing the fictitious top of the plate and corresponding at the bottom of the adhesive.

Create node N2 at a height of half the thickness of the adhesive above N1. This node represents the middle of the adhesive layer.

Create a node N3 coincident with node N2. Please record the number of nodes N2 and N3. Finally create node N4 above N2/N3 at a height corresponding to half the thickness of the adhesive from N2/N3. This node represent the top of adhesive corresponding to the fictitious bottom of the strap.

Step 8. Connect the node N1 to node N2 (to distinguish between N2 and N2 it should be enough to look at the ID of the element; the lower ID should be node N2) by using a rigid element (RBE2) (R1) with N1 being independent node and N2 having all degrees of freedom constrained to N1. Similarly connect node N4 to node N3 using a rigid element (R2) where N4 is the independent node.

Step 9. The next step is to create the spring elements between the coincident nodes. Create the three properties peel Z , shear X and shear Y as men-

tioned in chapter 4. Now create a DOF spring element (CELAS2) (S1) between node N2 and node N3 using the peel Z property. Create another spring element (S2) between these nodes using the shear X property. Finally, create a third spring element (S3) between them using shear Y property. **Ascertain that the properties are created in the order mentioned above.**

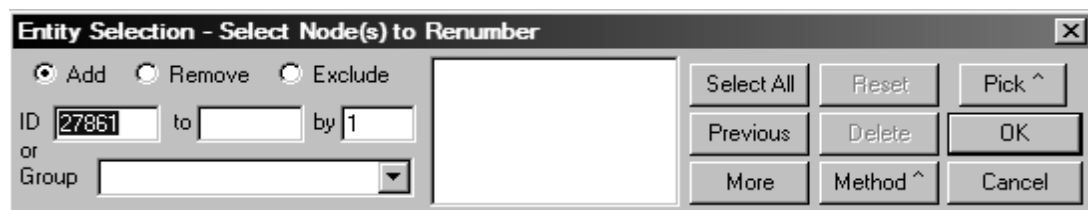
Step 10. Steps 7-9 should be repeated for each adhesive group. More easily, the group of elements can be copied and pasted in order to create the adhesive layer for each strap. Remember to leave the sides of the strap free in order to allow disbond initiation.

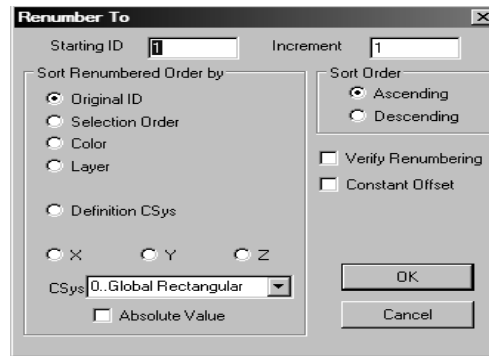
Step 11. Constrain the rotation degrees of freedom (Rx, Ry and Rz) of all the nodes on the top and bottom of the adhesive (N1 and N4).

D.1.5 Preparing the model for analysis

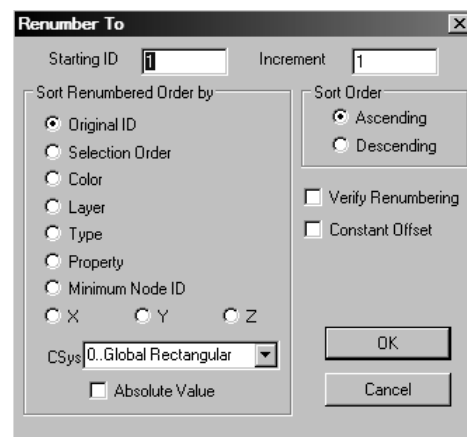
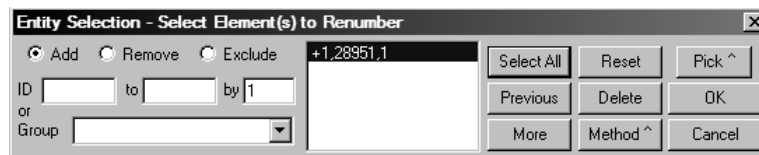
The following steps are described by using as example the pre-post processing commercial code FEMAP. The same operations described in the following steps can be made in any other pre-post processor program, such as PATRAN.

Step 12. Renumber the nodes of the model. This is done by selecting the renumber nodes option in the toolbar, selecting all nodes and renumbering them firstly by original ID and then by direction (Y-axis).





Step 13. Renumber all the elements in the model. Firstly by original ID and then by element type.



D.1.6 Creating files for analysis

The following files can be obtained with FEMAP or any other pre-processor. The format of the files though the one used by FEMAP, thus some editing work might be required to build this files with other pre-processor than FEMAP.

File 1: modello.dat. Model file (for all analysis). This is the NASTRAN file for the analysis often call also *.bdf. In the next page an example is shown. It does not matter which pre-processor translates the model to the *.dat or *.bdf file but **the order of the blocks must be as in the previous**

```

INIT MASTER(S)
SOL_SESTATIC
TIME 10000
CEND
ECHO = NONE
DISPLACEMENT(PLOT) = ALL
SPCFORCE(PLOT) = ALL
OLOAD(PLOT) = ALL
FORCE(PLOT,CORNER) = ALL
STRESS(PLOT,CORNER) = ALL
SPC = 1
LOAD = 1
BEGIN BULK
PARAM,POST,-1
PARAM,OGEOM,NO
PARAM,AUTOSPC,YES
PARAM,K6ROT,100.
PARAM,MAXRATIO,1.E+8
PARAM,GRDPNT,0
CORD2C      1      0      0.      0.      0.      0.      0.      0.      1.+NX NAC1
+NX NAC1    1.      0.      1.
CORD2S      2      0      0.      0.      0.      0.      0.      0.      1.+NX NAC2
+NX NAC2    1.      0.      1.
$ NX Nastran for FEMAP Load Set 1 : load
FORCE       1 25935      0      1.      0.      18470.      0.
$ NX Nastran for FEMAP Constraint Set 1 : constrain
SPC         1      1      156      0.
SPC         1      2      156      0.
SPC         1      3      156      0.
[...]
SPC         1 45082 13456      0.
$ NX Nastran for FEMAP Property 1 : AL
PSHELL     1      1      10.      1      0.
$ NX Nastran for FEMAP Property 2 : GLARE
PCOMP      2      0.
+          3      0.13      90.      YES      3      0.13      90.      YES+
+          3      0.13      90.      YES      2      0.34      90.      YES+
+          3      0.13      90.      YES      3      0.13      90.      YES+
+          3      0.13      90.      YES      2      0.34      90.      YES+
+          2      0.34      90.      YES      3      0.13      90.      YES+
+          3      0.13      90.      YES      3      0.13      90.      YES+
+          2      0.34      90.      YES      2      0.34      90.      YES+
+          3      0.13      90.      YES      3      0.13      90.      YES+
+          2      0.34      90.      YES      2      0.34      90.      YES+
+          3      0.13      90.      YES      2      0.34      90.      YES+
+          3      0.13      90.      YES      2      0.34      90.      YES
$ NX Nastran for FEMAP Property 6 : reigid
PBEAM      6      4 314.159 7853.98 7853.98      0. 15694.7      0.+PR      6
+PR        6      0.      -10.      10.      0.      0.      10.      -10.      0.+PA      6
+PA        6      YESA      1.
+PC        6 0.88615 0.88615
$ NX Nastran for FEMAP Material 1 : AA 7085-T7651
MAT1       1 71000.      0.33      0.
$ NX Nastran for FEMAP Material 2 : aluminium GLARE
MATS      2 70300. 70300. 0.33 26439.      0.      0.      0.+MT      2
+MT        2      0.      0.
+MA        2
$ NX Nastran for FEMAP Material 3 : GFRP GLARE
MATS      3 48900. 5500. 0.33 5500.      0.      0.      0.+MT      3
+MT        3      0.      0.
+MA        3
$ NX Nastran for FEMAP Material 4 : rigid
MAT1       4 1.E+9      0.33      0.      0.
GRID       1      0      0.      1.5      0.      0
GRID       2      0      0.      2.      0.      0
GRID       3      0      0.      2.5      0.      0
[...]
GRID       45082      0      70.      135.      0.      0
CBEAM      1      6 25935      209      0.      0.      1.
CBEAM      2      6 25935      983      0.      0.      1.
[...]
CBEAM      36      6 25935      45082      0.      0.      1.
CELAS2     37 4750. 11725      3 11726      3      0.      0.
CELAS2     38 1552.5 11725      1 11726      1      0.      0.
CELAS2     39 1552.5 11725      2 11726      2      0.      0.
CELAS2     40 4750. 12814      3 12815      3      0.      0.
CELAS2     41 1552.5 12814      1 12815      1      0.      0.
CELAS2     42 1552.5 12814      2 12815      2      0.      0.
[...]
CELAS2     10239 1552.5 32111      2 32112      2      0.
COUAD4     10240      1 3312      3100 3099      3311 180.
COUAD4     10241      1 3503      3312 3311      3502 180.
[...]
COUAD4     41375      2 31385 32473 32475 31387      0.
RBE2       41376 11724 123456 11725
RBE2       41377 11727 123456 11726
[...]
RBE2       48177 32113 123456 32112
ENDDATA
    
```

Analysis Options

Coordinate system

Force

Constraints

FE properties

Material properties

node coordinates

Elements

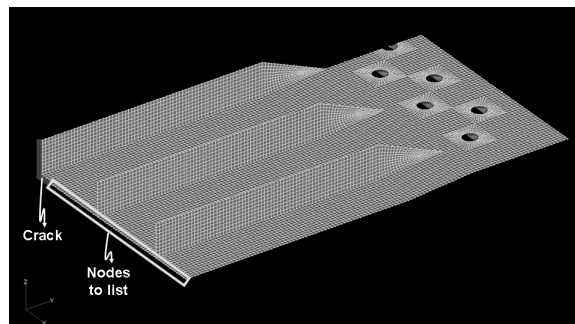
figure. If this order is not respected, LICRA will terminate with errors in the best of the cases or can give some erroneous results. If the pre-processor used does not translate to file in described order and format, some editing work on the NASTRAN file is required.

1. Analysis options. This part is not really important because the final analysis options will be written by LICRA
2. Coordinate systems.
3. Nodal forces. If temperature loads are present they should follow the force. For linear analysis only the final temperature is required so the load block should contain only the FORCE 1 and TEMP 2 parameters. For non-linear analysis a intimal temperature must be input. In this case the order of the load conditions should be: FORCE 1, TEMP 3 (final temperature), and TEMP 2 (initial temperature). In the case of a curing temperature of $120^{\circ}C$ and a test carried out at $20^{\circ}C$, TEMP 3 is $-100^{\circ}C$ on all nodes and TEMP 2 is $0^{\circ}C$ on all nodes.
4. Constraints. This part cannot be written in a compact form but each single swingle Point Constraint must be explicit.
5. Finite elements properties. In the example file PSHELL are used for the substrate, PCOMP for the GLARE strap, and PBEAM as a rigid for the load application.
6. Material properties. In the example file MAT1 (isotropic)is used for the substrate aluminium, MAT8 for the GFRP and aluminium in the GLARE strap, and MAT1 again for the rigid beam.
7. Node coordinates or GRID matrix.
8. Element connectivity matrix. In the example file CBEAM are used to apply the load, CELAS2 for the mechanical properties of the adhesive, CQUAD4 for both strap and substrate, and RBE2 for the adhesive groups.

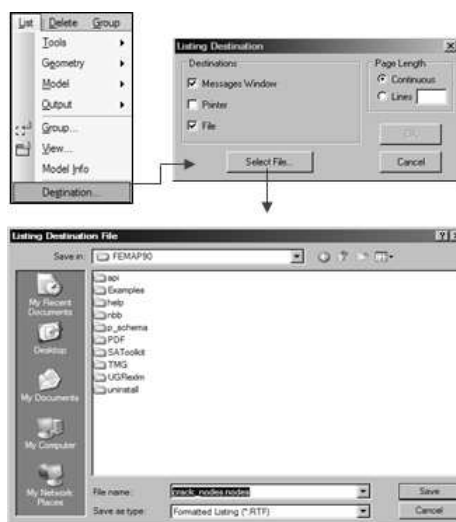
If this file is for the analysis of a un-reinforced panel then the analysis option block should be deleted from the file and the file should be renamed **modello.mesh**.

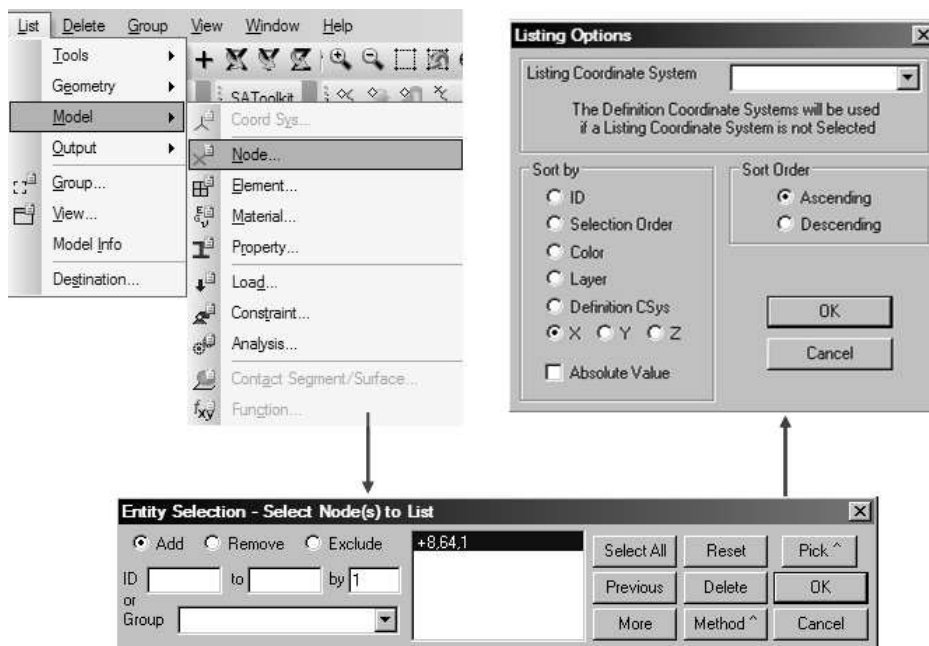
In the case of a reinforced panel this will be done during the application of the MPC by the MPC program (section D.2).

File 2: crack_nodes.nodes. Crack node file (for all analysis). This file contains the list of all nodes along the substrate crack front. For creating this file, these nodes need to be listed to a file. Please refer the picture below to see the nodes that need to be listed in this file. All the nodes of the substrate on the crack front need to be listed apart from the nodes representing the initial crack length.



The screen-shot below shows the step for listing these nodes. Please ascertain that the nodes are sorted to X direction.





Now opening the crack node file with a text editor, the file should look as shown below.

ID	Def CS	Out CS	X1	X2	X3	Color	PermBC>	Layer	#Elem	#Load	#BC
2	0	0	10.	0.	0.	46	-----	1	2	0	1
3	0	0	15.	0.	0.	46	-----	1	2	0	1
4	0	0	20.	0.	0.	46	-----	1	2	0	1
5	0	0	25.	0.	0.	46	-----	1	2	0	1
6	0	0	30.	0.	0.	46	-----	1	2	0	1
7	0	0	35.	0.	0.	46	-----	1	2	0	1
8	0	0	40.	0.	0.	46	-----	1	2	0	1
9	0	0	45.	0.	0.	46	-----	1	2	0	1
10	0	0	50.	0.	0.	46	-----	1	2	0	1
11	0	0	55.	0.	0.	46	-----	1	2	0	1
12	0	0	60.	0.	0.	46	-----	1	2	0	1
13	0	0	65.	0.	0.	46	-----	1	2	0	1
14	0	0	70.	0.	0.	46	-----	1	2	0	1
15	0	0	75.	0.	0.	46	-----	1	2	0	1
16	0	0	80.	0.	0.	46	-----	1	2	0	1
17	0	0	85.	0.	0.	46	-----	1	2	0	1

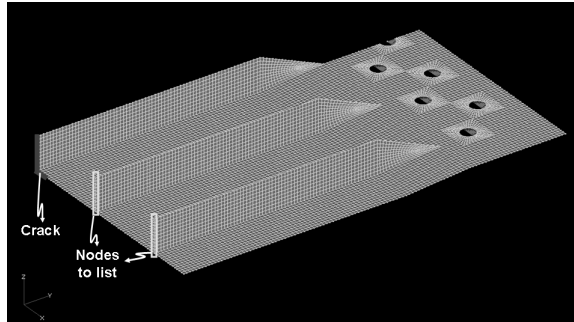
The first four lines contain only general writings, please delete those four lines along with all the other data and just leave the node ID (first column). The final file follows.

```

2
3
4
5
6
7
8
9
10
11
12
13
14
15
    
```

As can be seen all the other information has been deleted and the numbers are aligned to the left.

File 3: stringer_nodes.nodes. Stringer nodes (only in the presence of integral stringer). This file contains all the nodes along the stringer. Please refer to figure below to see the nodes to be listed. It is recommended to list all the nodes of each stringer to a separate file. In the case below, two files are to be created. The procedure is same as used to create File 2 with the only change being that the nodes are to be listed by sorting to Z direction.



The two files created are shown below. The highlighted lines are the nodes lying on the substrate and are to be deleted. Other information, apart from node ID, has to be deleted.

ID	Def CS	Out CS	X1	X2	X3	Color	PermBC>	Layer	#Elem	#Load	#BC
86	0	0	130.	0.	0.	46	-----	1	3	0	1
85	0	0	130.	0.	5.1	46	-----	1	2	0	1
84	0	0	130.	0.	10.2	46	-----	1	2	0	1
83	0	0	130.	0.	15.3	46	-----	1	2	0	1
82	0	0	130.	0.	20.4	46	-----	1	2	0	1
81	0	0	130.	0.	25.5	46	-----	1	2	0	1
80	0	0	130.	0.	30.6	46	-----	1	2	0	1
79	0	0	130.	0.	35.7	46	-----	1	2	0	1
78	0	0	130.	0.	40.8	46	-----	1	2	0	1
77	0	0	130.	0.	45.9	46	-----	1	2	0	1
76	0	0	130.	0.	51.	46	-----	1	1	0	1

ID	Def CS	Out CS	X1	X2	X3	Color	PermBC>	Layer	#Elem	#Load	#BC
51	0	0	260.	0.	0.	46	-----	1	3	0	1
96	0	0	260.	0.	5.1	46	-----	1	2	0	1
95	0	0	260.	0.	10.2	46	-----	1	2	0	1
94	0	0	260.	0.	15.3	46	-----	1	2	0	1
93	0	0	260.	0.	20.4	46	-----	1	2	0	1
92	0	0	260.	0.	25.5	46	-----	1	2	0	1
91	0	0	260.	0.	30.6	46	-----	1	2	0	1
90	0	0	260.	0.	35.7	46	-----	1	2	0	1
89	0	0	260.	0.	40.8	46	-----	1	2	0	1
88	0	0	260.	0.	45.9	46	-----	1	2	0	1
87	0	0	260.	0.	51.	46	-----	1	1	0	1

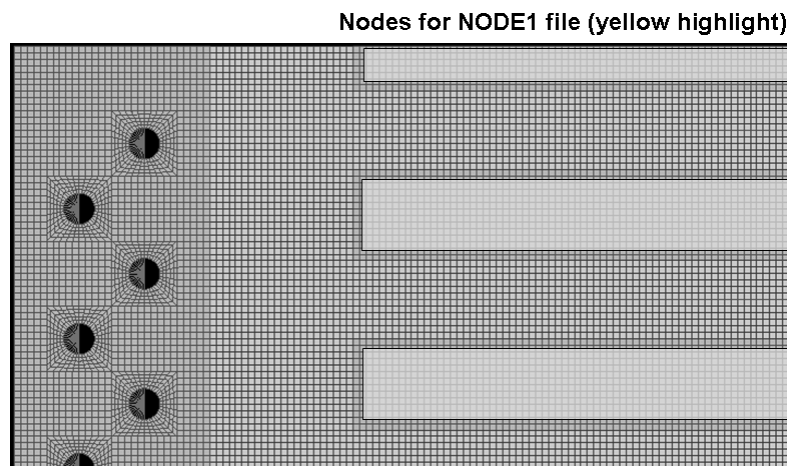
Finally create a new file called “stringer_nodes.nodes” and copy the node ID from previous files into this file. As can be seen the ID highlighted in the red box is deleted. Also the number 130 and 260 are added into the file which give the position of the stringer in X direction. Between the list of one stringer and the other to empty lines should be left.

```

130
85
84
83
82
81
80
79
78
77
76

260
96
95
94
93
92
91
90
89
88
87
    
```

File 4: nodes_1.LST. Node 1 file (only for strap analysis). This file contains the list of all the nodes on the substrate which have to be connected to the adhesive. The adhesive elements were not built along the border of the strap, hence this file lists only the nodes of the substrate below the adhesive groups, i.e. the nodes on the substrate corresponding to the strap borders should be left out. The box in the figure below highlights all the nodes to be listed. Follow same procedure as before to list these nodes. No sorting filter needs to be specified for this file. The file has to be named “nodes_1.LST”.



The final file should look as in the next page.

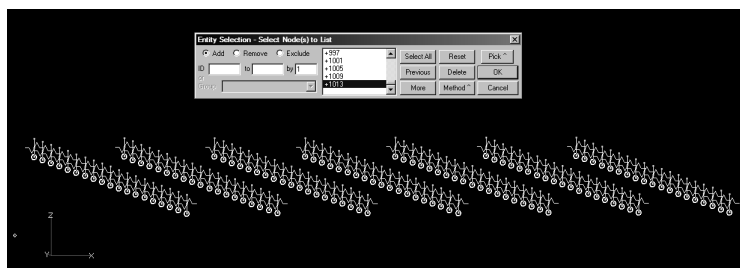
ID	Def CS	Out CS	X1	X2	X3	Color	PermBC>	Layer	#Elem	#Load	#BC
240	0	0	305.	5.	0.	46	-----	1	4	2	0
241	0	0	310.	5.	0.	46	-----	1	4	2	0
244	0	0	295.	5.	0.	46	-----	1	4	2	0
245	0	0	300.	5.	0.	46	-----	1	4	2	0
267	0	0	215.	5.	0.	46	-----	1	4	2	0
268	0	0	220.	5.	0.	46	-----	1	4	2	0
269	0	0	225.	5.	0.	46	-----	1	4	2	0
272	0	0	210.	5.	0.	46	-----	1	4	2	0
279	0	0	165.	5.	0.	46	-----	1	4	2	0
280	0	0	170.	5.	0.	46	-----	1	4	2	0
281	0	0	175.	5.	0.	46	-----	1	4	2	0
282	0	0	180.	5.	0.	46	-----	1	4	2	0
301	0	0	90.	5.	0.	46	-----	1	4	2	0
302	0	0	95.	5.	0.	46	-----	1	4	2	0
308	0	0	80.	5.	0.	46	-----	1	4	2	0
309	0	0	85.	5.	0.	46	-----	1	4	2	0
316	0	0	45.	5.	0.	46	-----	1	4	2	0
317	0	0	50.	5.	0.	46	-----	1	4	2	0
320	0	0	35.	5.	0.	46	-----	1	4	2	0
321	0	0	40.	5.	0.	46	-----	1	4	2	0
339	0	0	35.	10.	0.	46	-----	1	4	2	0
340	0	0	40.	10.	0.	46	-----	1	4	2	0
341	0	0	45.	10.	0.	46	-----	1	4	2	0

If the pre-processor used is different from FEMAP, this node file and the following should be made by using the following specific format:

1. 4 empty lines on the top of the file;
2. column 1-8 for the node IDs;
3. column 26-38 for the node X coordinate (it must be a real number, i.e. include the decimal point);
4. column 39-51 for the node Y coordinate (it must be a real number, i.e. include the decimal point);
5. column 52-64 for the node Z coordinate (it must be a real number, i.e. include the decimal point);
6. 1 empty line at the end of the file;

If this format is not complied with, the analysis ends with an error.

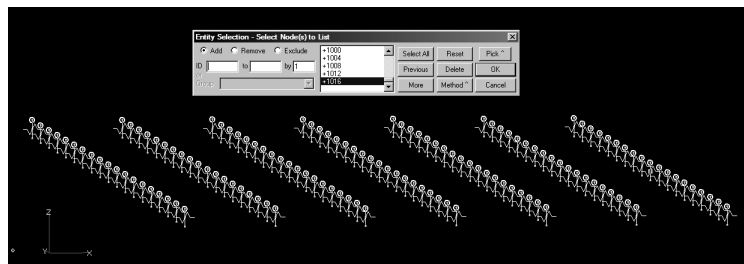
File 5: nodes.2.LST. Node 2 file (only for strap analysis). This file contains the list of all the nodes (N1) on the bottom of adhesive. The figure below helps understand the nodes to be listed. This file is to be named “nodes.2.LST”.



The final file should look as in the next page.

ID	Def CS	Out CS	X1	X2	X3	Color	PermBC>	Layer	#Elem	#Load	#BC
130	0	0	35.	5.	2.	46	-----	10	1	2	1
134	0	0	40.	5.	2.	46	-----	10	1	2	1
138	0	0	45.	5.	2.	46	-----	10	1	2	1
142	0	0	50.	5.	2.	46	-----	10	1	2	1
146	0	0	80.	5.	2.	46	-----	10	1	2	1
150	0	0	85.	5.	2.	46	-----	10	1	2	1
154	0	0	90.	5.	2.	46	-----	10	1	2	1
158	0	0	95.	5.	2.	46	-----	10	1	2	1
162	0	0	165.	5.	2.	46	-----	10	1	2	1
166	0	0	170.	5.	2.	46	-----	10	1	2	1
170	0	0	175.	5.	2.	46	-----	10	1	2	1
174	0	0	180.	5.	2.	46	-----	10	1	2	1
178	0	0	210.	5.	2.	46	-----	10	1	2	1
182	0	0	215.	5.	2.	46	-----	10	1	2	1
186	0	0	220.	5.	2.	46	-----	10	1	2	1
190	0	0	225.	5.	2.	46	-----	10	1	2	1
194	0	0	295.	5.	2.	46	-----	10	1	2	1
198	0	0	300.	5.	2.	46	-----	10	1	2	1
202	0	0	305.	5.	2.	46	-----	10	1	2	1
206	0	0	310.	5.	2.	46	-----	10	1	2	1
429	0	0	35.	10.	2.	46	-----	10	1	2	1
433	0	0	40.	10.	2.	46	-----	10	1	2	1

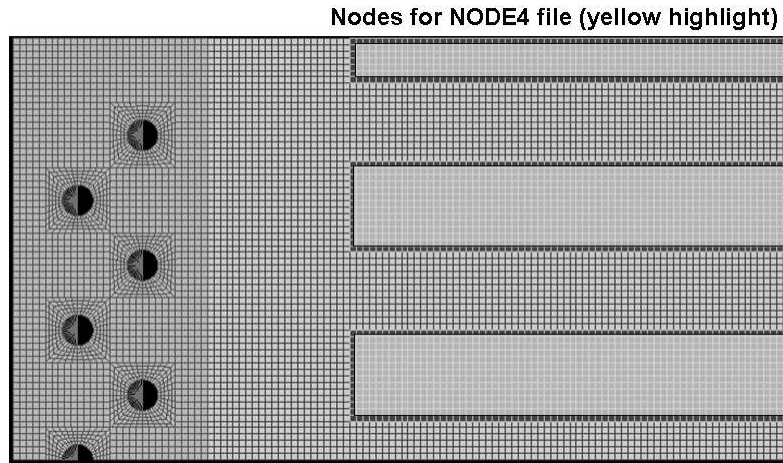
File 6: nodes_3.LST. Node 3 file (only for strap analysis): This file contains the list of all the nodes (N4) on the top of adhesive. The figure bellows helps understand the nodes to be listed. This file is to be named “nodes_3.LST”.



The final file should look as below.

ID	Def CS	Out CS	X1	X2	X3	Color	PermBC>	Layer	#Elem	#Load	#BC
133	0	0	35.	5.	2.1	46	-----	9	1	2	1
137	0	0	40.	5.	2.1	46	-----	9	1	2	1
141	0	0	45.	5.	2.1	46	-----	9	1	2	1
145	0	0	50.	5.	2.1	46	-----	9	1	2	1
149	0	0	80.	5.	2.1	46	-----	9	1	2	1
153	0	0	85.	5.	2.1	46	-----	9	1	2	1
157	0	0	90.	5.	2.1	46	-----	9	1	2	1
161	0	0	95.	5.	2.1	46	-----	9	1	2	1
165	0	0	165.	5.	2.1	46	-----	9	1	2	1
169	0	0	170.	5.	2.1	46	-----	9	1	2	1
173	0	0	175.	5.	2.1	46	-----	9	1	2	1
177	0	0	180.	5.	2.1	46	-----	9	1	2	1
181	0	0	210.	5.	2.1	46	-----	9	1	2	1
185	0	0	215.	5.	2.1	46	-----	9	1	2	1
189	0	0	220.	5.	2.1	46	-----	9	1	2	1
193	0	0	225.	5.	2.1	46	-----	9	1	2	1
197	0	0	295.	5.	2.1	46	-----	9	1	2	1
201	0	0	300.	5.	2.1	46	-----	9	1	2	1
205	0	0	305.	5.	2.1	46	-----	9	1	2	1
209	0	0	310.	5.	2.1	46	-----	9	1	2	1
432	0	0	35.	10.	2.1	46	-----	9	1	2	1
436	0	0	40.	10.	2.1	46	-----	9	1	2	1

File 7: nodes_4.LST. Node 4 file (only for strap analysis): This file contains the list of all the nodes on the strap, which are to be connected to the adhesive. As it was done for nodes_1.LST file, the nodes on the strap borders must not be selected. The box in the figure below highlights all the nodes to be listed. The file is to be named “nodes_4.LST”.



The final file should look as below.

ID	Def CS	Out CS	X1	X2	X3	Color	PermBC>	Layer	#Elem	#Load	#BC
212	0	0	35.	5.	4.375	46	-----	6	4	2	0
213	0	0	40.	5.	4.375	46	-----	6	4	2	0
214	0	0	45.	5.	4.375	46	-----	6	4	2	0
215	0	0	50.	5.	4.375	46	-----	6	4	2	0
218	0	0	80.	5.	4.375	46	-----	6	4	2	0
219	0	0	85.	5.	4.375	46	-----	6	4	2	0
220	0	0	90.	5.	4.375	46	-----	6	4	2	0
221	0	0	95.	5.	4.375	46	-----	6	4	2	0
224	0	0	165.	5.	4.375	46	-----	6	4	2	0
225	0	0	170.	5.	4.375	46	-----	6	4	2	0
226	0	0	175.	5.	4.375	46	-----	6	4	2	0
227	0	0	180.	5.	4.375	46	-----	6	4	2	0
230	0	0	210.	5.	4.375	46	-----	6	4	2	0
231	0	0	215.	5.	4.375	46	-----	6	4	2	0
232	0	0	220.	5.	4.375	46	-----	6	4	2	0
233	0	0	225.	5.	4.375	46	-----	6	4	2	0

File 8: thickness.txt. Thickness file (only for panels with variable thickness along the crack front). This file has to be created manually and must contain the distance of node from X-axis followed by the thickness of the panel at that section. The file has to be called "thickness.txt".

1	6
2	6
3	6
4	6
5	6
6	6
7	6
8	6
9	6
10	6
11	6
12	6
13	6
14	6
15	6
16	6
17	6
18	6
19	6
20	6
21	6
22	6
23	6
24	6
25	4
26	4
27	4
28	4
29	4
30	4
31	4
32	4
33	4
34	4

File 9: result.txt. Result (for all analysis): This is a blank file which needs to be created for the code to write the result in. This file should be called “result.txt”. In case of Maximum/Minimum alternate analysis, this file is to be replaced by two files called “result_max.txt” and “result_min.txt”.

At this point all this nodes should be placed in the same folder where the analysis is supposed to run. This folder will be called working directory (WD).

D.2 Multi point constrain application program: MPC.m

This Matlab function applies the multi point constraints and prepares the modello.mesh file for the SIF computation analysis (section D.3).

To run the program follow the steps.

Step 1. Open the Matlab and run the program.

Step 2. Select the WD folder.



Step 3. The program automatically selects the node files (1,2,3,4) and the modello.DAT file, applies the MPC to link substrate, adhesive and strap and writes as output a modello.mesh file. A typical scree out is shown below.

```
-----
-----MPCs-----
-----
-----25-Feb-2009 11:59:09-----
-----
Acquiring input analysis...
-----
Acquiring input file...
Input file acquired!
Acquiring nodes_1 file...
  Reading and sorting node-input file...
  Node-input file read and sorted!
Nodes_1 file acquired!
Acquiring nodes_2 file...
  Reading and sorting node-input file...
  Node-input file read and sorted!
Nodes_2 file acquired!
Acquiring nodes_3 file...
  Reading and sorting node-input file...
  Node-input file read and sorted!
Nodes_3 file acquired!
Acquiring nodes_4 file...
  Reading and sorting node-input file...
  Node-input file read and sorted!
Nodes_4 file acquired!
-----
Input analysis acquired!
-----
-----
Writing mesh file...
-----
  Skipping Bulk section...
  Bulk section skipped!
  Writing MPCs...
  MPCs writtem!
  Writing the rest of the file...
  File written!
-----
Mesh file written!
-----
-----ANALISYS TIMES-----
-----
CPU time: 0.87969 mins
System time: 1.5303 mins
-----
-----25-Feb-2009 12:00:41-----
-----
-----END MPCs-----
-----
```

D.3 SIF computation program: analysis_v2.m

This Matlab function computes the SIF of the structure for different crack lengths by computing disbond failure for each crack length. This is the main program which needs to be run to study the structure.

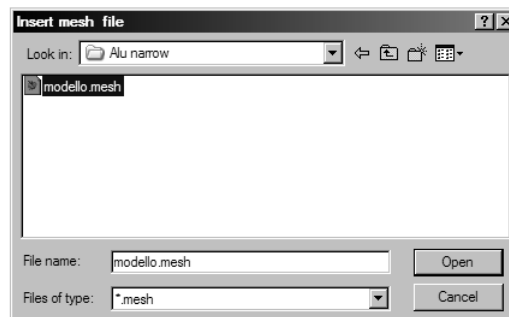
D.3.1 How to run the program

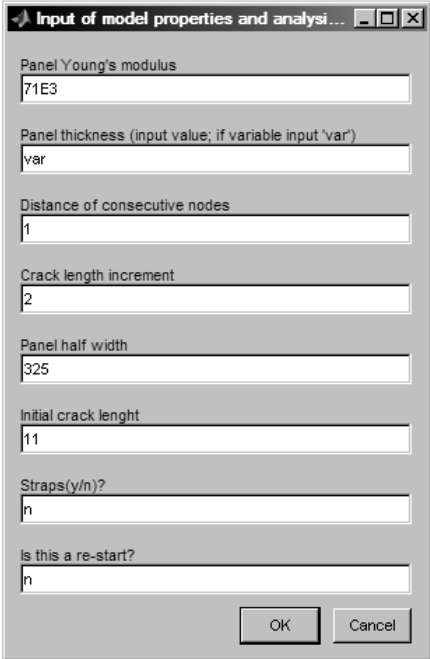
Step 1. Before running the program, the complete path to NASTRAN executable file should be inserted in lines 227, 434 and 1229 in order to allow LICRA to interface NASTRAN.

Step 2. Open the Matlab and run the program.

Step 3. Insert modello.mesh file.

```
-----  
-----VCCT analysis-----  
-----  
  
-----  
-----22-Feb-2009 20:38:00-----  
-----  
  
-----  
-----Copyright Marco Boscolo-----  
-----Last modified: 20 July 2008-----  
-----Cranfield Univerity-----  
-----
```



Step 4. Input model properties and analysis options.

Input of model properties and analysis...

Panel Young's modulus
71E3

Panel thickness (input value; if variable input 'var')
var

Distance of consecutive nodes
1

Crack length increment
2

Panel half width
325

Initial crack length
11

Straps(y/n)?
n

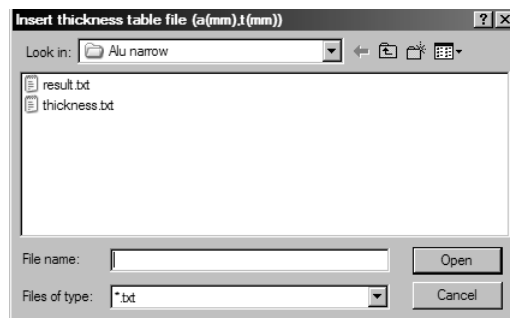
Is this a re-start?
n

OK Cancel

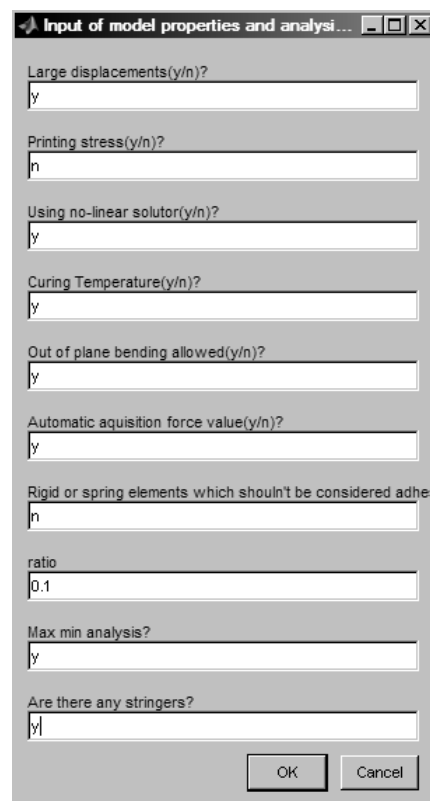
Description:

1. Substrate Young's modulus
2. Thickness of the substrate; input the thickness (mm) if it constant otherwise write "var". In the latter case the thickness file will be required.
3. Distance of the nodes on the crack path (mm). This distance must be constant in the FE model.
4. Crack propagation step for the computation of the SIF (mm).
5. Substrate half width for quarter plate models or total width for half models (mm).
6. Initial crack length (mm). The FE model must have been built with the same crack length crack length.
7. Strap? y = there is at least one strap and disbond must be analysed; n = there are no straps or, although there are straps, disbond should not be studied.
8. The code offers the possibility to re-start an analysis that accidentally stopped. It this is a restart input "y" otherwise input "n"

Step 5. If variable thickness was selected, then input the thickness file.



Step 6. Input analysis options.



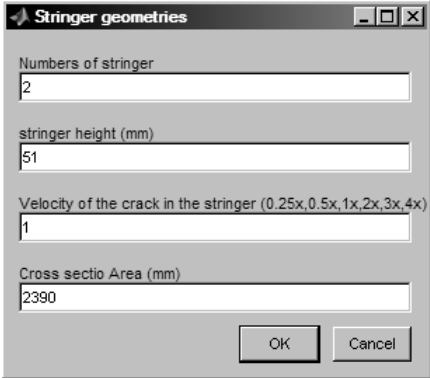
Description:

1. If a geometric non linear FE analysis is needed, select “y”, otherwise “n”.
2. If the stress analysis with crack propagation is needed, select “y”, otherwise “n”. If “y” is selected the analysis dimension will be much bigger and more hard drive space is required because stress and dis-

placement of all the structure will be printed in the *.f06 instead of just the needed ones on the crack tip.

3. Non linear solutor must be used in conjunction with large displacement analysis or if the plasticity in the strap is considered.
4. Select wheatear thermal analysis is needed or not.
5. “y” is the substrate is free to bend in the out of plane direction, “n” otherwise.
6. “y” if you want LICRA to read the force from the file, “n” if you want to insert a difference force value. Note that this value is the one used to compute the stress by dividing it to the width of the plate input in the previous window.
7. “y” if the load is applied by rigid elements, “n” otherwise. If “y” is selected then a rigid element file needs to be input where the ID of the rigid elements is listed. This option has not been completely debugged, thus it is advisable to apply the load with beam elements and select “n” on this option.
8. Input the applied R -ratio needed to conduct an alternate load analysis (section 4.3.1).
9. “y” is an alternate load analysis (section 4.3.1) is needed, “n” otherwise.
10. “y” if the structure has integral stringer which will fail, “n” otherwise. “n” should also selected for riveted stringer so that stringer failure as a function of the substrate crack length is not modelled.

Step 7. Input stringer geometry. This window appears only if “y” is input in step 6, point 10.



Stringer geometries

Numbers of stringer
2

stringer height (mm)
51

Velocity of the crack in the stringer (0.25x, 0.5x, 1x, 2x, 3x, 4x)
1

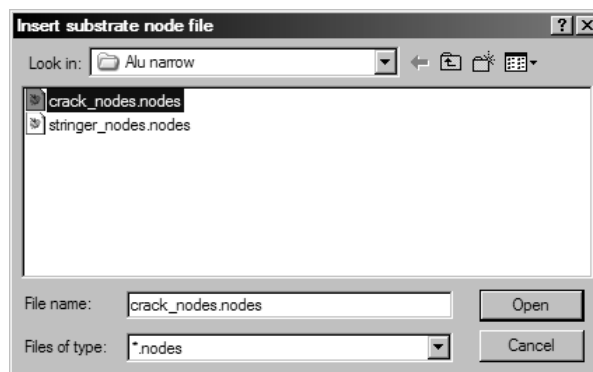
Cross sectio Area (mm)
2390

OK Cancel

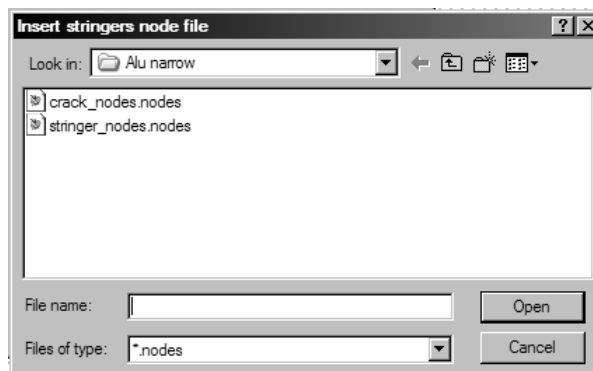
Description:

1. Input the number of intact stringer at the begging of the analysis.
This window appears only if “y” is input in step 6, point 10.
2. Input the height of the stringer (mm).
3. Input the velocity of the crack in the stringer as a function of the crack n the substrate ($\times 0.25, 0.5, 1, 2, 3, 4$)
4. input the cross section area of the stinger (mm^2) used to compute the stress in the substrate.

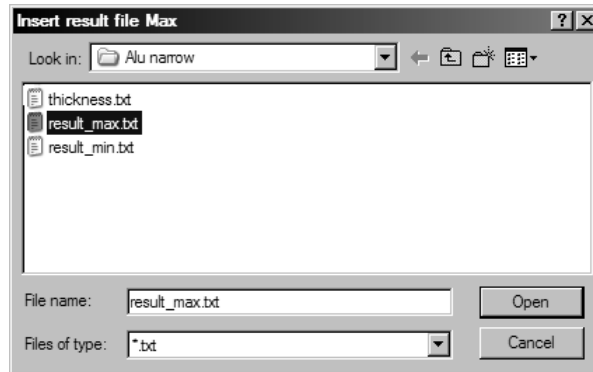
Step 8. Input the crack nodes file.



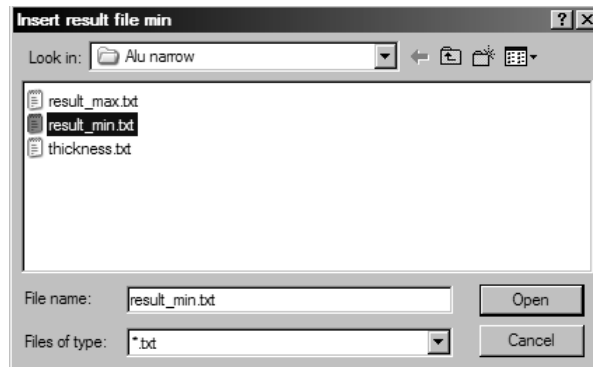
Step 9. Insert the stringer node file. This window appears only if “y” is input in step 6, point 10.



Step 10. Input the result file for the maximum applied load.

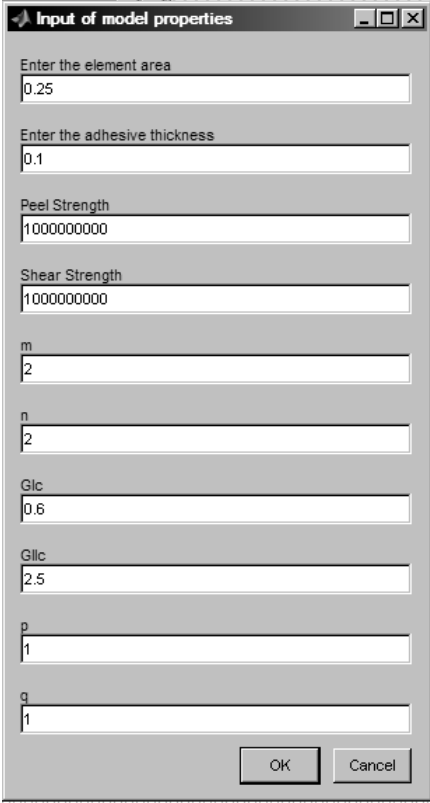


Step 11. Input the result file for the minimum applied load.



If "n" was input in the alternate analysis option (step 6, point 9) then step 10 and 11 are substitute by only one step where only one result file is asked.

Step 12. Input adhesive properties. Only if “y” is input under the strap option (step 4, point 7).



The screenshot shows a dialog box titled "Input of model properties". It contains the following fields and values:

- Enter the element area: 0.25
- Enter the adhesive thickness: 0.1
- Peel Strength: 1000000000
- Shear Strength: 1000000000
- m: 2
- n: 2
- Glc: 0.6
- Gllc: 2.5
- p: 1
- q: 1

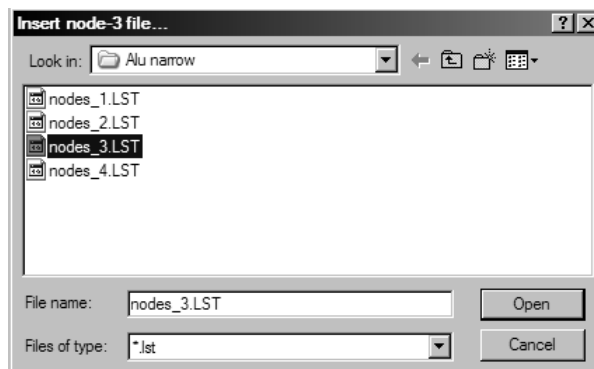
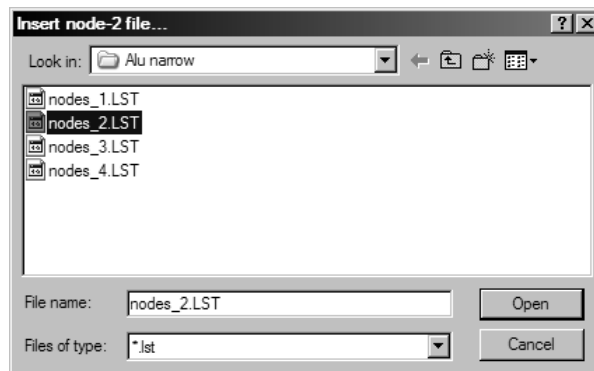
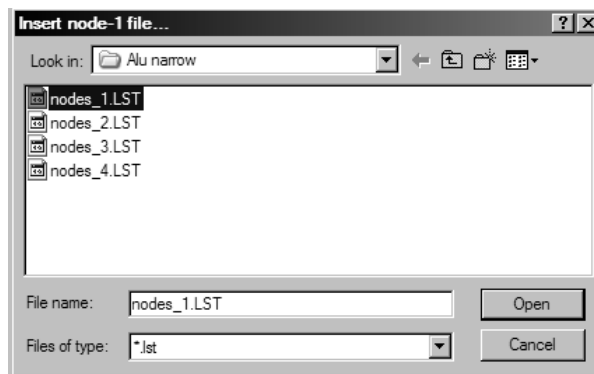
Buttons: OK, Cancel

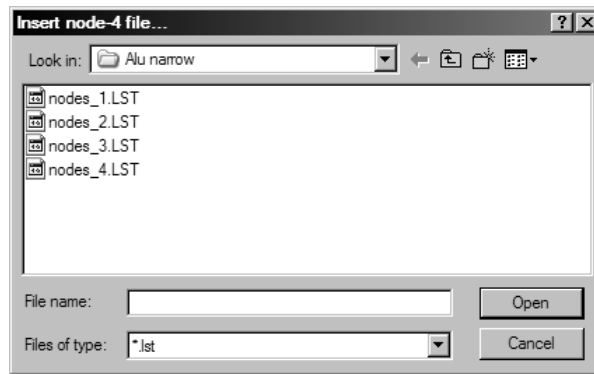
Description:

1. Adhesive element area (mm^2).
2. Adhesive thickness (mm).
3. Peel strength (MPa). This value is used no longer by LICRA. It was used in the first versions to computed disbond initiation based on a stress criterion.
4. Shear strength (MPa). This value is used no longer by LICRA. It was used in the first versions to computed disbond initiation based on a stress criterion.
5. Exponent used for peel in the mixed-mode stress-based failure criterion. This value is used no longer by LICRA.
6. Exponent used for shear in the mixed-mode stress-based failure criterion. This value is used no longer by LICRA.
7. Critical strain energy release rate for mode I (J/mm^2).

8. Critical strain energy release rate for mode II (J/mm^2).
9. Exponent used for mode I in the mixed-mode failure criterion. (1 as default)
10. Exponent used for mode II in the mixed-mode failure criterion. (1 as default)

Step 13. Insert the four node files: nodes_1.LST, nodes_2.LST, nodes_3.LST and nodes_4.LST





Step 14. The analysis starts running.

A Linux version has been created as well to run on a GRID of computers. The only difference with the Windows version is that the data must be input in a Matlab script (script_v8.m), the script must be run and it calls the main function (analysis_v8.m) which needs to be located in the same folder.

D.3.2 Output files

File 1: data.echo. The analysis input are recorded in this file.

File 2: VCCT_computation.log. It is the log file of the output on screen.

File 3: VCCT_analysis.mat. The Matlab database is stored in this file for debugging reasons.

File 4: result_max.txt The result at the maximum applied load are printed. An example is shown in the next figure.

```

a          v          Rx          Fy          Mx          GI          KI          Beta          GI_r          KI_r          beta_bot_2          beta_top_2
11| 5.82541e-003|-1.84020e-005|-1.83888e+003| 4.86901e+001| 2.14245e+000| 1.23335e+001| 1.10577e+000| 1.79199e-004| 1.95371e-001| 1.08825e+000| 1.12329e+000
13| 6.23051e-003| 1.95614e-005|-1.96320e+003|-6.07171e+001| 2.44635e+000| 1.31793e+001| 1.08691e+000| 2.37543e-004| 2.24938e-001| 1.10552e+000| 1.06829e+000
15| 6.43711e-003| 1.49912e-004|-2.02941e+003|-3.89033e+002| 2.61271e+000| 1.36200e+001| 1.04570e+000| 1.16642e-002| 1.57623e+000| 1.16672e+000| 9.24677e-001
17| 6.58786e-003| 2.80348e-004|-2.08278e+003|-7.01308e+002| 2.74421e+000| 1.39586e+001| 1.00668e+000| 3.93220e-002| 2.89408e+000| 1.21545e+000| 7.97872e-001
19| 6.76231e-003| 3.79687e-004|-2.14115e+003|-9.47884e+002| 2.89583e+000| 1.43390e+001| 9.78173e-001| 7.19799e-002| 3.91560e+000| 1.24537e+000| 7.10919e-001
21| 6.96548e-003| 4.57931e-004|-2.20692e+003|-1.14760e+003| 3.07445e+000| 1.47746e+001| 9.58695e-001| 1.05104e-001| 4.73154e+000| 1.26579e+000| 6.51521e-001
23| 7.39919e-003| 4.74442e-004|-2.34004e+003|-1.19878e+003| 3.46288e+000| 1.56802e+001| 9.72212e-001| 1.13750e-001| 4.92231e+000| 1.27746e+000| 6.66918e-001
25| 7.72020e-003| 5.20915e-004|-2.44072e+003|-1.32162e+003| 3.76858e+000| 1.63576e+001| 9.72802e-001| 1.37691e-001| 5.41558e+000| 1.29491e+000| 6.50648e-001
27| 8.05208e-003| 5.69541e-004|-2.54444e+003|-1.45093e+003| 4.09760e+000| 1.70568e+001| 9.76088e-001| 1.65273e-001| 5.93326e+000| 1.31566e+000| 6.36481e-001
29| 8.39329e-003| 6.21363e-004|-2.65068e+003|-1.59086e+003| 4.44958e+000| 1.77743e+001| 9.81446e-001| 1.97700e-001| 6.48928e+000| 1.33979e+000| 6.23072e-001
31| 8.83214e-003| 6.47070e-004|-2.78536e+003|-1.66831e+003| 4.92014e+000| 1.86905e+001| 9.98192e-001| 2.15903e-001| 6.78144e+000| 1.36038e+000| 6.35994e-001
33| 9.25576e-003| 6.86474e-004|-2.91781e+003|-1.77109e+003| 5.40131e+000| 1.95831e+001| 1.01367e+000| 2.43162e-001| 7.19682e+000| 1.38621e+000| 6.41124e-001
35| 1.00545e-002| 5.54456e-004|-3.16009e+003|-1.45626e+003| 6.35463e+000| 2.12411e+001| 1.06762e+000| 1.61486e-001| 5.86490e+000| 1.36240e+000| 7.72839e-001
37| 1.07912e-002| 4.77316e-004|-3.38903e+003|-1.25634e+003| 7.31437e+000| 2.27888e+001| 1.11402e+000| 1.19934e-001| 5.05435e+000| 1.36110e+000| 8.66940e-001
39| 1.16738e-002| 3.72367e-004|-3.66460e+003|-9.79716e+002| 8.55955e+000| 2.46471e+001| 1.17357e+000| 7.29627e-002| 3.94224e+000| 1.36128e+000| 9.85857e-001
41| 1.23669e-002| 3.59061e-004|-3.88228e+003|-9.42705e+002| 9.60234e+000| 2.61108e+001| 1.21256e+000| 6.76978e-002| 3.79735e+000| 1.38890e+000| 1.03621e+000
43| 1.32413e-002| 3.01472e-004|-4.15639e+003|-7.91001e+002| 1.10072e+001| 2.79557e+001| 1.26768e+000| 4.76929e-002| 3.18728e+000| 1.41221e+000| 1.12315e+000
45| 1.40784e-002| 2.82537e-004|-4.41954e+003|-7.40417e+002| 1.24440e+001| 2.97243e+001| 1.31759e+000| 4.18390e-002| 2.98527e+000| 1.44992e+000| 1.18526e+000
47| 1.49828e-002| 2.69130e-004|-4.70425e+003|-7.04538e+002| 1.40965e+001| 3.16365e+001| 1.37219e+000| 3.79224e-002| 2.84211e+000| 1.49546e+000| 1.24891e+000
49| 1.60058e-002| 2.50976e-004|-5.02649e+003|-6.56431e+002| 1.60906e+001| 3.38001e+001| 1.43580e+000| 3.29496e-002| 2.64922e+000| 1.54834e+000| 1.32326e+000
51| 1.71359e-002| 2.39672e-004|-5.38256e+003|-6.26319e+002| 1.84470e+001| 3.61906e+001| 1.50690e+000| 3.00222e-002| 2.52880e+000| 1.61219e+000| 1.40160e+000
53| 1.84458e-002| 2.24431e-004|-5.79597e+003|-5.86176e+002| 2.13822e+001| 3.89636e+001| 1.59146e+000| 2.63112e-002| 2.36735e+000| 1.68815e+000| 1.49476e+000

```

Description:

1. a: crack length.
2. v: opening displacement of the back node for MVCCT application.
3. Rx: rotation of the back node for MVCCT application with bending.
4. Fy: Constraint force at the crack tip node for MVCCT application.
5. Mx: Constraint moment at the crack tip node for MVCCT application with bending.
6. GI: middle plane SERR.
7. KI: middle plane SIF.
8. Beta: β computed by the middle plane SIF.
9. GI_r: bending contribution to the SERR.
10. KI_r: bending contribution to the SIF.
11. Beta_{bot_2}: β computed by the value of SIF at the bottom of the plate.
12. Beta_{top_2}: β computed by the value of SIF at the top of the plate.

File 5: result_min.txt The result at the minimum applied load are printed. the file format is the same of the previous one.

In the case no alternate analysis was selected in the analysis option input window, only one result file is printed.

Now that the displacements, rotations, constraint forces and moments have been computed for each crack length the average values of SIF, SIF range and effective R ratio need to be computed. This is done by the following program.

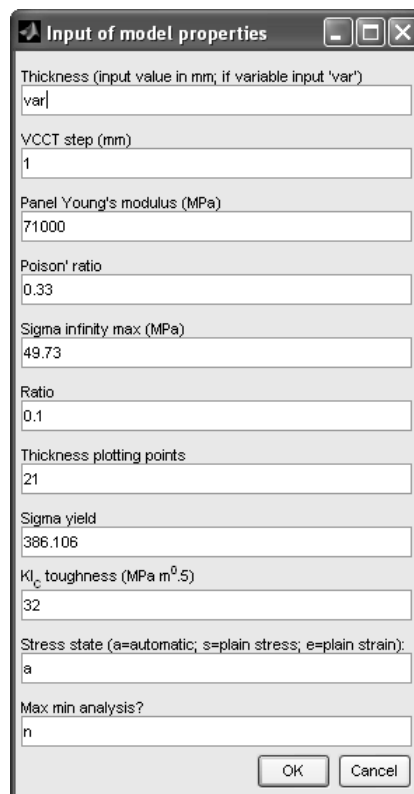
D.4 Averaged SIF range computation program: beta_Max_min.m

D.4.1 How to run the program

This is a Matlab script which computed the RMS and weighted SIF range and the effective R -ratio.

Step 1: Run the script.

Step 2: Input the analysis options.



Input of model properties

Thickness (input value in mm; if variable input 'var')
var

VCCT step (mm)
1

Panel Young's modulus (MPa)
71000

Poison' ratio
0.33

Sigma infinity max (MPa)
49.73

Ratio
0.1

Thickness plotting points
21

Sigma yield
386.106

KI_c toughness (MPa m^{0.5})
32

Stress state (a=automatic; s=plain stress; e=plain strain):
a

Max min analysis?
n

OK Cancel

Description:

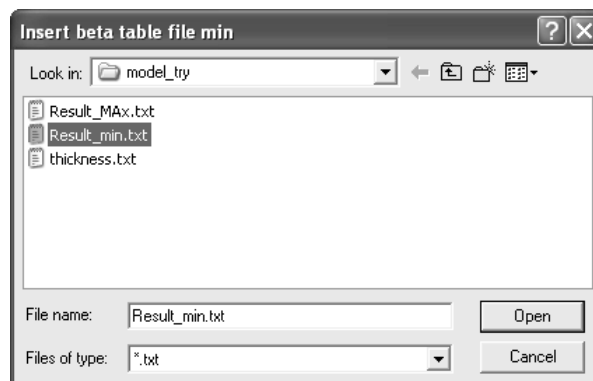
1. Input thickness of the substrate (mm) (same as section D.3 step 4 point 2).
2. Input the VCCT step used in the analysis (mm) (same as section D.3 step 4 point 3).
3. Input the elastic modulus of the substrate (MPa).

4. Poisson's ratio.
5. The maximum applied stress (MPa).
6. Applied R -ratio.
7. Number of points through the thickness where you want to know the SERR and SIF.
8. Yield stress of the substrate (MPa)
9. Substrate toughness (MPa \sqrt{m}).
10. Stress state
11. Input whether or not the program should analyse an alternate load analysis.

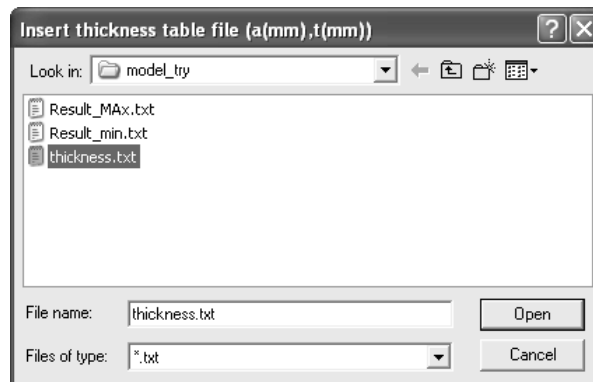
Step 3: Input the result at the maximum applied load file.



Step 4: Input the result at the minimum applied load file.



Step 5: Input the thickness file if required.



D.4.2 Output files

File 1: delta_K_Max_min.mat. Matlab database containing all the analysis variables.

File 2: delta_K_RMS.txt. The results corresponding to the RMS value of the SIF through the thickness are reported here. An example of output file follows.

```

10 25.714 0.24793 34.19 8.4767 3.2414
15 27.709 0.25268 37.078 9.3689 2.852
20 28.226 0.25679 37.979 9.7528 2.5159
25 32.344 0.26183 43.816 11.472 2.5786
30 28.958 0.26737 39.526 10.568 2.1075
35 24.467 0.27389 33.696 9.2288 1.6486
40 22.228 0.27731 30.758 8.5295 1.401
[... ]
220 34.8 0.27286 47.859 13.059 0.93527
225 34.118 0.27093 46.796 12.678 0.90668
230 38.263 0.26948 52.378 14.115 1.0057
235 38.829 0.26771 53.024 14.195 1.0097

```

Column description:

1. Crack length.
2. Effective SIF range.
3. Effective R ratio.
4. SIF at the maximum load.
5. SIF at the minimum load.
6. Equivalent β -solution.

File 3: delta_K_w.txt. The results corresponding to the weighted value of the SIF through the thickness are reported here. Same format as previous file.

File 4: delta_K_top.txt. The results corresponding to the top value of the SIF through the thickness are reported here. Same format as previous file.

File 5: delta_K_bot.txt. The results corresponding to the bottom value of the SIF through the thickness are reported here. Same format as previous file.

D.5 FCG life computation program: FCG_tabular.m

This program computed the FCG life of the structure by integration of the material law along with the SIF range solution found by the previous programs.

D.5.1 Input files

File 1: delta_K_“position”.txt. one of the output files of the previous program. usually integration are carried out with the RMS values and weighted values.

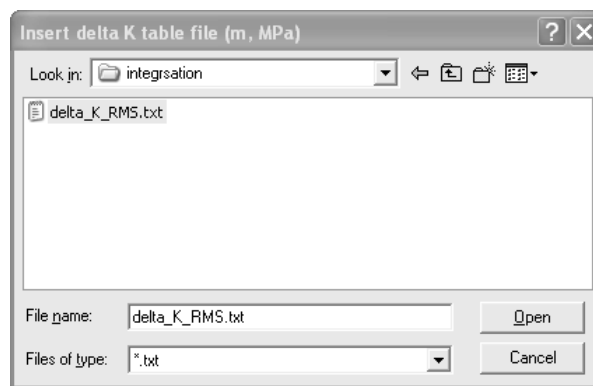
File 2: materiallaw.inp. The material law for different ratios. The file is composed by three columns, i.e. each line has 3 fields composed respectively by 10, 8, and 8 digits. On the first line there must be the number of material law curves the program needs to read. On the second line, the first field must be empty and in the following fields it reads the stress ratio of the curves. From the third row on, in the first field there must be da/dN (m/cycle), and on the next fields the values of ΔK (MPa \sqrt{m}). an example of the file follow.

2	0.1	0.6
1.1698e-8	6	3.5359
1.5334e-8	6.2	3.7487
1.9392e-8	6.4	3.9604
2.386e-8	6.6	4.168
2.8726e-8	6.8	4.3696
3.9604e-8	7.2	4.7768
[...]		
1.8572e-6	33	30.532
3.1347e-6	36	33.521
5.3784e-6	39	36.693
9.0390e-6	42	39.941

D.5.2 How to run the program

Step 1: Run the function.

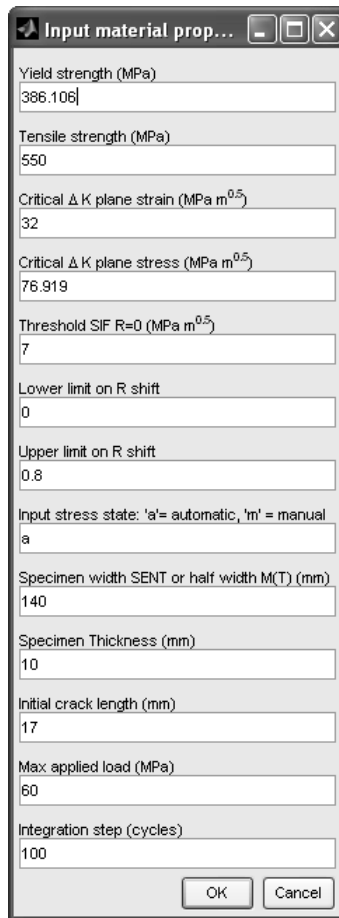
Step 2: Input the delta_K_“position”.txt file



Step 3: Input the material law file.



Step 4: Input the analysis options.



The screenshot shows a dialog box titled "Input material prop...". It contains several input fields with the following values:

- Yield strength (MPa): 386.106
- Tensile strength (MPa): 550
- Critical ΔK plane strain (MPa $m^{0.5}$): 32
- Critical ΔK plane stress (MPa $m^{0.5}$): 76.919
- Threshold SIF $R=0$ (MPa $m^{0.5}$): 7
- Lower limit on R shift: 0
- Upper limit on R shift: 0.8
- Input stress state: 'a' = automatic, 'm' = manual: a
- Specimen width SENT or half width M(T) (mm): 140
- Specimen Thickness (mm): 10
- Initial crack length (mm): 17
- Max applied load (MPa): 60
- Integration step (cycles): 100

At the bottom of the dialog box are "OK" and "Cancel" buttons.

Description:

1. Substrate yield strength (MPa).
2. Substrate ultimate tensile strength (MPa).
3. Substrate fracture Toughness (MPa \sqrt{m}).
4. Substrate Plain stress critical SIF (MPa \sqrt{m}).
5. Threshold SIF at 0 R -ratio (MPa \sqrt{m}).
6. Lower limit on the R -ratio shift to use for the extrapolation of the material laws with Harter T-method.
7. Upper limit on the R -ratio shift to use for the extrapolation of the material laws with Harter T-method.
8. Stress state.
9. Specimen width (as input in section D.3 step 4 point 5).

10. Substrate thickness (mm).
11. Initial crack length (mm).
12. Maximin applied stress (MPa).
13. Integration step in cycles. Small integration step means an accurate but time consuming analysis.

D.5.3 Output files

File 1: FCG_integration.mat. Matlab database containing all the analysis variables.

File 1: integration.log. Log file.

File 1: FCG_life.txt. File containing all the integration steps till final fracture.

File 1: FCG_life.plt. File containing a summary of the FCG life for easy plot.

```

17      0      23.703  7.3561e-007
20.242 4300   24.738  7.8415e-007
24.098 8600   28.409  1.0757e-006
28.775 12900  27.629  9.9057e-007
32.644 17200  25.593  8.3013e-007
36.003 21500  24.003  7.4598e-007
[...]
117.93 1.29e+005  26.104  8.5656e-007
118.18 1.293e+005 26.122  8.5756e-007

```

Column description:

1. Crack length (mm).
2. Number of cycles.
3. SIF range (MPa \sqrt{m}).
4. FCG rate da/dN (m/cycle).

The output on screen gives the final FCG life values and the failure criteria. An example is shown in the next page.

```

-----FCG integration-----
-----
26-Feb-2009 10:36:03
-----

Copyright Marco Boscolo
Last modified: 16 January 2008
Cranfield University
-----

Instruction

This program integrates the material law as a function crack length a, delta K,
and R effective.
Two input files are required:
1.Delta K file (*.txt) where there must be three columns of values separated by
one space. The first column must contain the crack length (mm), the second
column Delta K values (MPa m0.5), and the third column the effective ratio
2.The material law for different ratios (.inp). The file is composed by three
columns, i.e. each line has 3 fields composed, respectively by 10, 8, and 8
digits. On the first line there must be the number of material law curves the
program needs to read. On the second line the first field must be empty and in
the following fields it will read the stress ratio of the curves it needs to
read. From the third row on, in the first field there must be da/dN as m/cycle,
and on the next fields the values of Delta K (MPa m0.5).
The results will be written in 3 files in the working directory (the same of the
input files):
1.'FCG_life.txt' where there are all the integration steps and you can find
4 columns containing a(mm), N(cycles), Delta K(MPa m0.5),and da/dN(m/cycles)
2.'FCG_life.plt' it is equal to the previous one but there are less step so it is
easier to plot
3.it is a log file 'integration.log' where all the writings on the screen are
recorded.
The final life and crack length is showed on screen.

Press any key to continue...

-----
Acquiring input analysis...
-----
Acquiring delta K table file...
Input delta K table acquired!
Acquiring material law file...
Material law file acquired!
Computing Walker equation exponent m using the harter T-method point by point..
Walker equation exponent m computed!
Acquiring analysis inputs...
Analysis inputs acquired!
Computing critical crack lenght for net section yield and fracture toughness...
Apparent Fracture toughness= 90.286 MPa m0.5
Net section yield crack length = 118.2443 mm
Critical crack lenght for net section yield and fracture toughness computed!

Input analysis acquired!
-----

Integrating...
-----
Net section yield
FCG life = 129300 cycles
Final crack length = 118.18 mm
-----
Integration computed!
-----

Printing results...
-----
Results printed!
-----

-----ANALISYS TIMES-----
-----
CPU time: 3.1094 secs
System time: 58.3912 secs
-----

26-Feb-2009 10:37:02
-----

-----END FCG integration-----
-----

```

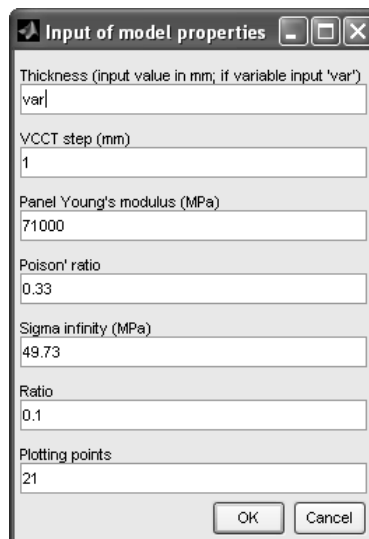
D.6 Through-thickness SERR and SIF distribution: plot_2D_result.m

This last Matlab script included in the LICRA package is to compute the distribution of SERR and SIF through the thickness if needed.

D.6.1 How to run the program

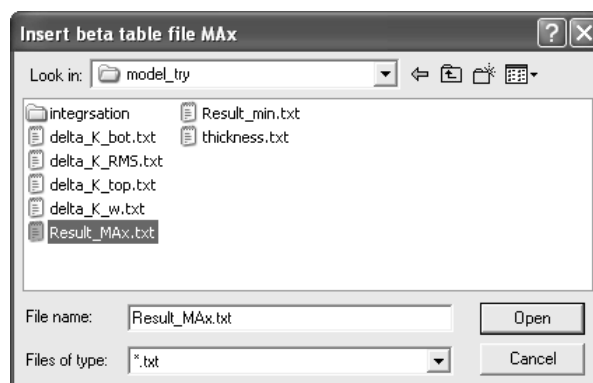
Step 1. Run the script.

Step 2. Input analysis options.



Each of the input parameters has been described previously.

Step 3. Input the result file from the analysis_v2.m program.



D.6.2 Output files

File 1: result_crack_2D.out. For each crack length some of the representative fracture mechanics parameters are reported. An example follows.

```
#####
# RESULTS
#####
# a      KI_Max  KI_min  KI_mean  KI_bending  V_RMS  GI_total  GI_Max  GI_min  betaI_Max  betaI_min
# 3.10e+01 6.62547586e+00 6.00407811e+00 6.31452999e+00 3.10548856e-01 6.31748040e+00 5.61112011e-01 6.18257897e-01 5.07776330e-01 1.12526613e+00 1.01997015e+00
# 3.40e+01 6.88339856e+00 6.09760116e+00 6.48047751e+00 3.02817745e-01 6.48425333e+00 5.82182708e-01 6.61489742e-01 5.21875129e-01 1.13283351e+00 1.00470119e+00
# 3.60e+01 7.12827371e+00 6.08212130e+00 6.40978031e+00 5.18492216e-01 6.61657823e+00 6.16558493e-01 7.13585589e-01 5.22581768e-01 1.14148210e+00 9.75074234e-01
# 3.80e+01 7.59028407e+00 5.59802491e+00 6.59455501e+00 9.35289576e-01 6.61994713e+00 6.17248491e-01 8.11410362e-01 4.41530416e-01 1.18298541e+00 8.72637591e-01
# 4.00e+01 8.13395651e+00 4.80371711e+00 6.44697891e+00 1.66604961e+00 6.54091019e+00 6.10257878e-01 9.12270794e-01 3.25005167e-01 1.23358086e+00 7.12972731e-01
[...]
# 1.20e+02 2.12704109e+01 8.12531450e+00 1.47478631e+01 6.32154872e+00 1.52226316e+01 3.26779375e+00 6.17217066e+00 9.50885721e-01 1.86551355e+00 7.12198367e-01
# 1.22e+02 2.22076831e+01 8.54824531e+00 1.51784646e+01 6.82321891e+00 1.38773898e+01 3.55023391e+00 6.94611594e+00 1.02941648e+00 1.89168866e+00 7.49370755e-01
# 1.24e+02 2.33059716e+01 8.90928311e+00 1.61079490e+01 7.13802261e+00 1.68771160e+01 3.88540471e+00 7.65014982e+00 1.11810796e+00 2.01080301e+00 7.68734603e-01
```

File 2: result_step_2D.out. The distribution of SERR and SIF through the thickness for each crack length is printed. The next figure shows an example.

```
#####
# SERR RESULTS
#####
#
#-----
# STEP = 1 ; crack length = 32
#-----
#
# z      KI      GI      betaI
# 5.00e-01 6.62547586e+00 6.18257897e-01 1.12526613e+00
# 01 6.59442280e+00 6.12476024e-01 1.11999210e+00
# 1.50e+00 6.56336962e+00 6.06721297e-01 1.11471805e+00
# 02 6.53231628e+00 6.00993705e-01 1.10944397e+00
# 2.50e+00 6.50126278e+00 5.95293248e-01 1.10416987e+00
# 03 6.47020211e+00 5.89619926e-01 1.09899374e+00
# 3.50e+00 6.43915533e+00 5.83993740e-01 1.09362158e+00
# 04 6.40810136e+00 5.78354689e-01 1.08834740e+00
# 4.50e+00 6.37704724e+00 5.72762773e-01 1.08307319e+00
# 05 6.34599294e+00 5.67197992e-01 1.07779895e+00
# 5.50e+00 6.31493849e+00 5.61660347e-01 1.07252468e+00
# 06 6.28388386e+00 5.56149837e-01 1.06725039e+00
# 6.50e+00 6.25282906e+00 5.50666462e-01 1.06197606e+00
# 07 6.22177408e+00 5.45210222e-01 1.05670170e+00
# 7.50e+00 6.19071899e+00 5.39781118e-01 1.05142732e+00
# 08 6.15966359e+00 5.34327914e-01 1.04615290e+00
# 8.50e+00 6.12860808e+00 5.29004314e-01 1.04087846e+00
# 09 6.09755238e+00 5.23656615e-01 1.03560398e+00
# 9.50e+00 6.06649649e+00 5.18336052e-01 1.03032947e+00
# 10 6.03544041e+00 5.13042624e-01 1.02505493e+00
# 1.01978035e+00
#-----
# STEP = 2 ; crack length = 34
#-----
#
# z      KI      GI      betaI
# 5.00e-01 6.86329485e+00 6.63439742e-01 1.13085353e+00
# 01 6.82501579e+00 6.56058906e-01 1.12454635e+00
# 1.50e+00 6.78673647e+00 6.48720297e-01 1.11823913e+00
# 02 6.74845689e+00 6.41422914e-01 1.11193187e+00
# 2.50e+00 6.71017705e+00 6.34166759e-01 1.10562457e+00
# 03 6.67189695e+00 6.26951830e-01 1.09931722e+00
# 3.50e+00 6.63361658e+00 6.19778129e-01 1.09300983e+00
# 04 6.59533593e+00 6.12645654e-01 1.08670239e+00
# 4.50e+00 6.55705500e+00 6.05554406e-01 1.08039491e+00
#-----
# STEP = 47 ; crack length = 124
#-----
#
# z      KI      GI      betaI
# 5.00e-01 2.33059716e+01 7.65014982e+00 2.01080303e+00
# 01 2.25865716e+01 7.18515503e+00 1.94873431e+00
# 1.50e+00 2.18671543e+01 6.73472789e+00 1.88666410e+00
# 02 2.11477180e+01 6.29886840e+00 1.82459226e+00
# 2.50e+00 2.04282606e+01 5.87757657e+00 1.76251859e+00
# 03 1.97087800e+01 5.47085239e+00 1.70044292e+00
# 3.50e+00 1.89892733e+01 5.07869586e+00 1.63896500e+00
# 04 1.82697376e+01 4.70110599e+00 1.57628458e+00
# 4.50e+00 1.75501692e+01 4.33808576e+00 1.51420134e+00
# 05 1.68305641e+01 3.98963218e+00 1.45211492e+00
# 5.50e+00 1.61109172e+01 3.65574626e+00 1.39002491e+00
# 06 1.53912227e+01 3.33642800e+00 1.32793078e+00
# 6.50e+00 1.46714735e+01 3.03167738e+00 1.26583195e+00
# 07 1.39516613e+01 2.74149442e+00 1.20372767e+00
# 7.50e+00 1.32317758e+01 2.46587911e+00 1.14161706e+00
# 08 1.25118042e+01 2.20483146e+00 1.07949903e+00
# 8.50e+00 1.17917909e+01 1.95835145e+00 1.01737223e+00
# 09 1.10715359e+01 1.72643910e+00 9.55234923e-01
# 9.50e+00 1.03511940e+01 1.50909440e+00 8.93084936e-01
# 10 9.63067198e+00 1.30631736e+00 8.30919418e-01
# 7.68734603e-01
```

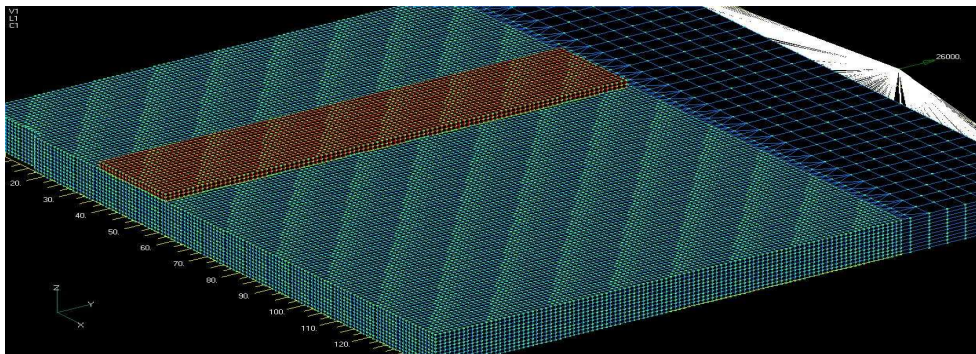

Appendix E

User's instructions to the 3D-VCCT program code

This program is still developing. It was design to include LICRA package and expand it to 3D FE analysis with progressive development of the through-thickness crack front. Unfortunately it is not completed at this time and only 3D FE analysis with straight crack front without any disbond progression are fully functional.

E.1 How to build the FE model

The only mandatory disposition to build the model is that elements of the same dimension need to be used on the crack front. The whole model should be built with 3D 8-node brick elements (see following picture).



Two input files need to be created.

File 1: modello.nas. It contains the model in NASTRAN language. the file must be organised as file 1 in section D.1.6. The analysis option part of the file needs to be delated.

File 2: nodes.RTF. It contains all the nodes on the crack surface. There is no need to sort the nodes but they must be printed to file as described for file 2 in section D.1.6. Some post processing of the file is required, the first 4 lines should be delated and also all the columns after the sixth one. An example of the node file is shown in the next figure.

```

2023      0      0      121.      0.      0.
2124      0      0      120.      0.      0.
2235      0      0      119.      0.      0.
2337      0      0      118.      0.      0.
2439      0      0      117.      0.      0.
2543      0      0      116.      0.      0.
2653      0      0      115.      0.      0.
2756      0      0      114.      0.      0.
[...]
```

157390	0	0	33.	0.	10.
157492	0	0	32.	0.	10.
160925	0	0	125.	0.	10.
160927	0	0	124.	0.	10.
160929	0	0	123.	0.	10.
160930	0	0	122.	0.	10.
161165	0	0	53.	0.	10.
161268	0	0	51.	0.	10.
161312	0	0	50.	0.	10.
161415	0	0	48.	0.	10.
161607	0	0	44.	0.	10.
161803	0	0	40.	0.	10.
161939	0	0	37.	0.	10.

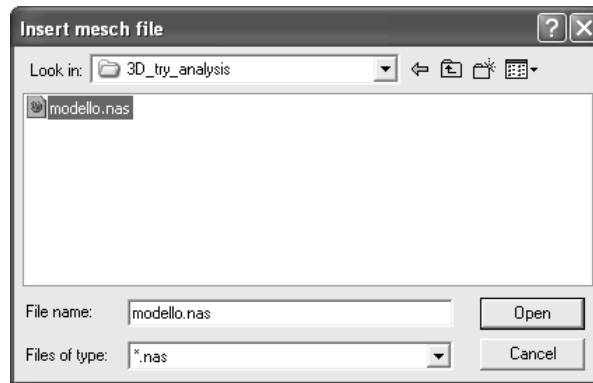
E.2 SIF computation program

E.2.1 How to run the code

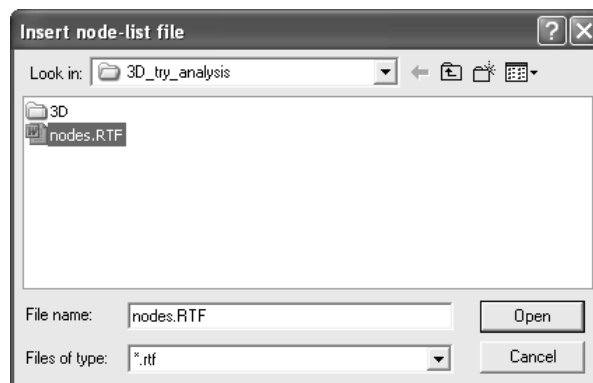
In order to run the program follow the steps.

Step 1. Write the complete path to NASTRAN executable file in line 48 in order to allow the code to interface NASTRAN.

Step 2. Input the model file.



Step 3. Input the node file.



Step 4. Input the analysis options.

Analysis options

Dimensions of the model?(2/3)
3

Disbond study (y/n)?
n

How many disbond surfaces?
1

Plastic analysis for the strap(y/n)?
n

Elastic or Elasto-plastic fracture mechanics(e/p)?
e

Geometric non-linearity?(y/n)
y

Printing stress?(y/n)
n

Curing temperature of the adhesive different from room temp?(y/n)
n

Out of plane bending allowed?(y/n)
y

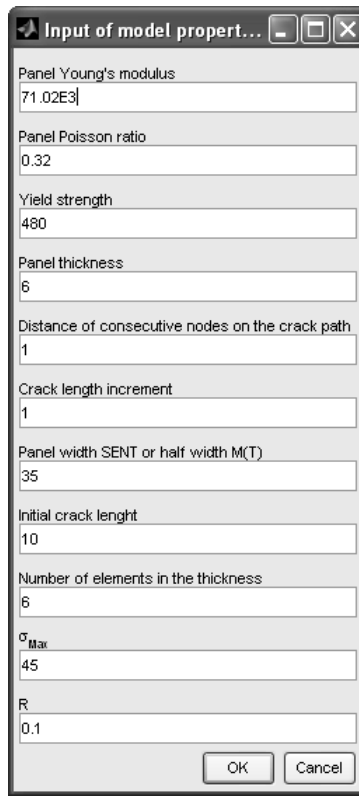
Automatic acquisition force value?(y/n)
y

Plane stress/strain factor, 0=plain stress; 1=plain strain; 0 <=q<= 1
0

OK Cancel

Description:

1. Whether the input is a 3D model or a 2D model. At this time only 3D analysis is implemented.
2. Whether disbond should be studied. At this time disbond study is not implemented.
3. Disbond is not implemented so 1 is left as default.
4. Whether plastic deformation in the strap should be considered.
5. Only linear elastic fracture mechanics is implemented.
6. Whether a non linear analysis needs to be run.
7. Whether the stress analysis of the structure should be done at each crack length.
8. Whether the are TRS.
9. Whether out of plane deformation is allowed in the model
10. Whether the applied force value needs to be read from the model file.
11. Stress condition.

Step 4. Input model properties.

Input of model properties dialog box showing the following values:

- Panel Young's modulus: 71.02E3
- Panel Poisson ratio: 0.32
- Yield strength: 480
- Panel thickness: 6
- Distance of consecutive nodes on the crack path: 1
- Crack length increment: 1
- Panel width SENT or half width M(T): 35
- Initial crack length: 10
- Number of elements in the thickness: 6
- σ_{max} : 45
- R: 0.1

Description:

1. Elastic modulus of the substrate (MPa).
2. Poisson's ratio.
3. Yield strength (MPa)
4. Thickness of the panel (mm).
5. Element size on the crack path (mm).
6. Analysis step. It must be a multiple of the element size and determines the crack lengths at which the results are printed.
7. Substrate width (mm).
8. Initial crack length (mm)
9. Number of elements through the thickness on the crack path surface.
10. Maximum applied stress (MPa)
11. Applied R -ratio.

Step 5. The code starts running. A classical output screen is shown in the next picture.

```

-----ANALYSIS-----
STEP = 1 ; crack lenght = 32
-----
Applying the VCCT...
Computing back and front nodes for VCCT...
Back and front nodes computed
Releasing nodes to apply VCCT...
Nodes released
Writing NASTRAN input file...
NASTRAN input file written
Starting NASTRAN analysis...
XXXXXXXXXXXXXXXXXXXXXXXXXXXXXXXXXXXXXXXXXXXXXXXXXXXXXXXXXXXXXXXXXXXXXXXXXXXX
MSC.Nastran V2005.0 (Intel Windows XP 5.1 (Build 2600)) Thu Jun 12 10:48:17 2008
*** SYSTEM INFORMATION MESSAGE (pgm: nastran, fn: estimate_job_requirements)
Starting ESTIMATE, please wait...
MSC.Nastran beginning job 32_1_model10.
MSC.Nastran started Thu Jun 12 10:48:19 GST 2008
MSC.Nastran finished Thu Jun 12 11:25:46 GST 2008
MSC.Nastran job 32_1_model10 completed.OCC
*** USER INFORMATION MESSAGE (pgm: nastran, fn: estimate_job_requirements)
Estimated DOF=502593
Estimated memory=237.7MB
Estimated disk=5086.0MB
XXXXXXXXXXXXXXXXXXXXXXXXXXXXXXXXXXXXXXXXXXXXXXXXXXXXXXXXXXXXXXXXXXXXXXXXXXXX
NASTRAN analysis completed
Reading NASTRAN outputs...
Reading displacements...
Displacements read
Reading forces...
Forces read
NASTRAN outputs read
Computating SERR...
Sorting output vectors...
Output vectors sorted
Computening SERR and SIF...
SERR and SIF computed
Computening max min Beta...
Max min Beta computed
SERR computed
VCCT applied!
-----
Saving and Printing step results...
Writing result files...
Result files written
Plotting...
Plotted
Step results saved and printed!
-----
[...]
STEP = 10 ; crack lenght = 122
-----
Applying the VCCT...
Computing back and front nodes for VCCT...
Back and front nodes computed
Releasing nodes to apply VCCT...
Nodes released
Writing NASTRAN input file...
NASTRAN input file written
Starting NASTRAN analysis...
XXXXXXXXXXXXXXXXXXXXXXXXXXXXXXXXXXXXXXXXXXXXXXXXXXXXXXXXXXXXXXXXXXXXXXXXXXXX
MSC.Nastran V2005.0 (Intel Windows XP 5.1 (Build 2600)) Thu Jun 12 18:05:32 2008
*** SYSTEM INFORMATION MESSAGE (pgm: nastran, fn: estimate_job_requirements)
Starting ESTIMATE, please wait...
MSC.Nastran beginning job 122_10_odel10.
MSC.Nastran started Thu Jun 12 18:05:35 GST 2008
MSC.Nastran finished Thu Jun 12 18:55:55 GST 2008
MSC.Nastran job 122_10_odel10 completed.OCC
*** USER INFORMATION MESSAGE (pgm: nastran, fn: estimate_job_requirements)
Estimated DOF=503533
Estimated memory=239.1MB
Estimated disk=5099.2MB
XXXXXXXXXXXXXXXXXXXXXXXXXXXXXXXXXXXXXXXXXXXXXXXXXXXXXXXXXXXXXXXXXXXXXXXXXXXX
NASTRAN analysis completed
Reading NASTRAN outputs...
Reading displacements...
Displacements read
Reading forces...
Forces read
NASTRAN outputs read
Computating SERR...
Sorting output vectors...
Output vectors sorted
Computening SERR and SIF...
SERR and SIF computed
Computening max min Beta...
Max min Beta computed
SERR computed
VCCT applied!
-----
Saving and Printing step results...
Writing result files...
Result files written
Plotting...
Plotted
Step results saved and printed!
-----
Saving and Printing final results...
Plotting...
Plotted
Step results saved final printed!
-----
-----ANALYSIS TIMES-----
CPU time: 491.7274 mins
System time: 491.7256 mins
-----
12-Jun-2008 18:56:15
-----
-----END ANALYSIS-----

```


E.2.2 Output files

File 1: workspace.mat. Matlab database containing all the analysis variables.

File 2: analysis.log. Log file of the analysis.

File 3: result_crack.out SERR and SIF are written for each crack length. The file format is the same of the output file reported in section D.6.2 file 1.

File 4: result_step.out The distribution of SERR and SIF through the thickness for each crack length is printed. The file format is the same of the output file reported in section D.6.2 file 2.

Plot files. For each crack length the plot of β , SERR, and SIF through the thickness is saved in two format: *.jpg and *.eps.

